PAUL SCHERRER INSTITUT

Final Report

Bundesamt für Energie - Contract EF-REN (92)033

Research & Development of the Process Technology for Converting Concentrated Solar Energy into Chemical Fuels

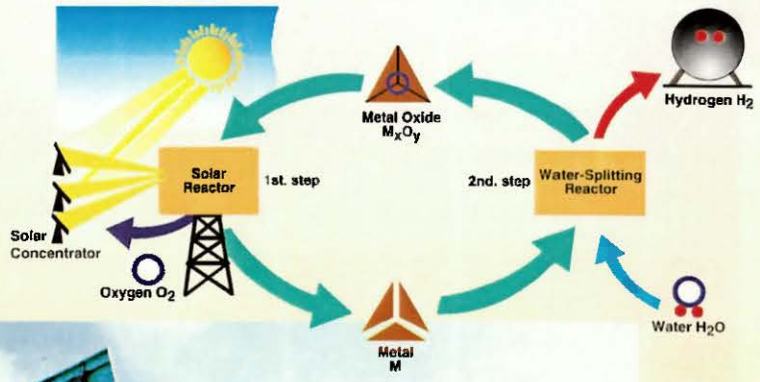

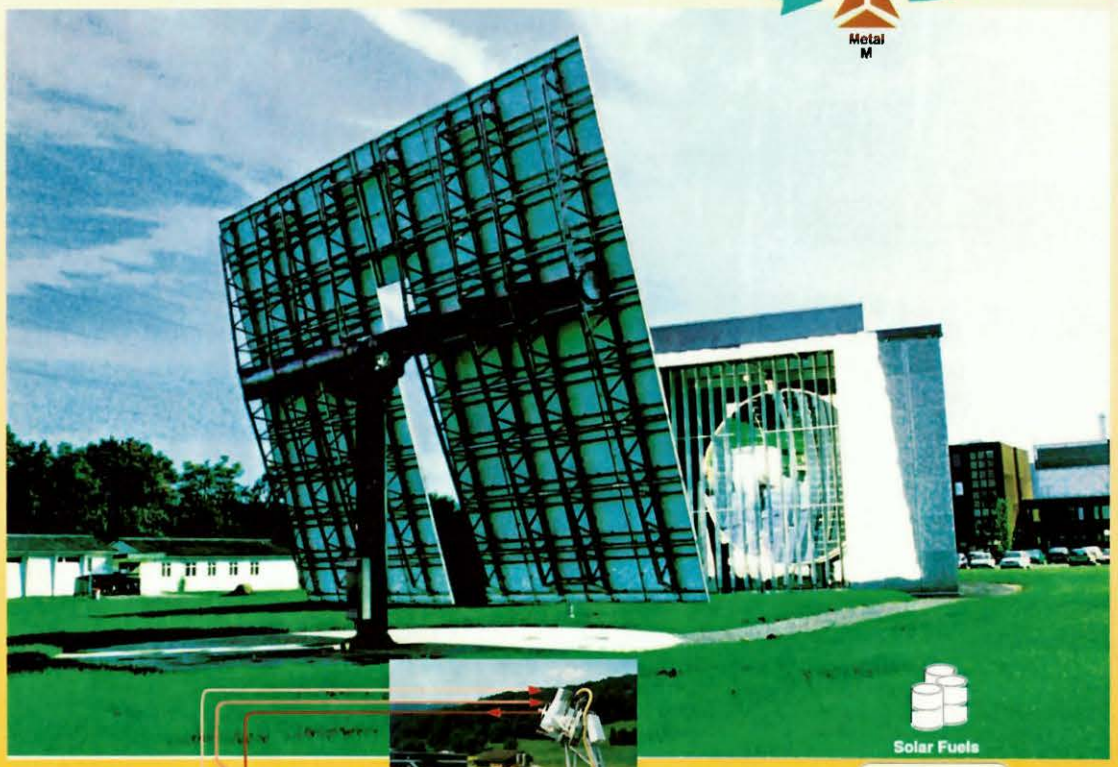

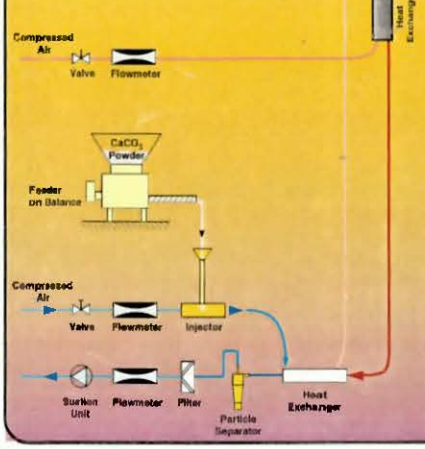

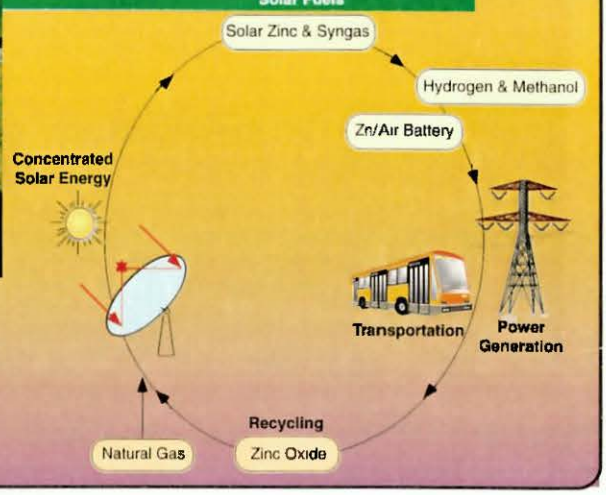

LOUEGROUE

Final Report

Bundesamt für Energie - Contract EF-REN (92)033

Research & Development of the Process Technology for Converting Concentrated Solar Energy into Chemical Fuels

December 1998

Paul Scherrer Institute
Solar Technology
CH-5232 Villigen PSI

Telephone (Exchange) +41 56 310 21 11
Telephone (Secretary) +41 56 310 29 86
Telefax (central) +41 56 310 21 99

Acknowledgments

We thank the Bundesamt für Energie (*BFE)* for financial support of this Project.

The work described in this report was conducted at the Paul Scherrer Institute (*PSI*) by the members of the Solar Process Technology Group (Head Dr. A. Steinfeld) of the Solar Technology Section (Head Prof. Dr. R. Palumbo):

M. Brack

J. Ganz

P. Haueter

A. Imhof

A. Meier

D. Mischler

St. Moeller

R. Palumbo

Th. Schelling

A. Schwarz

Th. Seitz

A. Steinfeld

A. Weidenkaff

D. Wuillemin

We thank all the technical and administrative personnel of the PSI who have been contributing to this work.

External Collaboration

Bühler AG, Uzwil, Switzerland	Pulsar reactor (completed 1995)
A. Ferrier, CNRS-Odeillo, France	Solar flux measurement (since 1996)
Prof. E. Fletcher, University of Minnesota, USA	Solar processing of carbides and nitrides (1994-1995) Solar decomposition of ZnO (since 1997)
Dr. H. Funken, DLR-Köln, Germany	Reaction cell experiment (completed 1994)
Prof. A. Kirillov, Boreskov Institute, Russia	Thermal cracking of hydrocarbons (1995-1998)
T. Lang, Holderbank-Management AG	Solar cement (1996-1998)
Dr. J. Lédé, CNRS-Nancy, France	Solar decomposition of ZnO (since 1996)
Prof. J. Murray, Portland State University, USA	Solar processing of carbides and nitrides (1994-1995)
Prof. R. Palumbo, Valparaiso University, USA	Exergy analysis of solar thermocycles (completed 1994) Thermal reduction of CO_2 (1995-1996)
Prof. A. Reller, University of Hamburg, Germany	CH_4-Reduction of ZnO (1994) Reduction of metal oxides (since 1995)
Dr. D. Rose, Krupp-Polysius	Solar cement (1996-1997)
Dr. C. Sasse, DLR-Stuttgart, Germany	Optical properties of particle suspensions (completed 1994)
Prof. P. Suter, ETH-Zürich	Ph.D. Thesis of D. Mischler (completed 1995)

Prof. Y. Tamaura, Tokyo Inst. of Techn., Japan	H_2O-Splitting using activated ferrites (completed 1994) Coal gasification with metal oxides (1995-1997)
Prof. R. Von Rohr, ETH-Zürich	Ph.D. Thesis of J. Ganz (completed 1996)
Prof. A. Wokaun, ETH-Zürich	Ph.D. Thesis of A. Weidenkaff (since 1996) Ph.D. Thesis of S. Möller (since 1997)
Prof. A. Yogev, Weizmann Inst. Israel	Laser diagnostics of solar chemical reactions (1994-1995) Carbothermic reduction of zinc oxide (1996-1998)
SolarPACES Program of the International Energy Agency	

Table of Contents

1 Introduction

This report is a detailed description of the work conducted under contract EF-REN (92)033, titled *Research and Development of the Process Technology for Converting Concentrated Solar Energy into Chemical Fuels.* The research was motivated by the fact that using only 0.1% of the earth's land space with solar receivers that operate with a collection efficiency of only 10%, there is more than enough energy to supply the current yearly energy needs of everyone on earth. The problem, however, is that solar energy is unequally distributed on the earth, with most of it in desert regions. If solar energy is to have a larger role in the world economy, it will be necessary to learn to economically capture it in the sunbelt and transport it to the population centers. To help accomplish this task, it is necessary to develop the science and technology for high temperature solar thermal chemical processes. These processes can be those that convert solar radiant energy to chemical fuels, or processes that substitute solar energy for fossil fuels for the production of valuable commodities. This report describes PSI's development effort.

Each chapter in this report represents an important aspect of the work: Chapter 2 describes the solar furnace facilities that were greatly updated since the start time of the contract. For example, one finds a description of the newly constructed 45 kW furnace. This new laboratory enables us to reach higher concentration ratios and to supply more power to a fixed reactor. In Chapter 3 one finds a fundamental investigation of several processes for storing sunlight as chemical energy. The work in this chapter reveals how chemical thermodynamics and kinetics must be used in evaluating a potential solar chemical process. Furthermore, one also sees how chemical thermodynamics and kinetics influence the intelligent design of a solar chemical reactor. Chapter 4 describes development work on volumetric reactors for three types of reactors; a very high temperature open to the air particle cloud reactor, a modest temperature open to the air reactor, and a modest temperature closed particle cloud reactor.

The work described in these chapters, is held together by several research themes and strategies that were developed in the course of the research program. Firstly, the long term objective for the research is to develop an economically viable means for storing sunlight as chemical energy. For us, economically viable means having processes that are competitive when compared to other sustainable energy processes. To date, the best alternative to any solar thermal chemical process for producing fuels is a solar thermal system producing electricity that is used to produce hydrogen by electrolyzing water. This process, therefore, serves as a benchmark for solar chemistry.

For reaching the long term objective, one sees in this report the theme that we follow two research paths. On one, we are developing solar processes that mix fossil fuels and sunlight either directly or with a hybrid solar conventional fossil fuel process to produce fuels or chemical commodities. This work is described both in Chapters 3 and 4 for producing Zn and synthesis gas from ZnO and natural gas, for calcining $CaCO_3$ for cement production, and for producing carbon nanotubes by cracking hydrocarbons. On the second research path we are attempting to produce a solar fuel with solar energy alone. Chapter 3 shows an evaluation of two processes, one for producing Zn from ZnO, the other for producing H_2 in a two-step process where a high temperature step involves the production of FeO from Fe_3O_4. These two paths differ in a very practical way: the temperatures for the mixed fossil fuel processes are near 1200 K, while those of the uniquely solar processes are near 2300 K. Because we ultimately want a uniquely solar process, it was self-evident that we need to work on such processes, but because we are also interested in learning to transfer our ideas to industry it was important to us to work also on the mixed fuel/solar processes where the engineering challenges are somewhat less formidable.

The reactor development work that is described principally in chapter 4 but with some important work also shown in Chapter 3 initially focused on developing technically feasible high-temperature reactors for generic metal oxide reactions. This initial work was primarily that of the high-temperature open-to-air volumetric reactor development described in Chapter 4. Our goal was to develop a reactor made from conventional materials that would operate continuously without problems under the severe environment of transient intense solar radiation. We started the work by de-coupling the boundary conditions that a specific chemical reaction would place on the reactor design so that we could learn to first deal with these difficult mechanical engineering problems. As we gained more maturity in our work, we began to more and more include chemical boundary conditions along with the mechanical engineering boundary conditions in our design and reactor development work. The volumetric reactor for producing synthesis gas from ZnO and natural gas described in Chapter 4 is an example of a design where we attempted to respect all important boundary conditions. In Chapter 3, we propose a reactor concept for dissociating Fe_3O_4 to FeO that attempts to meet mechanical engineering and chemical boundary conditions.

With all of this reactor development work, we were motivated to develop reactors that would be reliable and be part of processes whose efficiency for converting sunlight to a fuel is better than that of our benchmark process.

Finally, the work described in this report is foremost experimental in nature, although the reactor development was also done in concert with numerical modeling of the processes.

Experimental and theoretical results described in this report have been reported in the peer reviewed literature (see Chapter 6). It is also important to note that to a certain extent the experience gained by working with high temperature solar energy is also an important result. But it cannot be described in papers or in this report. However the benefits are manifested in having developed individuals with skills that are essential for the advancement of the field of solar chemistry.

A list of publications resulting from the work within this contract EF-REN (92)033 is found in Chapter 6, and the references are given in Chapter 7. The nomenclature, in turn, is found at the end of each individual Section.

2 Infrastructure

This Chapter describes the infrastructure available to the Solar Technology Section at *PSI*[1]. It includes solar furnace facilities, solar flux measurement systems, equipment for chemical analysis, and computer hardware and software.

2.1 Solar Concentrating Research Facilities

During the course of this project, *PSI*'s High-Temperature Solar Technology Section has developed its solar concentrating research facilities in order to provide experimental platforms for developing and testing the solar chemical processes and reactors described in this report. At present, the solar facilities include

1. a parabolic concentrator (Figure 2.1) consisting of 82 mirror facets having a total normal projected area of 87 m^2, nominal focal length of 7.5 m, and rim angle of 38.6°. It delivers a total power of 60 kW with a peak concentration ratio of 4100 suns (1 sun = 1 kW/m^2).
2. a small two-stage solar furnace (Figure 2.2) consisting of a sun-tracking heliostat of 51.8 m^2 area, 100 m focal length, and a stationary parabolic dish of 5.7 m^2 area, 1.93 m focal length, and rim angle of 41°. It delivers about 15 kW power with a peak concentration ratio of 3500 suns.
3. a larger solar furnace (Figure 2.3) consisting of a 124 m^2 flat heliostat on-axis with a 8.5 m-diameter parabolic concentrator, having a focal length of 5.13 m, and a rim angle of 45°. It delivers up to 40 kW at peak concentration ratios exceeding 5000 suns.

Figure 2.1 *PSI*'s 60 kW parabolic concentrator

1. Technical information on *PSI*'s solar facilities may be obtained at www1.psi.ch/www_f5_hn/Solar/solar_home.html.

2.2 Solar Flux Characterization

All three concentrating facilities have been characterized for their power output and solar concentration. Power flux intensities were measured optically by recording the image of the sun on a water-cooled plate positioned at the focal plane. Such a plate has been plasma-coated with alumina so that it reflects diffusely and closely approaches a *Lambertian* target. A charge-couple device (*CCD*) camera is used to record the image of the sun and is calibrated by simultaneously measuring the flux intensity with an absolute point radiometer. (A new type of solar radiometer has been constructed at *PSI* [Kreetz, 1996; Braunschweig, 1997].) The power flux distribution is calculated by multiplying the gray value of each pixel of the recorded image with the calibration factor. The *CCD* camera is also used to monitor continuously the position of solar reactors relative to the flux map. That way the positioning can be optimized in order to intercept the regions of maximum flux intensity.

Typical solar flux contours obtained at the focus of the larger solar furnace, recorded on March 9, 1998, at 12:35 UT, are shown in Figure 2.4, and correspond to a measured normal beam insolation of 1014 W/m^2. The concentration ratio profile approaches a Gaussian distribution that peaks at 5530. Stagnation temperatures[2] exceeding 3000 K are achievable with this peak concentration [Haueter, 1998].

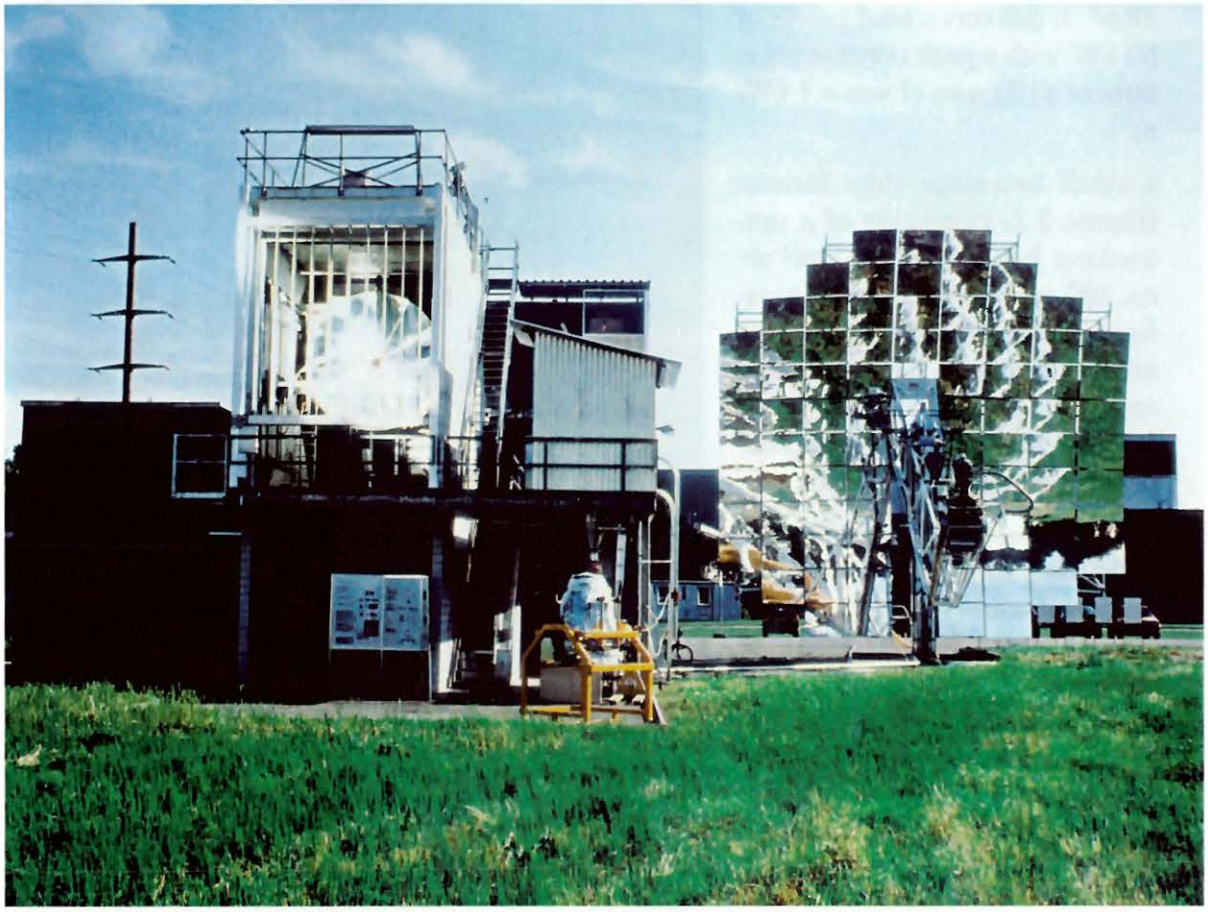

Figure 2.2 *PSI*'s 15 kW solar furnace (left) and 60 kW parabolic concentrator (right)

2. Stagnation temperature is defined as the highest attainable temperature of a blackbody absorber, given by $T_{stagnation}=(IC/\sigma)^{0.25}$, where C is the concentration ratio, I is the normal beam insolation, and σ the Stefan-Boltzmann constant. The efficiency with which energy can be used by a process at the stagnation temperature is clearly zero: energy is being re-radiated as fast as it is being received.

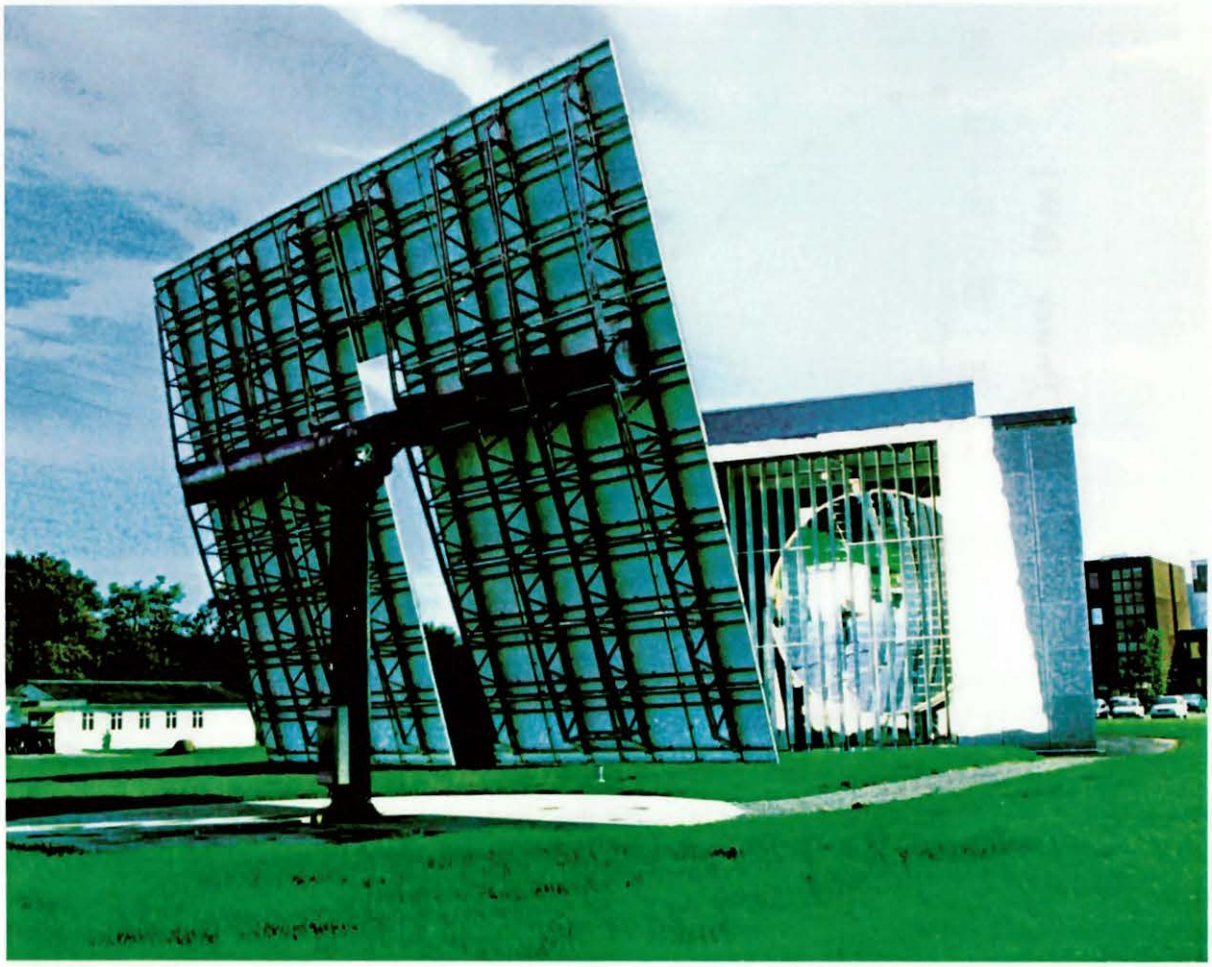

Figure 2.3 *PSI*'s 40 kW solar furnace

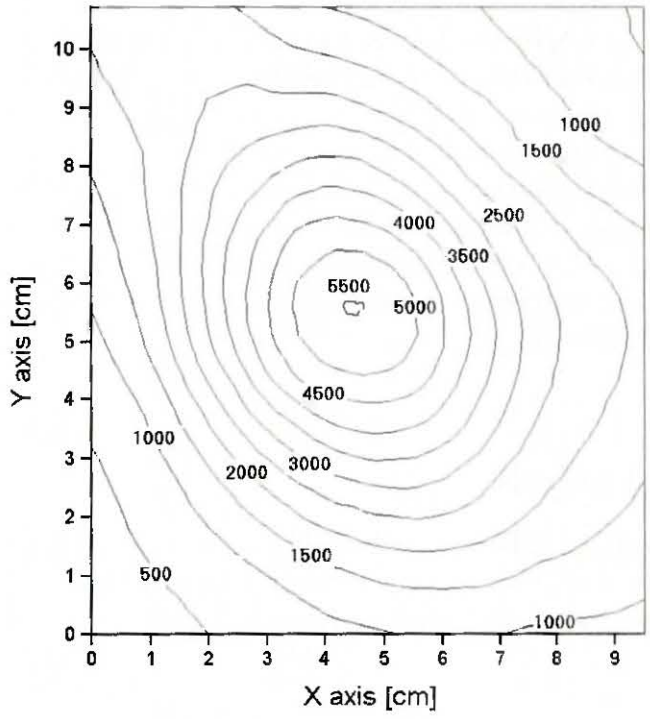

Figure 2.4 Measured solar Concentration ratios at the focal plane of *PSI*'s new solar furnace

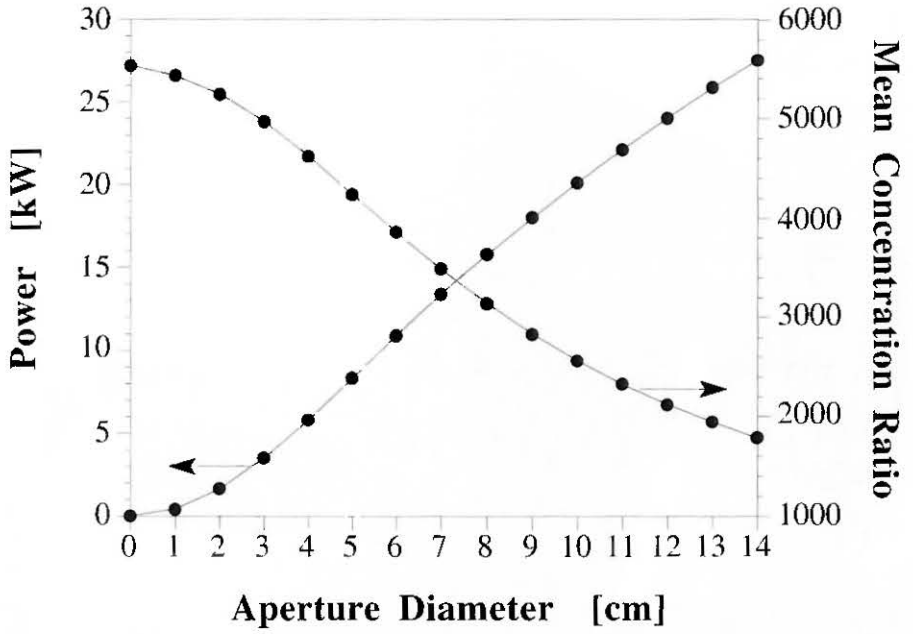

Figure 2.5 Power and mean concentration ratio through a circular aperture as a function of its diameter (calculated by numerical integration of the power flux intensities), when the aperture is positioned at the focal plane with its center at the point of maximum flux concentration.

Figure 2.5 shows the power intercepted by a circular aperture as a function of its diameter (calculated by numerical integration of the power flux intensities), when the aperture is positioned at the focal plane with its center at the point of maximum flux concentration. Also shown is the mean concentration ratio over the aperture. An aperture of 6 cm-diameter intercepts about 10 kW at a mean concentration ratio of 3860, while a 10 cm-diameter aperture intercepts 20 kW at a mean concentration ratio of 2560. Larger apertures intercept more sunlight reflected from imperfect and imperfectly matched heliostat and concentrator, but they also re-radiate more energy when operating with high-temperature solar cavity-receivers. Therefore, the optimum aperture size results from a compromise between maximizing radiation capture and minimizing re-radiation losses, and has been calculated for Gaussian power flux distributions [Steinfeld and Schubnell, 1993]. Figure 2.6 shows the power intercepted by an aperture of 1, 5, and 10 cm diameter at different planes perpendicular to the concentrator axis (z-axis). The "-" and "+" signs on the abscissa are in the direction towards and away from the concentrator, respectively, while plane "0" is the focal plane. It is observed that the power through an aperture is only weakly affected from deviations within 5 cm from the focal plane; however, the power and peak concentration ratio are strongly influenced by the positioning of the aperture's center relative to the point of maximum flux intensity.

2.3 Chemical Analysis

Along with the concentrating facilities, a well-equipped chemical laboratory offers the possibility of a complete chemical analysis of the reaction products, including X-ray diffraction, gas chromatography, thermo-gravimetry, mass spectrometry, scanning and transmission electron microscopy.

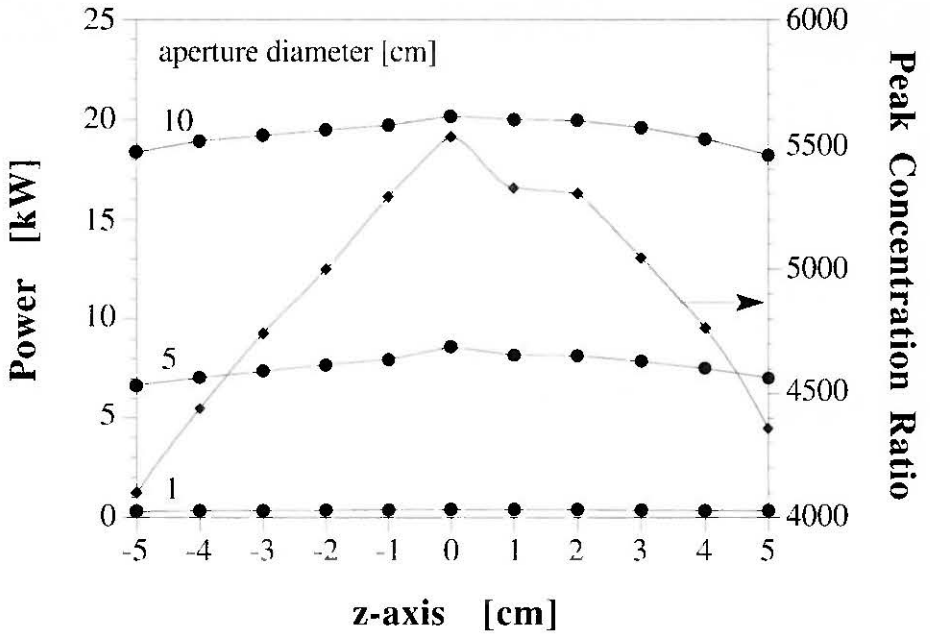

Figure 2.6 Power intercepted by an aperture of 1, 5, and 10 cm-diameter and peak concentration ratio at different planes perpendicular to the concentrator axis (z-axis). The "-" and "+" signs on the abscissa are in the direction towards and away from the concentrator, respectively, while plane "0" is the focal plane.

2.4 Computer Hardware & Software

The computer hardware and software that was utilized during this project include:

1. Thermodynamics: NASA CET-85 and HSC-Outokumpu computer codes for calculating the chemical equilibrium composition of complex systems (running on *PC*s).
2. Computational Fluid Dynamics (*CFD*) code CFX-4 (formerly called CFDS-FLOW3D) for solving 3-dimensional fluid flow and heat transfer problems (running on a *DEC* Alpha workstation).
3. Monte-Carlo ray-tracing simulation for analyzing radiation heat transfer in solar reactors (running on *VAX* mainframe).
4. *ACRO*/Labtech data acquisition system for conducting solar experiments (running on *PC*s).

3 Solar Chemical Processes

We explored several solar thermal chemical processes. Two processes were for the solar production of H_2. As described in the Introduction in Chapter 1, this work follows our research path involving sunlight alone. These were cyclic processes involving the solar decomposition of iron oxide and zinc oxide. Three processes were investigated that involved in some manner the mixing of sunlight and fossil fuels either to produce a fuel or valuable chemical commodities. These processes include reforming of natural gas with sunlight and ZnO, a hybrid solar cement process, and the cracking of hydrocarbons to produce nano-phase materials. This chapter describes our research effort on these various solar thermal processes. We begin by first describing the fundamental principles associated with analyzing such processes.

3.1 Solar Energy Conversion Fundamentals

3.1.1 Solar Absorption Efficiency

The capability of a solar receiver to absorb the incoming solar power is a function of its geometrical configuration, its heat transfer characteristics and, above all, its operating temperature. Previous studies of receivers and reactors for highly concentrated solar systems have featured the use of cavity-type configurations [Diver, 1987]. A cavity-receiver is a well insulated enclosure with a small opening, the *aperture*, that intercepts incoming solar radiation. Because of multiple reflections among the inner walls, the fraction of the incoming energy absorbed by the cavity exceeds the surface absorptance of the inner walls. However, at temperatures above about 1000 K, the net power absorbed is diminished mostly by radiative losses through the aperture. The solar energy absorption efficiency of a cavity-receiver $\eta_{absorption}$ accounts for this phenomenon. It is defined as the net rate at which energy is being absorbed divided by the solar power coming from the concentrator. For a perfectly insulated cavity receiver (no convection or conduction heat losses), it is given by [Fletcher and Moen, 1977; Steinfeld and Schubnell, 1993]

$$\eta_{absorption} = \frac{\alpha_{eff} Q_{aperture} - \varepsilon_{eff} A_{aperture} \sigma T_{cav}^4}{Q_{solar}}, \tag{3.1}$$

where Q_{solar} is the total power coming from the concentrator, $Q_{aperture}$ the amount intercepted by the aperture of area $A_{aperture}$, α_{eff} and ε_{eff} are the effective absorptance and emittance of the cavity-receiver, respectively[1], T_{cav} is the nominal cavity temperature, and σ is the *Stefan-Boltzmann* constant. The first term in the numerator denotes the total power absorbed and the second term denotes the re-radiation losses, viz.,

$$Q_{absorbed} = \alpha_{eff} Q_{aperture} \tag{3.2}$$

$$Q_{rerad} = \varepsilon_{eff} A_{aperture} \sigma T_{cav}^4 \tag{3.3}$$

1. α_{eff} is defined as the fraction of energy entering through the aperture that is absorbed by the cavity walls. For a gray-walled cavity and diffusely incident radiation, α_{eff} is equal to the apparent absorptance, defined as the fraction of energy flux emitted by a blackbody surface stretched across the aperture that is absorbed by the cavity walls [Sparrow and Cess, 1966]

Their difference yields the net power absorbed by the reactor

$$Q_{reactor,net} = Q_{absorbed} - Q_{rerad} \tag{3.4}$$

Q_{solar}, the incoming solar power, is determined by the normal beam insolation I and by the collector area A_{coll} normal to the sun's rays, i.e.

$$Q_{solar} = \eta_{coll} A_{coll} I \tag{3.5}$$

where η_{coll} accounts for the optical imperfections of the collection system (e.g., reflectivity, specularity, tracking imperfections). Because of spilled radiation, $Q_{aperture} \leq Q_{solar}$. The capability of the collection system to concentrate solar energy and minimize spillage is often expressed in terms of its mean flux concentration ratio $\tilde{C}$ over an aperture, normalized to the incident normal beam insolation as follows:

$$\tilde{C} = \frac{Q_{aperture}}{I \cdot A_{aperture}} \tag{3.6}$$

The flux concentration ratio can be increased by increasing the optical precision of our primary collection system or by using non-imaging secondary reflectors (e.g., a compound parabolic concentrator, often referred to [Welford and Winston, 1989] as *CPC*). Higher $\tilde{C}$ would allow a smaller aperture to intercept the same amount of energy, thus reducing Q_{rerad}. Although larger apertures intercept more sunlight reflected from imperfect and imperfectly matched heliostats and concentrators, they also re-radiate more energy. Therefore, the optimum aperture size results from a compromise between maximizing radiation capture and minimizing re-radiation losses. Such optimization strongly depends on the incident solar flux distribution at the aperture plane of the receiver. The case of a Gaussian distribution has been examined analytically [Steinfeld *et al.*, 1993]. For simplification, we assume an aperture size that captures all incoming power so that $Q_{aperture} = Q_{solar}$. With this assumption, equations (3.1) and (3.6) are combined to yield:

$$\tilde{C} = \eta_{coll} \frac{A_{coll}}{A_{aperture}} \tag{3.7}$$

and

$$\eta_{absorption} = \alpha_{eff} - \varepsilon_{eff} \frac{\sigma \cdot T_{cav}^4}{I \cdot \tilde{C}} \tag{3.8}$$

With real receivers the absorption efficiency is even lower than stated in equation (3.8), because the inner walls of the cavity are usually at the highest temperature of the system and conductive losses to the outer shell become significant. These heat losses can be lowered to acceptable levels by lining the receiver with proper insulation.

Novel receiver concepts have been proposed as alternatives to the conventional insulated cavity-receiver. For example, volumetric reactors use directly irradiated gas-particle suspensions to serve as radiant absorbers, heat transfer medium, and chemical reactants [Ganz *et al.*, 1994, Steinfeld *et al.*, 1992a]. Also, receivers having specular reflective inner walls prevent infrared radiation emitted by hot reactors and reactants from escaping the receiver or from being absorbed at the walls; instead, radiation is re-directed back to the reaction site [Steinfeld *et al.*, 1992b]. These innovative configurations offer intriguing advantages in some specific applications. However, they are also subject to radiation losses from hot surfaces/gases towards the

opening through which solar radiation enters. If the aperture is sufficiently small compared to the cavity enclosure, the fraction of intercepted radiation escaping becomes negligible regardless of the absorptivity of the inner walls. Thus, a perfectly insulated isothermal cavity, with a non-selective window, approaches a blackbody. In the analysis that follows, we assume $\alpha_{eff} = \varepsilon_{eff} = 1$.

3.1.2 Overall System Efficiency

The absorbed concentrated solar radiation drives the endothermic chemical reaction given by equation (3.1). The overall system efficiency of such thermochemical conversion is defined as the ratio of the *Gibbs* free energy change of the reaction to the solar power input, i.e.,

$$\eta_{overall} = \frac{-\Delta G|_{Reactants \rightarrow Products}}{Q_{solar}} \tag{3.9}$$

The conversion of solar process heat to the ΔG of the reaction is limited by both the solar absorption efficiency and the *Carnot* efficiency. The overall *ideal* system efficiency is then represented by

$$\eta_{overall,ideal} = \eta_{absorption} \times \eta_{Carnot} = \frac{Q_{absorbed} - Q_{rerad}}{Q_{solar}} \times \left(1 - \frac{T_L}{T_H}\right) \tag{3.10}$$

where T_H and T_L are the upper and lower operating temperatures of the equivalent *Carnot* heat engine. Therefore, from a thermodynamic standpoint, one should try to operate thermochemical processes at the highest upper temperature possible; however, from a heat transfer perspective, the higher the temperature, the higher the re-radiation losses. The highest temperature an ideal solar cavity-receiver is capable of achieving is calculated by setting equation (3.10) equal to zero, which yields

$$T_{max} = \left(\frac{I \cdot \tilde{C}}{\sigma}\right)^{0.25} \tag{3.11}$$

For $\tilde{C} = 2000$ and a typical normal beam solar insolation of 900 W/m^2, the highest attainable temperature is 2374 K. At this temperature, $\eta_{overall,ideal} = 0$ because energy is being re-radiated as fast as it is received. An energy-efficient process must run at temperatures that are substantially below T_{max}. If T_H is taken to be equal to T_{cav}, there is an optimum temperature for maximum efficiency obtained by setting

$$\frac{\partial \eta_{overall}}{\partial T} = 0 \tag{3.12}$$

Assuming uniform power flux distribution, this relation yields the following implicit equation for T_{opt}:

$$T_{opt}^5 - (0.75T_L)T_{opt}^4 - \frac{\alpha_{eff} T_L I \tilde{C}}{4\varepsilon_{eff}\sigma} = 0 \tag{3.13}$$

Equation (3.13) was solved numerically [Steinfeld and Schubnell, 1992]. For uniform power-flux distributions (which are likely to be obtained when non-imaging secondary concentrators are used in tandem with paraboloidal reflectors), T_{opt} varies between 1100 and 1800K for concentrations between 1000 and 13000. For example, when $\tilde{C} = 2000$, $I = 900$ W/m^2, and $T_L = 298$ K, $\eta_{overall,ideal}$ is a maximum at about 1250 K. For a gaussian incident power flux dis-

tribution having peak concentrations between 1000 and 12000, T_{opt} varies from 800 to 1300 K. In practice, when considering convection and conduction losses in addition to radiation losses, the efficiency will peak at a somewhat lower temperature. Nevertheless, the chemical reaction under consideration (3.1) proceeds at temperatures that are within the optimal range for typical concentrations.

Equation (3.10) denotes the maximum achievable efficiency for an ideal solar chemical process that absorbs heat from a high temperature thermal reservoir at T_H, and rejects heat to a low temperature thermal reservoir at T_L. Equation (3.13) serves to guide our choice for the cavity temperature. It presumed that $T_H = T_{cav}$. However, the actual source temperature for a solar process is the surface temperature of the sun. From this point forward, we fix $T_H = 5800$ K because this will provide a standard baseline for comparing the performance of different solar processes. The surroundings act as the low temperature thermal reservoir at 298 K. Thus, our solar reactor operates between temperatures that are significantly different from those of the hot and cold thermal reservoirs. Such temperature gradients introduce irreversibilities and, consequently, reduce the system's overall efficiency. The result is $\eta_{overall} < \eta_{overall,ideal} < \eta_{Carnot}$.

3.1.3 Radiation Heat Transfer Analysis

This Section presents a *Monte Carlo* radiative transfer analysis of a non-isothermal non-gray absorbing-emitting-scattering suspension of Fe_3O_4 particles under concentrated solar irradiation [Mischler and Steinfeld, 1995].

3.1.3.1 Motivation

In recent years there has been an increasing interest in volumetric receivers/reactors for solar thermochemical processes. Their design concept uses gas-particle suspensions or selective-absorbing gases to serve the functions of direct energy absorption of concentrated solar radiation, heat transfer, catalysis, and chemical reactants as well [Hunt *et al.*, 1986]. Volumetric, or direct-absorption particle receivers, have been experimentally demonstrated for heating air [Hunt and Brown, 1983, Rightley *et al.*, 1992] and are presently being investigated for solar driven chemistry at *PSI*. In contrast to cavity-type receivers in which the incident radiation is mostly absorbed at the inner surfaces and from there indirectly transferred to the reactor, volumetric receivers provide instead efficient heat transfer directly to the reaction site, where the energy is needed. Moreover, the direct irradiation of the reactants may result, under proper conditions, in photochemical enhancement of the reaction kinetics. Among energy-intensive reactions which may be well adapted to direct-absorption processes, the thermal reduction of magnetite (Fe_3O_4) at 2300 K to form wustite (FeO) is of special interest. If we were to use cavity-receivers at such high temperatures, one might encounter difficulties with suitable refractory materials of construction since the entire inner wall of the enclosure is at the highest temperature in the system. [Campbell and Sherwood, 1967]. To the contrary, by directly illuminating a dense Fe_3O_4 particle cloud with the concentrated solar beam, a gradient of temperatures could be achieved between the reaction zone and the reactor inner walls. Such shielding effect would reduce the thermal load on the walls and temperature requirements of the containment. Radiative transport in a volumetric reactor is the dominant heat transfer mode at high temperatures (2000 K and above). The design of innovative reactor concepts requires a detailed and accurate radiation model.

The fundamental concepts and the formulation of the governing equation of radiative transfer for absorbing, emitting, and scattering media are presented in the basic text of Siegel and Howell [Siegel and Howell, 1992]. The radiant interchange in particle clouds among gas, particles, and reactor walls is a complex mathematical problem, requires solving the integro-differential

equation of radiative transfer which involves, among other tasks, the integration over all wavelengths and directions of the radiation flux coming from surrounding surfaces and surrounding gas-particle medium, and the absorption, emission, and scattering of energy at all locations in the medium and boundaries. Simplifying assumptions in the geometry and optical properties are necessary in order to be able to solve approximations to real situations. For example, approximate solutions have been derived for a gray non-scattering gas and particles in a coal furnace using Hottel's zoning method [Canadas *et al.*, 1990], for an isothermal non-gray slab containing carbon particles and CO_2 using the absorption mean beam length concept and *Edwards*'s narrow-band model [Yuen and Ma, 1992], for a free falling particle laden flow within a 2-dimensional rectangular solar cavity-receiver using a 2-band isotropic radiation and the discrete-ordinates method [Evans *et al.*, 1987, Houf and Greif, 1987], and for a box-type geometry with incident light coming along one coordinate axis using *Schuster-Schwarzchild* two-flux model [Miller and Koenigsdorff, 1990]. The radiative transfer in a planar participating medium which scatters anisotropically has been considered in numerous previous investigations because approximates well many physical problems without introducing geometrical complexities [Hsia and Love, 1967; Modest and Azad, 1980, and literature cited therein]. Gray, isothermal, and isotropic scattering medium are some of the assumptions commonly used in engineering calculations. The gray assumption can lead to considerable error when modeling solar particle-receivers since particle clouds may exhibit strong selective properties for absorption in the solar spectrum and emission in the *IR* [Abdelrahman *et al.*, 1979], was already demonstrated that gray gas formulations cannot predict even qualitatively the experimental measurements of absorption and emission of non-isothermal CO_2 and H_2O gases [Edwards *et al.*, 1967], would be reasonable to extend the same conclusions for selective particle suspensions. Non-gray solutions for plane parallel media bounded by black walls have been obtained by Kim [Kim *et al.*, 1991] using the discrete ordinates method and a statistical narrow-band model. The isotropic assumption, often justified in radiation heat transfer modeling of cavity-receivers, may also result in discrepancies when applied to directly irradiated particle clouds because of the strong angular dependence of the scattering phase function. Sasse [Sasse, 1992] measured the scattering intensity as a function of the scattered angle for single carbon particles and oil droplets suspended in an electrodynamic levitator and observed significant deviation from isotropic scattering. Gupta *et al.* [Gupta *et al.*, 1983] considered both isotropic and anisotropic scattering fly ash cloud using *Mie* theory and the *Monte Carlo* method. It was found that neglecting scattering overestimates radiative transfer to the sink of the furnace, while assuming isotropic scatter underestimates radiative transfer, both resulting in errors up to 30%. Finally, the isothermal assumption is obviously not valid for the temperature-gradient reactor under investigation.

In the present work we incorporate wavelength-dependent and directional-dependent optical properties of magnetite to simulate by *Monte Carlo* a non-gray, non-isothermal, absorbing, emitting, and anisotropic-scattering particle suspension under concentrated solar irradiation. The focus of this study is to find out how much of the incident radiation is transmitted through the cloud, to obtain the temperature distribution within the cloud, and to present the effect of spectral and directional dependencies.

3.1.3.2 Analysis

The system configuration is depicted schematically in Figure 3.1.The particle suspension is contained in a slab of constant thickness D, is bounded between two infinite parallel planes assumed blackbody at 0 K, i.e. the planes absorb all incident radiation coming from the medium but do not emit any radiation. The front plane contains a circular aperture of radius r_{ap} through which concentrated solar irradiation enters. The incoming solar flux is assumed diffusely and uniformly distributed over the circular aperture since this is the power flux distribution likely to be ob-

tained when non-imaging secondary elements, such as *CPC*'s, are used in tandem with imaging primary reflectors for augmenting the concentration [Winston and Welford, 1989]. The spectral distribution of the incoming solar intensity is approximated by the *Planck* distribution of a 5780 K blackbody source. Thus, the hemispherical spectral emissive power entering through the aperture is proportional to:

$$e_{\lambda b}(\lambda, T) = \frac{2\pi C_1}{\lambda^5 (e^{C_2/(\lambda T)} - 1)} \tag{3.14}$$

for T=5780 K.

The particulate medium is modeled as a pseudo-continuous medium, i.e. a mono-disperse distribution of particles, with some number density N, surrounded by a non-participating gas with a refractive index of 1. The optical characteristics of the discrete particles are used to determine the extinction properties of the whole medium [Tien and Drolen, 1987]. Each particle is assumed opaque (no transmission), with infinite thermal conductivity (isothermal), spherical (a generally good assumption for most irregularly-shaped randomly-oriented particles) and having independent scattering (a condition whereby the scattering from a single particle in the assembly is not influenced by the proximity of its neighbors). The independent scattering assumption is justified by referring to the independent/dependent scattering regime map, as given by Yamada [Yamada *et al.*, 1986], for the range of particle volume fractions (f_v) and size parameters (λ) used in this study. Particle diameter has been taken equal to 5 the average diameter we have been using in our experimental studies. The mono-dispersity assumption will permit a better detection and understanding of the effect of spectral and directional dependency of the cloud optical properties.

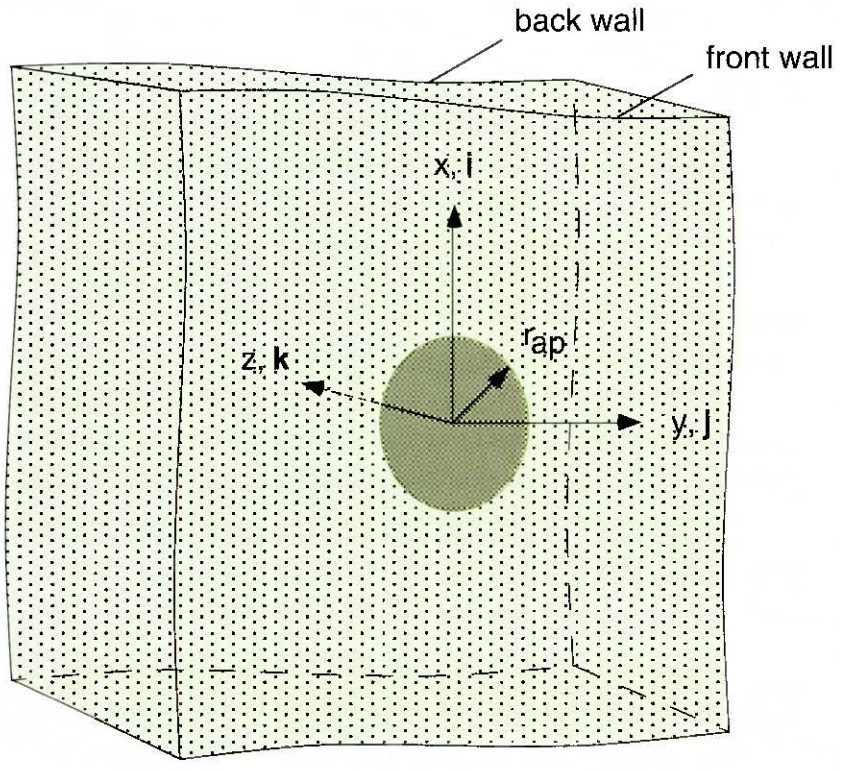

Figure 3.1 Schematic diagram of the system [Mischler and Steinfeld, 1995]. The particle suspension is contained in an infinite slab. The incoming solar flux is assumed diffusely and uniformly distributed over a circular aperture of radius r_{ap}, and has a 5780K *Planck* spectral distribution.

Special attention is devoted to the realistic case of non-gray and anisotropically scattering particles. The *Mie* anisotropic scattering theory is applied. The *Mie* theory adequately describes the range $0.6<\lambda<5$, but can also be practically applied for spherical particles of arbitrary size [Siegel and Howell, 1992; Bohren and Huffman, 1983]. We have performed our *Monte Carlo* computations over a wider range of size parameters. However, because incident and emitted radiation are confined mostly in the visible and infrared spectra, the statistically active range of particle size parameters falls within $0.5<\lambda<30$. Scattering characteristics depend also on the optical properties of the particles under consideration. The complex refractive index of Fe_3O_4, expressed in terms of the complex dielectric constant as a function of wavelength, has been taken from Landolt-Boernstein Series [Landolt-Boernstein, 1982].

Given the size parameter and the complex refractive index, we have used *Mie* theory (*BHMIE* subroutine by Bohren and Huffman [Bohren and Huffman, 1983]) to calculate the scattering phase function $\Phi_\lambda(\xi, \eta)$, defined as the ratio of scattered intensity in the direction (ξ,η) to the intensity of isotropic scattering. ξ denotes the angle between the scattered and incident direction and η denotes the azimuthal angle of the scattered beam. For spherical or random-oriented particles, Φ_λ is independent of η. For isotropic scattering, $\Phi_\lambda=1$. For all wavelengths in the range 0.158-10 μm, the Fe_3O_4 particles exhibit significant preference for forward scattering, becoming more pronounced as the wavelength decreases. For λ approximately 0.5, scattering is exclusively forward. Thus, solar rays perpendicularly incident on the external layer of a particle cloud are most likely to be either absorbed or scattered more into the heart of cloud rather than backscattered, which favors heat transfer to the particles by direct solar irradiation.

Additional output from the *Mie* theory are the spectral efficiencies Q_a, Q_s, and Q_K ($Q_K=Q_a+Q_s$), i.e. the ratio of the absorption, scattering and extinction cross sectional areas to the physical particle cross sectional area. These efficiencies are plotted in Figure 3.2 as a function of wavelength.

They reveal an increasing trend with wavelength up to about 20 μm. Peak attenuation occurs for radiation at 17 μm, giving an apparent particle area up to 3.25 times bigger than the actual physical area. Therefore, from a standpoint of maximizing the attenuation of radiation through a particle-cloud, would be better to have this radiation coming from an infrared source in the 10-20 μm range rather than from a visible source. However, for $\lambda>20$ μm, the efficiencies decrease dramatically to the extent that for $\lambda>50$ μm the medium is practically transparent. It is seen that a cloud of magnetite particles behaves differently than, for example, a fly ash cloud. In a pulverized-coal-fired furnace, a fly ash cloud has instead an absorption efficiency that monotonically decreases with wavelength in the 1-10 μm range [Gupta *et al.*, 1983].

Given the amount of particles per unit volume of the medium, the spectral absorption and scattering coefficients can be calculated as:

$$a_\lambda = 1.5 Q_a f_v / d \tag{3.15}$$

$$s_\lambda = 1.5 Q_s f_v / d \tag{3.16}$$

respectively. These are usually combined in the extinction coefficient K_λ, which, when constant over the whole domain, becomes the reciprocal of the so-called mean penetration distance, i.e. the average distance radiation propagates through the medium before absorption or scattering occurs. Since the incident radiation has a *Planck* spectral distribution of a 5780 K blackbody, is convenient to define the *Planck* mean extinction coefficient, $\bar{\kappa}$, as:

$$\tilde{K} = \frac{\int_0^x K_\lambda e_{\lambda b}(\lambda,T)d\lambda}{\int_0^x e_{\lambda b}(\lambda,T)d\lambda} = \frac{1}{\sigma T^4}\int_0^x K_\lambda e_{\lambda b}(\lambda,T)d\lambda \qquad (3.17)$$

for T=5780 K. $\tilde{K}$ is the mean of the spectral extinction coefficient when weighted by a 5780 K blackbody emission spectrum. A dimensionless parameter that describes radiation attenuation by a uniform medium depth x of constant K_λ is the optical thickness κ_λ, defined as: $\kappa_\lambda = K_\lambda x$. Similarly, the *Planck* mean optical thickness over a slab of thickness D, is defined as the spectrally-averaged optical thickness when weighted by a 5780 K blackbody emission spectrum: $\tilde{\kappa} = \tilde{K}D$. Results of this study are presented in terms of κ.

The relative importance of scattering to absorption is measured by the albedo Ω_λ, $\Omega_\lambda = s_\lambda / K_\lambda$. The albedo for Fe_3O_4 particles, obtained via *BHMIE* subroutine, is a function of wavelength. Statistically, indicates the probability of an incident ray being scattered. For λ<15 μm, the incident rays have about 60 percent chance of being scattered, 40 percent chance of being absorbed. As the wavelength of the incident ray increases, so does the probability of absorption. At λ=100 μm, an incident ray is more likely to be absorbed rather than scattered. However, we have already seen in Figure 3.2 that at such a long wavelength there would be practically no rays interacting with particles. A representative mean value of the albedo for the incident radiation is obtained by integrating, over all wavelengths, the spectral albedo weighted by a 5780 K blackbody emission spectrum. Thus, the *Planck* mean albedo is defined as:

$$\tilde{\Omega} = \frac{1}{\sigma T^4}\int_0^x \Omega_\lambda e_{\lambda b}(\lambda,T)d\lambda \qquad (3.18)$$

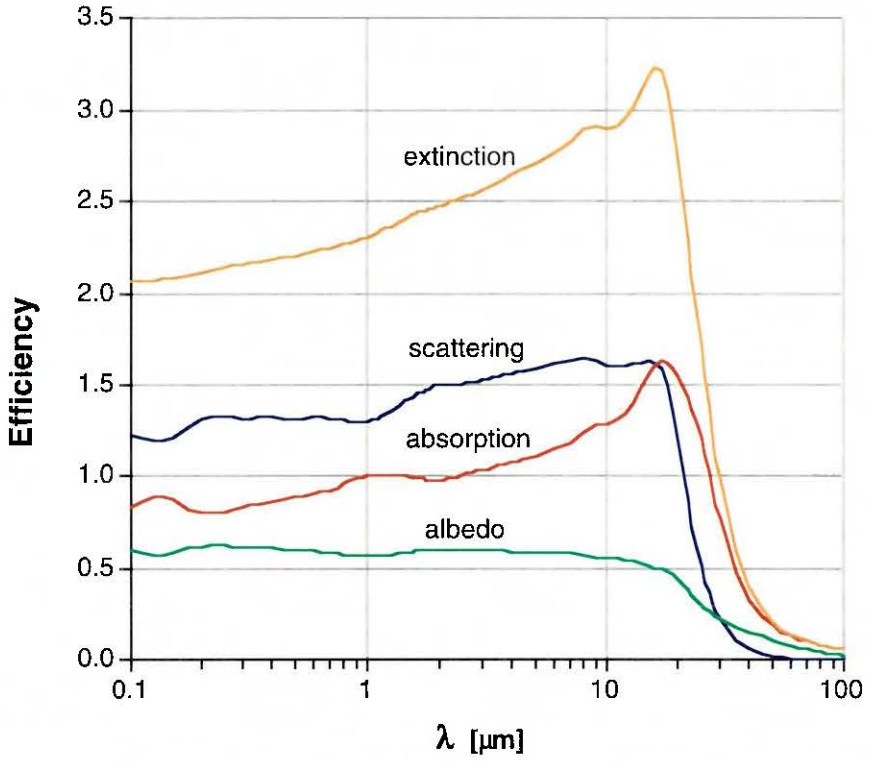

Figure 3.2 The absorption, scattering, and extinction efficiencies, and the albedo, as a function of wavelength, calculated for Fe_3O_4 particles using *Mie*-scattering theory [Mischler and Steinfeld, 1995]. Input parameters are the size parameter and the complex refractive index.

For T=5780 K andΩ_λ given, Ω=0.5894.

The *Monte Carlo* ray-tracing method was used. This technique, widely employed for the analysis of radiative transport [Siegel and Howell, 1992, Howell and Perlmutter, 1964], enables the treatment of problems beyond the reach of analytical techniques, and is flexible enough to remove any or all of the diffuse-gray-isotropic simplifying assumptions. The methodology will be briefly outlined in the following paragraphs. consists of following stochastic paths of a large number of discrete bundles of energy as they travel through the interacting medium. Each energy bundle carries the same amount of energy (equal to the incident power divided by number of bundles), and has a certain direction and a certain associated wavelength which are determined from the appropriate probability density functions.

Cartesian coordinates are centered at the center of the circular aperture with z-axis normal to it, as shown in Figure 3.1. Our generic incident ray, or energy bundle path, enters the slab through the opening at point P_1 and has a direction parallel to the unit vector **u**. The equation that gives the coordinates of a generic point P_i on the ray is, in vectorial notation, $(P_i-P_1)\times\mathbf{u}=0$. Since incoming irradiation is diffuse and uniformly distributed over the aperture, the number of energy bundles through a certain ring of radius r on the aperture is proportional to its area 2, and their direction is chosen randomly from a set that is weighted according to Lambert's cosine law. Thus, the direction of the ray should satisfy $\mathbf{u}\cdot\mathbf{k}=\cos(\sin^{-1}\Re_1^{1/2})$, where $\Re_1$ is a random number drawn from a uniformly distributed set between zero and one. Incoming intensity has a *Planck* spectral distribution of a 5780 K blackbody source. Thus, a wavelength of radiation assigned to the incident ray is given implicitly by:

$$\Re_2 = \frac{1}{\sigma T^4}\int_0^{\lambda} e_{\lambda b}(\lambda,T)d\lambda \qquad \textbf{(3.19)}$$

λ is numerically calculated using equation (3.14) for T=5780 K. Note that bundles cannot be considered photons since they all have the same energy, independent of the wavelength. The incident bundle will intercept a particle after traveling a distance l (path length to probable point of absorption/scattering), given by begin equation $l=-(1/K_\lambda)\cdot\ln\Re_3$. The point of intersection, P_2, is simply $P_2=P_1+l\cdot\mathbf{u}$. Here, another random choice, depending on the albedo, determines whether the bundle is absorbed or scattered. The probability of absorption is equal to 1- Ω_λ, evaluated at the bundle wavelength. If the bundle is scattered by the particle, the direction of scattering forms an angle ξ with the incident direction, obtained by numerically solving:

$$\Re_4 = \frac{1}{2}\int_0^{\xi}\Phi_\lambda(\xi,\eta)\sin\xi d\xi \qquad \textbf{(3.20)}$$

where the scattering phase function $\Phi_\lambda(\xi, \eta)$ gives, in statistical terms, the probability of scattering in a certain direction. The azimuthal angle of the scattered beam, η, is randomly chosen between 0 and $2\Phi_\lambda$ is independent of η. The wavelength of the scattered bundle is unchanged (elastic scattering). If the bundle is absorbed by the particle, a count is recorded and its history is terminated. However, to ensure no energy accumulation in radiative equilibrium, a new bundle must be emitted from the same particle. The direction of isotropic emission is randomly determined by the polar and circumferential angles, (θ,φ), given by: $\theta=\cos^{-1}(1-2\Re_5)$ and $\varphi=2\Re_6$. The new bundle is emitted by a non-gray particle at a wavelength corresponding to the temperature of the particle. This new wavelength assigned to the new bundle is found by solving:

$$\Re_7 = \frac{\int_0^{\lambda} a_\lambda e_{\lambda b}(\lambda,T)d\lambda}{\int_0^{\infty} a_\lambda e_{\lambda b}(\lambda,T)d\lambda} \tag{3.21}$$

evaluated at the particle temperature. Once we know the direction and wavelength of the *new* emitted bundle or of the *old* scattered bundle, we can again track the ray to determine the new point of interception with a particle and repeat the algorithm until the bundle reaches a black-body boundary. Eventually, each bundle of energy would undergo either scattering, absorption (and subsequent emission), or would leave through the plane boundaries. The history of a bundle is then a complete random sequence which terminates when a boundary is encountered. This procedure is repeated for a large enough sample of bundles so that the results are statistically meaningful.

Since the complex refractive index is spectrally dependent, the *Mie* subroutine *BHMIE* for calculating Φ_λ and Ω_λ would need to be executed for each incident energy bundle in each *Monte Carlo* iterative run. For the large number of bundles used in this study, the computing time consumed would be prohibitive. Instead, external to the *Monte Carlo* simulation code, we have used the *Mie* subroutine to compute the monochromatic scattering phase function Φ_λ as a function of the cone angle ξ, for a set of wavelengths in the 0.158-100 μm range. Next, we have numerically integrated the probability density phase functions over ξ to obtain a set of cumulative distribution functions according to equation (3.20). Finally, after exchanging axes, we have produced a 3-D interpolation to surface-fit the angle ξ as a function of the independent variables $\Re_4$ and λ. The technique used to produce this surface fitting is based on the bi-cubic *Bezier*-Spline algorithm [Engeln-Muellges and Reutter, 1987].

Similarly, the integrals of equation (3.21) were numerically carried out over λ to obtain the cumulative distribution functions of the probability of emission of an energy bundle at a certain wavelength from a particle at a given temperature. Again, after exchanging axes, we have used the bi-cubic *Bezier*-Spline interpolation to surface-fit the wavelength as a function of the independent variables $\Re_7$ and T. The surface $\lambda = \lambda(\Re_7,T)$ can be directly used in a *Monte Carlo* simulation to calculate the wavelength of emission for a given random number and particle temperature.

In equation (3.21), the particle temperature is *a priori* unknown. A temperature distribution within the medium is assumed for a first *Monte Carlo* run. Then, a new temperature is obtained by solving the radiative equilibrium equation for a volume element dV:

$$\text{Energy absorbed} = \text{Energy emitted} = 4dV\int_0^{\infty} a_\lambda e_{\lambda b}(\lambda,T)d\lambda \tag{3.22}$$

where the energy absorbed by dV is simply the number of bundles absorbed in that volume element times the energy carried by each bundle. The new temperatures obtained is used for the next *Monte Carlo* iteration until convergency. Because of the axial-symmetry of the geometry and power distribution, was found convenient to divide the slab into a fine grid of ring cells V_{ik}, as depicted schematically in Figure 3.1, and assume isothermal conditions for particles belonging to the same unit volume cell. Since particles are uniformly dispersed in the slab, each volume cell contains $N \times V_{ik}$ particles. We have counted the number of absorptions taking place at each cell and used equation (3.22) to calculate the average temperature of particles for each cell.

3.1.3.3 Results

A sample of 5 million energy bundles was employed for each *Monte Carlo* run. The accuracy of the *Monte Carlo* computation was checked against the exact analytical solutions available for the case of a non-isothermal absorbing-emitting-nonscattering gray medium between infinite parallel black walls. This specific idealized problem has been previously solved by Usiskin and Sparrow [Usiskin and Sparrow, 1960] using numerical integration, by Howell and Perlmutter [Howell and Perlmutter, 1964] using *Monte Carlo*, and by Heaslet and Warming [Heaslet and Warming, 1965] by means of tabulated functions. Heaslet and Warming [Heaslet and Warming, 1965] present the results to a considerable degree of precision and may be considered exact. The governing integral equation for the gas temperature distribution is given in dimensionless form by:

$$\int_0^{X_0} \phi(X)\left[\int_{\kappa(X_0-X)}^{\infty} \frac{e^{-\lambda}}{\lambda} d\lambda\right] dX + \int_{X_0}^{1} \phi(X)\left[\int_{\kappa(X-X_0)}^{\infty} \frac{e^{-\lambda}}{\lambda} d\lambda\right] dX + \frac{e^{[-\kappa(1-X_0)]}}{\kappa} = (1-X_0)\left[\int_{\kappa(X-X_0)}^{\infty} \frac{e^{-\lambda}}{\lambda} d\lambda\right] + \frac{2}{\kappa}\phi(X_0) \tag{3.23}$$

where Φ is the dimensionless emissive power, $\Phi=(T^4-T_1^4)/(T_2^4-T_1^4)$, X is the dimensionless normal coordinate x/D, and T_1,T_2 are the wall temperatures. Equation (3.23) was solved for Φ by numerical computation using *Mathematica* software package [Wolfram Research, Inc., 1993]. The dimensionless emissive power at the boundaries, $\Phi(0)$ and $\Phi(1)$, are within 0.3% of the numerical values reported by Heaslet and Warming [Heaslet and Warming, 1965]. Note that in contrast to the analytical solution, the *Monte Carlo* simulation needs to consider specific values for the wall temperatures. Our *Monte Carlo* program was run for the following parameters: front wall was taken at 5780 K, the back wall at 0 K, the albedo equal zero (no scattering), and the optical thickness equal 0.1 and 1 for every wavelength. Table 3.1presents the accuracy of the *Monte Carlo* solution when $T^4/5780^4$ is compared against the "exact" values.

Table 3.1 Error = maximum $|1-\phi_{Monte\ Carlo}/\phi_{exact}|$

κ_1	1 million	5 million	10 million
0.1	0.090	0.033	0.020
1	0.027	0.016	0.010

We now proceed to study the system configuration of Figure 3.1 for a non-isothermal non-gray absorbing-emitting-scattering suspension of Fe_3O_4 particles under concentrated solar irradiation. The boundary conditions and computational procedure have been described in Section 3.1.3.2. The ability of such a cloud to attenuate incident radiation by absorption and scattering is described in Figure 3.3. *Attenuation*, *Reflectance*, and *Absorptance* through the slab are defined in this study as:

$$Attenuation = 1 - \frac{\text{energy bundles arriving at the back wall}}{\text{total number of energy bundles entering through the aperture}} \tag{3.24}$$

$$Reflectance = \frac{\text{energy bundles scattered back to the front wall}}{\text{total number of energy bundles entering through the aperture}} \tag{3.25}$$

$$Absorptance = Attenuation - Reflectance \tag{3.26}$$

Note that this definition of *Attenuation* considers radiation at all wavelengths traversing through the slab and exiting in any direction. *1-Attenuation* is plotted in Figure 3.3 as a function of the *Planck* mean optical thickness κ.

Four cases are being investigated: (1) *Mie*-scattering particles under diffuse incident radiation; (2) *Mie*-scattering particles under perpendicular incident radiation; (3) isotropic-scattering particles under diffuse incident radiation; (4) isotropic-scattering particles under perpendicular incident radiation. In all four cases, the incident radiation has a 5780 K *Planck* spectral distribution, and the cloud consists of non-gray Fe_3O_4 particles. The comparison between these four cases presents the influence of the directional dependency of the incident radiation and the scattering phase function. As expected, perpendicular incident radiation, impinging normally to

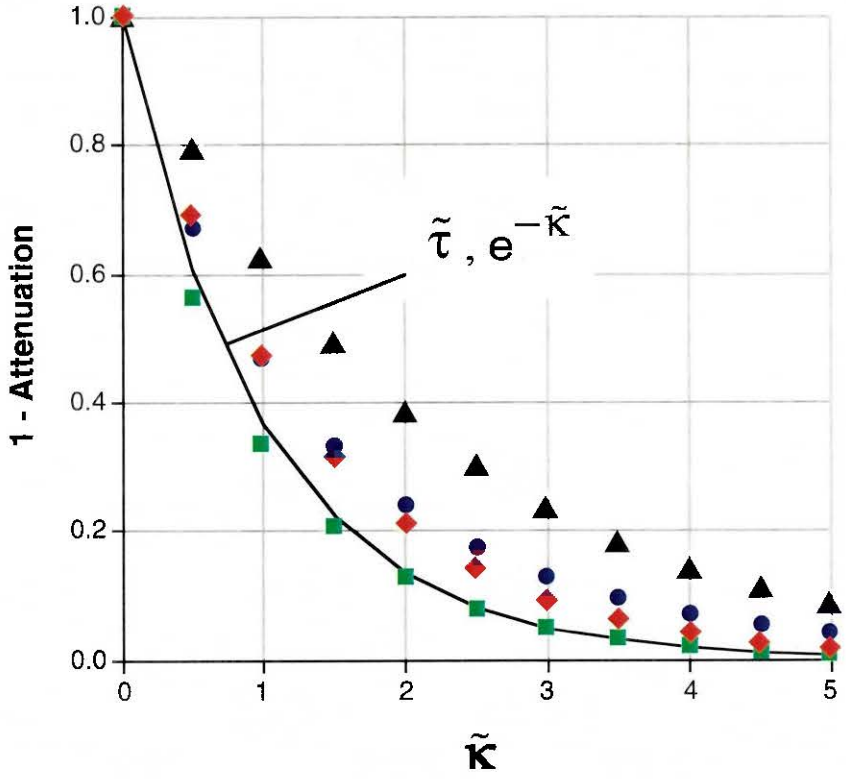

Figure 3.3 *1-Attenuation*, i.e. portion of incident radiation reaching the back boundary wall, as a function of the *Planck* mean optical thickness [Mischler and Steinfeld, 1995].
●Case 1: *Mie*-scattering, diffuse incident radiation
▲Case 2: *Mie*-scattering, perpendicular incident radiation
■Case 3: isotropic-scattering, diffuse incident radiation
◆Case 4: isotropic-scattering, perpendicular incident radiation

the front wall, is able to penetrate the cloud more efficiently than diffuse incident radiation having a directional distribution following Lambert's cosine law. Also, a cloud of *Mie*-scattering Fe_3O_4 particles permits radiation to penetrate deeper than a cloud of isotropic-scattering particles because Fe_3O_4 particles exhibit significant preference for forward scattering. Thus, case (2) (a cloud of *Mie*-scattering Fe_3O_4 particles under perpendicular incident radiation) gives the least attenuation, while case (3) (a cloud of isotropic-scattering particles under diffuse incident radiation) gives the largest attenuation. The difference is significant: case (3) needs a 2.25 optically thick slab in order to attenuate 90% of the incident radiation, while case (2) needs twice as much optical thickness to obtain the same result. For $\tilde{\kappa}=1$, about 35% of the incident radiation is transmitted for case (3), 65% is transmitted for case (2), and 50% is transmitted for cases (1) and (4). The isotropic-scattering assumption leads to an error in the calculation of attenuation of up to 79% for diffuse incident radiation and $\tilde{\kappa}=5$, and up to 80% for perpendicular incident radiation and $\tilde{\kappa}=5$. For $\tilde{\kappa}=1$, the error is 28% for diffuse incident radiation and 25% for perpendicular incident radiation.

When the objective is to utilize a cloud of particles as a means of shielding a surface from incident radiation, then case (3) is preferred. The optical thickness of the cloud could be optimized to meet the specific requirements of the reactor by changing either the volume fraction or the thickness of the cloud. The directional nature of the incident radiation could be modified by non-imaging optical elements. For example, in solar concentrators, the use of compound parabolic concentrators (*CPC*'s) can boost concentration at the expense of making the incident radiation more diffuse, and *vice-versa* [Welford and Winston, 1989].

The *Reflectance*, i.e. radiation reflected back to its source after single or multiple scattering, could considerably hinder the transport of radiation into the heart of a cloud. All four cases show back-scattering increasing with the optical thickness of the cloud and approaching a constant value after $\tilde{\kappa}=2.5$. Evidently, isotropic-scattering particles reflect more radiation than *Mie*-scattering Fe_3O_4 particles do. Quantitatively, this effect is about 4.2 times larger for diffuse incident radiation, and 5.6 times larger for perpendicular incident radiation. A bundle scattered by a *Mie*-scattering particle at the front layer of the cloud is most likely to penetrate further into the cloud. In contrast, a bundle scattered by an isotropic-scattering particle at the front layer has 50% chance of being reflected back and eventually lost.

The intensity of monochromatic radiation incident normally on an absorbing-scattering slab of thickness D is attenuated along its path according to *Bouguer*'s law by a factor $e^{-K_\lambda D}$, for K_λ independent of position in the medium. However, *Bouguer*'s law is a particular case of the general equation of transfer when emission and scattering along the optical path are not included. By integrating *Bouguer*'s law over the entire spectrum, a directional total transmittance for incident blackbody radiation can be defined as:

$$\tilde{\tau} = \frac{1}{\sigma T^4}\int_0^{\lambda} e^{-K_\lambda D} e_{\lambda b}(\lambda,T)d\lambda \qquad (3.27)$$

Strictly, $1-\tilde{\tau}$ gives the portion of *Planck* radiation lost by being absorbed or scattered away along the normal direction. The transmittance $\tilde{\tau}$, as defined by equation (3.27), is plotted in Figure Figure 3.3. A different approximation to calculate the mean attenuation of incident blackbody radiation over all wavelengths is to use *Bouguer*'s law form with the *Planck* mean optical thickness, i.e. incident radiation being attenuated by a factor $e^{-\tilde{\kappa}}$. The $e^{-\tilde{\kappa}}$-approximation, as well as $\tilde{\tau}$, cannot predict the effect of the angular dependency of Φ_λ, nor of the incident radiation. Nevertheless, their use is justified when compared with the complexity of handling detailed spectral calculations. They give practically the same results and their curves lie close to the *Monte Carlo* solution obtained for isotropic-scattering under diffuse incident radiation. Howev-

er, a large error (up to 82%, at $\tilde{\kappa}=5$) is committed when either $\tilde{\tau}$ or the $e^{-\tilde{\kappa}}$-approximation are employed for treating *Mie*-scattering particles under perpendicular incident radiation.

Under radiative equilibrium, the temperature distribution within the cloud is calculated iteratively using equation (3.22). As the baseline we take a slab thickness D=0.1 m, and a volume fraction $f_v=1.4641\cdot10^{-5}$ (0.075841 kg of Fe_3O_4 particles per m^3 of slab space), so that the *Planck* mean optical thickness $\tilde{\kappa}=1$. The aperture radius, r_{ap}=D/2. The power flux through this aperture is taken equal to 2500 kW/m^2 which is a solar flux intensity achievable with typical concentrating systems [Grasse *et al.*, 1987]. Thus, the total power entering the slab is 19.6 kW and each of the 5 million bundles carries $3.92\cdot10^{-6}$ kW. In addition, the baseline uses diffuse radiation with a 5780 K *Planck* distribution, incident upon a cloud of non-gray *Mie*-scattering particles.

Four new cases are analyzed in Figure 3.4: A) the baseline; B) the baseline with perpendicular incident radiation; C) the baseline with isotropic-scattering particles ($\Phi_\lambda=1$); D) the baseline for a gray-isotropic medium having $\kappa_\lambda=\tilde{\kappa}=1$, $\Omega_\lambda=\tilde{\Omega}=0.58942$, and $\Phi_\lambda=1$. Figure 3.4 presents the temperature distribution within the slab obtained for cases (A), (B), (C), and (D), respectively. Comparison between Figure 3.4A and Figure 3.4B shows a remarkable effect of the directional nature of the incident radiation. Radiation impinging normally to the slab is not absorbed efficiently by the cloud. This effect is explained by referring to Figure 3.3, which shows the least attenuation and the least absorptance for perpendicular incident radiation. A relatively small number of absorptions implies a small number of emissions as well, and consequently the improbability of radiation being distributed isotropically. Since forward-scattering is favored for *Mie*-scattering Fe_3O_4 particles, a bundle entering perpendicularly through the aperture is likely to travel a short distance in the cloud before exiting through the back wall. This reduces considerably the probability of intercepting a particle and being absorbed. In contrast, a bundle entering in a diffuse manner has evidently a longer path length to the back wall and, therefore, a higher probability of intercepting a particle, of being absorbed, and of being emitted isotropically. Comparison between Figure 3.4A and Figure 3.4C presents the effect of Φ_λ by taking either *Mie*-scattering or isotropic-scattering particles. The difference is practically negligible for $\tilde{\kappa}=1$. The number of absorptions for case (A) and (C) are nearly the same for $\kappa=1$. Since emission is isotropic for both cases, radiation transfer within the medium becomes less dependent on the directional properties of Φ_λ, is expected that temperatures will be underestimated by taking the isotropic approximation for $\tilde{\kappa}>1$. This was corroborated for $\tilde{\kappa}=5$.

The gray approximation, case (D), does not yield a sufficiently accurate solution, when compared to the baseline case (A). Temperatures are overestimated by about 27%. The reason is that, by definition, $\tilde{\kappa}$ and $\tilde{\Omega}$ are the mean of the spectral κ_λ and Ω_λ when weighted by a 5780 K blackbody emission spectrum, equations (3.17) and (3.18). However, the spectral distribution of the incident radiation does not remain unchanged as travels through the cloud. Instead, is shifted to longer wavelengths due to the emission of radiation by particles at temperatures much lower than 5780 K. We have calculated the probability density function of wavelengths assigned to all energy bundles entering through the aperture and emitted by particles in radiative equilibrium. The shift in the wavelength distribution from the one obtained for incident blackbody radiation to the one obtained for the baseline case (A) is the cause for the error in the gray approximation (case (D)). Longer wavelengths of emission result in higher absorption efficiencies Q_a, and consequently in higher values for a_λ, which according to *Kirchhoff*'s law is equal to the emission coefficient. Therefore, the non-gray cloud is absorbing radiation mostly in the spectral region around 0.5 μm, but emits radiation in the spectral region around 3 μm, where a_λ is somewhat higher. The gray cloud instead uses a constant absorption coefficient for both absorption and emission, independent of wavelength. This constant value is the *Planck* mean of the spectral a_λ, equal to $\tilde{\kappa}(1-\tilde{\Omega})/D$. By applying equation (3.22), the equilibrium temperatures

obtained for the gray-approximation are higher than those obtained for the non-gray cloud. For purposes of solar energy collection, would be desirable to have a cloud of particles with a high a λ in the visible spectrum where the solar energy peaks, but with a low a λ in the *IR* spectrum where emission peaks. Unfortunately, a cloud of Fe_3O_4 particles features just the opposite spectral behavior.

Finally, Figure 3.5 presents the temperature distribution within the slab obtained for the baseline case with $\tilde{\kappa}$=5. A cloud 5 times more dense or 5 times thicker achieves temperatures that are about 10% higher. For the given conditions, temperatures of the order of 2250 K are being attained in the proximity of the aperture, which are about the level of temperatures required to conduct the thermal reduction of Fe_3O_4 to FeO. Temperatures become moderate as we approach the back wall or as we go farther away from the z-axis, as a result of the shielding effect

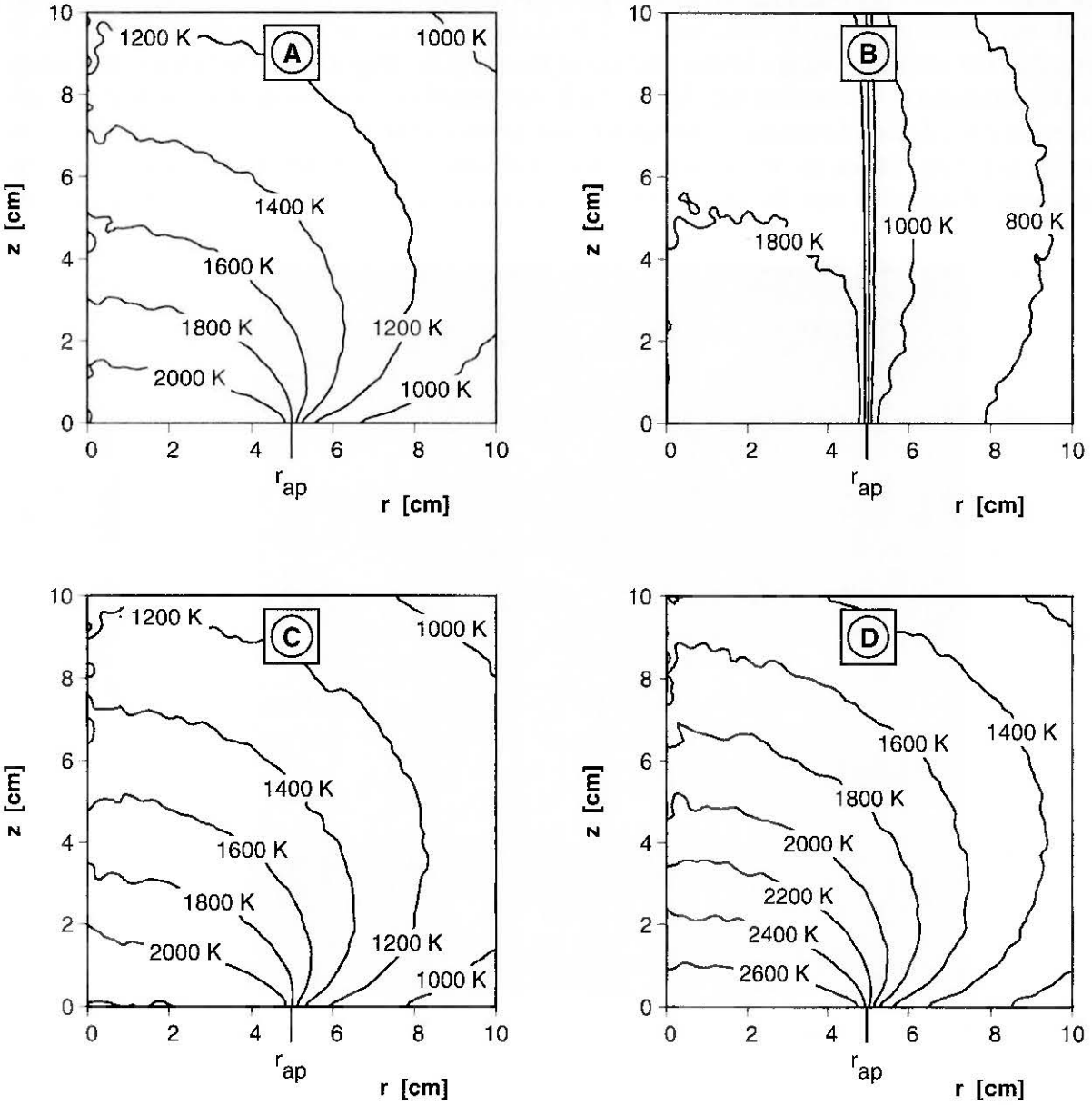

Figure 3.4 Temperature distribution under radiative equilibrium [Mischler and Steinfeld, 1995]. Input: slab thickness: 0.1 m, volume fraction: $1.4641 \cdot 10^{-5}$, mean optical thickness: κ=1, aperture radius: 0.05 m, power flux: 2500 suns. Case (A) is the baseline; case (B) is the baseline with perpendicular incident radiation; case (C) is the baseline with isotropic-scattering particles (Φ_λ=1); case (D) is the baseline with a gray-isotropic medium having $\kappa_\lambda=\tilde{\kappa}=1$, $\Omega_\lambda=\tilde{\Omega}=0.58942$, and $\Phi_\lambda=1$.

of the cloud. The temperature gradient between front and back layers is about 1000 K. A reactor design based on these results would require materials of construction able to withstand about 1200 K.

Although not considered in this study, polydispersions can be treated by integration of the phase function and attenuation efficiencies over the particle size distribution (see, for example, Mengüc and Viskanta, 1986; Gupta *et al.*, 1983]. These integrations are executed external to the *Monte Carlo* simulation and therefore have no influence on its computational time or accuracy. The mean properties obtained for coarse size distributions of polydispersions will most probably exhibit a lesser (or smoother) dependency on λ and ξ, and, as opposed to monodispersions, the cloud selectivity might become unimportant. Also not included in this study, reflections from non-gray and directional-dependent reflective boundary surfaces can be easily implemented in the *Monte Carlo* simulation. Reacting clouds undergoing exothermal/endothermal chemical transformations may be simulated by introducing a source/sink of energy in each particle equal to the enthalpy change of the reaction at the particle temperature. Particles or boundary walls subjected to convection heat losses could be treated in a similar manner, where the sink of energy is calculated from the heat transfer coefficient and the temperature difference between solids and flow. However, if the flow velocity and temperature fields are not prescribed, the equation of radiative transfer and the flow equations (continuity, momentum and energy) are

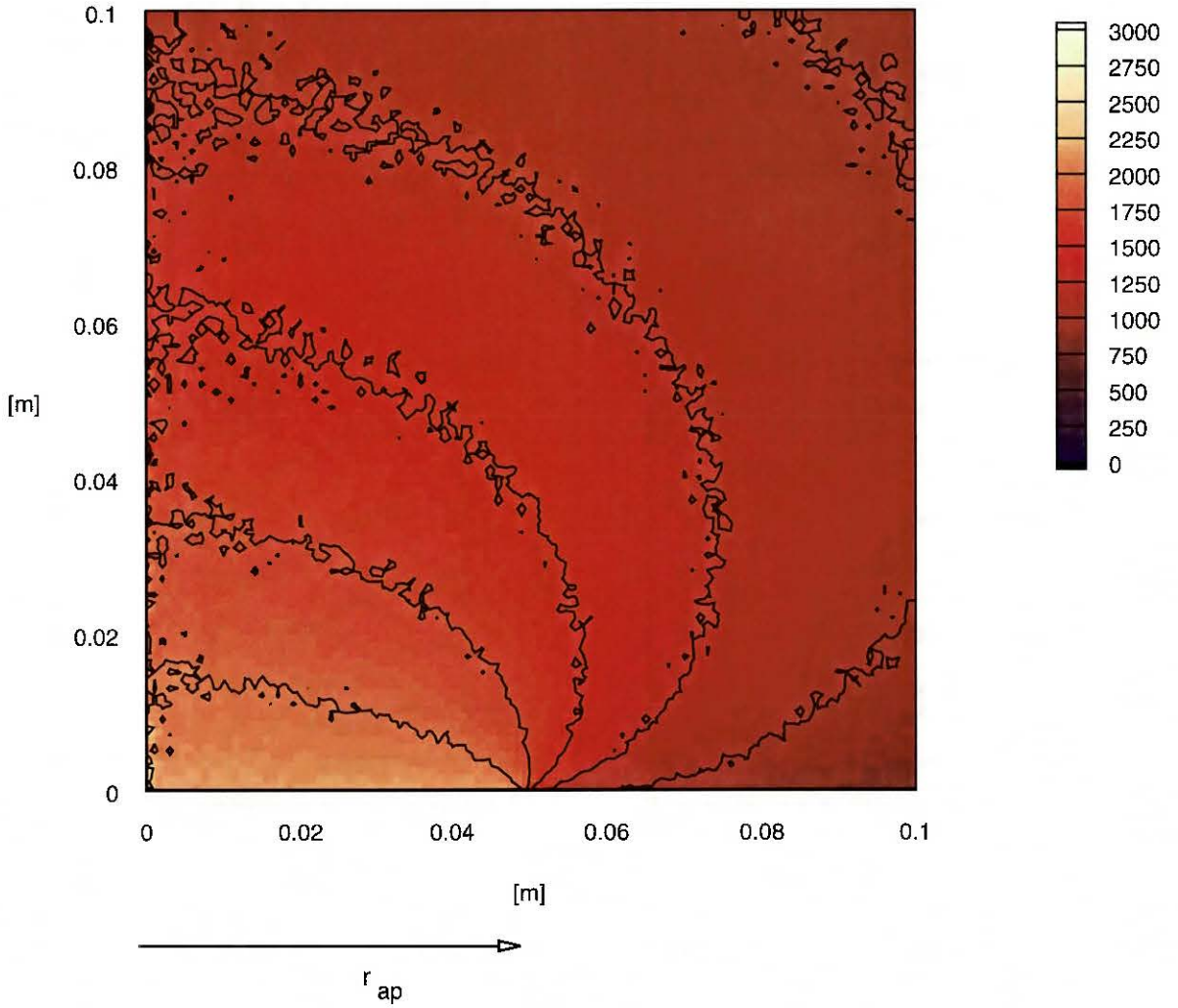

Figure 3.5 Temperature distribution under radiative equilibrium for the baseline case and $\tilde{\kappa}$=5 [Mischler and Steinfeld, 1995].

coupled, and their solution requires an iterative process. Simplified analysis of combined radiation and convection in a particulate-laden flow has been presented by Kumar and Tien [Kumar and Tien, 1990]. Insofar as the transient behavior is concerned, convective transfer rates have been found to be comparable to radiative ones for small particles (d<1 μm), while for particles larger than 1 mm in diameter, the gas temperature stays unchanged during rapid heating of the particles [Wang and Yuen, 1987].

3.1.3.4 Conclusions

A cloud of Fe_3O_4 particles under concentrated solar irradiation has been investigated by the *Monte Carlo* method. Special attention was devoted to the realistic case of a non-gray, non-isothermal, absorbing, emitting, and anisotropically scattering medium. The spectrally and directionally dependent optical properties of the particles were calculated using *Mie* theory. The appropriate cumulative distribution functions were incorporated in the *Monte Carlo* simulation via *Bezier* surfaces, which permitted the use of large samples of energy bundles (within a reasonable computational time) and consequently better accuracy and repeatability. The effect of directional dependency of the incident radiation and the scattering phase function was shown to be significant when calculating the attenuation of radiation at all wavelengths and directions. The transmittance τ, defined by equation (3.27), or the e^{-K}-approximation, can predict the attenuation by an isotropic-scattering medium under diffuse radiation, but is not suitable for treating a cloud of *Mie*-scattering particles under perpendicular incident radiation. The isotropic-scattering assumption leads to an error in the calculation of attenuation of up to 79% for diffuse incident radiation, and up to 80% for perpendicular incident radiation. Temperature distributions within the cloud were calculated under radiative equilibrium. The directional nature of the incident radiation was found to have a remarkable effect on the temperature solution, was demonstrated that the gray approximation does not yield accurate results because ignores the shift in the spectral distribution to longer wavelengths where the spectral absorption coefficient is higher. When the gray approximation with *Planck* mean values is used, temperatures are overestimated by about 27%.

Nomenclature

a_λ	Spectral absorption coefficient
C_1	Constant in *Planck* spectral energy distribution = $0.59552 \cdot 10^8$ W μm^2
C_2	Constant in *Planck* spectral energy distribution = 14388 μm K
D	Slab thickness, m
d	Particle diameter, m
$e_{\lambda b}(\lambda,T)$	Hemispherical spectral emissive power
f_v	Volume fraction
i, j, k	Unit vectors in cartesian system
K_λ	Spectral extinction coefficient, $K_\lambda=a_\lambda+s_\lambda$
$\tilde{K}$	*Planck* mean extinction coefficient
l	Probable mean free path, m
N	Number density, particles per unit volume
P_i	Generic point of ray

Q_a, Q_s, Q_K	Absorption, scattering, and extinction efficiency
r_{ap}	Aperture radius, m
$\Re$	Random number between [0,1]
s_λ	Spectral scattering coefficient
T	Absolute temperature, K
u	Unit vector parallel to the direction of a reflected ray
V_{ik}	Volume element in Figure 3.1
X	Dimensionless normal coordinate = x/D
η	Azimuthal angle of scattered beam
θ	Polar angle, measured from normal of surface
κ_λ	Spectral optical thickness
$\bar{\kappa}$	*Planck* mean optical thickness
λ	Wavelength
ξ	Angle between scattered and incident direction
σ	*Stefan-Boltzmann* constant, $5.6705 \cdot 10^{-8}$ W m^{-2} K^{-4}
$\bar{\tau}$	*Planck* mean directional total transmittance
Φ_λ	Scattering phase function, ratio of scattered intensity in the direction (ξ, η) to the intensity of isotropic scattering
ϕ	Dimensionless emissive power
φ	Circumferential angle
Ω_λ	Albedo = s_λ/K_λ
$\bar{\Omega}$	*Planck* mean albedo

3.2 2-Step Water-Splitting Cycle Using the Fe_3O_4/FeO Redox System

3.2.1 Solar Thermal Reduction of Fe_3O_4 (Magnetite)

The methods for selecting chemical reactions for storing sunlight, the methodology for studying these reactions, and the techniques for developing the technology for effecting the chemical reactions are all germane subjects for discussion. In this Chapter, we would like to focus on what we have found to be some of the main issues associated with the development of a solar reactor concept for a given chemical reaction [Steinfeld *et al.*, 1998c]. We present our ideas in the form of a case study. Specifically, we demonstrate how we arrived at reactor concepts for effecting the following chemical transformation:

$$Fe_3O_4(l) = 3FeO(l) + \frac{1}{2}O_2, \text{ where T<1875 K} \qquad \textbf{(3.28)}$$

This reaction is at the heart of two major ideas for storing sunlight in the form of chemical energy. FeO reacts exothermally at low temperature with either H_2O or CO_2 to produce H_2 or $C(gr)$ according to equations (3.29) and (3.30), respectively:

$$3FeO + H_2O = Fe_3O_4 + H_2 \tag{3.29}$$

$$3FeO + \frac{1}{2}CO_2 = Fe_3O_4 + \frac{1}{2}C(gr) \tag{3.30}$$

The Fe_3O_4 that is produced in either of these two reactions is recycled to a solar furnace where FeO is reproduced from reaction (3.28). In this manner, solar energy is used to produce either H_2 from H_2O or $C(gr)$ from CO_2 [Nakamura, 1977; Ehrensberger *et al.*, 1997]. The 2-step water splitting cycle represented by reactions (3.28) and (3.29) is schematically shown in Figure 3.6.

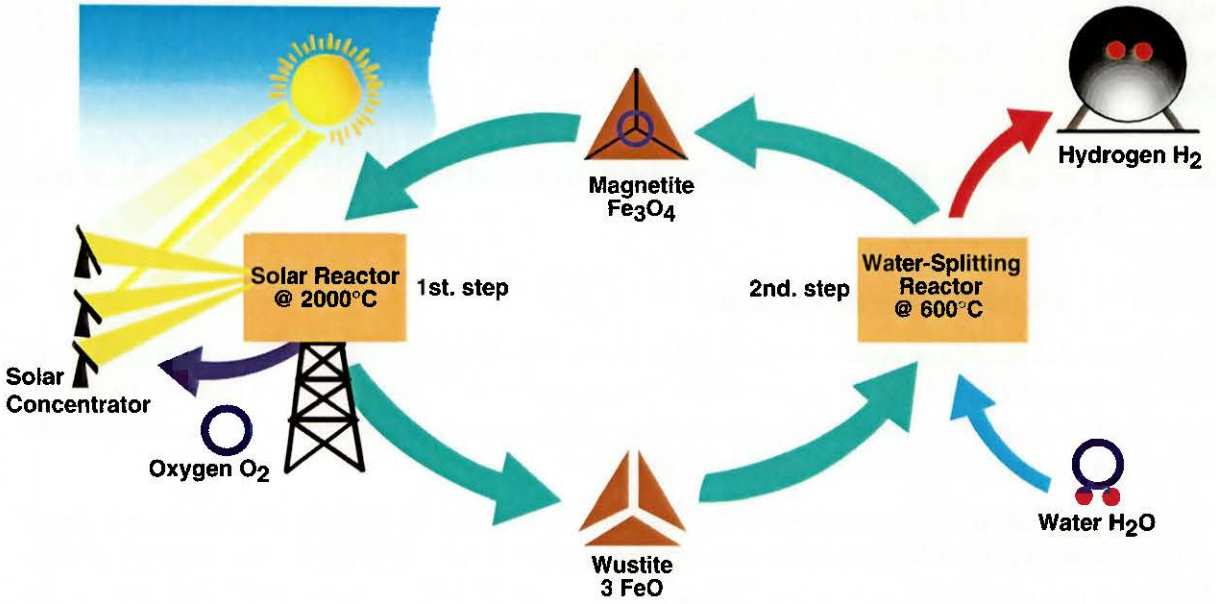

Figure 3.6 Schematic representation of a 2-step H_2O-splitting solar thermochemical cycle using the Fe_3O_4/FeO redox system. In the first, endothermic, solar step magnetite (Fe_3O_4) is thermally decomposed into wustite (FeO) and oxygen at elevated temperatures. Concentrated solar energy is the source of high-temperature process heat. In the second, exothermic step, wustite is reacted with water to form hydrogen; magnetite is recycled to the first step. The net reaction is: $H_2O = H_2 + 0.5\ O_2$; hydrogen and oxygen are produced in different steps, eliminating the need for high temperature gas separation.

3.2.2 General Constraints for the Solar Reactor Design Problem

Because a long term goal of the research is to have solar energy become the significant sustainable energy resource for the world economy, it is important that the development of the solar chemical reactor be shaped by economic considerations. It is pertinent to ask how one can be concerned with the economics of a technology that does not exist especially when its use is envisioned for a time at least 50 years into the future. Certainly a typical cost benefit analysis is inappropriate; if such a criteria were invoked in the 19th and early 20th century by potential entrepreneurs, it seems likely that they would have decided not to invent the telephone, oil refinery, automobile, aircraft, etc. In place of a cost benefit analysis, we consider very general economic constraints on the design problem. This approach means that we identify aspects of the technology that are likely to be costly and then attempt to make design decisions that favor the least expensive options relative to the choices at hand.

To date, the largest single cost element of a solar central receiver power plant is the heliostat field and it typically represents between 30 and 40% of the total capital cost [De Laquil, 1994]. Thus, economics suggests at one level that the solar chemical reactor effects the chemical transformation with the highest possible thermal efficiency so that the size of the heliostat field can be kept to a minimum. The cost of the reactor, however, can go up as one attempts to maximize its thermal efficiency. For example, a reactor closed by a transparent window may be more efficient than one open to the atmosphere, but its cost could be significantly higher with the window, both from initial investment and daily maintenance points of view. Heat exchanger equipment may substantially boost thermal efficiency by adding pre-heating to the process, but it comes with a price. Thus, it is important to accurately estimate the gain in thermal efficiency for a given design decision as well as develop alternate reactor concepts that can be followed as time elucidates the best economic path to follow.

We demonstrate that the chemistry of the reaction conducted in the solar chemical reactor plays a vital role in determining the reactor's thermal efficiency. We begin by presenting the chemical thermodynamics and kinetics for reaction (3.28).

3.2.3 Chemistry for Fe_3O_4 Decomposition and its Implications on Reactor Design

3.2.3.1 Chemical Thermodynamics

We expect the gas phase products in air to be O, O_2, N_2, NO, and $FeO(g)$. The liquid phase will be a mixture of $FeO(l)$ and $Fe_3O_4(l)$. Since the activity coefficients for a mixture of these two liquids are not known, equilibrium calculations were performed assuming either an immiscible mixture or an ideal solution of $FeO(l)$ and $Fe_3O_4(l)$.

Chemical equilibrium compositions were computed using the STANJAN computer code [Reynolds, 1986]. Thermochemical data was taken from [JANAF, 1985]. The reactants are 1 mole $Fe_3O_4(s)$ and x moles of air, where x depends on the loading ratio of iron oxide in air. The results are shown in Table 3.2. Species with mole fractions less than 10^{-5} have been omitted. The conversion ratio is defined as the number of FeO moles in equilibrium (in any phase) divided by 3 (which corresponds to the complete conversion of 1 mole of Fe_3O_4 to 3 moles of FeO and 0.5 moles of O_2). CASE 0 is the only case where we presume the condensed phase to be an immiscible mixture and obtain 100% conversion ratio. All the other cases assume chemical equilibrium composition for an ideal solution. Computations were made for 3 different air/Fe_3O_4 molar ratios (0, 1, and 10) and for 4 different reactor temperatures (1900K, 2100K, 2300K, and 2500K). The different cases are grouped as CASE 1, 2, and 3 for air/Fe_3O_4 molar ratios 0, 1, and 10, respectively; and are further grouped in CASE _1, _2, _3, and _4 for temperatures 1900, 2100, 2300, and 2500K, respectively.

For all cases, the conversion increases with temperature and with air/Fe_3O_4 molar ratio, ranging from 11% for case 1_1 (lowest temperature and air/Fe_3O_4 molar ratio) to 52% for case 3_4 (highest temperature and air/Fe_3O_4 molar ratio). As the temperature increases, $FeO(l)$ becomes the major component in the condensed phase. For example, for cases 2_1 to 2_4, the mole percent of FeO in the liquid phase for an equilibrium system goes from 33% to 73% when the temperature varies between 1900K and 2500K. There is little $FeO(g)$ present in the gas phase and we must presume that it will re-oxidize to Fe_3O_4 and Fe_2O_3, as evidenced by solar experimentation [Tofighi and Sibieude, 1980; Sibieude *et al.*, 1982; Tofighi and Sibieude, 1984].

If the number of moles of air is markedly increased, slightly more $FeO(l)$ is produced at each temperature, but substantially more $FeO(g)$ is also produced. Thus, for an atmospheric-open re-

actor, it will be necessary to continuously remove the liquid phase, if the forming of $FeO(g)$ is to be avoided. When no air is present in the system (cases 1_1 to 1_4), the mole percent of FeO in the liquid phase goes from 27% to 67% between 1900 and 2500 K. At 2500 K, FeO(g) starts to become significant. This result is important too, because under air more FeO is obtained than in the case of no air, but a portion of the delivered solar energy is used to heat the air. An additional drawback when effecting the reaction in air is the formation of NO_x compounds. However, a technical advantage is that an open reactor eliminates the need for a transparent window at the reactor aperture. The added complexity of a window must be evaluated along with any potential thermodynamic gains.

3.2.3.2 Chemical Kinetics

The available rate expression for the decomposition of liquid Fe_3O_4 is described by [Tofighi, 1982]:

$$\frac{d\xi}{dt} = k \cdot \xi^{0.5} \cdot (1 - \xi)^{0.77} \tag{3.31}$$

where ξ is the degree of reaction varying between 0 and 1, as measured by the amount of O_2 that is produced, and k is the rate constant: $k = 2.66 \exp(-1250/T)$ min^{-1}. This expression was shown to have limited applicability because it does not account for the partial pressure of oxygen. Although the kinetic experiments from which the above rate expression was established were conducted under a 20 l/hr flow of Ar, it was shown that as the Ar flow rate increased, the rate increased [Tofighi, 1982]. Nonetheless, several conclusions can be drawn from the study. Under Ar flowing at 20 l/hr, and a temperature of 2100 K, the decomposition rate reaches a maximum value near 40% completion [Tofighi, 1982]. The rate of decomposition is being limited by the gas phase mass transport of O_2 from the liquid surface. We expect the reaction in air to be slower than that predicted by equation (3.31).

It is important to note that partial substitution of iron in Fe_3O_4 by metals M such as Mn, Mg, and Co, forms mixed metal oxides $(Fe_{1-x}M_x)_3O_4$ that may be reducible at lower temperatures than those required for the reduction of Fe_3O_4, while the reduced phase $(Fe_{1-x}M_x)_{1-y}O$ is still capable of splitting water [Kuhn *et al.*, 1995; Tamaura *et al.*, 1995]. Reduction yields between 4% to 37% were obtained using a suspension of 4 µm particles in N_2 that were exposed for short times (less than 1 second) to solar flux intensities of 5000 kW/m^2 [Steiner, 1997]. Under similar conditions, but using air instead as the carrier gas, the products revealed no reduction but rather further oxidation. Thus, although such chemical system would require moderate (and more workable) upper operating temperature for the reduction, the experimental results with particle suspensions suggest the need to provide either fast quenching or an oxygen-free atmosphere to avoid re-oxidation. Segregation effects, due to different affinity to oxygen and different diffusion coefficients, were observed during the thermal reduction in N_2 atmosphere that lasted 10 seconds [Nüesch, 1996]; no such effects were found in faster solar experiments with residence times of less than 1 second. Segregation, unless reversible, would severely hinder the recycling capability of mixed metal oxides redox systems. Laboratory experiments on the water-splitting reaction have shown that the rate of reaction is slower; the reaction time to 50% completion is about twice as long when using the reduced form of Fe-Mn mixed oxides than when using wustite [Ehrensberger *et al.*, 1995]. For each of these reasons, we prefer Fe_3O_4 as the starting material.

To see all of the consequences of the decomposition kinetics on the design of a reactor would require solving for various reactor concepts the energy and mass balance equations simultaneously with a valid expression given for the rate of the reaction. This numerical task is beyond

the scope of this study. Nevertheless, a look at the rate expression gives some insights on the reactor design. Because the reaction rate peaks at a given conversion, the reactor should not be operated beyond the condition where the rate is a maximum. Such a design constraint attempts to maximize the production rate of FeO.

It has been demonstrated that the back reaction between $FeO(l)$ and O_2 is very fast [Tofighi, 1982]. Quenching the decomposition products at a rate of 10,000 K s^{-1} were necessary to obtain good FeO yields. It will be shown in the following section that this fact places severe constraints on the reactor designer attempting to maximize the thermal efficiency of a solar process using the Fe_3O_4 decomposition step.

3.2.4 Thermodynamic Cycle Analysis and its Implications on Reactor Design

In this section we present a second-law analysis that assesses the maximum possible efficiency of a 2-step water-splitting solar thermochemical cycle using the Fe_3O_4/FeO redox system. This cycle, represented by equations (3.28) and (3.29), has been previously analyzed [Nakamura, 1977], but this previous study did not account for the solar energy absorption efficiency and did not consider equilibrium compositions nor the effect of heating and quenching. The present 2nd-law analysis accounts for these important constraints and follows the derivation of [Steinfeld *et al.*, 1996a].

A quasi-cyclic system that allows for energy and mass to cross the boundaries is considered. The process flow sheet is shown in Figure 3.7. It is an archetypal model which uses a solar reactor, a quenching device, a water-splitter reactor, and a fuel cell. A mixture of 1 mol/s of $Fe_3O_4(s)$ and x moles/s of air is fed into the process at $T_1 = 298$ K and pressure of 1 bar. The complete process is carried out at constant pressure. In practice, pressure drops will occur throughout the system. If one assumes, however, frictionless operating conditions, no pumping work is required.

Solar Reactor

The solar reactor is assumed to be a cavity-receiver having a small aperture to let in concentrated solar radiation. Its solar energy absorption efficiency, $\eta_{absorption}$, is defined as the net rate at which energy is being absorbed divided by the solar power coming from the concentrator. For a perfectly insulated blackbody cavity receiver (no convection or conduction heat losses; only radiation losses through the aperture are considered; $\alpha_{eff} = \varepsilon_{eff} = 1$), it is given by:

$$\eta_{absorption} = \frac{Q_{reactor,net}}{Q_{solar}} = 1 - \frac{\sigma \cdot T_{reactor}^4}{I \cdot \tilde{C}} \tag{3.32}$$

The reactants enter the solar reactor at T_1 and are further heated to the reactor temperature $T_{reactor}$. Chemical equilibrium is assumed inside the reactor. Thus, the reactants undergo a chemical transformation as they are heated to $T_{reactor}$. Q_{solar} is the total power coming from the solar concentrator. Q_{rerad} is the power lost by re-radiation through the reactor aperture. Radiation gain from the environment is ignored. The net power absorbed in the solar reactor should match the enthalpy change of the reaction, i.e.,

$$Q_{reactor,net} = \Delta H|_{Reactants(T_1,\,p) \rightarrow Products(T_2,\,p)} \tag{3.33}$$

Products exit the solar reactor at $T_2 = T_{reactor}$, having an equilibrium composition.

Quench

After leaving the reactor, the products are cooled rapidly to ambient temperature, $T_3 = 298$ K. The product composition remains unchanged as they are quenched, except for the phase changes (e.g., $FeO(l)$ to $FeO(s)$; $Fe_3O_4(l)$ to $Fe_3O_4(s)$) and the reformation of O_2 and N_2 from O and NO. This assumption is reasonable provided the kinetics of the reoxidation of FeO is slower than the time it takes to quench. The amount of thermal power lost during quenching is

$$Q_{quench} = -\Delta H|_{Products(T_2,\, p) \rightarrow Products(T_3,\, p)}. \tag{3.34}$$

The irreversibility associated with quenching is

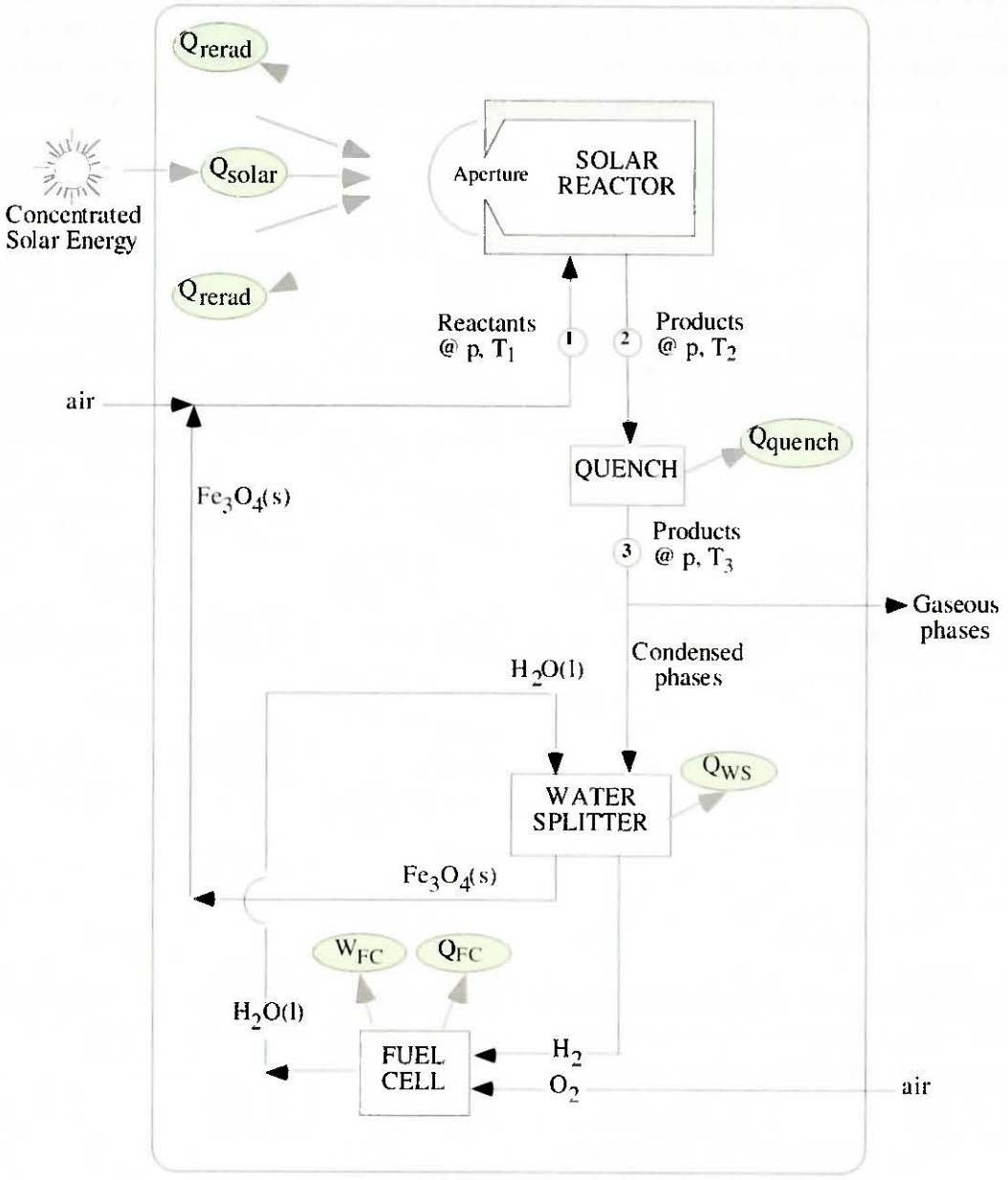

Figure 3.7 The process flow diagram modeling the 2-step H_2O-splitting thermochemical cycle using Fe_3O_4/FeO and solar energy [Steinfeld *et al.*, 1996a]. It is an archetypal model which uses a solar reactor, a quenching device, a water-splitter reactor, and a fuel cell. A mixture of 1 mol/s of $Fe_3O_4(s)$ and x moles/s of air is fed into the process at $T_1 = 298$ K and pressure of 1 bar.

$$Irr_{quench} = \frac{Q_{quench}}{298K} + \Delta S|_{Products(T_2,\,p) \rightarrow Products(T_3,\,p)}. \tag{3.35}$$

Quenching is a completely irreversible step causing a significant drop in the system efficiency.

From point 1 to 3 in the flow sheet, the chemical transformation

$$Reactants(298K,\,p) \rightarrow Products(298K,\,p) \tag{3.36}$$

has been effected. The products separate naturally into gaseous and condensed phases without expending work; gases are discarded to the atmosphere.

Water-Splitter

FeO reacts exothermally with water to form molecular H_2 according to equation (3.29), which takes place in the WATER-SPLITTER reactor of Figure 3.7. The heat liberated could be used in an auto-thermal reactor for conducting the water-splitting reaction at temperatures above ambient conditions. In this study, however, we consider this heat lost to the surroundings, as given by

$$Q_{WS} = -\Delta H|_{3FeO(s) + H_2O(l) \rightarrow Fe_3O_4(s) + H_2}. \tag{3.37}$$

Fuel Cell

The hydrogen produced in the water-splitter reactor may be burned in air and the heat of combustion converted into work via a heat engine, or it may be used more efficiently in a fuel cell to generate electric work directly. The theoretical maximum available work that could be extracted from hydrogen is calculated by introducing a reversible fuel cell, represented in Figure 3.7 as FUEL CELL. In this ideal cell, the products recombine to form the reactants and thereby generate electrical power in an amount W_{FC}. The work output of the fuel cell is given by

$$W_{FC} = -\Delta G|_{H_2 + 0.5O_2 \rightarrow H_2O(l)}. \tag{3.38}$$

The fuel cell operates isothermally; Q_{FC} is the amount of heat rejected to the surroundings:

$$Q_{FC} = -298K \times \Delta S|_{H_2 + 0.5O_2 \rightarrow H_2O(l)} \tag{3.39}$$

Since the O_2 fed to the fuel cell is extracted from air, equations (3.38) and (3.39) need to be corrected for the work expenditure for unmixing N_2 and O_2. The overall system efficiency of the closed-cycle is then calculated as

$$\eta_{overall} = \frac{W_{FC}}{Q_{solar}}. \tag{3.40}$$

If we take into account, in addition to the work output of the cell, also the maximum available work (i.e. exergy) that can be extracted from essentially the sensible and latent heat of the products, the overall efficiency is then calculated as

$$\eta_{overall,max} = \frac{W_{FC} + 298K \times Irr_{quench}}{Q_{solar}} \tag{3.41}$$

Equations (3.40) and (3.41) allow one to evaluate complex solar thermochemical processes by considering the maximum thermodynamic value of the chemical products as they recombined to form the reactants via an ideal reversible fuel cell. The calculation makes it possible to isolate

the solar process and analyze it as a cyclic system: a heat engine that uses reactants and products as the *working fluid*, exchanges heat with the surroundings, and converts solar process heat into work. This analysis provides an especially useful basis for comparing the efficiencies of different solar processes.

3.2.4.1 Results and Discussion

The baseline case is conducted at a constant total pressure of 1 atm. Reactants are fed at $T_1 = 298$K and products are quenched to $T_3 = 298$K. The reactor temperature T_2 is taken arbitrarily equal to 1900, 2100, 2300, and 2500 K. The mean flux concentration ratio is $\tilde{C}$=5000 suns (1 sun = 1kW/m^2). A concentration ratio of 5000 is within the reach of large-scale solar collection facilities, provided that secondary concentrators, e.g. compound parabolic concentrators (*CPC*), are implemented [Welford and Winston, 1989]. The mass flow rate is 1 mol/s of $Fe_3O_4(s)$ and x moles/s of air. Unless otherwise stated, the aforementioned baseline parameters are used. Table 3.2 shows the energy balance with and without quenching.

The solar absorption efficiency, $\eta_{absorption}$, decreases with temperature due to re-radiation losses; it varies from 85% at 1900K to 58% at 2500K. A simple expression for the direct calculation of the change in $\eta_{absorption}$ as a function of the change in temperature ΔT is given by

$$\frac{1-\eta_{absorption(T)}}{1-\eta_{absorption(T+\Delta T)}} = \left(\frac{T}{T+\Delta T}\right)^4. \qquad (3.42)$$

The overall system efficiency with quenching, $\eta_{overall}$ of equation (3.40), increases with temperature because the chemical conversion increases as well. Its value is 20% when complete conversion is assumed (CASE 0), but is lower than 8% for all the remaining cases considered. The reason for such a low efficiency is clearly the loss of sensible heat by quenching, which amounts up to 80% of the solar energy input. There is a severe penalty for the large amount of energy needed to heat the reactants and air up to the reactor temperature and the subsequent quenching to avoid re-oxidation.

The irreversibilities in the reactor and during the quench reduce the efficiency from the *Carnot* value. They are produced by heat transfer across a finite temperature difference and by irreversible chemical reactions. Specifically, irreversibilities associated with heat transfer occur because the reactor at $T_{reactor}$ re-radiates energy to the surroundings through the aperture; during the quench heat transfer takes place between the hot products leaving the reactor and the cold sink. One can reduce the reactor irreversibility by increasing the concentration ratio (increasing $\tilde{C}$ improves $\eta_{absorption}$ by reducing the portion of incoming radiation that is re-radiated to the sink). One may be able to reduce the irreversibility of the quench. For example, if the kinetics or the reactor design permit the products to be cooled with a heat exchanger, one could pre-heat the reactants going into the solar receiver, or utilize the sensible and latent heat of the products to generate electric work via a heat engine. The maximum overall efficiency, $\eta_{overall,max}$ of equation (3.41), takes into account, in addition to the work output of the cell, also the maximum available work (i.e. exergy) that can be extracted from the products. These efficiencies, listed in the last row of Table 3.2, are remarkably higher, varying between 61% and 42% as the temperature varies between 1900 K and 2500 K.

The effect of doubling the solar concentration on the overall efficiency is shown in Table 3.3 for the baseline CASE 0. The higher the concentration, the smaller the aperture, the less re-radiation losses, and consequently the higher the absorption and overall efficiencies. Concentration ratios of 10,000 and higher are theoretically achievable in solar central receiver plants, provided a *CPC* or other secondary concentrators are coupled to a narrow view angle of the he-

liostat field [Welford and Winston, 1989], but its technical and economical feasibility need still to be demonstrated.

Chemical by-products

The chemical products from each system component are either recycled or discarded. The gaseous products of the solar reactor after quenching are N_2 and O_2, which are discharged to the atmosphere. The products of the WATER SPLITTER are $Fe_3O_4(s)$ and H_2; $Fe_3O_4(s)$ is recycled to the solar reactor while H_2 is directed to the FUEL CELL. The product of the FUEL

Table 3.2 Molar composition of the products at the exit of the solar reactor and energy balance on the 2-step water-splitting cycle scheme. Species with mole fractions less than 10^{-5} have been omitted. The baseline configuration is used unless otherwise stated. Mass flow rate of reactants is 1 mole/s Fe_3O_4 + x mol/s air

CASE	0	1_1	1_2	1_3	1_4
x, air / Fe_3O_4 molar ratio	0	0			
$T_{reactor}$ [K]	2300	1900	2100	2300	2500
Product Composition	---	CHEMICAL THERMODYNAMIC EQUILIBRIUM			
Fe_3O_4 (l)	0	0.8890	0.8160	0.7180	0.5960
FeO (l)	3	0.3330	0.5510	0.8460	1.2101
FeO (g)	0	<1e-5	<1e-5	<1e-5	1.05e-4
O_2	0.5	5.55e-2	0.0918	0.1410	0.2003
N_2	0	<1e-5	<1e-5	<1e-5	<1e-5
NO	0	<1e-5	<1e-5	<1e-5	<1e-5
O	0	1.64e-5	1.27e-4	6.95e-4	2.90e-3
Conversion ratio [%]	100%	11.1%	18.4%	28.2%	40.3%
ENERGY BALANCE					
Q_{solar} [kW]	1148.6	578.3	708.8	905.8	1240.2
Q_{rerad} [kW]	364.6	85.5	156.3	287.5	549.4
$Q_{reactor,net}$ [kW]	784.0	492.8	552.4	618.3	690.8
Q_{quench} [kW]	478.3	458.9	496.3	532.2	567.5
Q_{WS} [kW]	18.0	2.0	3.3	5.1	7.3
Q_{FC} [kW]	53.8	6.0	9.9	15.2	21.7
$\eta_{absorption}$ [%]	68.3%	85.2%	77.9%	68.3%	55.7%
W_{FC} [kW]	233.9	26.0	43.0	66.0	94.4
Irr_{quench} / Q_{solar} [K^{-1}]	1.02e-3	1.91e-3	1.71e-3	1.45e-3	1.15e-3
$\eta_{overall}$ [%]	20.4%	4.5%	6.1%	7.3%	7.6%
$\eta_{overall,max}$ [%]	50.7%	61.3%	57.0%	50.6%	41.8%

CELL is H_2O, which is recycled to the WATER SPLITTER. An external source of air is required for the carrier or quenching gas in the solar reactor, and as the oxidant of the fuel cell.

3.2.5 Solar Chemical Reactor Concepts for Fe_3O_4 Decomposition

The preceding analysis defines the constraints that the chemistry of the Fe_3O_4 decomposition reaction places on the design for a solar thermal chemical reactor. From the thermodynamic and kinetic calculations we determine the product composition and the optimum operating temperature for maximum chemical conversion ratio. The yield of FeO also depends on the quenching rate to avoid its re-oxidation, unless FeO is withdrawn from the reaction chamber in the absence of oxygen. From the 2nd-law analysis we conclude that a viable cycle efficiency can be obtained for a process that uses not only the work output of the fuel cell but also the maximum available work that can be extracted from the hot products exiting the solar reactor. It was shown that

Table 3.2 cont'd

CASE	2_1	2_2	2_3	2_4	3_1	3_2	3_3	3_4
x, air / Fe_3O_4 molar ratio	1				10			
$T_{reactor}$ [K]	1900	2100	2300	2500	1900	2100	2300	2500
Product Composition	CHEMICAL THERMODYNAMIC EQUILIBRIUM							
Fe_3O_4 (l)	0.8579	0.7680	0.6510	0.5148	0.8527	0.7549	0.6253	0.4741
FeO (l)	0.4262	0.6960	1.0470	1.4500	0.4420	0.7352	1.1230	1.5700
FeO (g)	<1e-5	<1e-5	<1e-5	<1e-5	<1e-5	<1e-5	7.86e-4	6.14e-3
O_2	0.2770	0.3192	0.3720	0.4300	2.142	2.166	2.191	2.206
N_2	0.7860	0.7835	0.7790	0.7730	7.8690	7.8470	7.8160	7.7770
NO	6.93e-3	0.0129	0.0219	0.0342	0.0609	0.1068	0.1682	0.2406
O	1.60e-4	8.33e-4	3.26e-3	0.0105	1.38e-3	6.46e-3	2.33e-2	6.85e-2
Conversion ratio [%]	14.2%	23.2%	34.9%	48.3%	14.7%	24.5%	37.4%	52.3%
ENERGY BALANCE								
Q_{solar} [kW]	649.6	802.2	1031.7	1418.7	1218.3	1516.3	1960.9	2714.9
Q_{rerad} [kW]	96.0	176.9	327.4	628.5	180.1	334.4	622.3	1202.7
$Q_{reactor,net}$ [kW]	553.6	625.3	704.3	790.2	1038.2	1181.8	1338.5	1512.2
Q_{quench} [kW]	510.3	554.4	597.7	642.1	993.4	1107.1	1224.2	1350.7
Q_{WS} [kW]	2.6	4.2	6.3	8.7	2.7	4.4	6.7	9.4
Q_{FC} [kW]	7.6	12.5	18.8	26.0	7.9	13.2	20.1	28.2
$\eta_{absorption}$ [%]	85.2%	77.9%	68.3%	55.7%	85.2%	77.9%	68.3%	55.7%
W_{FC} [kW]	33.2	54.3	81.7	113.1	34.5	57.3	87.6	122.4
Irr_{quench} / Q_{solar} [K^{-1}]	1.88e-3	1.68e-3	1.43e-3	1.13e-3	1.89e-3	1.73e-3	1.51e-3	1.23e-3
$\eta_{overall}$ [%]	5.1%	6.8%	7.9%	7.9%	2.8%	3.8%	4.5%	4.5%
$\eta_{overall,max}$ [%]	61.0%	56.7%	50.4%	41.7%	59.2%	55.4%	49.6%	41.2%

quenching the reaction products results in an unacceptable low cycle efficiency. This implies that $FeO(l)$ and O_2 must be *in-situ* separated (while they are hot in equilibrium inside the reactor) and subsequently the sensible and latent heat of the two product streams must be recovered.

Before proceeding with our design concepts, we summarize what we call the chemical boundary conditions for the reactor designer.

1. The reactor should operate at a temperature between 2100-2500 K. Thermal efficiencies are higher for the lower temperatures, but at the expense of moving more mass during the cycle because the chemical conversion ratio decreases with decreasing temperature.
2. The reactor should be open to the air. Little is gained in terms of thermal efficiency or conversion ratio by working under an inert atmosphere.
3. One must be able to control the residence time of the reactants so that one can maximize the daily yield of FeO. The kinetics of the decomposition reaction demonstrate that the reaction reaches a maximum rate near 40% completion.
4. The gas phase products must be in-situ separated from the condensed phase products to avoid the recombination reaction or to avoid producing an unacceptably high irreversibility by separating the products with a quench. FeO should be withdrawn from the reactor chamber in the absence of oxygen.

We present two reactor design concepts that address these boundary conditions. One is a continuous gravity separation reactor to be used for a nearly vertical axis solar furnace. The second is a centrifugal reactor with semi-continuous separation to be used for a nearly horizontal axis solar furnace. Both reactor concepts feature three common characteristics: 1) they have a cavity-

Table 3.3 Effect of doubling the solar concentration ratio on the efficiency of the cycle for baseline CASE 0.

CASE	0_1	0_2
Loading ratio	0	0
$T_{reactor}$ [K]	2300	2300
Conversion ratio [%]	100%	100%
Concentration ratio	5,000	10,000
ENERGY BALANCE		
Q_{solar} [kW]	1148.6	932.2
Q_{rerad} [kW]	364.6	148.2
$Q_{reactor,net}$ [kW]	784.0	784.0
Q_{quench} [kW]	478.3	
Q_{WS} [kW]	18.0	
Q_{FC} [kW]	53.8	
$\eta_{absorption}$ [%]	68.3%	84.1%
W_{FC} [kW]	233.9	
$\eta_{overall}$ [%]	20.4%	25.1%
$\eta_{overall,max}$ [%]	50.7%	62.5%

receiver configuration; 2) they use the reactants for lining the reactor inner walls; and 3) they offer the direct absorption of concentrated solar radiation. Cavity-receivers are insulated enclosures designed to effectively capture incident solar radiation entering through a small aperture. Because of multiple internal reflections, the cavity-receiver approaches a blackbody absorber. The shell of the cavity is made from conventional steel materials and lined with Fe_3O_4 particles, the same material as the reactants themselves. This aspect of the design eliminates the need for using expensive and difficult-to-fabricate ceramic insulating materials for ultra-high temperatures. It also offers excellent resistance to thermal shocks that are intrinsic in short start-up solar applications. Direct absorption is usually attributed to the absorption of concentrated solar energy by directly irradiated fluids, particles, or surfaces, which serve simultaneously the functions of energy absorbers, heat transfer, and chemical reactants. Such concept provides efficient radiation heat transfer directly to the site where the energy is needed, by-passing the limitations imposed by indirect heat transport via heat exchangers. The direct absorption concept has been experimentally demonstrated with gas-particle suspensions [Hunt *et al.*, 1986; Rightley *et al.*, 1992; Steinfeld *et al.*, 1994], with metallic wire mesh, perforated graphite disks, and ceramic honeycombs, grids, foams, cloths, and foils for absorbing and transferring heat to reactants or to air [Kappauf *et al.*, 1985; Böhmer and Chaza, 1991)], with molten salt as the energy working medium [Klimas *et al.*, 1991], with fluidized beds [Rizzuti and Yue, 1983; Flamant *et al.*, 1988; Ingel *et al.*, 1992; Steinfeld *et al.*, 1993], with rotary-kiln and cyclone configurations for calcining limestone [Flamant *et al.*, 1980; Steinfeld *et al.*, 1992a], with catalytic surfaces and particles in the methane-reforming and methane-cracking reaction [Levy *et al.*, 1992; Buck *et al.*, 1991; Steinfeld *et al.*, 1997], and with various solar photochemical applications [Blake, 1995].

The Gravity Separation Reactor Concept

Figure 3.8 illustrates the concept. A cavity-receiver is positioned vertically and concentrated solar radiation is impinging directly on the reactants from the top. It is initially filled with Fe_3O_4 that also serves as the lining for the reactor inner walls in such a way that a temperature gradient is created between the hot reaction zone and the cooler reactor walls. As Fe_3O_4 melts and decomposes to $FeO(l)$, oxygen is liberated from the top while molten FeO is withdrawn from the bottom in the absence of air. The principle feasibility of this concept has been demonstrated in solar furnace experiments with a simple prototype reactor.

The Centrifugal Reactor Concept with In-Situ Separation

Figure 3.9 illustrates the concept. A cavity receiver rotates around the horizontal axis. Reactants are continuously fed and products are continuously removed while effecting an in-situ separation of condensed and gas phases by centrifugal force. These two streams of products are then used to preheat the incoming reactants. A batch of preheated reactants undergo thermal decomposition while hot O_2 and air are continuously removed out the back of the reactor. The gases pass through the next batch of Fe_3O_4 particles, thereby preheating them. After a specified residence time under solar irradiation, the reactor stops rotating. The FeO is allowed to drain from the reactor by mechanically removing a plug made from dense ZrO_2. The sensible energy in the FeO would be also used to preheat the incoming reactants, however the details of this step are not shown. A new batch of Fe_3O_4 would be supplied and the process repeated.

These two reactor concepts satisfy the chemical boundary conditions dictated by the chemistry of the decomposition reaction. They each allow for a way to obtain FeO from the decomposition of Fe_3O_4 while minimizing the irreversibility of the separation step. The reactor can be designed to work in air at temperatures near 2500 K. The operator of the reactor has complete control of the residence time.

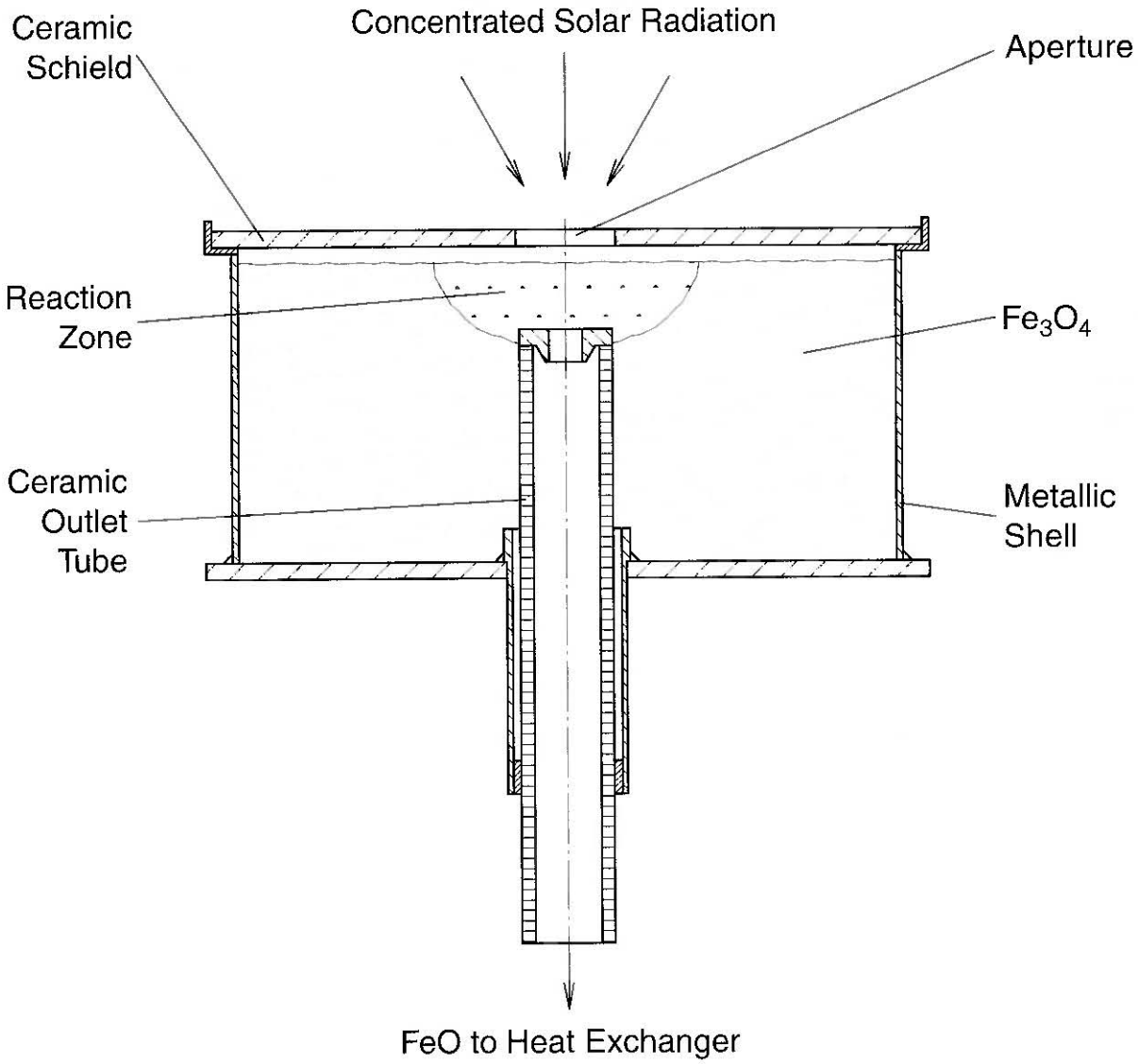

Figure 3.8 Schematic of the "gravity-separation" reactor concept for conducting the solar thermal reduction of Fe_3O_4 and in-situ separation of FeO and oxygen [Steinfeld *et al.*, 1998c]. It consists of a cavity-receiver, lined with Fe_3O_4, that is positioned vertically. Concentrated solar radiation is impinging directly on the reactants from the top. As Fe_3O_4 melts and decomposes to $FeO(l)$, oxygen is liberated from the top while molten FeO is withdrawn from the bottom in the absence of air.

3.2.6 Closing Remarks on the Fe_3O_4 Reduction Studies

The purpose of this Chapter was to demonstrate a methodology by which one can begin to proceed with the development of a solar thermal chemical reactor that some day may be economically viable for producing fuels from sunlight. The method demonstrates that the chemistry of the reaction to be effected in the reactor places important initial constraints on the reactor design. The design work, though is far from complete. At this juncture a number of fundamental design questions remain that must be systematically answered by experimental and analytical work. The answers in turn will likely force several iterations on the initial reactor concepts.

For example, the reactor ultimately must be economically and technically feasible. In this regard one must demonstrate the feasibility of the in-situ separation. More physico-chemical data must be obtained for Fe_3O_4 and FeO. Our current understanding of the thermodynamics of the

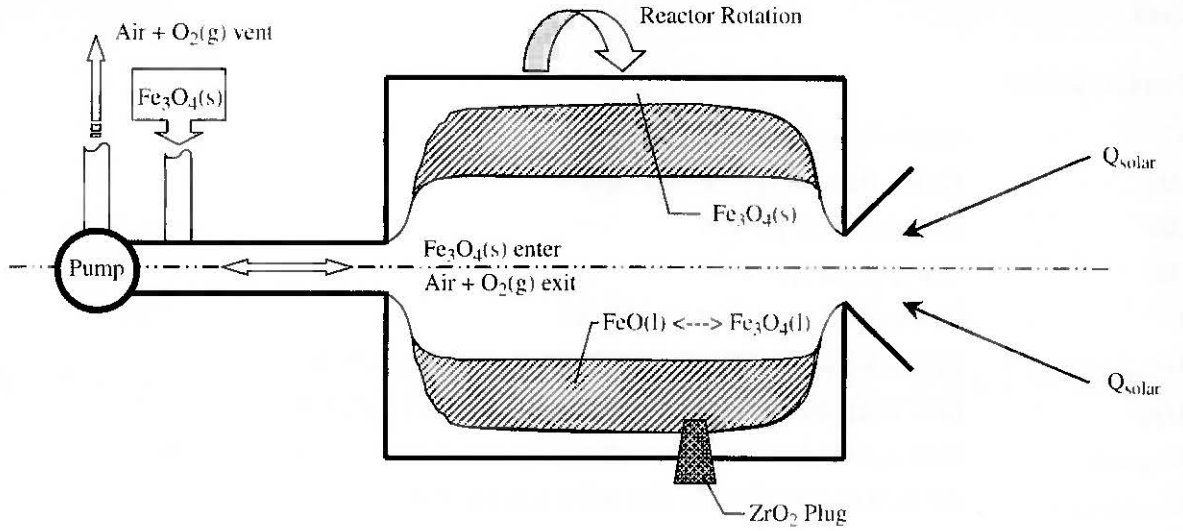

Figure 3.9 Schematic of the "centrifugal" reactor concept for conducting the solar thermal reduction of Fe_3O_4 and in-situ separation of FeO and oxygen [Steinfeld *et al.*, 1998c]. It consists of a cavity-receiver that rotates around the horizontal axis. Reactants are continuously fed and products are continuously removed while effecting an in-situ separation of condensed and gas phases by centrifugal force.

FeO and Fe_3O_4 liquid system prevents us from confidently estimating thermal efficiencies and mass flow rates. We need a better understanding of the kinetics of the decomposition reaction if we are to accurately predict daily FeO yields. One must demonstrate the conditions for which the reactor will function with a high solar absorption efficiency and low convection losses using conventional materials. The irreversibility of the pre-heating steps must be minimized through careful heat transfer design. Design features must enable the reactor to be scaled up to large solar power inputs and to remain intact for thousands of hours of operation even while experiencing severe thermal shocks.

Our experience suggests that these important remaining questions, design problems, and demonstrations are most comfortably approached if one has a clear picture of how the reactor in the end will efficiently deal with the chemistry of the reaction. Much of the work in developing a new technology is necessarily done in a shroud of unknowns and uncertainties. Using the Fe_3O_4 decomposition as a case study, we have presented the initial steps necessary for the design of a solar chemical reactor.

3.2.7 Mechanistic Studies of the Water-Splitting Reaction for Producing Solar Hydrogen

The research conducted on producing H_2 by splitting H_2O with reaction (3.29) was done by the Section's Physical Science Group. This work will be described in the *BFE* final report for contract EN-REF(96) 55022. But for completeness of this report, we summarize the major findings of the study.

The kinetics and mechanism of the water splitting reaction with wustite phases depends upon whether the nearly stoichiometric wustite phase is formed or not, i.e. on the temperature range. Oxidation of non-stoichiometric wustite is much easier, probably because of the large amount of defect clusters, which can serve as nuclei for the magnetite formation as mentioned before. Water splitting out of the "nearly stoichiometric" wustite phase or out of iron, which is formed during the disproportionation, do both occur in the lower temperature range, but the reaction is

much slower. Thus, it will be most desirable for the solar process to produce non-stoichiometric FeO.

Nomenclature

$\tilde{C}$	mean flux solar concentration
ΔG	*Gibbs* free energy change, kW
ΔH	enthalpy change, kW
ΔS	entropy change, kW
I	normal beam insolation, kW/m^2
Irr_{quench}	irreversibility associated with the quenching, kW K^{-1}
Q_{FC}	heat rejected to the surroundings by the fuel cell, kW
Q_{quench}	heat rejected to the surroundings by the quenching process, kW
$Q_{reactor,net}$	net power absorbed by the solar reactor, kW
Q_{rerad}	power re-radiated through the reactor aperture, kW
Q_{solar}	total solar power coming from the concentrator, kW
Q_{WS}	heat rejected to the surroundings by the water-splitter, kW
$T_{reactor}$	nominal cavity-receiver temperature, K
W_{FC}	work output by the fuel cell, kW
α_{eff}, ε_{eff}	effective absorptance and emittance of the solar cavity-receiver
$\eta_{absorbtion}$	solar energy absorption efficiency
$\eta_{overall}$	Overall system efficiency
$\eta_{overall,max}$	Overall efficiency of an ideal solar *Carnot* system
σ	*Stefan-Boltzmann* constant, 5.6705·10^{-8} W m^{-2} K^{-4}

3.3 Production of *Zn* from *ZnO* in a Solar Decomposition Quench Process

In this section a theoretical and experimental study of a solar decomposition process for producing *Zn* and O_2 from *ZnO(s)* is presented [Palumbo *et al.*, 1998]. Several papers deal with the subject of solar produced *Zn* [Fletcher *et al.*, 1985; Parks *et al.*, 1987; Palumbo and Fletcher, 1988; Palumbo *et al.*, 1992; Palumbo *et al.*, 1995; Murray *et al.*, 1995; Steinfeld *et al.*, 1995a; Boutin, 1996; Möller, 1996; Millar *et al*, 1997]. The solar decomposition reaction is a means for storing solar energy in the form of chemical energy. Although *Zn* is often thought of as a commodity, it can be used as a fuel in zinc-air batteries. *Zn*-air fuel cells and batteries are being developed for large scale electricity production and for electric cars [Salas-Morales and Evans, 1994]. Furthermore, it has been suggested that when hydrogen is needed to supply a market, zinc be transported from the prime energy source and that it be used to split water to produce hydrogen on-site rather than pumping it through a pipe-line.

Figure 3.10 shows a schematic representation of the cycle using the *Zn/ZnO* redox pair for hydrogen production. As an energy source, concentrated sunlight provides high-temperature process heat for the decomposition of *ZnO*. In this way, solar radiation can be directly converted into the chemical potential of zinc and oxygen (1st step). The solar energy stored in the condensed zinc phase can then be used to split water (2nd step).

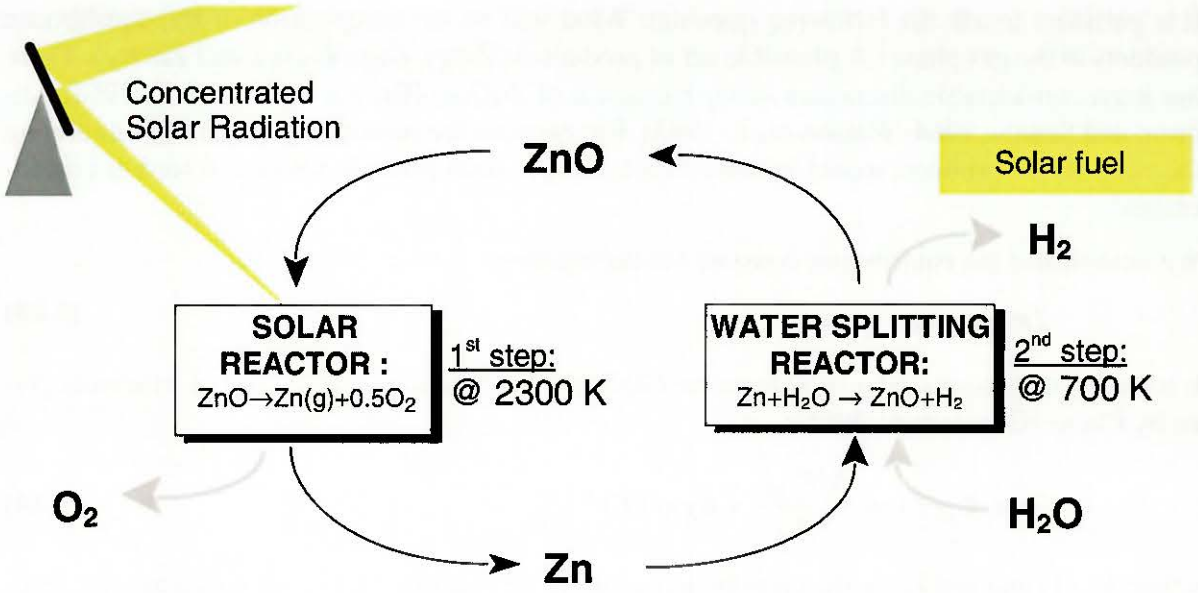

Figure 3.10 Schematic representation of a two-step water-splitting thermochemical cycle using the *Zn/ZnO* redox system. In the first endothermic solar step at elevated temperatures, zinc oxide is thermally decomposed into zinc and oxygen. Concentrated solar radiation is the source of the required high-temperature process heat. In the second exothermic step, zinc reacts with water to produce hydrogen; the resulting zinc oxide is then recycled back to the first step. The reaction is: $H_2O=H_2+0.5O_2$; hydrogen and oxygen are produced in different steps, eliminating the need for high temperature gas separation.

It is interesting to note that the cost of this valuable metal is directly tied to the cost of the energy required to produce it. Assuming an energy consumption of 50 GJ/ton of *Zn* when produced electrolytically, at today's prices of 1 \$/kg of *Zn* [Rodier, 1995] and 0.05 \$/kWh, the cost of the energy represents more than 50% of the value of *Zn*.

As the cost of conventional fossil fired energy increases, solar energy becomes an attractive alternative energy resource for *Zn* production. The use of solar energy to replace fossil fuels also helps reduce pollution and greenhouse effects [Fletcher, 1997].

To date, several solar studies have focused on either electrolytic [Fletcher *et al.*, 1985; Parks *et al.*, 1987; Palumbo and Fletcher, 1988], or multiple step [Palumbo *et al.*, 1992; Palumbo *et al.*, 1995; Millar *et al.*, 1997], or carbo-thermic processes [Murray *et al.*, 1995; Steinfeld *et al.*, 1995a].

Zinc and O_2 also have been separated by quenching the vapor produced in a solar furnace [Bilgen *et al.*, 1977]. But more information about the rates and mechanisms of such processes is needed. With this fact in mind, we explored some of the underlying science and the prospect of using a quench to produce *Zn* from *ZnO* by high temperature solar thermal processing.

3.3.1 Thermodynamics of the Decomposition Products

The triple point temperature and pressure of *ZnO* are in the neighborhood of 2250 K and 1 bar, [Fletcher and Noring, 1983; Coughlin, 1954; Brown, 1976; Stull and Prophet, 1971] and the melting point is insensitive to pressure. Thus, in an equilibrium situation, at a temperature above about 2250 K, the condensed phase will be liquid and the pressure of a two phase system will be the saturation pressure at that temperature of the liquid. At temperatures below about 2250 K, the condensed phase will be solid.

It is pertinent to ask the following question: What will be the composition of the equilibrium products in the gas phase? A plausible set of products is *Zn(g)*, *O(g)*, O_2 *(g)*, and *ZnO(g)*. There has been considerable discussion of the existence of *ZnO(g)* [Brewer and Mastick, 1951; Anthrop and Searcy, 1964; Watson *et al.*, 1993]. But because the presence of much *ZnO(g)* among the equilibrium products would be unfavorable for the solar process, we give it further consideration.

We determined the equilibrium constant for the reaction

$$Zn(g) + 0.5O_2 \Leftrightarrow ZnO(g) \tag{3.43}$$

It is most conveniently calculated from the *Gibbs* energy functions (*gef*) by use of a formula given by Chase [Chase *et al.*, 1985]:

$$-R\ln K_p(T) = \frac{\Delta H^\circ_{298}}{T} + \Delta gef(T) \tag{3.44}$$

where $K_p(T)$ and *gef(T)* are the equilibrium constant for reaction (3.43) and *Gibbs* energy functions for the molecules of reaction (3.43) at temperature *T*. Watson, who sought and failed to observe *ZnO(g)* in a mass spectrometric study of the effluent from a Knudsen cell at temperatures up to 1700 K, provides upper values for the *Zn-O* bond dissociation energy and a minimum value for the standard enthalpy of formation of *ZnO(g)* at 298 K, 151 kJ mol^{-1}. Watson *et al.* also provides high temperature *Gibbs* functions for *ZnO(g)*. Using the information provided by [Watson *et al.*, 1993; Stull and Prophet, 1971 and Pankratz, 1982] we calculated the equilibrium constant for reaction (3.43) at 1700 K. Assuming a constant $\Delta H_{reaction}$ of 20.6 kJ and using the van't Hoff formula, we obtained an expression for the variation of the equilibrium constant with temperature for reaction (3.43).

$$\ln K_p = -4.855 - \frac{2474}{T} \tag{3.45}$$

Table 3.4 shows for reversible vaporization the saturation pressure at temperatures ranging from 1700 to 2400 K. The equilibrium composition was calculated with the Thermochemical Equilibrium Program, STANJAN [Reynolds, 1986]. The thermochemical properties were taken from [JANAF,1985], except for those for *ZnO(l)*, which was taken from [Barin, 1993]. The saturation pressure of *ZnO(c)* is 0.006 bar at 1700 K and 0.75 bar at 2200 K. The mole fraction of *ZnO(g)* in the saturated vapor is, at most, $5 \cdot 10^{-5}$ at 1700 K and 10^{-3} at 2200 K. We therefore chose to eliminate further consideration of *ZnO(g)* in this study.

Table 3.4 The saturation pressure and mole fractions of the gas phase species above condensed *ZnO* at various temperatures.

Temperature [K]	$P_{saturation}$ [bar]	Mol fraction Zn	Mol fraction O_2	Mol fraction O	ZnO condensed
2400	2.624	0.666	0.331	0.003	liquid
2300	1.480	0.666	0.332	0.002	liquid
2200	0.754	0.666	0.332	0.002	solid
2100	0.343	0.666	0.332	0.001	solid
1900	0.055	0.666	0.332	0.001	solid
1700	0.006	0.667	0.333	----------	solid

3.3.2 Kinetics of the Decomposition and Recombination Reactions

3.3.2.1 Decomposition Reaction

A number of papers have been written on the subject of the decomposition rate of *ZnO* [Hirschwald and Stolze, 1972; Koumoto *et al.*, 1980; Moore and Williams, 1959; Secco, 1960]. The results are not all in agreement. The published activation energies vary between 250 and 375 kJ mol^{-1}. There is also scatter in the values for the pre-exponential term. We decided, however, to use the results described by Hirschwald. In this section, we present the proposed rate expression and give the reasons for our confidence in it.

Hirschwald measured the vaporization rate of *ZnO* in a thermogravimetric study conducted at a total pressure less than 10^{-5} torr at temperatures between 1130 and 1385 K. The sample was a film of 100 μm thick of 99.99% pure *ZnO* deposited on the outside surface of a cylindrical crucible of a length of 0.04 m and an external diameter of 0.007 m. The following expression is Hirschwald's value for the rate constant:

$$k' = 4.28\times10^{8}\exp\left(\frac{-319000}{R\cdot T_s}\right) \quad \frac{mol}{m^2\cdot s} \tag{3.46}$$

Because it is more convenient for the numerical model that follows to work with a rate equation given in terms of kg s^{-1} m^{-3} we used the experimental data and sample surface area to establish a pre-exponential factor of $7.6\cdot10^{7}$ s^{-1} [Boutin, 1996]. Thus the rate of the reaction is given by

$$\Re = \rho\cdot 7.6\times10^{7}\exp\left(\frac{-319000}{R\cdot T_s}\right) \quad \frac{kg}{m^3\cdot s} \tag{3.47}$$

We verified that the reaction rate being measured was given by the chemical kinetics of the reaction as opposed to being one limited by heat transfer; for the conditions in Hirschwald's experiments, the *ZnO* sample was not experiencing strong internal temperature gradients as evidenced by the fact that we calculated a Biot number of 0.05; and the rate of diffusion of thermal energy by conduction throughout the sample was faster than the rate of the reaction, as evidenced by our calculation of a Weisz number less than 0.01.

The Weisz number is a measure of the time it takes for thermal energy to penetrate the sample in response to a change in the thermal environment in comparison to a characteristic time for the chemical reaction at a given temperature [Villermaux, 1995]. When this number is less than 0.01, one can be confident that the diffusion of thermal energy is much faster than the chemical reaction [Villermaux, 1995].

The activation energy obtained during these experiments is reasonable. One expects the change in the rate as a function of temperature to be proportional to the change in the sample's vapor pressure as a function of temperature. A thermodynamic argument where one sets the chemical potential of the condensed phase equal to that of the gas phase leads to

$$\frac{d\ln(P)}{d(1/T_s)} = \frac{\Delta H_{vap}}{1.5R}, \tag{3.48}$$

where ΔH_{vap} is the enthalpy change for reaction

$$ZnO(s) \Leftrightarrow Zn + 0.5O_2. \tag{3.49}$$

The factor 1.5 occurs because there are 1.5 moles in the gas phase. Thus the activation energy should be $\Delta H_{vap}/1.5$, which is close to Hirschwald's value.

We also conducted our own thermo-gravimetry (TG) experiments in which we measured the decomposition rate of $ZnO(s)$. We worked in a N_2 atmosphere at 1 bar in the temperature range of 1300 to 1800 K. We found an activation energy E_a of 312 kJ mol^{-1}, which is similar to Hirschwald's value.

3.3.2.2 Reoxidation Reaction for Modeling Purposes

The only quantitative expression that we found for the recombination reaction was given by Kashireninov *et al.*, 1978 and 1982. The articles state the reaction is essentially a bimolecular reaction between Zn and O_2. The published expression for the rate is

$$\Re_{-1} = 5.9 \times 10^8 \cdot \exp\left(\frac{-70300}{R \cdot T_g}\right)[Zn][O_2] \quad \frac{mol}{m^3 \cdot s} \tag{3.50}$$

The rate was determined by the flame diffusion method in the temperature range of 820-920 K. The authors of the study state that their experimental method did not allow them to "apportion unambiguously between the elementary gas-phase reactions, the nucleation of particles of condensed products, etc...".

Because of this ambiguity, we are concerned about the generality of the published expression. We expect the reaction to be one that must take place on a surface. A number of studies, of which [Lewis and Cameron, 1995] is an example, show that $Zn(g)$ in CO and CO_2-mixtures reacts at a surface to form $ZnO(s)$. It seems reasonable that a reaction between $Zn(g)$ and O_2 would also be a heterogeneous surface reaction. The published rate expression, however, is not in a form that allows one to account for the surface effects that will differ from one reactor to the next. It is clear that further research is needed on the fundamental kinetics of this reaction. In a following section we present our preliminary research with regard to this subject. Our use of this rate data in the subsequent model of the quench step should be viewed as a first approximation of our understanding of the quench process; it is a mathematical description based on the data available in the literature.

3.3.3 Numerical Model of the Decomposition and Quench Processes

3.3.3.1 Decomposition Step

We estimate the reaction temperature for the decomposition step and the extent of decomposition as a function of time, by postulating that we have a shrinking particle of constant density reacting throughout its volume with no temperature gradients and at a reaction rate limited by chemical kinetics. Such a model has been successfully utilized to study other related solar processes and non solar processes [Villermaux, *et al.*, 1986; Lédé and Villermaux, 1993; Lédé, 1994; Boutin, 1996]. Our model is that for a shrinking core chemical control reaction.

We chose chemical control because we envision our first reactor being one where small ZnO particles decompose in a reaction regime where the Biot and Weisz numbers are much less than one. We chose to assume that the particles will decompose at constant density because we have not observed in our experimental work that the density of the ZnO decreases in the course of the reaction: None of our samples became more porous. On the other hand, we recognize that future experimental work should address the question as to what extent the density of the ZnO may increase.

The energy equation per unit of volume is

$$\frac{3q}{R_{rad}} = \Re \cdot \Delta H_d + \rho \cdot C \cdot \frac{dT_s}{dt} \tag{3.51}$$

where,

$$q = \alpha q_{solar} - \varepsilon \sigma T_s^4 \tag{3.52}$$

$\Re$ is given in (3.47).

Conservation of mass requires that

$$\frac{dR_{rad}}{dt} = \frac{-R_{rad} \cdot \Re}{3\rho} \tag{3.53}$$

Using equations (3.47) and (3.52) the differential equations (3.51) and(3.53) were solved simultaneously with a *Runge-Kutta* numerical technique for various values of q_{solar}, R°_{rad}, α, and ε. We used $\rho = 5600$ kg m^{-3}, $C = 500$ J kg^{-1} K^{-1}, and $\Delta H_d = 5.65$ 106 J kg^{-1}. The extent of *Zn*-production is calculated at each moment in time from the equation,

$$X = 1 - \left(\frac{R_{rad}}{R^{\circ}_{rad}}\right)^3 \tag{3.54}$$

A 3 μm-particle vaporizing to *Zn* and O_2 under a flux density of 1.5 MW m^{-2} with an effective α and ε of 1, reaches nearly 80% completion within 0.5 s. The particle reaches a quasi steady state temperature of 2250 K in less than 0.01 seconds, which is well before the end of the reaction.

Table 3.5 is a sampling of results from such calculations. It shows that solar furnaces developing modest flux densities (10 MW m^{-2} have been achieved using *CPC*'s) can bring small *ZnO(s)* particles up to temperatures greater than 2100 K. Furthermore, 75% decomposition is possible between 0.25 and 1.25 seconds, depending on R°_{rad}, α, and ε, and the flux density. It is also clear that *ZnO* can easily be melted in a solar furnace. A reactor designed to operate near 1 bar when interfaced to a modest concentrating solar furnace could in fact create a thermodynamically unstable state for the *ZnO(s)* particles. As Table 3.4 shows, the saturation pressure above

Table 3.5 Calculated reaction temperature and reaction times for given flux densities, particle diameters, and absorptivity.

Flux Density [kW/m^2]	Initial Particle Diameter [mm]	Quasi Steady-State Particle Temperature [K]	$\alpha=\varepsilon$	Time (in sec) for $X = 0.5$ and $X = 0.75$	
1500	3	2250	1	0.225	0.450
1500	30	2175	1	0.450	0.800
1500	3	2200	0.5	0.250	0.500
1500	30	2150	0.5	0.700	1.200
2000	3	melts	1	no data	no data
2000	30	melts	1	no data	no data
2000	3	melts	0.5	no data	no data
2000	30	2250	0.5	0.350	0.650

liquid *ZnO* exceeds 1 bar, thus the particles could spatter in response to internal bubbles of superheated vapor forming explosively. A stable vaporization process will require matching the solar flux on the particles to the kinetics of vaporization so that the rate of heat flow is slow enough for the vaporization to be fast enough to keep the temperature near 2250 K.

3.3.3.2 Quench Step

Figure 3.11 shows that *Zn* and O_2 flow from the decomposition reactor into the quenching device, where the pressure is 1 bar. We neglect radial concentration, temperature, and velocity gradients. An inert gas is added at the temperature of the products to improve the quench. We suppose this mixing is perfect and instantaneous for the purpose of developing an initial simplified model of the quench process. Furthermore, the rate equation given by equation (3.50) is a global expression for the re-oxidation reaction. Thus, in the model we freeze the oxidation reaction until the re-oxidation reaction is thermodynamically possible. Thus, our model is some what of an ideal device — presuming a quench with instantaneous dilution would give overly optimistic quench results, but the effect of instantaneous dilution is partly compensated for because the quench gas in the model is introduced into the system at a high rather than at a low temperature.

The steady state mass balance equation of this model is

$$\frac{dX_{-1}}{dV} = \frac{\Re_{-1}}{F^e} \tag{3.55}$$

The rate of the re-oxidation reaction as described by equation (3.50) can be written in terms of X_{-1}, the total pressure, and the temperature by expressing the concentrations of *Zn* and O_2 in terms of these variables.

But, before equation (3.55) can be numerically evaluated for X_{-1} versus V, T_g must be expressed in terms of V. This expression is obtained from the energy equation as it applies to a differential element of the quenching device shown in Figure 3.11. Under steady state conditions, the energy equation for the gas phase when thermal energy is being removed by convection through the walls of the reactor is

$$C_p \cdot Q_m \cdot dT_g + \Re_{-1} \cdot \Delta H_r \cdot dV = h(T_w - T_g)dS. \tag{3.56}$$

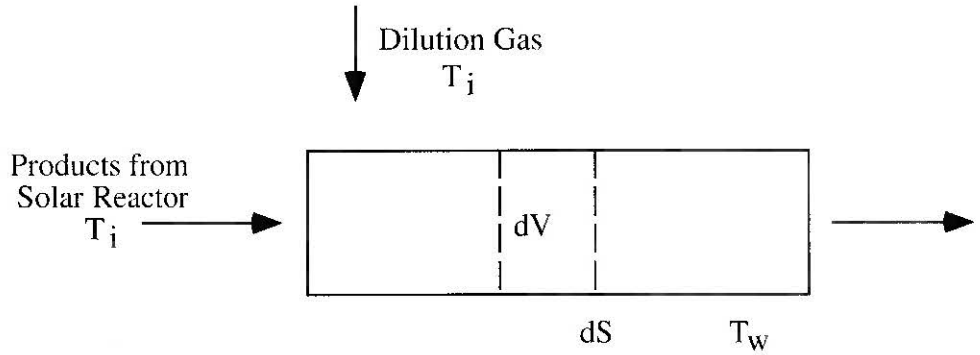

Figure 3.11 Schematic of the quench reactor [Palumbo *et al.*, 1998]. Products from the solar reactor and a dilution gas enter the quench device at T_i, the maximum temperature at which the Zn oxidation reaction is thermodynamically possible. The gases flow through the device in the plug flow regime, transferring heat by convection to the walls at temperature T_w. An element of differential volume, dV, and surface area, dS, are shown for which the energy and mass balance equations can be applied.

dV and dS are the differential volume and surface area. Q_m is the gas mass flow rate. We can express dS in terms of dV and the radius, R_{reac}, of the quench reactor. Because we substantially dilute the gas phase with an inert gas, we neglect the contribution of the chemical reaction to the energy equation. Also, Q_m is essentially constant. For constant C_p, equation (3.56) can be integrated to give the needed equation for T_g in terms of V,

$$T_g = T_w + (T_i - T_w) \times \exp \frac{-2 \cdot h \cdot V}{R_{reac} \cdot C_p \cdot Q_m}. \tag{3.57}$$

It is convenient to cast the exponential function into the form, $\exp(-\tau/\tau_c)$ [Lapicque, 1983]. Using the gas volume flow rate at STP conditions, Q_o, τ is V/Q_o, which is the space time of the gas in the reactor, and

$$\tau_c = \frac{R_{reac} \cdot C_p \cdot Q_m}{2Q_0 \cdot h} \tag{3.58}$$

is a characteristic time based on the heat transfer conditions in the quenching reactor.

If one neglects the chemical energy term in equation (3.56), the quench rate is given by

$$\frac{dT_g}{dt} = \frac{(T_w - T_g)T_g}{T_0 \cdot \tau_c}, \tag{3.59}$$

where T_0 is the temperature of the gas at STP conditions.

The residence time of the products in the quench reactor at a given T_g is calculated from,

$$t_s = \tau_c \ln \frac{T_g(T_i - T_w)}{T_i(T_g - T_w)}, \tag{3.60}$$

according to [Lapicque *et al.*, 1985]. This equation applies for our case of a reactive gas mixture diluted with an inert gas (no chemical expansion) flowing in the plug flow regime.

The calculation for the case of a total pressure of 1 bar and a dilution ratio of 1500, shows that the Zn yield is 50% (the mole percent of *Zn* that enters the quench reactor that does not react to form *ZnO(s)*) for a maximum quench rate of $4 \cdot 10^6$ K s^{-1}. (The quench rate is in absolute value.) Also this typical calculation shows that the back reaction is essentially over somewhere near 1200 K. Such a result was fortuitous, firstly because we recognize that somewhere below this temperature, *Zn* would start to condense out of the gas phase. Secondly, it means that one has the potential of recovering some of the sensible energy in the products in the solar process.

When one examines the *Zn* yield as a function of the maximum quench rate, the calculation suggests that a quench rate near $2 \cdot 10^7$ K s^{-1} is needed to obtain *Zn* yields greater than 80%. Furthermore, the yield drops off quickly for maximum quench rates below 10^6 K s^{-1}. Quench rates above 10^6 K s^{-1} are marginally obtainable with real systems. Consider the tube diameter required for quenching in our plug flow reactor. The h in equation (3.57) can be written in terms of a Nusselt number, which in turn can be expressed in terms of a Reynolds number. For fully developed turbulent flow in a cylindrical tube and a Reynolds number near 16,000, the Nusselt number is 37, the maximum quench rate is 10^6 K s^{-1}. In this case, the tube diameter for the plug flow reactor is 9 mm and the gas volumetric flow rate is $6.67 \cdot 10^{-3}$ m^3 s^{-1}. Rates near 10^7 probably need to be developed with a supersonic nozzle [Sundstrom and DeMichiell, 1971]. In short, our theoretical calculation suggests that it will be difficult but not impossible to quench the *ZnO* decomposition products fast enough to produce high *Zn*-yields. But we present more insight on this issue in our experimental section.

3.3.4 Thermodynamic Cycle Analysis of the Overall Process

A Second Law analysis of the *ZnO* decomposition/quench process established the maximum theoretical efficiency. Figure 3.12 is a schematic of the thermodynamic model. *Ar* and *ZnO* enter a solar reactor at 298 K, where the oxide decomposes to its equilibrium products at various reactor temperatures. The products are perfectly quenched to 298 K. The solar reactor is presumed to be a perfect black body cavity with frictionless mass transport.

The quenched products are sent to a fuel cell (*FC*). This device should be thought of as an intellectual construct that enables one to place a work value on the *Zn*. The work from the *FC* is equivalent to the ΔG for the reaction,

$$Zn(s) + 0.5O_2 + aAr \rightarrow Zn(s) + aAr \qquad \textbf{(3.61)}$$

The pressure is 1 bar. By including the *Ar* in the calculation, we account for the minimum thermodynamic price of unmixing the O_2 from the *Ar*.

The maximum efficiency of the process, $\eta_{th} = W_{out} / Q_{solar}$, where W_{out} is the work of the fuel cell and Q_{solar} is the solar energy entering the solar reactor. The details for doing the calculation have been described in several other studies, a good example being [Steinfeld *et al.*, 1996a].

Table 3.6 shows that η_{th} is a strong function of the reactor temperature and the amount of *Ar* present. It ranges from 55 to 22% for the cases that we investigated. As the reactor temperature increases the reradiation loss increases which lowers the efficiency. The *Ar* primarily reduces the process efficiency by convective heat exchange with the *ZnO(s)* in the solar reactor.

A good maximum efficiency can be obtained so long as the *Ar/Zn* molar ratio that is actually at the decomposition temperature is kept below 10 and so long as the reactor temperature does not exceed 2300 K. During the quench, our calculation suggests we may need a much higher *Ar/Zn* molar ratio. Thus, a viable reactor concept may be one that separates the decomposition zone from the quench zone.

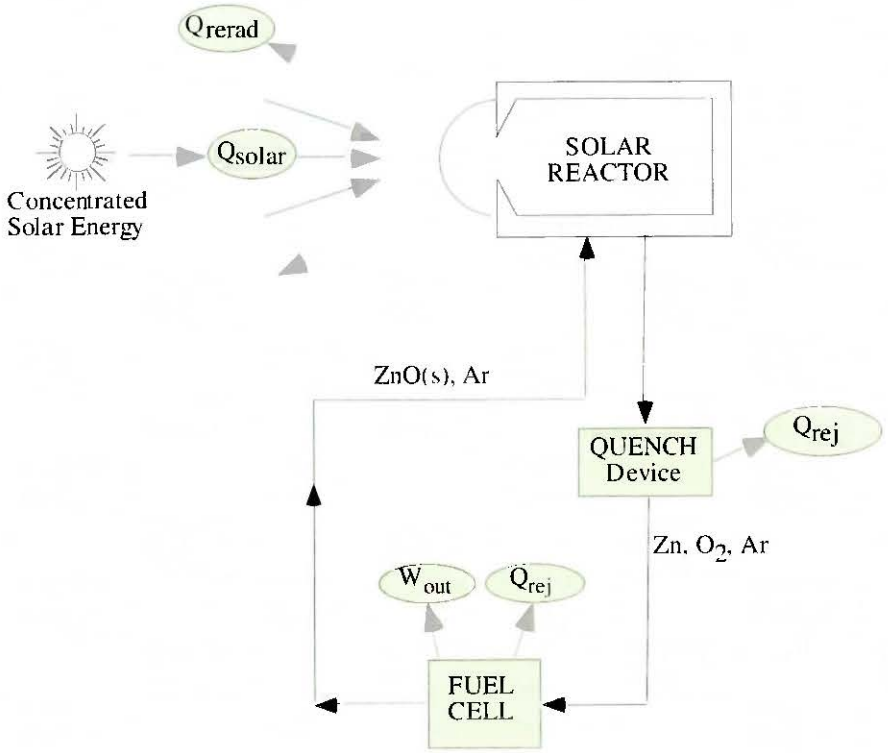

Figure 3.12 Scheme of the *ZnO* cycle [Palumbo *et al.*, 1998].

Table 3.6 Maximum cycle efficiency for the solar *ZnO(s)* decomposition process. The calculation was done with *Ar* because we wanted a true inert gas from a thermodynamic point of view in our system. We recognize that *Ar* will not be the quench gas of any real process.

	T_{cav} [K]	Flux Density [kW/m^2]	Cycle Efficiency [%]
Molar ratio *Ar:ZnO(s)* 0.1:1	1800	6,000	53
		10,000	55
	2200	6,000	43
		10,000	49
	2300	6,000	40
		10,000	47
Molar ratio *Ar:ZnO(s)* 1:1	1800	6,000	50
		10,000	52
	2200	6,000	40
		10,000	45
	2300	6,000	37
		10,000	44
Molar ratio *Ar:ZnO(s)* 10:1	1800	6,000	33
		10,000	35
	2200	6,000	25
		10,000	28
	2300	6,000	23
		10,000	27

The quench efficiency must be high to achieve a thermal efficiency near these maximum theoretical values, because the thermal efficiency drops linearly with decreasing quench efficiency. All the values in the table are for a perfect quench and thus are very optimistic values. However, we presumed a pessimistic quench temperature of 298 K given that our quench model suggests we may only need to quench to 1200 K.

Finally, it is important to note that the efficiency of a real process will greatly depend on the way in which the *ZnO* is fed to the solar reactor. In the above calculations, we picked a flux density and reaction temperature as if they were independent of each other. Our *ZnO(s)* decomposition study shows that the heat and mass balance equations (3.51) and (3.53) fix the reaction temperature for a given flux density and particle size. When particles of 3 to 30 μm particles experience a flux density near 1.5 MW m^{-2}, they reach a quasi steady state temperature near 2250 K. Neglecting conduction and convection losses, the rate of energy supplied to the particles is nearly equal to the rate of reradiation. When these two rates are equal, the thermal efficiency is zero. This condition occurs when T_s = (Flux density / σ)$^{0.25}$, which is 2268 K for a flux density of 1.5 MW m^{-2}. High efficiencies require the solar reactor to operate under high flux densities. Thus, it will be necessary to match the chemical kinetics of the reaction to the *ZnO* flow condition (small vs. large particles, liquid vs. solid *ZnO*, etc.).

As an example, one may want to consider a solar reactor where the *ZnO* melts, but operating above 1 bar just below the saturation pressure of the liquid as given in Table 3.4. The rate of

vaporization would be substantially above those rates calculated for the solid: one could produce nucleate boiling enabling the rate to be limited only by the rate of heat transfer to the sample and the rate of removal of the gas phase above the liquid. Under such conditions, a solar process conceivably could run at maximum temperatures near 2300 K and with high flux densities.

3.3.5 Experimental Program and Results

Experiments were carried out in the 15 kW solar furnace at the Paul Scherrer Institute (*PSI*) and in the 5 kW imaging furnace at the *CNRS*-Nancy Laboratory. The description of the solar furnace as well as the details of how it is operated have been described in earlier publications [Steinfeld *et al.*, 1995a]. A sketch of the *CNRS*-Nancy furnace is shown in Figure 3.13. The light

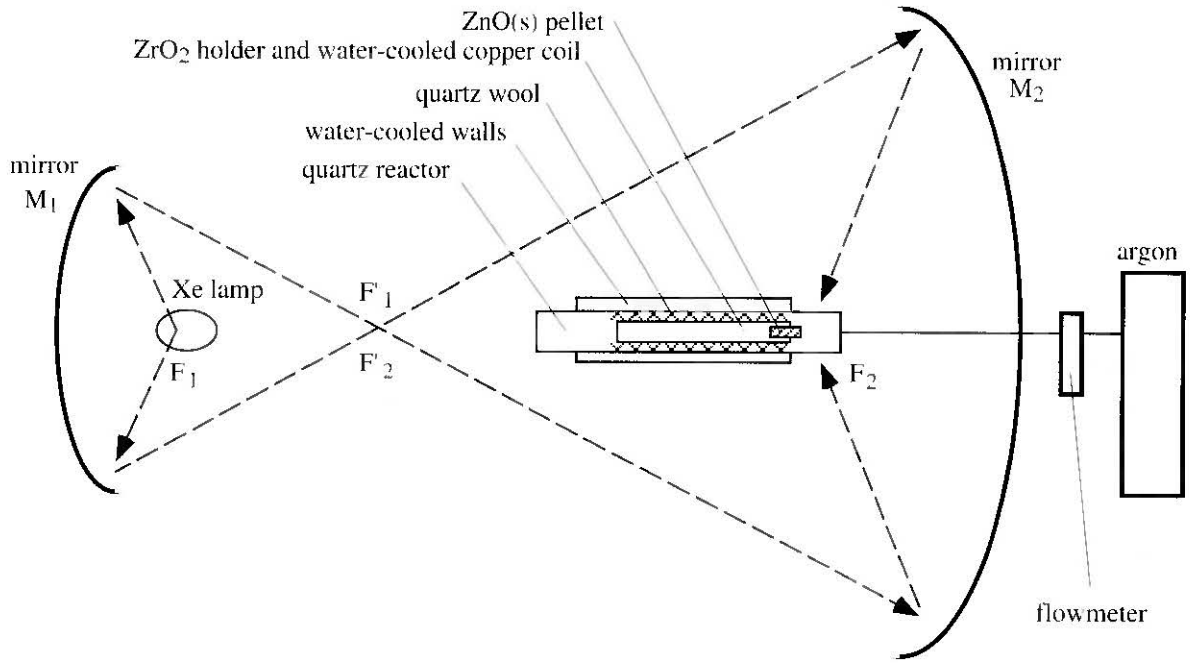

Figure 3.13 The experimental set-up using the imaging furnace [Palumbo *et al.*, 1998].

source is a 5 kW 9 bar Xenon lamp. It is located at *F1*, a focal point of the elliptical mirror *M1*. The reflected light arrives at this mirror's second focal point, *F1'*, which is also the second focal point, *F2'*, of a second elliptical mirror *M2*. The second mirror receives the radiation and again concentrates the light to about a 0.8 cm diameter circle at *F2*. In both facilities, one can reach temperatures greater than 2700 K.

The experimental objectives were to demonstrate that one could decompose *ZnO(s)* and recover *Zn* after a quench. X-ray diffraction was used to identify the products. The amount of *Zn* produced was determined by reacting the products with *HCl* and measuring the evolved moles of H_2. The *Zn* yield was the mole percent zinc in the recovered products. Although the experimental results cannot be compared directly to our theoretical study, they supplement that study by giving one further insight into the decomposition and quench processes.

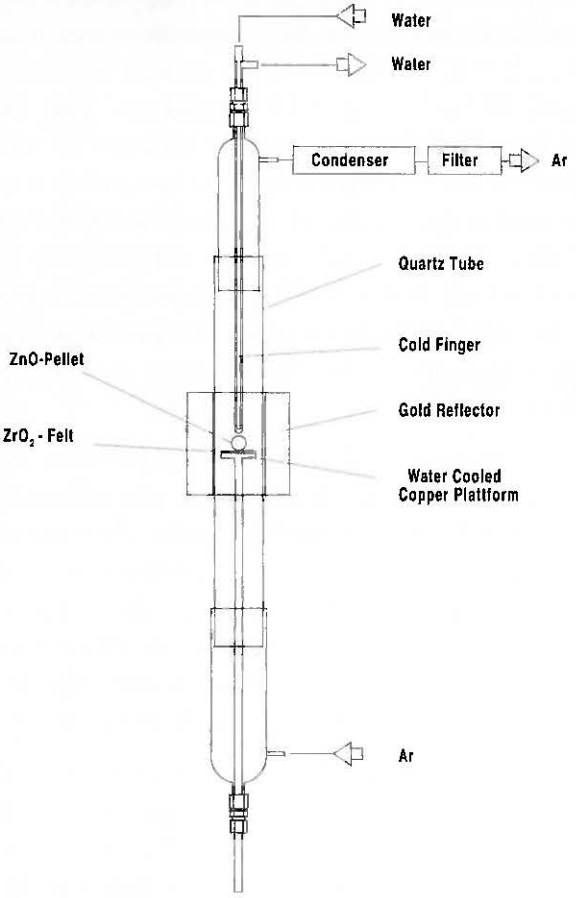

Figure 3.14 The experimental set-up using the solar furnace [Palumbo *et al.*, 1998].

Figure 3.14 is a description of the *PSI* experimental set-up. A tubular quartz reactor was located at the focal line of a gold plated reflector. We acknowledge that our reactor (and the one used at the *CNRS*-Nancy laboratory) is not designed to optimize process and quench efficiency. Rather it is a device that gives us the insight and motivation to begin a systematic design process. Inside the reactor, an Al_2O_3 crucible containing a ZnO pellet rested at the focal point of the solar furnace supported by a copper cooling coil. A continual flow of Ar purged the reactor. Some of the products were quenched on a quartz cold finger located just above the sample and on the walls of the reactor. Other products were recovered on filter paper located just downstream of the quartz reactor as shown in Figure 3.14.

The temperature was not measured directly. In some experiments, we melted a portion of the Al_2O_3 crucible, indicating that the temperature was at least 2250 K. In other experiments, we stopped increasing the energy to the $ZnO(s)$ when a laminar plume became visible above the surface of the ZnO pellet to prevent the temperature of the sample from exceeding 2250 K.

During experiments at this lower temperature, Zn condensed on the walls of the reactor, the cold finger, and in the filter. Although ZnO was found, the products were nearly 90 mole-% Zn. When the reaction temperature was more than 2250 K, 95% of the products were $ZnO(s)$ for Ar flow rates of $2.5 \cdot 10^{-4}$ m^3 s^{-1} at STP conditions.

Figure 3.15 is a photograph of the quartz reactor after an experiment where the sample temperature was at first below 2300 K and then above this value at the low Ar flow rate. (During this experiment the Al_2O_3 crucible was located on a graphite rod, not the cooling coil.) When the sample of ZnO was below 2300 K, the region of the quartz reactor that is white in the photograph, was, during the first part of the experiment, clean and transparent. Zn deposited on the wall as shown in the photograph. Then when the temperature went above 2250 K, $ZnO(s)$ deposited on the quartz and on the previously formed Zn. Figure 3.16 is a photograph of a cross section of material recovered on the cold finger. One sees Zn formed at the low reaction temperature followed by the deposition of $ZnO(s)$ when the reaction temperature exceeded 2250 K.

When the reaction temperature is above 2250 K and the pressure is 1 bar, Table 3.4 indicates that the ZnO would experience nucleate boiling, vaporizing as a superheated vapor. At these high evaporation rates, the Ar would not as effectively penetrate into the gas phase products to dilute them as for the case at lower reaction temperatures. The higher O_2 partial pressures in the vicinity of the decomposing oxide at the higher sample temperatures could lead to $ZnO(s)$ as the dominate product.

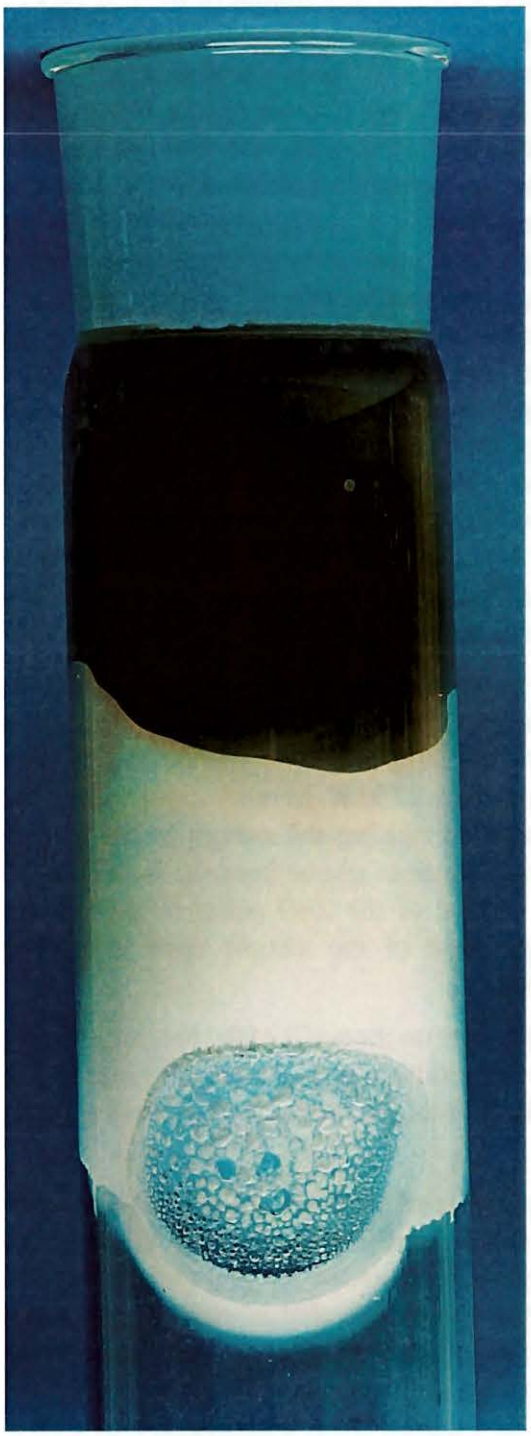

Figure 3.15 Photograph of the reactor tube on which some of the *ZnO* decomposition products formed [Palumbo *et al.*, 1998]. The white regions are *ZnO*. The dark regions are essentially *Zn*.

This hypothesis is supported by supplementary experiments. In one run, the temperature was at or above 2250 K, but the Ar flow rate was increased to $6.67 \cdot 10^{-4}$ m^3 s^{-1} at STP conditions. The *Zn* yield increased from nearly 0 to between 35 and 55 mole-% *Zn*. The higher of these two yields was recovered in the condenser and the lower yield on the filter. In the second case, the temperature of the sample was below 2250 K, but the quench gas was *Ar* and 2 mole-% oxygen. The products that formed throughout the reactor were essentially *ZnO(s)*.

We recognize that the surface temperature on which the products are forming also can influence the nature of the condensed products. *Zn* solid or liquid can't form unless the temperature is at or below its saturation temperature. The experiments conducted at the *CNRS*-Nancy laboratory in conjunction with those at *PSI* illustrate the importance of the quenching surface's temperature.

Figure 3.13 is a sketch of the *CNRS* experimental reactor. It evolved from several experiments. A quartz tube served as the reactor. The portion of the tube near the reaction zone was water- cooled. *Ar* impinged on the front irradiated surface of a cylinder of *ZnO*. The *ZnO* was supported by a ZrO_2 plug. The ZrO_2 in turn rested on a copper water-cooled tube. The tube and ZrO_2 were surrounded by 10 cm of quartz wool. The wool acted as a filter to trap the solid decomposition products. During a typical run with this set up one finds black to grey powder on the quartz, the filter, and the copper tube. An X-ray diffraction analysis of the recovered products revealed a mixture of *Zn* and *ZnO*. We estimate that nearly 80 mole% of this recovered mixture is *Zn*. (The mass of recovered products, however, was only 30% of the measured mass loss from the *ZnO* pellet. But it is conceivable that some of the mass loss from the pellet occurred while handling the pellet. Thus the 80 mole-% *Zn* is our best estimate of how well the products were quenched.) In an earlier version of the apparatus, the quartz tube was not water cooled. During these experiments, one found white powder, indicative of very high concentrations of *ZnO(s)*. Black powder was deposited on the tube beyond the white powder, where the temperature was cooler. Also in the *PSI* experiments, when *ZnO(s)* and *Zn(s)* formed on the quartz reactor walls, the *ZnO(s)* was always deposited in the hottest regions of the reactor followed by *Zn* in the cooler regions of the reactor.

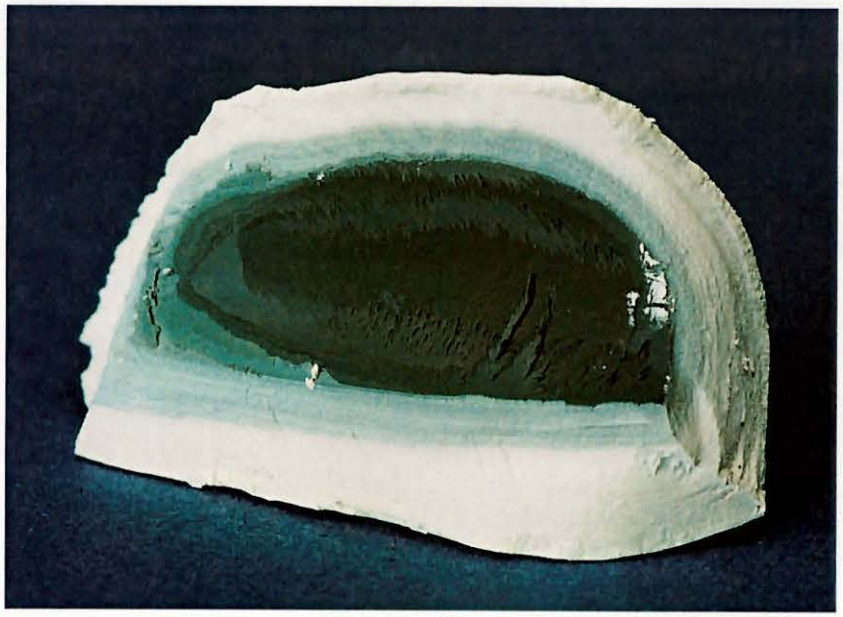

Figure 3.16 Photograph of a cross section of the products that were recovered on the cooling coil [Palumbo *et al.*, 1998]. The dark region is essentially *Zn*, and it was in direct contact with the coil. On top of the *Zn*, one sees white *ZnO*.

At the *CNRS*-Nancy Laboratory, we visually observed that the decomposition reaction slowed considerably. The *ZnO* appeared to change form during an experiment. It became black and very hard. Furthermore, *ZnO* crystals formed creating spindles of *ZnO(s)* on the surface of the *ZnO* pellet for both the Nancy and PSI experiments, probably because of poor micro-local quenching due to bad micro-mixing conditions.

Although differences exist between these experiments and our numerical model of the quench, one can say that the high *Zn* yields obtained during the experiment occurred without achieving a quench rate of 10^7 K s^{-1}. This fact suggests that the quench model over-estimates the quench requirements for high *Zn* yields. We see this difference between the experimental results and the quench model as further evidence that the rate equation given by Kashireninov [Kashireninov *et al.*, 1978 and 1982] is not general enough for reactor design: specifically, his rate equation does not account for surface effects.

3.3.6 Exploratory Work on the Mechanism for the Zn/O_2 Reaction

The oxidation reaction involves three different phases: oxygen and zinc vapor, condensed liquid zinc and solid *ZnO*. This section describes the laboratory study conducted on the oxidation of zinc vapor and condensed zinc by the evaporation and re-crystallization of zinc in the presence of oxygen in the temperature range of 295 K < T < 1173 K [Weidenkaff *et al.*, 1998].

3.3.6.1 Experimental

The apparatus used for studying the condensation of zinc in the presence of oxygen is similar to the set-up for thermochromatographic studies in [Eichler *et al.*, 1992]. This set-up allowed us to investigate the influence of temperature, partial pressure, and gas flow rate of the gases on the yield of zinc. The apparatus consists of an electric furnace for the vaporization of zinc followed by a temperature gradient tube furnace (see Figure 3.17). A well defined temperature gradient from the water cooled side to the hot zone is generated by winding a heating wire around a silver tube with increasing pitch angle. Small glass targets were placed inside the reactor along

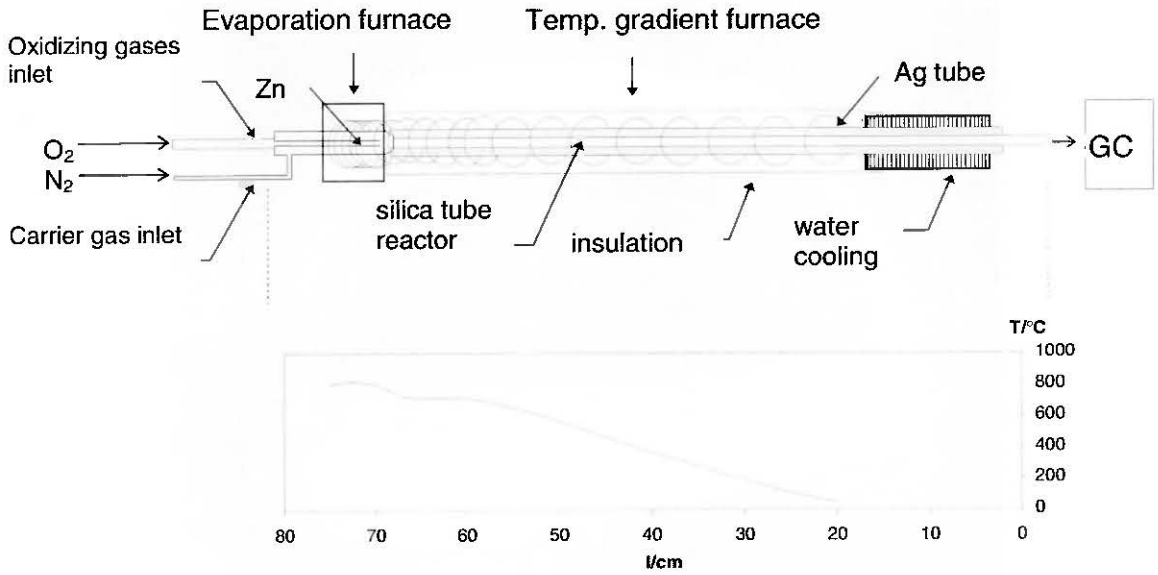

Figure 3.17 Scheme of the temperature gradient furnace set-up for the examination of zinc vapor reactivity [Weidenkaff *et al.*, 1998]. Zinc is vaporized in the evaporation furnace and the condensable products are deposited along the temperature gradient furnace while the non-condensable reactants are measured by gas chromatography.

the condensation zone. A filter was placed at the outlet of the reactor to ensure trapping any aerosols formed during the experiments.

The products that deposited on the glass targets were examined by scanning electron microscopy (*CamScan* CS44) and X-ray diffractometry (*Phillips* X'pert). The oxygen partial pressure at the end of the column was measured with a MTI P200 gas chromatograph.

At the beginning of each experiment, the furnaces were heated to the desired temperatures. Then a quartz tube reactor of 1cm diameter was inserted into the *Ag*-tube. Nitrogen (in a range of 30 to 100 ml/min) was flown over 200 mg zinc (*Merck* purity >95%). Various flows of O_2 and N_2 are mixed with the zinc vapor in the carrier gas stream. The reacting gases (O_2 and Zn) and possibly the solid products were transported downstream by the carrier gas in the direction of decreasing temperature. Deposition started at locations where the temperature of the saturation partial pressure is reached. The position of condensation or desublimation depends upon the volatility of the compound. After approximately 20 min., the products were quenched with cold nitrogen while the reactor was withdrawn quickly from the furnace.

The products were identified by X-Ray powder diffraction using a X'pert-MPD *Phillips* diffractometer with *CuKa* radiation. The zinc yield was determined by measuring the total volume of the evolving hydrogen when the *Zn/ZnO*-mixture was completely dissolved in *HCl* (3,5%) [Weidenkaff *et al.*, 1998].

3.3.6.2 Results and Discussion

Thermochromatography

Since the deposition temperature of a compound depends on its specific volatility, condensable gaseous substances can be separated by condensation in a temperature gradient tube.

The parameters influencing the crystallization in this experimental set-up are the condenser wall temperature (given by the temperature gradient), the reaction time, the amount of carrier gas,

the oxygen partial pressure, and the zinc partial pressure. The zinc partial pressure can be controlled by changing the temperature of the evaporation furnace and by varying the amount of carrier gas for different experiments. The results of the experiments are summarized in Table 3.7. The deposition occurs axis-symmetrically around the reactor walls. An opaque white coverage was mostly found at temperatures between 913 K < T < 973 K, a first zinc mirror-like coating at around 853 K < T < 923 K, and a second mirror-like zinc coating at T < 693 K. The adsorptivity of zinc and zinc oxide on the reactor walls is low. Practically no influence of the gas flow rate on the deposition temperature was observed.

In selective experimental runs we found zinc oxide needles on the surface of silica wool placed in the hot part of the reactor. Similarly long zinc oxide needles were formed on the surface of

Table 3.7 Evaporation temperatures, gas flow rates, and deposition temperatures of thermochromatographic experiments

				Deposition Temperatures		
Exp.No.	Evapor. T[K]	N_2+O_2 Gas flow [ml/min]	O_2 Gas flow [ml/min]	Opaque white from T [K]	*Zn* mirror I (gray) [K]	*Zn* mirror II (glitter) [K]
1	1103	30	0,02	-	873	683
2	1103	30	0,02	-	903	693
3	1123	50	0,03	943	903	693
4	1003	100	0,5	-	873	-
5	1093	100	0,5	913	833	683
6	1113	50	0,5	973	923	693
7	1183	100	0,5	973	853	693
8	1093	50	0,5	-	933	-
9	1123	30	0,5	943	893	673
10	1123	30	0,5	943	893	silica wool
11	1123	30	0,5	943	883	-
12	1153	50	1	903	893	693
13	973	30	1	913	873	-
14	1103	30	1	913	893	-
15	1123	30	1	-	873	693
16	1123	30	1	933	913	silica wool
17	1143	30	2	963	913	-
18	1183	100	3	973	853	693
19	1123	30	4	973	943 (*Zn*/*ZnO*)	-
20	1183	100	5	-	933 (*ZnO*)	-
21	1183	100	10	-	943 (*ZnO*)	-

the oxidizing gas inlet tube. The *Zn* yield of the deposits depended on the oxygen partial pressure and varied in the range of 90% zinc yield (in 0,5% O_2) to 1% zinc yield (in 20% O_2).

When zinc was evaporated in a 30 ml/min flow of nitrogen, a well defined region consisting of a mirror-like deposit was found at the condensation temperature of 903 K. The transport of substances through a temperature gradient tube furnace is a dynamic process of alternating transport in the gas phase, deposition and re-volatilization of the compounds. When the saturation partial pressure (depending on the partial pressure and the gas volume) is reached the main fraction is deposited [Eichler *et al.*, 1992].

In an experiment under identical conditions, in which the zinc/nitrogen stream was seeded with 1% oxygen before entering the condenser tube, we found the same result as the one obtained in N_2-atmosphere. Oxygen was still measured at the outlet of the reactor (see Figure 3.18).

The deposition temperature for zinc oxide is much higher than for zinc. No deposition was found at $T > 973$ K, therefore no reaction takes place at these temperatures.

A small amount of an "opaque white coverage" was found on most of the reactors at temperatures between 833 K< T <973 K. Zinc begins to condense in small amounts at $T < 1100$ K. The deposit can react with oxygen to *ZnO* or with the silica reactor to form zinc silicate, but it might re-evaporate, condense again at lower temperatures and be transported before it is oxidized to *ZnO*. More "opaque white coverage" can be found when the amount of deposited zinc is low and the oxygen partial pressure is high.

At temperatures around 873 K, the gas stream is over-saturated in *Zn*. At this temperature, the main deposition takes place (see Figure 3.18). The X-ray diffraction pattern indicates that the yield of zinc is between 70-90%, depending on the oxygen pressure.

The zinc vapor pressure in the gas stream depends on the temperature of the evaporation furnace and on the amount of carrier gas stream over the zinc. Modeling the amount of zinc evaporation under these special conditions is difficult, because the surface of the liquefied zinc can only be estimated. We measured that a maximum of 20 to 30 mg *Zn* can be evaporated in this apparatus at 1173 K in 20 min. The stoichiometric mass for totally oxidizing this amount of evolving zinc would be 0,5 ml/min of O_2 at normal conditions. By measuring the excess oxygen partial pressure during the experiment at the outlet of the reactor, we found that most of the oxygen passed the zinc without reacting.

The experiments carried out in 10 ml/min O_2 flow lead to a white deposit at $T < 973$ K, while oxygen was still detected at the outlet. The X-ray diffraction pattern shows that the condensed zinc phase is reoxidised to more than 95% *ZnO*. In contrast to the other experiments, *ZnO* was also found in the filter at the outlet of the reactor.

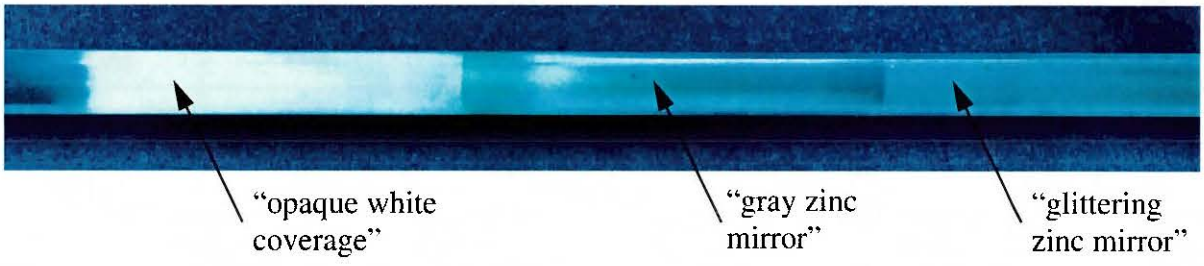

Figure 3.18 Photo of reactor after an experiment in diluted oxygen atmosphere: The deposition fields are divided in three mirrors surrounding the reactor walls: 973-853 K "opaque white" *ZnO* with the appearance of *Zn*-droplets, 853-693 K with a gray zinc mirror (90% *Zn*) and 693-573 K with a glittering zinc mirror (90% *Zn*) [Weidenkaff *et al.*, 1998].

A tube furnace (Heraeus RO 4/25) with an isothermal section was used to verify that at high temperatures no formation of zinc oxide takes place. The experiment was carried out in a 3 cm diameter tubular reactor. Zinc was evaporated and oxygen was mixed into the gas stream. No deposition was found on a 10 cm long region in which the temperature was 1273 K [Weidenkaff *et al.*, 1998].

Morphology and Crystal Growth Mechanisms

The morphology of the crystallized products depends on the nucleation conditions, the temperature, the O_2 partial pressure and the condenser material, etc. The products were examined by X-ray diffraction and by scanning electron microscopy.

No deposit was found at temperatures above 973 K. At temperatures of 873 K $<T<$ 973 K less than 1% of the total mass of deposit was found in the form of a white material which could not be removed mechanically from the reactor walls (the remainder was a mirror-like zinc deposit). In the temperature range 693 K $<T<$ 873 K we observed the formation of small sphere-like particles with growing prismatic facets towards lower temperatures. The form of the deposit is similar to that described for the vapor-liquid-solid (*VLS*) growth of *Cd*-crystals with *Bi* impurities [Hasiguti *et al.*, 1981]. Hexagonal prismatic *Cd*-crystals grew with "hemispherical rounded tips" observed by *in-situ* microscopy. The growth mechanism was found to be the *VLS* in contrast to vapor-solid (*VS*) growth, where the *Cd*-vapor deposits directly on solid *Cd* and the morphology of the deposit changes to hexagonal prismatic crystals.

The surface of the condensate is rough, because of re-evaporation of some zinc and partial oxidation. At temperatures below 693 K (zinc melting point), the crystal growth is a result of desublimation. Atoms from the vapor phase are impinging directly on the formed *Zn* solid. The morphology of the deposit changes drastically to crystals of hexagonal prismatic platelets, that grew in a 2-dimensional growth mode layer by layer [Wang *et al.*, 1993].

Depending on the experimental conditions, the deposits can be more or less re-oxidized. The deposit from experiment No. 12 shows the first stage of oxidation. On the particle surface initial formation of a hexagonal nucleus and zinc oxide needles at wrinkles of the particle was observed. In concentrated oxygen atmosphere most of the deposit is reacted to *ZnO*. The *SEM* pictures show long needles of *ZnO*.

Tetrapod shaped *ZnO*, like that described by Iwanaga and co-workers [Iwanaga *et al.*, 1994] can be formed if the zinc partial pressure is low and the oxygen partial pressure is high.

3.3.7 Conclusions

Concentrated solar energy can be used to produce *Zn* from *ZnO* in a single step high temperature solar decomposition process in which the elements *Zn* and O_2 are unmixed by a quench. Our evidence for this claim is both theoretical and experimental in nature. A chemical equilibrium study reveals that the products from the decomposition of *ZnO(s)* at temperatures above 2000 K are essentially *Zn(g)* and O_2. The decomposition of zinc oxide to zinc and oxygen is an attractive process for the storage of solar energy. Both products are evolved from the surface of a shrinking ZnO particle into the gaseous state. Thus, in contrast to other metal oxides reduction processes, the kinetics are not limited by the diffusion of ions through a condensed phase (see e.g. *FeO* cycle [Weidenkaff *et al.*, 1997]. Furthermore, our numerical model of the decomposition and quench steps showed that one can obtain reaction temperatures above 2200 K with solar flux densities of 2 MW m^{-2}, and it showed that the required quench rate to obtain good *Zn(s)* yields is physically possible. These results were obtained with kinetic data available in the lit-

erature. Finally, we demonstrated that the theoretical maximum efficiency of this solar decomposition process can be greater than 35%.

Experimentally, we produced *Zn* from *ZnO* in high temperature reactors. The experiments were conducted in a solar furnace and a solar furnace simulator. *Zn* yields were as high as 90%. Besides corroborating our theoretical claim that *Zn* can be produced from *ZnO*, these experiments revealed qualitative information that will be helpful to anyone designing a solar reactor for the decomposition process. Photographs of the quenched products from both the solar and electric furnace experiments in combination with a chemical analysis of the products show that the efficiency of the quench is sensitive to the dilution ratio and surface temperature on which the products are quenched. Furthermore, the experiments suggest that our quench model over-estimates the required severity for a quench leading to high *Zn*-yields, indicating that better kinetic data is needed for the Zn/O_2 reaction.

Our preliminary exploration into the mechanism for the Zn/O_2 reaction shows that in a diluted atmosphere zinc vapor and oxygen can coexist, if the formation and growth of *ZnO* nuclei is suppressed. However, *Zn* liquid can easily be oxidized. The interpretation of the sample morphologies obtained in the temperature region of $873\ \mathrm{K} > T > 693\ \mathrm{K}$ reveals that the formation of zinc oxide needles begins at wrinkles and furrows. These needles start from hexagonal nuclei on the surface of *Zn*.

Lastly our study implicitly suggests to those conducting solar chemistry research a methodology for approaching the problems inherent in developing high temperature solar technology. We demonstrate that the science of obtaining the knowledge to develop a solar reactor for a solar chemistry process is tied closely to the science of chemical reaction engineering. We used thermodynamics and chemical kinetics to develop our arguments. Next we developed models that linked the chemistry of our reaction to the conservation of mass and energy equations. The insights obtained from these first and albeit simple models and our experimental results reveal the steps required of future research: We need to obtain a better understanding of the kinetics for the oxidation reaction; we need to learn to optimize the mixing of gases if the products are to be efficiently quenched with an inert gas; we need to begin designing reactors, making decisions about batch or continuous flow as well as shape, size, phase, and flow rate of the *ZnO*.

Nomenclature

C	Heat capacity for solid particle, J kg^{-1} K^{-1}
C_p	Constant pressure heat capacity of gas, J mol^{-1} K^{-1}
E_a	Apparent activation energy for ZnO(s) decomposition reaction
F^e	Molar flow rate of Zn, mols s^{-1}
ΔG	Change in *Gibbs* function at 298 K and total pressure of 1 bar for $Zn(s) + 0.5\ O_2 + a\ Ar$ to $ZnO(s) + a\ Ar$, kJ mol^{-1}
Δgef	Change in the *Gibbs* energy function, kJ mol^{-1} K^{-1}
ΔH_{vap}	Enthalpy of vaporization, J kg^{-1}
ΔH_d	Enthalpy change for decomposing $ZnO(s)$ to $Zn(g) + 0.5\ O_2$, J kg^{-1}
ΔH_r	Enthalpy change for the recombination of $Zn(g) + 0.5\ O_2$ to $ZnO(s)$, J mol^{-1}
ΔH^o_{298}	Enthalpy of formation of $ZnO(g)$ at 298 K, kJ mol^{-1}
h	Convection heat transfer coefficient, W m^{-2} K^{-1}
K_p	Constant pressure equilibrium constant
k'	Specific rate constant, mol m^2 s^{-1}

P	Pressure, N m^{-2}
Q_m	Total gas mass flow rate, kg s^{-1}
Q_o	Volume flow rate at STP, m^3 s^{-1}
Q_{solar}	Solar power delivered to solar receiver, kJ s^{-1}
q_{net}	Net radiation flux, W m^{-2}
q_{solar}	Solar flux, W m^{-2}
R	Universal gas constant, 8.314 J mol^{-1} K^{-1}
R_{rad}	Particle radius, m
R^o_{rad}	Initial particle radius, m
R_{reac}	Radius of quench reactor, m
T	Temperature, K
T_s	Temperature of solid ZnO-particle, K
T_g	Gas temperature, K
T_i	Gas temperature at start of reoxidation reaction, K
T_o	Reference gas temperature for STP conditions, K
T_w	Wall temperature of quench reactor, K
t	Time, s
t_s	Residence time in quench reactor, s
V	Volume swept out by gases flowing in quench reactor, m^3
W_{out}	Power of fuel cell, kJ s^{-1}
X	Extent of Zn production for the (vaporization) decomposition reaction
X_{-1}	Extent of Zn oxidation in the recombination reaction
$\Re$	Rate of vaporization (decomposition) reaction, kg m^{-3} s^{-1}
$\Re_{-5}$	Rate of oxidation reaction, mol m^{-3} sec^{-1}
α	Absorptivity, emissivity
ρ	Density of $ZnO(s)$, kg m^{-3}
σ	*Stefan-Boltzmann* constant, $5.67 \cdot 10^{-8}$ W m^{-2} K^{-4}
τ	Space time, V/Q_o, s
τ_c	Heat transfer characteristic time, $R_{reac}\, C_p\, Q_m / (2\, Q_o\, h)$, s
η_{th}	Thermal efficiency

3.4 Carbothermic Reduction of Metal Oxides

This Chapter considers the solar thermal reduction of metal oxides using fossil fuels (C, CH_4) as chemical reducing agents [Steinfeld, 1997]. Industrially, metals are extracted from their oxidic ores either electrolytically (e.g., the Hall-Héroult process for aluminum production) or thermochemically (e.g., blast furnaces for iron production). In either case, an amount of energy equal to the *Gibbs* free energy change of the reaction ΔG needs to be supplied as *high-quality* energy. This energy is supplied, for example, in the form of electrical work in electrolytic processes or in the form of chemical energy (by introducing a reducing agent) in thermochemical processes. The remainder of the required energy ΔH-ΔG may be delivered in the form of heat.

However, in many commercial electrolytic processes and reducing furnaces, electricity and/or reducing agents are frequently used in excess of ΔG in order to compensate for the process heat.

The extractive metallurgical industry is a major consumer of high-temperature process heat. It is, consequently, a major contributor of CO_2 emissions derived from the combustion of fossil fuels for heat and electricity generation. Table 3.8 gives an estimate of CO_2 emissions discharged during the production of iron, aluminum, zinc, and synthesis gas: column 1 shows the annual world metal production [Ullmann, 1988]; column 2 shows the annual world CO_2 emissions for iron [Gretz *et al.*, 1991], aluminum [Abrahamson, 1992], and zinc[2]; and column 3 shows the percentage contribution to the world's total anthropogenic CO_2 emissions (approximately $20.7 \cdot 10^{12}$ kg).

3.4.1 Carbothermic Processes

Coal as coke is a preferred reducing agent in blast furnace processes because of its availability and relatively low price. However, carbothermic reduction processes usually use coke not only as the reductant but as the primary source of process heat as well. The combustion of coal and other conventional fossil fuels in air releases a great deal of nitrogen contaminated with CO, CO_2, NO_x, SO_x, and other pollutants. Carbothermic reductions occurring in commercial blast furnaces are complex, but their overall reaction may be represented by[3]

$$M_xO_y + \frac{y}{2}C(gr) \rightarrow xM + \frac{y}{2}CO_2 \qquad \textbf{(3.62)}$$

For example, for the carbothermic reduction of hematite, (3.62) becomes

$$Fe_2O_3 + \frac{3}{2}C(gr) \rightarrow 2Fe + \frac{3}{2}CO_2 \qquad \Delta H^\circ_{298K} = 235 \text{ kJ mol}^{-1} \qquad \textbf{(3.63)}$$

Table 3.8 Annual world production and corresponding CO_2 emissions for the production of iron, aluminum, zinc, and synthesis gas [Ullmann, 1988; Gretz *et al.*, 1991; Abrahamson, 1992; Encyclopedia of Chemical Technology, 1985; Hassmann *et al.*, 1993; Kola, 1985].

	Annual Production [kg]	Annual CO_2 emission [kg]	Total World CO_2 emission %
Iron (Blast Furnace)	505×10^9	1.11×10^{12}	5.4% of Total
Aluminum (Hall-Electrolysis)	14×10^9	0.52×10^{12}	2.5% of Total
Zinc (Electrolysis + ISF)	6×10^9	0.07×10^{12}	0.3% of Total
Synthesis gas (Natural Gas Reforming)	2×10^{11}	0.30×10^{12}	1.4% of Total

2. Assumptions: zinc production is 85% by electrolysis and 15% in an imperial smelting furnace (*ISF*) [Encyclopedia of Chemical Technology, 1985]; CO_2 total emissions from electrolysis are estimated assuming 0.87 kg CO_2/kWh$_e$ for coal-fired electricity [Hassmann and Kühne, 1993] and energy consumption of 50 GJ/ton *Zn* produced; CO_2 total emissions from *ISF* assuming carbon consumption of 0.78 ton C/ton *Zn* produced [Kola, 1985].

3. M denotes a metal; M_xO_y denotes the corresponding metal oxide.

If carbon were used exclusively as a reducing agent according to equation (3.63), the stoichiometric mass ratio of carbon consumed to iron produced should be 0.16. In contrast, real blast furnaces use 0.9 tons of coke to produce 1 ton of pig iron and release vast amounts of greenhouse gases and other contaminants. For the carbothermic reduction of zinc oxide, equation (3.62) is

$$ZnO + \frac{1}{2}C(gr) \rightarrow Zn + \frac{1}{2}CO_2 \qquad \Delta H^\circ_{298K} = 151 \text{ kJ mol}^{-1} \qquad \textbf{(3.64)}$$

Similarly, if carbon were used only as a reductant according to equation (3.64), the stoichiometric mass ratio of carbon consumed to zinc produced should be 0.09. In contrast, commercial smelting furnaces use 0.8 tons of coke to make 1 ton of zinc while causing concomitant environmental pollution.

The amount of fuel needed to reduce metal oxides to metals could be substantially reduced if it were used exclusively as a reducing agent and process heat were supplied by an alternative clean energy source like solar energy. Concentrated solar radiation can provide the high-temperature process heat required to drive these highly endothermic reactions. Examples of metal oxides reduction processes that have been studied experimentally in solar furnaces include the production of Fe, Al, Mg, Zn, TiC, SiC, CaC_2, TiN, Si_3N_4, and AlN by carbothermic reduction of their oxides in Ar or N_2 atmospheres [Steinfeld and Fletcher, 1991; Duncan and Dirksen, 1980; Eicher, 1985; Palumbo, *et al.*, 1992; Murray *et al.*, 1995], high-temperature electrolysis of ZnO and MgO [Palumbo, 1987; Palumbo and Fletcher, 1988], and the thermal decomposition of Fe_3O_4, Mn_3O_4, and other oxides [Sibieude *et al.*, 1982; Tofighi, 1982; Kuhn *et al.*, 1995]. An idealization of a solar blast furnace is given in [Steinfeld and Fletcher, 1991].

3.4.2 Combined M_xO_y-Reduction / CH_4-Reforming Process

The use of natural gas as reducing agent for metal oxides offers some intriguing advantages with regard to the gaseous products. Methane, the main constituent of natural gas, can undergo partial catalytic oxidation to form synthesis gas (syngas, a mixture of primarily H_2 and CO). Syngas is widely utilized in the chemical industry as feedstock for the direct production of methanol and other organic commodity chemicals. Most syngas is obtained from natural gas using steam as the oxidant. Alternatively, one can use a metal oxide as an oxygen donor. This approach is formally equivalent to combining two processes, viz., methane reforming to produce syngas and metal-oxide reduction to produce the metal. The overall reaction may be represented as [Steinfeld, 1997]

$$M_xO_y + yCH_4 \rightarrow xM + y(2H_2 + CO)\,. \qquad \textbf{(3.65)}$$

For example, for $M = Fe$, Zn, and Mg, (3.65) becomes

$$Fe_2O_3 + 3CH_4 \rightarrow 2Fe + 3(2H_2 + CO) \qquad \Delta H^\circ_{298K} = 719 \text{ kJ mol}^{-1}; \qquad \textbf{(3.66)}$$

$$ZnO + CH_4 \rightarrow Zn + (2H_2 + CO) \qquad \Delta H^\circ_{298K} = 313 \text{ kJ mol}^{-1}; \qquad \textbf{(3.67)}$$

$$MgO + CH_4 \rightarrow Mg + (2H_2 + CO) \qquad \Delta H^\circ_{298K} = 566 \text{ kJ mol}^{-1}. \qquad \textbf{(3.68)}$$

The resulting syngas mixture has a molar ratio of H_2 to CO equal to 2, which makes it especially suitable for methanol synthesis. Thus, as opposed to carbothermic processes, the evolved gases are sufficiently valuable commodities to justify their collection, thereby eliminating the discharge of gaseous reaction products to the environment.

The chemical equilibrium composition of the system $M_xO_y + y\ CH_4$ has been studied for various metal oxides of industrial interest [Steinfeld, 1993a; Steinfeld *et al.*, 1998a]. The temperature for which the equilibrium constant equals 1 is 900 K for equation (3.66), 1100 K for equation (3.67), and 1800 K for equation (3.68). These temperatures are within the reach of large-scale solar collection facilities such as central receivers which have concentrations of 1000 suns and more (1 sun = 1kW/m^2) [Winter *et al.*, 1991]. Higher concentrations that permit delivery of energy at higher temperatures may be achieved in paraboloidal tracking dishes and by using non-imaging secondary concentrators. The CH_4-reduction of ZnO has also been proposed using process heat from gas-cooled nuclear reactors [Huwyler *et al.*, 1975]. The kinetics of the reduction of Fe_2O_3, Fe_3O_4 and ZnO with CH_4 have been investigated in laboratory electric furnaces [Barret, 1972; Ghosh *et al.*, 1986; Haas *et al.*, 1985; Ruprecht *et al.*, 1971; Hutchings *et al.*, 1988; Steinfeld *et al.*, 1995b]. The Fe_3O_4-CH_4 and ZnO-CH_4 reactions have also been studied experimentally at PSI's solar furnace and demonstrated to proceed at 1300 K in a small-scale fluidized bed reactor [Steinfeld *et al.*, 1993; Steinfeld *et al.*, 1995a]. Directly irradiated metal oxide particles fluidized in methane acted simultaneously as energy absorbers and chemical reactants, thereby providing efficient heat transfer directly to the reaction site. These previous experiences indicate that solar production technologies may be developed for the proposed processes.

3.4.3 H_2 / Electricity / Methanol Production Scheme

In an H_2O-splitting reaction, the metal is reacted with water at moderate temperatures to regenerate the metal oxide and form molecular H_2 as the only product component in the gas phase, i.e.

$$xM + yH_2O \rightarrow M_xO_y + yH_2. \qquad \textbf{(3.69)}$$

For example, the water-splitting reactions with iron, zinc, and magnesium, are

$$3Fe + 4H_2O \rightarrow Fe_3O_4 + 4H_2 \qquad \Delta H^\circ_{298K} = -23\ \text{kJ·mol}^{-1}; \qquad \textbf{(3.70)}$$

$$Zn + H_2O \rightarrow ZnO + H_2 \qquad \Delta H^\circ_{298K} = -62\ \text{kJ·mol}^{-1}; \qquad \textbf{(3.71)}$$

$$Mg + H_2O \rightarrow MgO + H_2 \qquad \Delta H^\circ_{298K} = -315\ \text{kJ·mol}^{-1}. \qquad \textbf{(3.72)}$$

Reactions (3.70) to (3.72) are thermodynamically favorable at temperatures below 1000 K. Preliminary experimental studies for iron and zinc have shown that these reactions proceed around 700 K. The heat liberated by these exothermic reactions could be used in an auto-thermal reactor for conducting the water-splitting reaction at temperatures above ambient conditions. Alternatively, the metal may be used to produce electrical work directly in a fuel cell or in a metal/air battery (the reaction in a Zn/air battery is $Zn + 0.5\ O_2 = ZnO$, ΔG°_{298K} =-316 kJ/mol).

An open process scheme for the production of methanol and H_2/electricity, using methane and water as feedstock, solar energy as source of process heat, and a metal as energy carrier, is shown in the diagram of Figure 3.19 [Steinfeld, 1997]. It consists of two main steps. In the first step, the metal oxide is reduced with CH_4 to form the metal and syngas in an endothermic, solar process (3.65); syngas is sent to a conventional methanol-producing plant. In the second step, the metal is used to split H_2O and form H_2 (Equation (3.69)) or, alternatively, the metal is used in a metal/air fuel cell (or metal/air battery) to produce electrical work. In either case, the chemical product of the second step is the metal oxide which, in turn, is recycled to the first step. In this scheme, the solar-made metal serves as a clean, compact and transportable solid fuel. It may be utilized to produce directly either H_2 or electricity. The only emissions of CO_2 arising from this thermochemical scheme are those resulting from methanol combustion; on the other hand, methanol, hydrogen, and electricity are produced with zero-CO_2 emissions.[4]

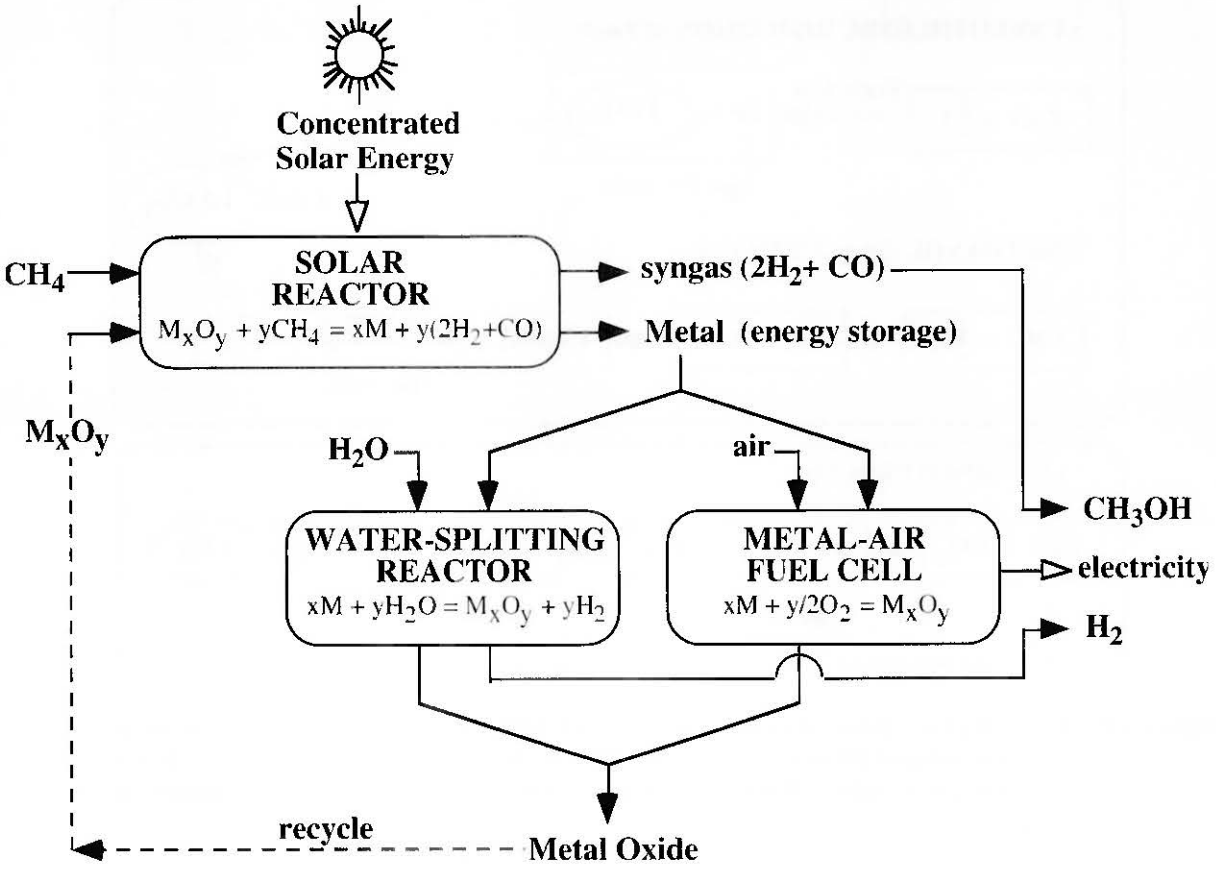

Figure 3.19 Schematic of a methanol and H_2/electricity producing process, using methane and water as feedstock, solar energy as source of process heat, and a metal as energy carrier [Steinfeld, 1997]. M denotes a metal, M_xO_y denotes the corresponding metal oxide.

The potential for CO_2 mitigation by the combined reduction/reforming process is illustrated in Figure 3.20, where the reduction of ZnO has been taken as a model [Steinfeld *et al.*, 1996b]. Only the CO_2 involved in the stoichiometric chemical reactions is considered. The desired final products are zinc and methanol. These two important industrial commodities are conventionally produced by two independent processes: zinc is assumed to be obtained by the carbothermic reduction of zinc oxide, while methanol is assumed to be derived from synthesis gas obtained by the reforming of methane.

CO_2 evolved from conventional chemical processes is depicted in the upper box diagram. It shows that the carbothermic reduction of ZnO releases 1/2 mole of CO_2 per mole of zinc produced, whereas the combustion of 1 mole of methanol releases 1 mole of CO_2. The total CO_2 contribution is 1.5 moles of CO_2 emitted per mole of zinc and methanol. In contrast, the lower diagram shows only 1 mole of CO_2 emitted per mole of zinc and methanol produced by the combined ZnO-reduction and CH_4-reforming process. This change results in saving 33% of total CO_2 emissions while producing the same amounts of desired final products. By using the combined process, the production of 1/2 mole of CO_2 per mole of zinc derived from the carbothermic reduction of ZnO, equation (3.64), has been avoided. Similarly, if reduction of Fe_2O_3

[4] In this work, the CO_2 mitigation potential that may be achieved on the basis of idealized process steps is demonstrated. Technical realizations might involve additional energy consuming steps, e.g., associated with the recycling of the metal oxide.

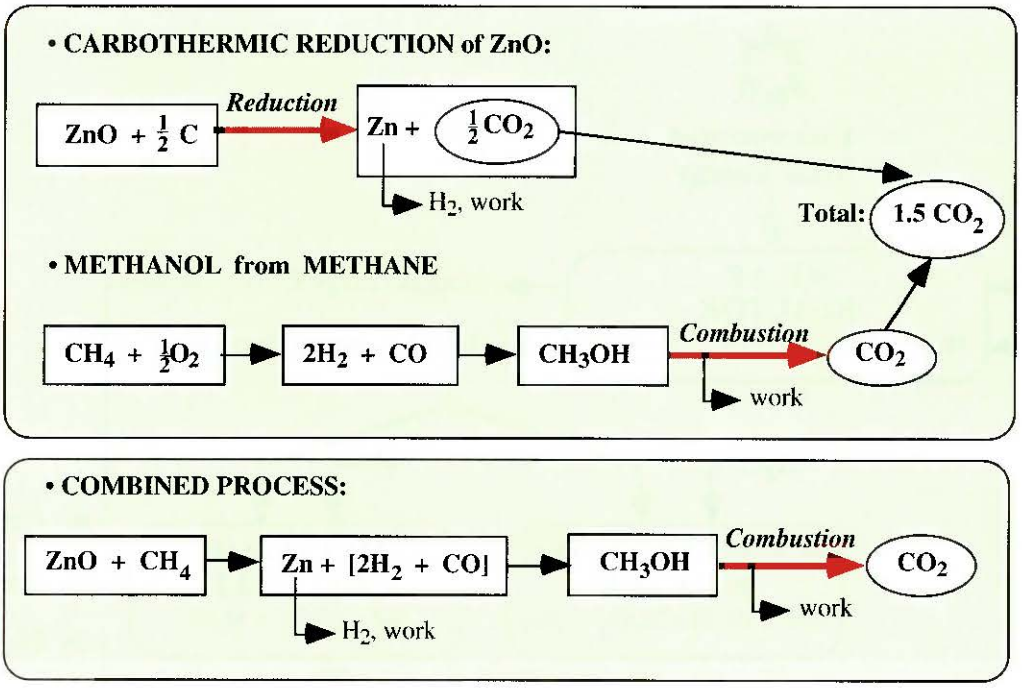

Figure 3.20 CO_2 mitigation potential by the combined ZnO-reduction/CH_4-reforming process for producing zinc and methanol [Steinfeld, 1997]. Only the CO_2 derived from the stoichiometric chemical transformations is considered. The CO_2 emitted by combustion of fuels for supplying process heat is excluded.

is combined with methane reforming, 3/2 moles of CO_2 derived from the carbothermic reduction of 1 mole of Fe_2O_3, equation (3.63), are avoided. In general, if reduction of M_xO_y is combined with methane reforming, $y/2$ moles of CO_2 derived from the carbothermic reduction of 1 mole of M_xO_y, equation (3.62), may be avoided. The only CO_2 emissions of the combined process are those resulting from the combustion of produced methanol. This change corresponds to an emission *reduction* equal to the amount of CO_2 derived in the classic carbothermic reduction of metal oxides.

The CO_2 mass balance of Figure 3.20 allows only for CO_2 derived from chemical transformations. It does not include CO_2 emitted from the combustion of fuels which are needed to supply process heats. The combined M_xO_y-reduction/CH_4-reforming is highly endothermic, as is indicated by ΔH in equations (3.66) to (3.68). For example, if the combustion of natural gas were to be used for supplying process heat to the ZnO-CH_4 reaction, approximately an extra 1/2 mole of CH_4 would be required per mole of CH_4 reformed. The use of solar energy for heating reactants to the operating temperature and providing the ΔH of reaction further eliminates the discharge of greenhouse gases from burning fossil fuels.

3.4.4 Combined ZnO-Reduction and CH_4-Reforming

This chapter describes the combined reduction of ZnO and the reforming of CH_4 for the co-production of zinc and synthesis gas [Steinfeld *et al.*, 1995a]. The overall reaction can be represented as:

$$ZnO + CH_4 = Zn + 2H_2 + CO \qquad (3.73)$$

The advantage would be threefold:

1. the reforming of methane in the absence of catalysts and with proper optimization may be made to produce high quality syngas;
2. the evolved gases are sufficiently valuable commodities to justify their collection, eliminating inherent gas emissions to the environment;
3. the integration of the *ZnO* reduction and the natural gas reforming into a single reactor could improve energy efficiencies through concurrent high temperature reactions.

Emissions of greenhouse-effect gases and pollutants could be further reduced to zero if CH_4 were used exclusively as a reducing agent and process heat were supplied by solar energy. By concentrating the sunlight that reaches the earth and capturing that radiative energy in a solar receiver, we can provide high-temperature process heat to drive reaction (3.73). The reduction of iron oxide with CH_4 has been previously investigated as an alternative to blast-furnace processes [Barret 1972; Ghosh *et al.*, 1986; Haas *et al.*, 1985; Ruprecht *et al.*, 1971; Hutchings et al. 1988], and recently demonstrated using solar energy [Steinfeld *et al.*, 1993]. The potential of CO_2 mitigation in the metallurgical industry via solar-driven processes has been thermodynamically analyzed [Steinfeld, 1997; Steinfeld *et al.*, 1996b]. The syngas industry is also a major consumer of high-temperature process heat with annual world emissions of $0.3 \cdot 10^{12}$ kg of CO_2 [Hassmann *et al.*, 1993], which could be minimized by substituting solar energy for fossil fuels. The amount of solar energy stored in the products of equation (3.72) can reach up to 55% of the energetic value of the methane in the reactants, which otherwise would have been consumed in excess as a fuel to supply for the process heat. In the proposed process, methane is to be employed only as a reducing agent. The use of solar energy to heat up the reactants from ambient to the operating temperature and to provide for the ΔH of the reaction would eliminate the cost of fuel consumption as well as the cost of removal and disposal of harmful pollutants. As it will be shown in the thermodynamic analysis that follows, this combined process can be conducted at temperatures that are within the reach of large-scale solar collection facilities, such as central receivers, having concentrations of up to 1000 suns (1 sun = 1 kW m^{-2}) [Winter *et al.*, 1991].

3.4.4.1 Thermodynamics

The variation of ΔH° (standard enthalpy change), ΔG° (standard *Gibbs* free energy change), and $T\Delta S^\circ$ ($T\Delta S^\circ = \Delta H^\circ - \Delta G^\circ$) of equation (3.73) with temperature are shown in Figure 3.21. The slopes of these curves are:

$$\left(\frac{\partial \Delta H}{\partial T}\right)_p = \Delta C_p, \tag{3.74}$$

and

$$\left(\frac{\partial \Delta G}{\partial T}\right)_p = -\Delta S. \tag{3.75}$$

The ΔC_p, the difference between the specific heat capacities of products and reactants is small. Thus, the total energy required to effect this endothermic transformation, i.e. ΔH°, is almost constant over a wide temperature range, except for the heat of fusion and vaporization at the *Zn* m.p. 692 K and at the *Zn* b.p. 1180 K, respectively. But ΔS is a large positive number and, therefore, ΔG° decreases with temperature, with slight discontinuity in the slope at the phase change. Consequently, as the temperature is raised, the ratio of work (e.g. electrical energy) to thermal energy $\Delta G^\circ / T\Delta S^\circ$ decreases. At 1105 K, $\Delta G^\circ = 0$. At above 1105 K, the reaction proceeds spontaneously to the right. $T\Delta S^\circ$ is the amount of energy that must be supplied as process heat for

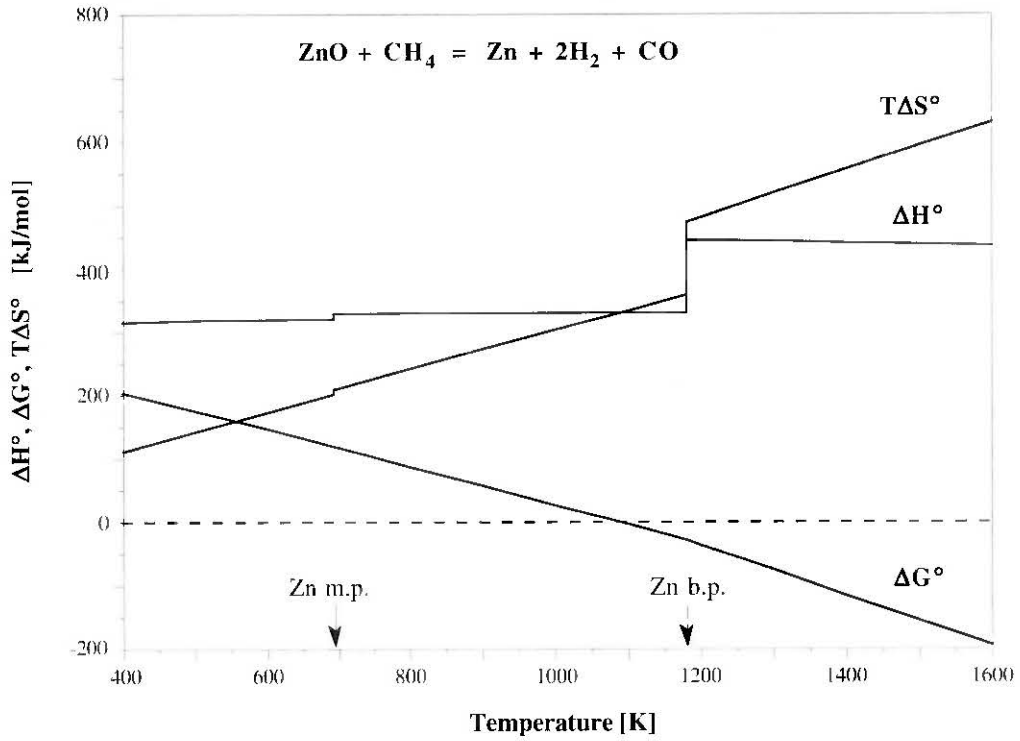

Figure 3.21 The variation of ΔH°, ΔG°, and $T\Delta S^\circ$ with temperature, for reaction (3.73) [Steinfeld *et al.*, 1995a].

the completely reversible process. Thus, at above 1105 K, if we simply permit the reaction to proceed without getting work from the system in addition to the products, we would have to supply ΔH of the reaction, about 440 kJ/mol of zinc produced.

Equation (3.73) summarizes the overall reaction, but significant intermediate reactions of the syngas chemistry need to be considered, viz.:

$$\text{methane-cracking: } CH_4 = C(gr) + 2H_2 \tag{3.76}$$

$$\text{reforming-methanation: } CO_2 + CH_4 = 2CO + 2H_2 \tag{3.77}$$

$$\text{water-gas shift: } CO_2 + H_2 = CO + H_2O \tag{3.78}$$

$$\textit{Boudouard: } C(gr) + CO_2 = 2CO \tag{3.79}$$

$$\text{carbon gasification: } C(gr) + H_2O = CO + H_2 \tag{3.80}$$

and the reduction of ZnO by hydrogen, carbon, and carbon monoxide:

$$ZnO + H_2 = Zn + H_2O \tag{3.81}$$

$$ZnO + CO = Zn + CO_2 \tag{3.82}$$

$$ZnO + C(gr) = Zn + CO \tag{3.83}$$

all of which depend strongly on the temperature and pressure, and determine the relative amounts of H_2, H_2O, CO, CO_2, CH_4, Zn in the gas phase, and ZnO, $C(gr)$ in the solid phase.

The NASA-CET85 code [Gordon and McBride, 1976] was used to compute the equilibrium composition of the system $ZnO + CH_4$ at 1 atm. and over the range of temperatures of interest, shown in Figure 3.22. Species whose mole fraction are less than 10^{-5} have been omitted. At ambient temperature, $ZnO(s)$ and CH_4 are the thermodynamically stable components. At around 800 K, CH_4 decomposes into $C(gr)$ and H_2. Over a small temperature range between 1000 and 1200 K, $ZnO(s)$ is reduced to Zn. $C(gr)$ is gasified by CO_2 and H_2O to form H_2 and CO, equations (3.79) and (3.80) respectively. When the reduction goes to completion, at above 1200 K, the system consists of a single gas phase of Zn and a 2:1 mixture of H_2 and CO.

An interesting feature of this system is that Zn is produced in the vapor phase, which permits winning the metal from its oxide by distillation in a very refined form. The separation of $Zn(g)$ from the syngas mixture is simply accomplished by condensing the product gases below its boiling point, 1180 K. Once free of any zinc, the syngas mixture may be cooled to ambient temperatures (by using heat exchangers to pre-heat reactants, or by expansion in a gas turbine to produce mechanical work, and that way recuperate some of the 63 kJ/molar-mixture of sensible heat in the products) and without fear of unwanted recombination between H_2 and CO because the reverse, methanation, reaction does not occur in the absence of a catalyst.

In practical industrial reactors, especially those operated in continuous mode, it is improbable that the process ever achieves the equilibrium conditions predicted by thermodynamics. Thus, the kinetics determine the final product composition. The following section presents the rates of the overall reaction and its dependence on temperature and CH_4 concentration.

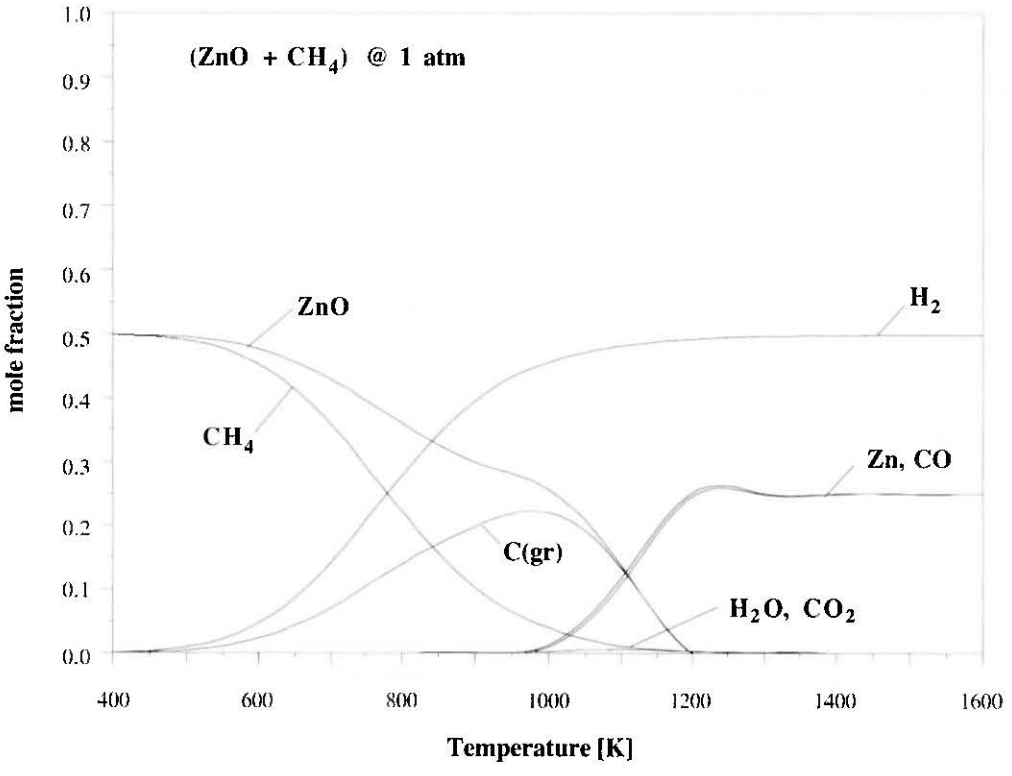

Figure 3.22 Equilibrium composition of the major components of the system $ZnO + CH_4$ at 1 atm., computed using NASA-CET85 code [Gordon and McBride, 1976]. Species whose mole fraction are less than 10^{-5} have been omitted [Steinfeld *et al.*, 1995a].

3.4.4.2 Thermoanalytic Experiments

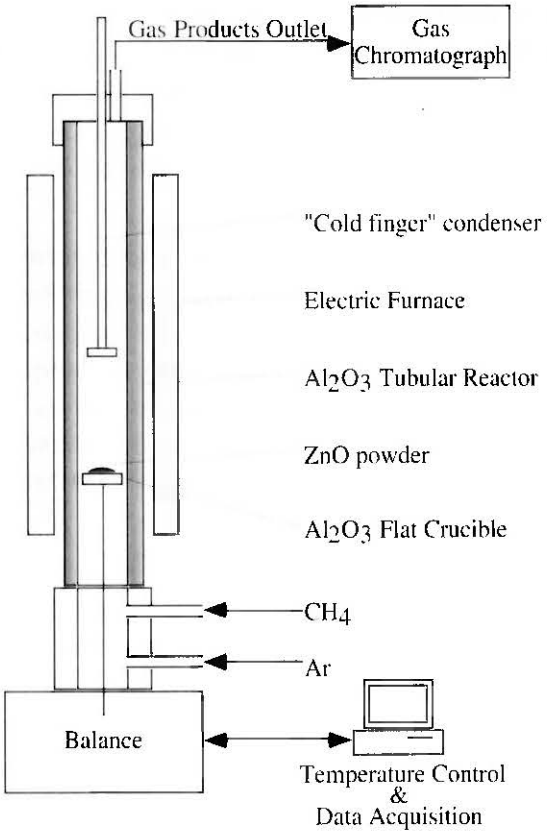

Figure 3.23 Experimental set-up of the thermogravimetric measurements [Steinfeld *et al.*, 1995a].

Thermogravimetric measurements were conducted using a *Netzsch* TASC-419 thermobalance. The experimental set-up is schematically depicted in Figure 3.23. The furnace consisted of an electrically heated Al_2O_3 tube, 3 cm-diameter, which contained a quartz "cold-finger" condenser for trapping *Zn* vapor. *ZnO* powder samples (*Merck* Art. 8849, mean particle size 1.2 μm) of about 30 mg were loaded on an alumina flat holder and placed in the thermobalance. Samples were first heated to the desired temperature under a flow of argon and then isothermally reduced to *Zn* under a flow of CH_4-*Ar* at slightly above atmospheric pressure. Various concentration of CH_4 in *Ar* were used in the reducing gas. Gas flow rate was 100 ml_N/min.

The reduction extent, α, was measured by the loss in weight of the sample, recorded every 10 seconds. Thermogravimetric results (α-curves) are presented in Figure 3.24 and Figure 3.25. In Figure 3.24, α is plotted as a function of time for 5% CH_4-*Ar* reducing gas; temperature is the parameter. In Figure 3.25, α is plotted vs. time for 1273 K; concentration of CH_4 in the reducing gas is the parameter. Both graphs show the

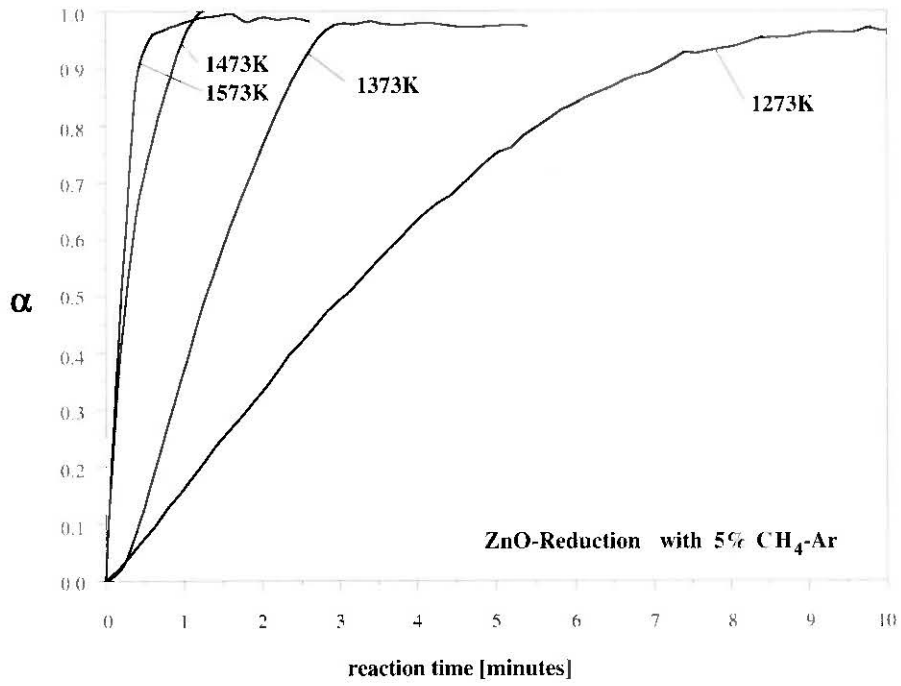

Figure 3.24 Extent of the reduction α vs. time for the reduction of ZnO with 5% CH_4-*Ar* reducing gas; temperature is the parameter [Steinfeld *et al.*, 1995a].

progress of the reaction for the first 10 minutes, time 0 being the instant when the reducing gas was introduced into the furnace chamber.

The same pattern is observed in all curves: a monotonically increasing function with slight negative concavity until completion. X-ray powder diffraction of solid products showed complete reduction to Zn in all cases. The fact that no curve reaches $\alpha=1$ (α calculated from the percentage weight loss of solid reactants) is due to some carbon deposition from CH_4-cracking at the hot crucible, equation (3.76). Although carbon deposition is thermodynamically favorable at temperatures below 1200 K (see Figure 3.22), it is unlikely that this reaction ever goes to a state of equilibrium because the kinetics are usually slow and requires the nucleation of carbon on some catalytic site. The presence of freshly formed zinc might under certain conditions weakly catalyze the CH_4 cracking reaction. Indeed, some carbon was detected (by X-ray diffraction) with the zinc collected at the condenser. At the alumina crucible, the extent of carburization at the most reached 2% of the initial weight.

The mechanism of the reduction may be described by applying a model for shrinking spherical particles because a ZnO particle shrinks during the reaction and finally disappears. In this model, the basic mechanism involving both physical transport and chemical reaction kinetics consists of three steps [Levenspiel, 1972]:

1. gaseous reactant diffusion through the gas boundary layer (film) surrounding the particle;
2. gas-solid interfacial chemical reaction at the surface;
3. gaseous product diffusion through gas film to the exterior into the main gas stream.

This simplistic model does not consider the rates of heat transfer across the solid-gas boundary layer[5], but it reasonably represents the reduction of ZnO in reducing atmospheres such as CH_4, CO, and H_2 [Levenspiel, 1972; Grunze, 1981; Guger *et al.*, 1971]. It does not describe the mechanism of CH_4-cracking and -reforming reactions over ZnO (adsorption-desorption phenomena), nor does it for $C(gr)$-nucleation or $C(gr)$-ZnO solid-solid reactions. The shape of the α-curves

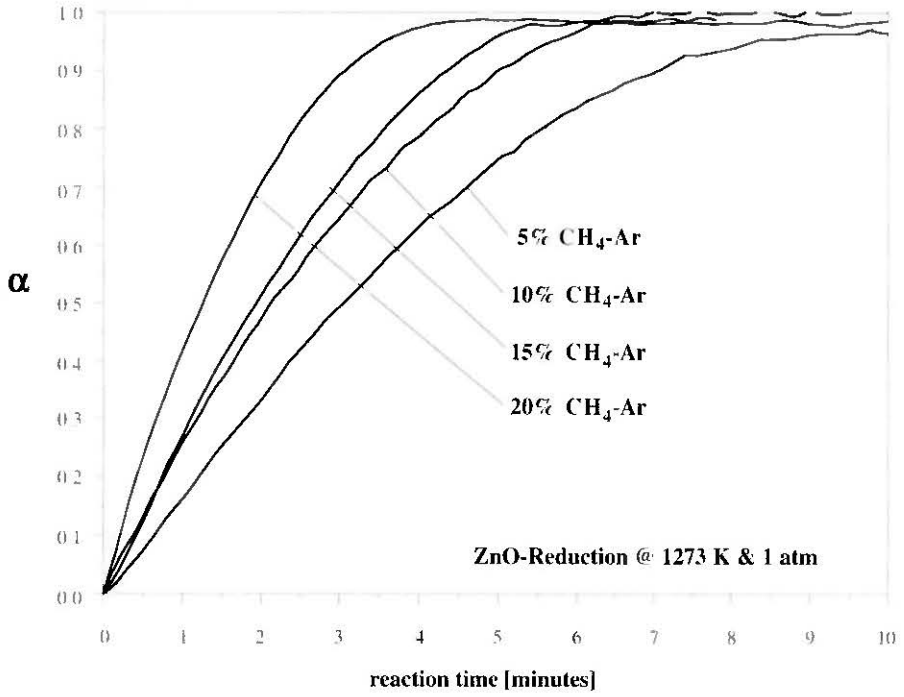

Figure 3.25 Extent of the reduction α vs. time for the reduction of ZnO at 1273 K; concentration of CH_4 in the reducing gas is the parameter [Steinfeld *et al.*, 1995a].

indicates that the rate is apparently controlled by gas film diffusion in the Stokes regime[6], but may also be a result of a mixed-rate controlling step. This result cannot necessarily be extrapolated for situations with different particles sizes under different flow regimes because, while film diffusion through stagnant gas is likely to be of large influence in packed bed reactors, such resistance would be negligible in fluidized-bed reactors.

A cross plot of Figure 3.25 (Figure 3.26) shows the variation of α with CH_4-concentration at 2, 3, and 4 minutes reaction time. The reduction extent is linearly proportional to CH_4 partial pressure between 0.05 and 0.20 bars, supporting a gas diffusion rate-controlling step for the given experimental conditions.

The temperature dependency of the overall reduction rate is given by Arrhenius law: $k = k_0 \exp(-E_a/RT)$. The frequency factor, k_0, may be also temperature dependent, but this effect has been neglected. The apparent activation energy, E_a, is determined by plotting $\ln(d\alpha/dt)$ versus $1/T$ and fitting a linear regression through the points, as shown in Figure 3.27 for $\alpha = 0.5$. From the slope we obtained E_a = 146 kJ/mol. This value is somewhat higher than the ones obtained for the reduction of ZnO powders with H_2 and CO, 114 to117 kJ/mol [Grunze, 1981; Grunze *et al.*, 1974].

The outlet gas composition was quantitatively analyzed at certain intervals by gas chromatography on an HP-5890 GC, using a *Supelco Carboxene*-1000 column, helium as carrier gas, and a thermoconductivity detector. Figure 3.28 shows the gas-phase mole fraction of CH_4, H_2, CO, CO_2, and H_2O in the outlet gas (argon not accounted) as a function of reaction time for the runs at 1273 K and 5% CH_4-Ar. The H_2O mole fraction is calculated from the mass balance. For the given gas-flow rate, about 25% of CH_4 is converted at 1273 K and the remainder leaves the furnace unreacted[7]. The CH_4 conversion increases with temperature; it is 51% at 1373 K, 84% at

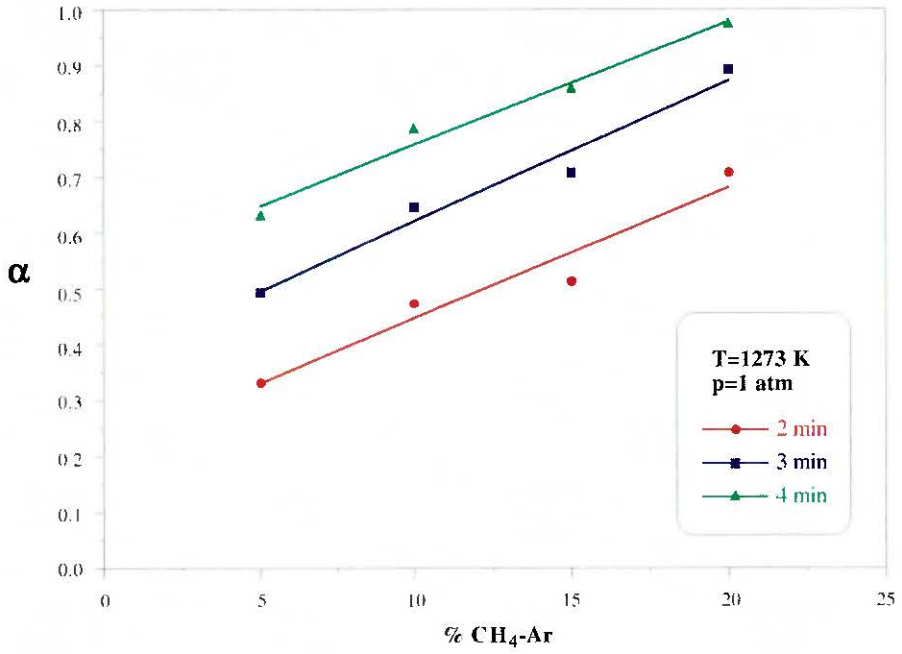

Figure 3.26 Extent of the reduction α vs. concentration of CH_4 in the reducing gas for the reduction of ZnO at 1273 K and 1 atm. [Steinfeld *et al.*, 1995a].

5. Heat transfer mechanisms are irrelevant in our laboratory experiments conducted under well-controlled isothermal conditions. In real industrial reactors, and especially in solar driven reactors, the rates of energy transport are important.
6. Mass transfer coefficient inverse proportional to the particle diameter.
7. The degree of CH_4 conversion is calculated as $[(1-x)/(2x+1)]$, where x is the CH_4 mole fraction.

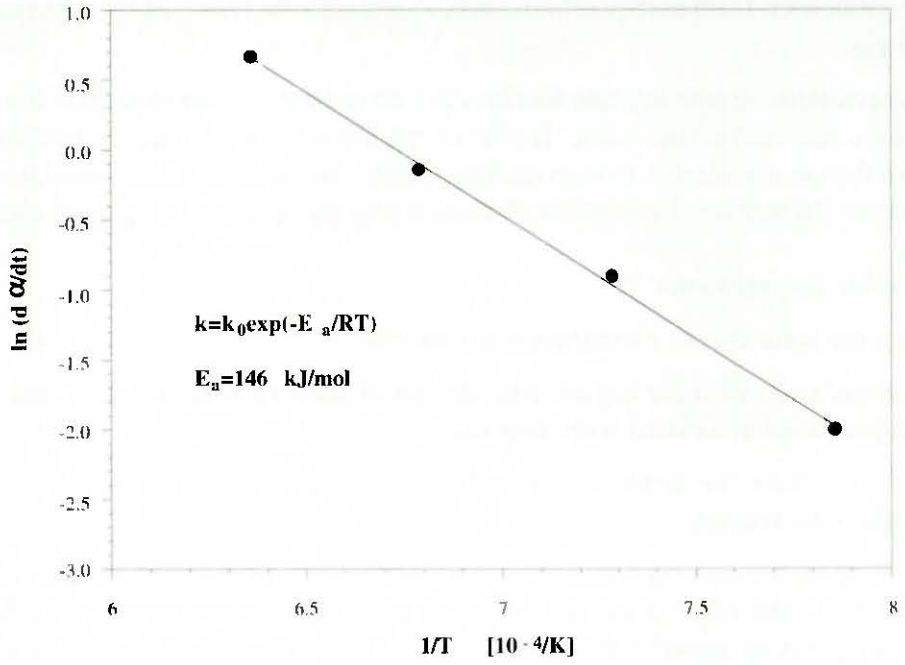

Figure 3.27 Arrhenius plot for the reduction of *ZnO* powder with 5% CH_4-*Ar*, at $\alpha = 0.5$ [Steinfeld *et al.*, 1995a].

1473 K, and almost 100% at 1573 K. Consequently, also the H_2-yield increases with temperature and reaches about 65% mole fraction at 1573 K, which is close to the thermodynamic equilibrium level of 67%. At all four temperatures, *CO* concentration is predominant over CO_2, as predicted by the equilibrium based calculations. A molar ratio of $H_2/CO > 2$ may be the result of CH_4-cracking occurring at the *Zn* surface, as evidenced by some *C(gr)* found with the *Zn* col-

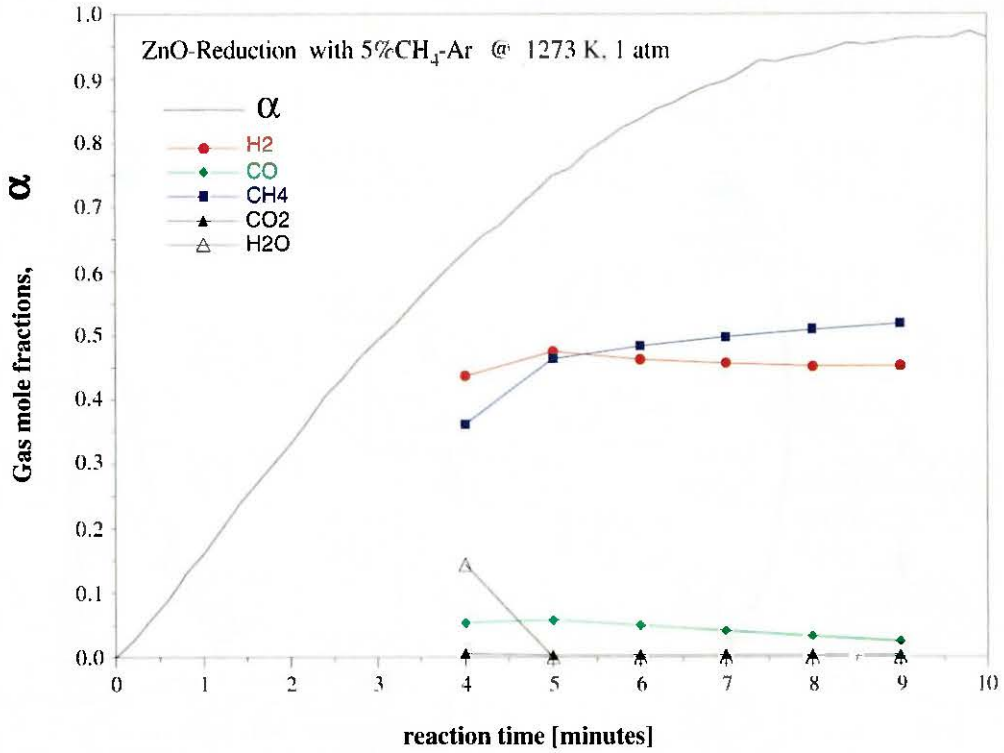

Figure 3.28 Outlet gas composition and α during the reduction of *ZnO* at 1273 K with 5% CH_4-*Ar* [Steinfeld *et al.*, 1995a].

lected in the condenser. Carbon deposition could in principle be removed by injecting H_2O with the reducing gas.

The thermogravimetric results indicate that kinetics do not prevent the reduction from achieving completion on a reasonable time scale. However, no attempts were made to optimize the conditions for maximum conversion to high quality syngas. Nevertheless, we found it important to next demonstrate the technical feasibility of conducting the reaction using solar energy.

3.4.4.3 Solar Experiments

We conducted the solar-driven experiments in order to

1. acquire experience with the engineering design of solar receiver-reactors and learn about practical problems associated with their use;
2. and to demonstrate the technical feasibility of conducting the $ZnO + CH_4$ reaction in a small-scale solar reactor.

The system components and experimental set-up at the solar furnace are shown schematically in Figure 3.29. The solar receiver-reactor system is schematically shown in Figure 3.30. The reactor is a 2 cm-diameter quartz tube containing a fluidized-bed. A 2-dimensional secondary concentrator [Welford and Winston, 1989], composed of a *CPC* (compound parabolic concentrator) and an involute, provides uniform irradiation on the tubular reactor periphery and boosts concentration by a factor of about 1.3. Its design is described in the Appendix of this Section 3.4.4. The receiver/reactor was placed with its axis perpendicular to the axis of the solar concentrator. The entrance of the *CPC* is positioned at the focal plane and re-directs incident radiation into the reactor. With this arrangement, the fluidized-bed virtually intercepts directly or after a single reflection all of the incoming power, providing very efficient heat transfer directly to the reaction site where the energy is needed. In contrast to conventional heavily insulated cavity-receivers, this design offers very low thermal capacitance, good thermal shock resistance, and adaptability to direct absorption processes.

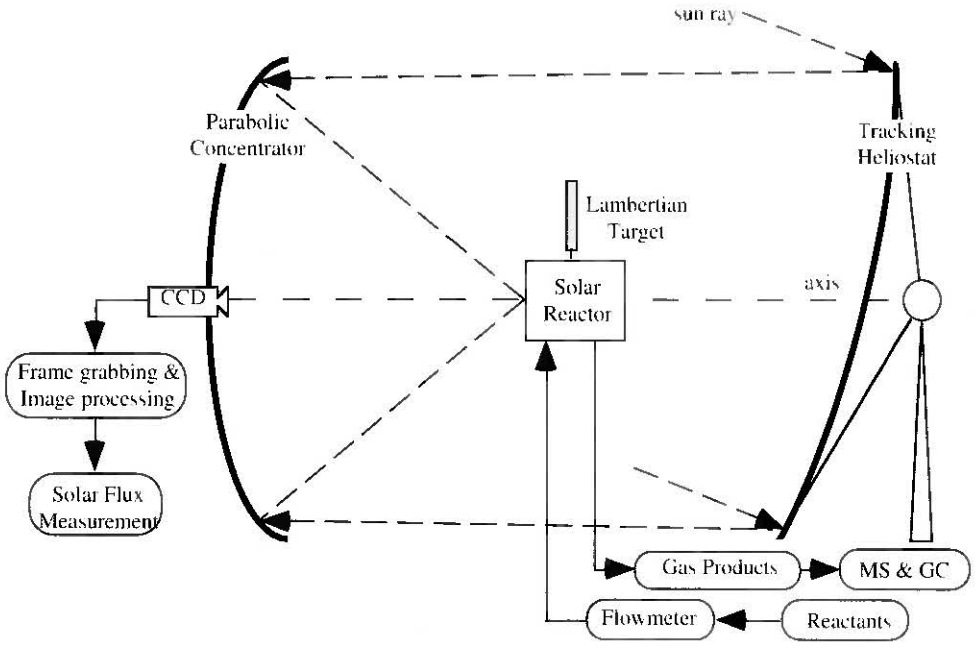

Figure 3.29 Experimental set-up of the solar experiments [Steinfeld *et al.*, 1995a]. The dimensions are not to scale.

The fluidized-bed, operated under vigorous bubbling conditions, was likely to be at uniform temperature. The nominal bed temperatures reported here were measured with a thermocouple type K in an Al_2O_3 protection tube, submerged in the fluidized-bed and not exposed to the direct irradiation. Power flux intensities coming from the concentrator were measured optically by recording the image of the sun on a white *Lambertian* target with a *CCD* camera. The camera was calibrated by simultaneously measuring the flux density with a Kendall point radiometer. The *CCD* camera was also used to continuously monitor the position of the *CPC* entrance relative to the flux map. That way we could optimize the positioning in order to intercept the regions of maximum flux intensity, or, alternatively, move the receiver to regions of lower flux intensity and have an indirect control on the temperature. The composition of the product gases was qualitatively monitored with a mass spectrometer (*Balzers* Quadropol-500) and quantitatively analyzed by gas chromatography (*HP*-5890) during the experimental run. Solid products collected after the experimental run were analyzed by x-ray powder diffraction (Siemens-D500). Data acquisition and recording was made via an *ACRO* data logger which allowed real time displaying of the parameters measured.

A mixture of *ZnO* powder (*Merck* Art. 8849, mean particle size 1.2 μm) and alumina grains (*Merck* Art. 13109, mean particle size 1 mm) in a ratio 1:1 by weight was dried in order to prevent sintering and help fluidization. A charge of 10 grams was loaded in the reactor, fluidized in 1 l_N/min of argon at slightly above ambient pressure and exposed to the direct irradiation. A large portion of the incoming power was blocked with the shutter to prevent overheating. The mean solar flux at the *CPC* entrance was 44 W/cm^2; the total incident power was about 2.9 kW. Assuming a *CPC* concentration of 1.3, the fluidized particles were exposed to flux intensities of about 570 suns. At any given moment, only the outer layer of particles is directly irradiated. A detailed heat transfer modeling of such fluidized-bed reactor system is given in [Sasse and Ingel, 1993]. The low thermal inertia of the system permitted the reactor to attain high temperatures quickly. When the bed temperature attained approximate steady state conditions at the desired temperature, the flow was then switched to 1 l_N/min of 10% CH_4-*Ar*. After about 30 minutes, when practically no *CO* was detected in the product gases by *MS* and *GC* (which indi-

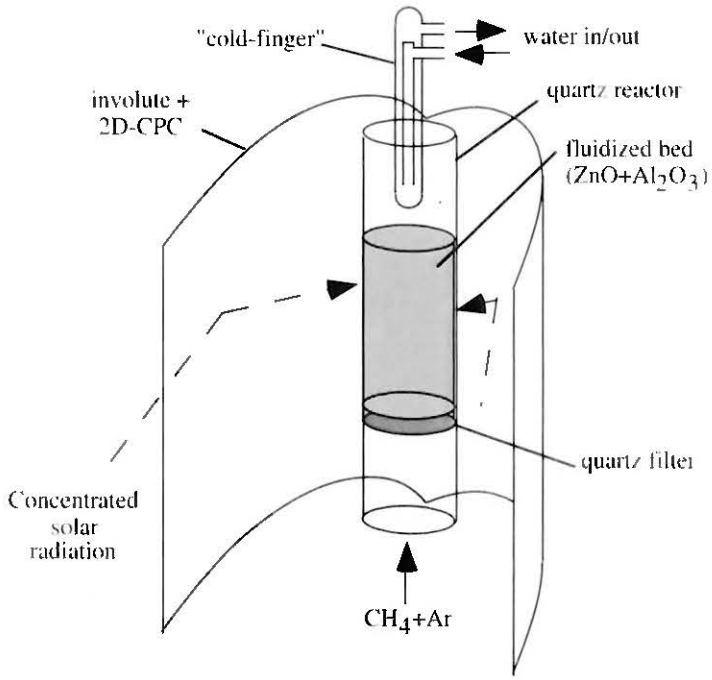

Figure 3.30 Scheme of the solar receiver-reactor configuration and secondary concentrator [Steinfeld *et al.*, 1995a].

cates complete reduction), the reactor was removed from the focus. Finally, the reactor was cooled to ambient temperature under pure argon. The solid products collected at the cold-finger consisted mostly of *Zn* in a sponge structure, but also some *ZnO* was found. The particles remaining at the fluidized-bed were the original charge of Al_2O_3 grains and some *ZnO* which did not dissociate. No carbon deposition was detected either in the cold finger nor in the fluidized bed. However, some negligible amounts of carbon, probably from the CH_4-cracking, might have been deposited in the fluidized bed close to the end of the run, as evidenced by the greyish color of the Al_2O_3 grains. Figure 3.31 shows the fluidized bed temperature and the outlet gas composition measured by mass spectroscopy (*MS*) and gas chromatography (*GC*), as a function of reaction time during a solar test[8].

An increase in the bed temperature is accompanied by an increase in the CH_4 conversion, H_2 and *CO* yield. For the given gas-flow rate, a maximum of 43% of the CH_4 in the reducing gas is converted; the remainder leaves the fluidized bed unreacted. Small amounts of CO_2 and H_2O were observed among the outlet gases and their formation might have been the result of the methanation and water-gas shift reactions (3.77) and (3.78), occurring close to the cold finger condenser, where temperatures were thermodynamically favorable and reactions could have been catalyzed by metallic zinc. As the fluidized bed becomes smaller, so does the syngas yield. After about 30 minutes, almost all *ZnO* has been dissociated.

The use of methane-reforming catalysts, such as *Ni*, *Pt* or *Rh*, will most probably result in higher rates of reaction, but their use would be subjected to the feasibility of recovering them from the

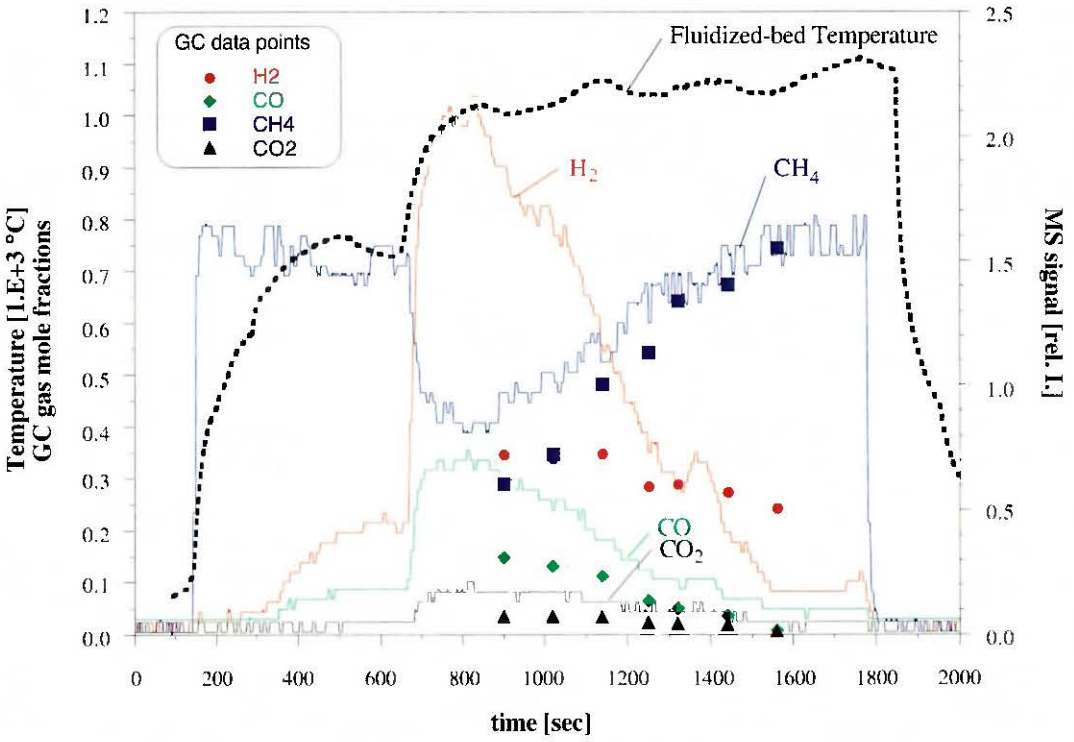

Figure 3.31 Fluidized bed temperature and outlet gas composition history during a solar test [Steinfeld *et al.*, 1995a]. The solid lines are the *MS* signals in arbitrary units. The data points correspond to the mole fractions measured by *GC* (*Ar* not accounted).

8. While the solid reactants reside in the reaction zone for as long as the experiment runs (about 30 minutes until complete reduction), the gaseous reactants flow through the fluidized-bed in 1.5 seconds. The product gas composition depends on the solid composition, but the progress of the *ZnO*-reduction is not monitored (*TG* measurements cannot be implemented in this experimental apparatus). Derivation of kinetic equations under these experimental conditions is difficult.

products. In addition, an increase in the inlet gas flow rate leads to an increase in the reduction rate but to a decrease in the methane conversion. Complete conversion of methane to syngas may be achieved if the fluidized bed is operated under reacting gas starvation and the effluent gases are recirculated through the bed.

3.4.4.4 H_2O-Splitting or Zn-Air Battery Recycling Scheme

As a H_2O-splitting reaction, Zn is reacted with water at moderate temperatures to regenerate ZnO and form H_2 as the only product component in the gas phase. Preliminary experimental studies have shown that such reaction proceeds quickly at 723 K and is exothermic ($Zn + H_2O = ZnO + H_2$, $\Delta H^\circ_{723K} = -107$ kJ/mol). Alternatively, Zn may be used instead to directly produce electrical work in a Zn-Air battery ($Zn + 0.5\ O_2 = ZnO$; $\Delta G^\circ_{298} = -316$ kJ/mol). Thus, an open scheme for syngas and H_2/electricity production is given in the diagram Figure 3.32.

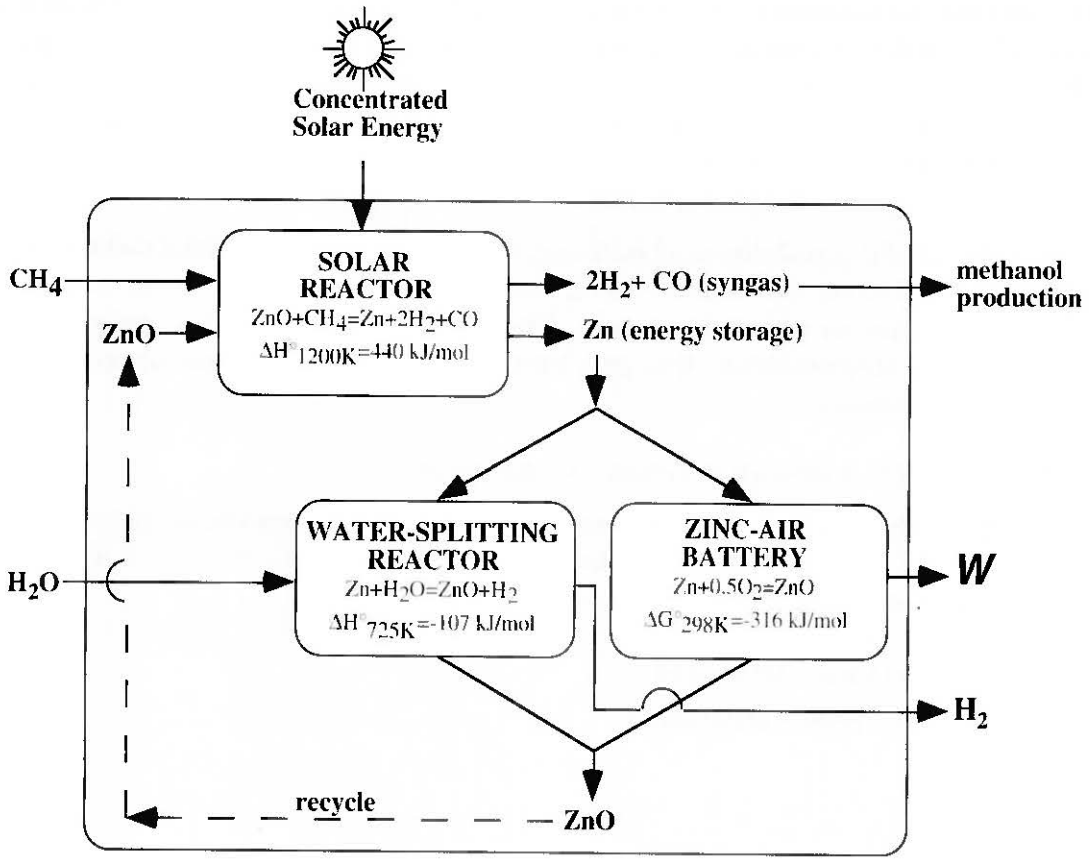

Figure 3.32 Representation of a syngas and H_2/electricity producing scheme [Steinfeld *et al.*, 1995a].

It consists of two steps:

1. ZnO is reduced with CH_4 to form Zn and syngas in the first, solar step by supplying about 440 kJ/mol at 1200 K; syngas (a 2:1 mixture of H_2 and CO) is fed to a conventional methanol producing plant.

2. a) Zn is oxidized back with H_2O to form H_2 in the second step, or alternatively
   b) Zn is oxidized in a Zn-Air battery to produce electrical work in the second step. In either 2a or 2b case, ZnO is recycled to the first step. The advantage of the proposed two-step scheme over the conventional steam reforming of methane lies on the intermediate storage of energy in Zn, as a compact and easy transportable solid fuel, and the subsequent flexibility of its utilization either to produce pure H_2, or to manufacture Zn-Air batteries.

3.4.4.5 Summary and Conclusions

We have examined the thermodynamics of the reduction of *ZnO* with CH_4. At 1200 K and 1 atm., the components in equilibrium consist of *Zn* (vapor) and a 2:1 mixture of H_2 and *CO*. The reaction is highly endothermic, about 440 kJ/mol *ZnO* reduced. We conducted thermogravimetric and gas-chromatographic measurements on this system using an electric furnace and a cold finger condenser to trap *Zn* vapor. The reaction mechanism was found to be complicated by side reactions of the synthesis gas system and the product gas composition was strongly dependent on temperature. CH_4 conversion and H_2 yield increased with temperature, and the reduction extent increased linearly with CH_4 concentration in the reducing gas. Carbon deposition at the crucible was negligible. However, CH_4 cracking occurred at the zinc surface, as evidenced by some *C(gr)* found together with the *Zn* collected in the cold-finger condenser, and by the ratio $H_2/CO > 2$ measured in the outlet gas composition. In general, the kinetics do not prevent the reduction of achieving completion on a reasonable time scale. Further work is needed to optimize the operating conditions for maximum conversion to high quality syngas. We have also demonstrated the technical feasibility of conducting such process using solar energy as the source of process heat. We used a tubular quartz reactor coupled to a *CPC*, containing a fluidized bed of *ZnO* particles and CH_4, operated at 1373 K and under uniform solar flux of 57 W cm^{-2}. The reactor-receiver system exhibited very low thermal inertia, good thermal shock resistance, and proved to be well adapted for direct absorption processes.

Our results indicate the possibility of eliminating CO_2 emissions in the production of *Zn* via a solar combined *ZnO*-reduction/CH_4-reforming process where the collection of the exhaust gases (syngas) is justified on economic grounds. The proposed thermochemical recovery of *Zn* from *ZnO* offers an environmental clean path for recycling zinc-air batteries, or producing H_2 in a water-splitting scheme.

APPENDIX: The CPC + Involute Secondary Concentrator.

The following development is for the 2-dimensional *CPC*. For cartesian coordinates centered at the center of the circular collector, the parametric equations of the 2-dimensional *CPC* + involute concentrator system [Sasse *et al.*, 1993] is given by:

$$\begin{cases} x = r(\sin\theta - M(\theta)\cos\theta) \\ y = r(-\cos\theta - M(\theta)\sin\theta) \end{cases} \tag{3.84}$$

where

$$M(\theta) = \begin{cases} \theta & \text{for} \quad 0 \le \theta \le \dfrac{\pi}{2} + \theta_a \\ \dfrac{\dfrac{\pi}{2} + \theta_a + \theta - \cos(\theta - \theta_a)}{1 + \sin(\theta - \theta_a)} & \text{for} \quad \dfrac{\pi}{2} + \theta_a \le \theta \le \dfrac{3\pi}{2} - \theta_a \end{cases} \tag{3.85}$$

θ_a is the half acceptance angle of the secondary and is taken equal to the rim angle of the small *PSI* primary parabolic concentrator, 41°. r is the radius of the circular collector and is taken equal to the radius of the tubular reactor, 1 cm. With this arrangement, any ray coming from the primary solar concentrator is redirected by the secondary to the reactor. The concentration is augmented by a factor of $\rho/\sin\theta_a \approx 1.3$, where ρ is the reflectivity of the secondary, about 0.85 for the solar spectrum.

3.4.5 Thermodynamic Analysis of the Co-Production of Zinc and Synthesis Gas

In this section, we present a second-law analysis that assesses the maximum possible efficiency of a solar thermochemical process converting ZnO and CH_4 into Zn and syngas [Steinfeld, *et al.*, 1996a]. We consider a closed cyclic system and one that is open but quasi-cyclic. In the closed system, only energy crosses the system boundaries, whereas energy and mass cross the boundaries of the open system. The two systems enable us to compare possible solar process schemes for extracting power from the chemical products. For each system, we investigate the influence of the operating temperature and pressure on its thermal performance and on the quality of its products. Furthermore, we identify the major sources of irreversibility and link them to the degradation in overall efficiency. The proceeding section presents a theoretical analysis used to evaluate $\eta_{overall}$ for the ZnO-CH_4 solar process.

3.4.5.1 Modeling the Process Flow

The process flow sheet is shown in Figure 3.33. It is an archetypal model which uses a solar reactor, a heat exchanger, a quenching device, a fuel cell, a water-splitter reactor, and a heat engine. An equimolar mixture of $ZnO(s)$ and $CH_4(g)$ is fed into the process at $T_1 = 298$ K and pressure p. The complete process is carried out at constant pressure. In practice, pressure drops will occur throughout the system. If one assumes, however, frictionless operating conditions, no pumping work is required.

Heat Exchanger — The reactants are pre-heated in an adiabatic heat exchanger where some portion of the sensible and latent heat of the products is transferred to the reactants. The reactants enter at T_1 and exit at T_2, while the products enter at T_3 and exit at T_4. The reactants undergo a change in their equilibrium composition as they are heated, but, except for phase changes, the products are assumed to have a frozen composition as they are cooled. Two heat exchanger configurations are considered: parallel flow and counter-current flow. The pinch points[9] of both configurations are determined. If Q_{ex} is the total amount of power transferred from the products to the reactants and η_{ex} the heat recovery factor, then

$$\begin{aligned} Q_{ex} &= \Delta H|_{\text{Reactants @ } (T_1,\, p) \rightarrow \text{Reactants @ } (T_2,\, p)} \\ &= -\Delta H|_{\text{Products @ } (T_3,\, p) \rightarrow \text{Products @ } (T_4,\, p)} \end{aligned} \tag{3.86}$$

$$\eta_{ex} = \frac{Q_{ex}}{\Delta H|_{\text{Reactants @ } (T_1,\, p) \rightarrow \text{Products @ } (T_3,\, p)}} \tag{3.87}$$

The chemical transformations and heat transfer across finite temperature differences during preheating produce the following irreversibilities that are intrinsic to the heat exchanger:

$$\begin{aligned} Irr_{ex} &= \Delta S|_{\text{Reactants @ } (T_1,\, p) \rightarrow \text{Reactants @ } (T_2,\, p)} \\ &\quad + \Delta S|_{\text{Products @ } (T_3,\, p) \rightarrow \text{Products @ } (T_4,\, p)} \end{aligned} \tag{3.88}$$

A process without a heat exchanger will be also considered.

---

[9] These are the limiting points where the temperature of the heating reactants equals the temperature of the cooling products.

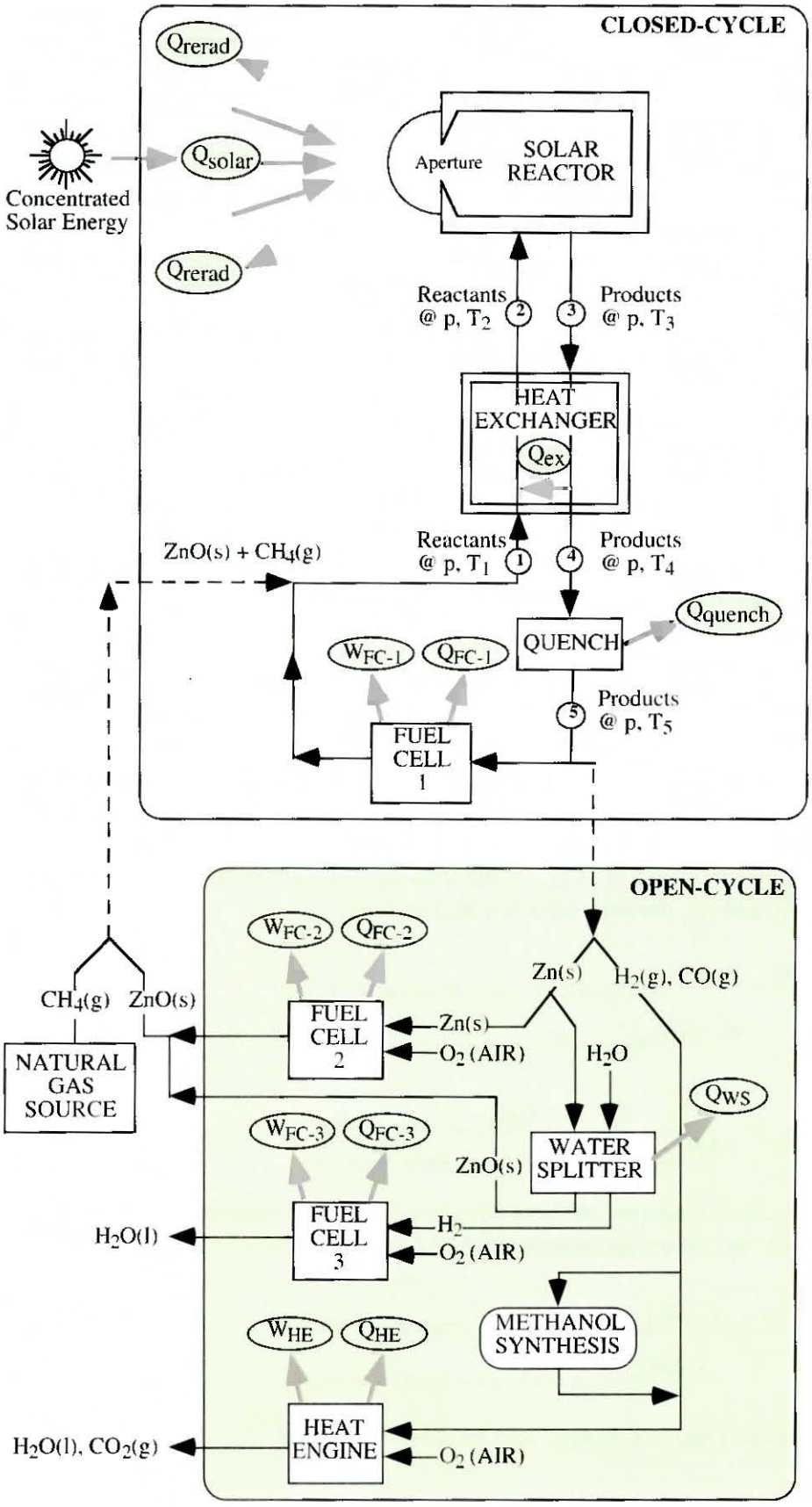

Figure 3.33 The process flow diagram modeling a closed-cycle scheme that recycles all materials and an open-cycle scheme that allows for material flow into and out of the system [Steinfeld *et al.*, 1996a].

Solar Reactor — After being pre-heated, the reactants enter the solar reactor at T_2 and are further heated to the cavity temperature T_{cav}. Chemical equilibrium is assumed inside the reactor. Thus, the reactants undergo a chemical transformation as they are heated to T_{cav}. Q_{solar} is the total power coming from the solar concentrator, as given by equation (3.5). The solar reactor is considered to be a perfectly insulated blackbody cavity-receiver; only radiation losses through the aperture are considered. Q_{rerad} is the power lost by radiation as given by equation (3.3). Radiation gain from the environment is ignored. The net power absorbed in the solar reactor should match the enthalpy change of the reaction, i.e.,

$$Q_{reactor,net} = \Delta H|_{\text{Reactants @ } (T_2,\, p) \rightarrow \text{Products @ } (T_3,\, p)} \tag{3.89}$$

If I, η_{coll}, $\tilde{C}$, T_2, T_3, p, and the mass flow rate are specified, equation (3.89) together with equations (3.2) to (3.8) establish the required collector surface A_{coll} for delivering Q_{solar} to the solar reactor. The irreversibility in the solar reactor arises from the chemical transformation and heat transfer from the sun at 5800 K to the receiver and from the receiver to the surroundings at 298 K. Thus,

$$Irr_{reactor} = \frac{-Q_{solar}}{5800K} + \frac{Q_{rerad}}{298K} + \Delta S|_{\text{Reactants @ } (T_2,\, p) \rightarrow \text{Products @ } (T_3,\, p)} \tag{3.90}$$

Products exit the solar reactor at $T_3 = T_{cav}$. They have an equilibrium composition which will remain unchanged as they are cooled to T_4 in the heat exchanger, except for the phase changes. This assumption is reasonable provided zinc vapor does not catalyze the kinetics of the reverse methanation reaction. Sensible and latent heat released by the products stream are transferred to the reactants stream (see equation (3.86)).

Quench — After leaving the heat exchanger, the products are cooled rapidly to ambient temperature, $T_5 = 298$ K. The amount of power lost during quenching is

$$Q_{quench} = -\Delta H|_{\text{Products @ } (T_4,\, p) \rightarrow \text{Products @ } (T_5,\, p)} \tag{3.91}$$

The irreversibility associated with quenching is

$$Irr_{quench} = \frac{Q_{quench}}{298K} + \Delta S|_{\text{Products @ } (T_4,\, p) \rightarrow \text{Products @ } (T_5,\, p)} \tag{3.92}$$

Quenching is a completely irreversible step causing a significant drop in the system efficiency.

Closed-Cycle Scheme

Fuel Cell — From point 1 to 5 in the flow sheet, the chemical transformation

$$\text{Reactants @ } (298K,\, p) \rightarrow \text{Products @ } (298K,\, p) \tag{3.93}$$

has been effected. At point 5, we could calculate the overall system efficiency by introducing a reversible fuel cell, represented in Figure 3.33 as FUEL CELL #1. In this ideal cell, the products recombine to form the reactants and thereby generate electrical power in an amount W_{FC_1}. Such a fuel cell does not exist and is not likely to become a reality for many years if ever; it is used here only as an intellectual concept for assigning a work value to the reaction products. It allows one to calculate the theoretical maximum available work that could be extracted from the chemical products during recombination. The work of the fuel cell is given by

$$W_{FC\_1} = -\Delta G|_{\text{Products @ } (298K,\, p) \rightarrow \text{Reactants @ } (298K,\, p)} \tag{3.94}$$

The fuel cell operates isothermally; Q_{FC_1} is the amount of heat rejected to the surroundings:

$$\begin{aligned} Q_{FC\_1} &= -298K \times \Delta S|_{\text{Products @ } (298K,\, p) \rightarrow \text{Reactants @ } (298K,\, p)} \\ &= -(\Delta H - \Delta G)|_{\text{Products @ } (298K,\, p) \rightarrow \text{Reactants @ } (298K,\, p)} \end{aligned} \tag{3.95}$$

The overall system efficiency of the closed-cycle is then calculated as

$$\eta_{overall_{CLOSED\ CYCLE}} = \frac{W_{FC\_1}}{Q_{solar}} \tag{3.96}$$

Equation (3.96) allows one to evaluate complex solar thermochemical processes by considering the maximum thermodynamic value of the chemical products as they recombined to form the reactants via an ideal reversible fuel cell. The calculation makes it possible to isolate the solar process and analyze it as a closed cyclic system: a heat engine [Fletcher, 1983]. This heat engine, shown schematically in Figure 3.34, uses reactants and products as the working fluid, exchanges heat with the surroundings, and converts solar process heat into work. This analysis provides an especially useful basis for comparing the efficiencies of different solar processes.

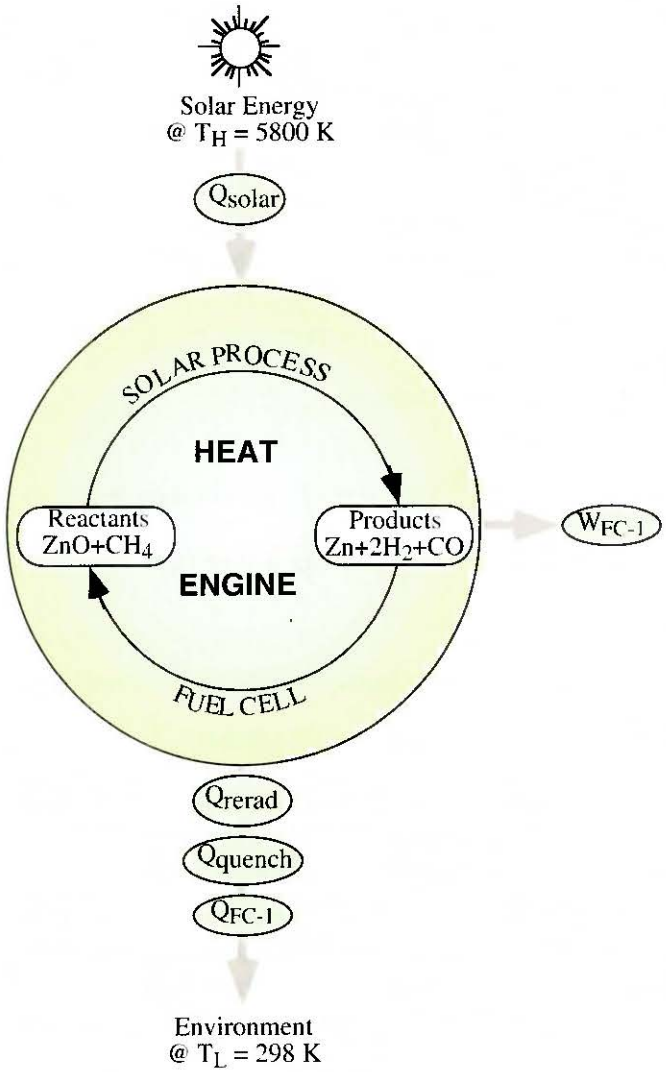

Figure 3.34 The closed-cycle scheme represented as a heat engine [Steinfeld *et al.*, 1996a].

Check — The thermodynamic analysis is verified by performing an energy balance and by evaluating the maximum achievable efficiency (*Carnot* efficiency) from the total available work and from the total power input. The energy balance confirms that

$$W_{FC\_1} = Q_{solar} - (Q_{rerad} + Q_{quench} + Q_{FC\_1}) \tag{3.97}$$

The available work is calculated as the sum of the fuel-cell work plus the lost work due to irreversibilities in the solar reactor, the heat exchanger and quenching. Thus,

$$\begin{aligned} \eta_{max} &= \frac{\sum Work + (T_L \times \sum Irr)}{Q_{input}} \\ &= \frac{W + 298K \times (Irr_{ex} + Irr_{reactor} + Irr_{quench})}{Q_{solar}} \end{aligned} \tag{3.98}$$

This maximum efficiency must be equal to that of a *Carnot* heat engine operating between T_H and T_L, i.e.

$$\eta_{max} = \eta_{Carnot} = 1 - \frac{T_L}{T_H} = 1 - \frac{298K}{5800K} = 0.949 \tag{3.99}$$

Open-Cycle Scheme

Syngas as Fuel — A fuel cell that receives zinc and syngas and produces zinc oxide and methane does not exist. Thus, a pragmatic process using current technologies to extract work from the chemical products is presented in the lower box of Figure 3.33. The products after quenching (point 5 in the diagram) separate naturally into *Zn(s)* and synthesis gas. Therefore, the separation is accomplished without expending work. Syngas, a mixture of primarily H_2 and *CO*, is widely utilized as a feedstock in the chemical industry for the production of synthetic fuels and commodity organic chemicals, as well as a reducing agent in the metallurgical industry (*Mydrex, HYL, Armco, Purofer, Fior*) [Davis *et al.*, 1982]. The syngas mixture obtained in our process has approximately a 2:1 H_2: *CO* molar ratio which makes it particularly suitable for methanol production. Thus, we have chosen to use syngas (or eventually methanol) as a fuel. Its combustion releases heat that is converted to work in our model via a heat engine with an efficiency of $\eta_{heatengine} = 35\%$, which is consistent with the value obtained in conventional power plants. The work output of the heat engine and the heat rejected to the surroundings are, respectively,

$$W_{HE} = \eta_{heatengine} \times \Delta H|_{2H_2 + CO + 1.5O_2 \rightarrow 2H_2O(l) + CO_2} \tag{3.100}$$

$$Q_{HE} = (1 - \eta_{heatengine}) \times \Delta H|_{2H_2 + CO + 1.5O_2 \rightarrow 2H_2O(l) + CO_2} \tag{3.101}$$

Zinc as Fuel — Metallic zinc, the other important reaction product, is currently used primarily as a raw material in the galvanizing industry. However, zinc exhibits various intriguing advantages when considered, not as a chemical commodity, but rather as a solid fuel. Its specific calorific value is 5320 kJ/kg. It can be safely handled in air and may be easily transported. The amount of work that can be extracted from zinc depends upon how it is used. The combustion of zinc in air releases 348 kJ/mol of heat, a portion of which may be converted to work by means of a heat engine, but the efficiency of such conversion is limited by the *Carnot* efficiency. More efficient conversion is possible using a commercially available *Zn*-air battery, or a *Zn*-air fuel cell which is under development [Salas-Morales *et al.*, 1994]. We have chosen to use a *Zn*-air

fuel cell, shown in Figure 3.33 as FUEL CELL #2, since it is not limited by the *Carnot* efficiency. Within the cell, Zn and O_2 (from air) combine electrolytically to form $ZnO(s)$. The process generates W_{FC_2} of work while rejecting Q_{FC_2} of heat to the surroundings

$$W_{FC\_2} = -\Delta G|_{Zn(s)+0.5O_2 \rightarrow ZnO(s)} \tag{3.102}$$

$$Q_{FC\_2} = -298K \cdot \Delta S|_{Zn(s)+0.5O_2 \rightarrow ZnO(s)} \tag{3.103}$$

H_2 as Fuel — Alternatively, Zn can react with water to form molecular H_2, according to

$$Zn(s) + H_2O \rightarrow ZnO(s) + H_2 \tag{3.104}$$

Reaction (3.104) takes place in the WATER-SPLITTER reactor of Figure 3.33. Preliminary experimental studies have shown that this reaction proceeds at about 700 K and is exothermic. The heat liberated could be used in an auto-thermal reactor for conducting the water-splitting reaction at temperatures above ambient conditions. In this study, however, we consider this heat lost to the surroundings, as given by

$$Q_{WS} = -\Delta H|_{Zn(s)+H_2O(l) \rightarrow ZnO(s)+H_2} \tag{3.105}$$

The hydrogen produced in the water-splitter reactor may be used to enrich and adjust the syngas mixture obtained in the solar process; it may be burned in air and the heat of combustion converted into work via a heat engine, or it may be used more efficiently in a fuel cell to generate work directly. Such a cell is represented by FUEL CELL #3 in Figure 3.33. W_{FC_3} is the work output and Q_{FC_3} is the heat rejected to the surroundings. The governing relations are

$$W_{FC\_3} = -\Delta G|_{H_2+0.5O_2 \rightarrow H_2O(l)} \tag{3.106}$$

$$Q_{FC\_3} = -298K \times \Delta S|_{H_2+0.5O_2 \rightarrow H_2O(l)} \tag{3.107}$$

The overall system efficiency of the open-cycle process is the ratio of work output to heat input. The work output is either $W_{HE} + W_{FC\_2}$ or $W_{HE} + W_{FC\_3}$, depending whether Zn is used directly in a fuel cell or to split water. The heat input is Q_{solar} plus the equivalent HHV (High Heating Value) of the methane introduced in the system. Thus,

$$\eta_{overall_{OPEN\ CYCLE}} = \begin{cases} \dfrac{W_{HE} + W_{FC\_2}}{Q_{input}} & \text{for a } Zn/O_2 \text{ fuel cell} \\ \dfrac{W_{HE} + W_{FC\_3}}{Q_{input}} & \text{for a } H_2/O_2 \text{ fuel cell} \end{cases} \tag{3.108}$$

where

$$Q_{input} = Q_{solar} + \Delta H|_{CH_4+2O_2 \rightarrow CO_2+2H_2O(l)} \tag{3.109}$$

3.4.5.2 Results and Discussion

The baseline case is conducted at a constant total pressure of 1 atm. Calculations are also carried out for higher pressures of 3, 5, and 10 atm. preferred by industry. The baseline cavity temperature is taken arbitrarily equal to a value for which the chemical equilibrium mole fraction of $ZnO(s)$ at 1 atm. is less than 10^{-5}, $T_{cav} = 1250K$. Table 3.9 shows the chemical equilibrium composition of the products at the exit of the solar reactor ($T_3 = T_{cav}$), at T_3 = 1250 K and p = 1,

Table 3.9 Chemical equilibrium composition of the products at the exit of the solar reactor, calculated using STANJAN computer code and verified using the NASA-CET85 computer code [Reynolds 1986, Gordon and McBride, 1976]. Species with mole fractions less than 10^{-5} have been omitted.

Species and Conversion	T_3 = 1250 K				T_3 = 1350 K
	p = 1 atm.	p = 3 atm.	p = 5 atm.	p = 10 atm.	p = 10 atm.
CH_4	0.01025	0.02947	0.04715	0.19255	0.04139
$ZnO(s)$	$< 10^{-5}$	$< 10^{-5}$	$< 10^{-5}$	0.15775	$< 10^{-5}$
$Zn(g)$	0.99999	0.99999	0.99999	0.63007	0.99999
$Zn(l)$	$< 10^{-5}$	$< 10^{-5}$	$< 10^{-5}$	0.21218	$< 10^{-5}$
H_2	1.97174	1.91880	1.87010	1.58861	1.88433
CO	0.98724	0.96333	0.94130	0.79893	0.95009
$H_2O(g)$	0.00775	0.02226	0.03559	0.02628	0.00329
CO_2	0.00250	0.00720	0.01154	0.00851	0.00852
H_2 / CO	1.99722	1.99184	1.98671	1.98842	1.98332
CH_4 conversion	98.9%	97.1%	95.3%	80.7%	95.9%
ZnO conversion	99.9%	99.9%	99.9%	84.2%	99.9%

3, 5, 10 atm., and at T_3 = 1350 K and p = 10 atm. Calculations were performed using the STANJAN computer code [Reynolds, 1986] and verified using the NASA-CET85 computer code [Gordon and McBride, 1976]. Species with mole fractions less than 10^{-5} have been omitted.

At 1 atm. and at $T_{cav} \geq 1250$ K, the reaction is nearly complete. At higher pressures, the thermodynamic equilibrium of equation (3.73) shifts to the left, as predicted by *Le Chatelier*'s principle. For example, at 10 atm., the equilibrium composition is shifted such that the reduction of ZnO to Zn only goes to completion at or above 1350 K. Also, at 10 atm. and at 1250K, condensed $Zn(l)$ exists in equilibrium with $Zn(g)$, but it becomes gaseous when the temperature is increased to 1350 K. The H_2: CO molar ratio is slightly altered by the pressure; it is 1.99 at 1 atm. and 3 atm., and 1.98 at higher pressures. A more complete study of the $ZnO + CH_4$ system at 1 atm. and over a wide temperature range can be found in Section 3.4.4.1.

Other baseline conditions include a mean flux concentration ratio of $\tilde{C}$ = 2000, an optical collector efficiency of η_{coll} = 100%, and a typical insolation of I = 900 W/m^2. A concentration ratio of 2000 is within the reach of large-scale solar collection facilities, such as central receivers [Winter *et al.*, 1991]. Calculations were also carried out for $\tilde{C}$ = 4000 and 8000 which can be achieved in parabolic tracking dishes or by using non-imaging secondary concentrators. The baseline mass flow rate is 1 mole/sec of $Zn(s)$ and 1 mole/sec of CH_4 at point 1 of the process flow sheet. Unless otherwise stated, the baseline parameters are used.

Closed-cycle scheme without heat exchanger

Table 3.10 shows the energy balance for a closed-cycle without a heat exchanger, i.e. $T_1 = T_2$ and $T_3 = T_4$. As the operating pressure is increased at constant reactor temperature, $Q_{reactor,net}$ decreases because the enthalpy change between products and reactants is smaller: as the pressure increases, the chemical conversion decreases. $Q_{reactor,net}$ drops by 17% as the pressure is doubled from 5 to 10 atm. A_{coll} and Q_{solar} also drop by 17%. The same applies to Q_{rerad} because $\tilde{C}$ and T_{cav} are kept constant while the reactor aperture becomes smaller [see equation (3.7)],

Table 3.10 Energy balance on the closes-cycle scheme without a heat exchanger. The baseline configuration is used: $\tilde{C}$ = 2000, I = 900 W/m2, $\alpha_{eff} = \varepsilon_{eff} = 1$.

	Energy Balance without Heat Exchanger $T_1 = T_2 = 298$ K, $T_3 = T_4$				
	T_3 = 1250 K				T_3 = 1350 K
	p = 1 atm.	p = 3 atm.	p = 5 atm.	p = 10 atm.	p = 10 atm.
Q_{solar} [kW]	595	590	586	486	619
Q_{rerad} [kW]	46	45	45	37	65
$Q_{reactor,net}$ [kW]	549	545	541	449	554
Q_{quench} [kW]	237	237	238	192	249
Q_{FC_1} [kW]	84	78	74	62	72
$Irr_{reactor} / Q_{solar}$ [K^{-1}]	10.6×10^{-4}	10.2×10^{-4}	9.9×10^{-4}	10.0×10^{-4}	10.3×10^{-4}
Irr_{quench} / Q_{solar} [K^{-1}]	8.3×10^{-4}	8.6×10^{-4}	8.7×10^{-4}	8.3×10^{-4}	8.8×10^{-4}
W_{FC_1} [kW]	228	230	229	195	233
$\eta_{absorption}$ [%]	92.3				89.5
η_{Carnot} [%]	94.9				94.9
$\eta_{overall,ideal}$ [%]	87.6				84.9
$\eta_{overall}$ [%]	38.6	38.9	39.1	40.2	37.8

and consequently the re-radiation losses become smaller. Although $Q_{rerad,net}$ and Q_{solar} vary substantially with the operating pressure, their ratio, i.e. the solar energy absorption efficiency $\eta_{absorption}$, remains constant with pressure, as expected from equation (3.8). But $\eta_{absorption}$ decreases considerably with temperature. When the reactor temperature is raised by 100 K, $\eta_{absorption}$ drops by 3% as a result of the larger re-radiation losses. A simple expression for the direct calculation of the change in $\eta_{absorption}$ as a function of the change in temperature ΔT is given by

$$\frac{1 - \eta_{absorption\ @\ T}}{1 - \eta_{absorption\ @\ T+\Delta T}} = \left(\frac{T}{T + \Delta T}\right)^4 \tag{3.110}$$

The overall system efficiency lies at a level of 39%. It is weakly influenced by the operating pressure, increasing monotonically with pressure in spite of the unfavorable chemical conversion. However, it drops when the temperature is increased from 1250 K to 1350 K. The energy balance and species composition for the closed-cycle scheme are presented schematically in Figure 3.35 for the baseline case.

The irreversibilities in the reactor and during the quench reduce the efficiency from the *Carnot* value. They are produced by heat transfer across a finite temperature difference. Specifically, the reactor at 1250 or 1350 K receives radiant energy from a heat source at 5800 K and rejects a portion of it to a heat sink at 298 K. During the quench, heat transfer takes place between the hot products leaving the reactor and the cold sink. Table 3.10 shows that the reactor produces slightly more irreversibility than the quench. Although one can reduce the reactor irreversibility by increasing the concentration ratio (increasing $\tilde{C}$ improves $\eta_{absorption}$ by reducing the portion of incoming radiation that is re-radiated to the sink) the primary irreversibility is associated with

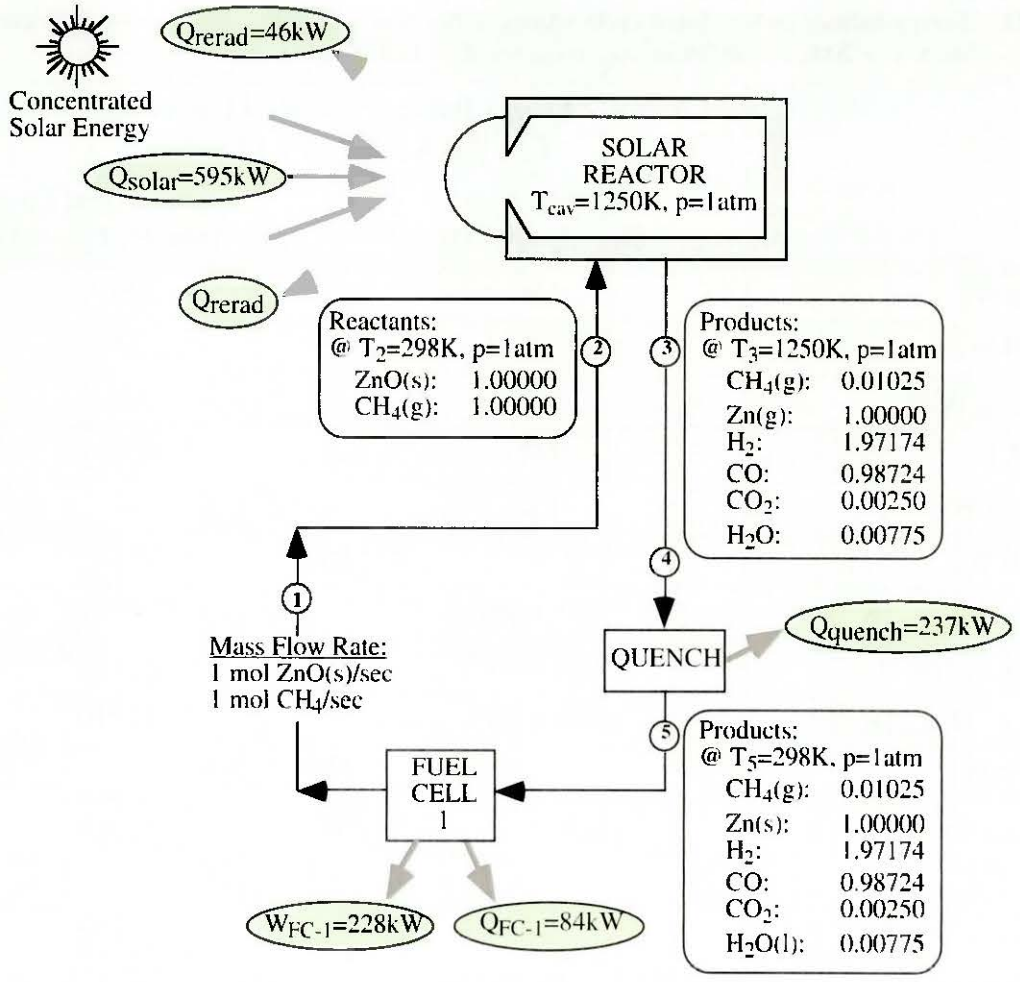

Figure 3.35 Energy balance of the closed-cycle scheme without a heat exchanger [Steinfeld *et al.*, 1996a]. The following baseline parameters are used: $C = 2000$, $I = 900$ W/m^2, $\eta_{eff} = \eta_{eff} = 1$, $T_3 = 1250$ K, $p = 1$ atm.

the heat transfer to the reactor across the temperature difference between T_H and T_{cav}. One may, however, be able to reduce the irreversibility of the quench. For example, if the kinetics permit the products to be cooled with a heat exchanger, one could preheat the reactants going into the solar receiver. Preheating would also reduce the irreversibility in the solar reactor, because less energy would be transferred across the large ΔT between the heat source and the reactor. We thus considered processes that included either a parallel or counter-flow heat exchanger.

Closed-cycle scheme with parallel-flow heat exchanger

Table 3.11 shows the energy balance calculation of the closed-cycle scheme when a parallel-flow heat exchanger is included, i.e. $T_1 = 298$ K $< T_2$, $T_3 = 1250$ K $> T_4$, and, at the limit, $T_2 = T_4$. The results are also presented schematically in Figure 3.36 for the baseline case. Note that the composition of the reactants varies through the heat exchanger as they are heated from point 1 at $T_1 = 298$ K to point 2 at $T_2 = 940$ K. Carbon is found in the equilibrium composition. Although carbon deposition is thermodynamically favorable at temperatures below 1200 K, it is unlikely that it ever reaches a state of equilibrium because the kinetics of carburization are usually slow and require the nucleation of carbon on some catalytic site. The presence of freshly formed zinc might under certain conditions weakly catalyze the CH_4-cracking reaction [Steinfeld *et al.*, 1995a]. The composition of the products remains constant as they are cooled in the heat exchanger, except for the $Zn(g)$ and $H_2O(g)$ that undergo condensation.

Table 3.11 Energy balance on the closed-cycle scheme with a heat exchanger. The baseline configuration is used: $\tilde{C}$ = 2000, I = 900 W/m^2, $\alpha_{eff} = \varepsilon_{eff}$ = 1, T_3 = 1250 K, p = 1 atm.

	Energy Balance with Heat Exchanger T_1 = 298 K < T_2, T_3 = 1250 K > T_4	
	Parallel Flow $T_2 = T_4$ = 940 K	Counter-current Flow T_2 = 1066 K, T_4 = 400 K
Q_{solar} [kW]	448	351
Q_{rerad} [kW]	34	27
$Q_{reactor,net}$ [kW]	414	324
Q_{ex} [kW]	135	225
Q_{quench} [kW]	102	12
Q_{FC_1} [kW]	84	
$Irr_{reactor} / Q_{solar}$ [K^{-1}]	9.31×10^{-4}	9.13×10^{-4}
Irr_{ex} / Q_{solar} [K^{-1}]	1.58×10^{-4}	0.76×10^{-4}
Irr_{quench} / Q_{solar} [K^{-1}]	3.90×10^{-4}	0.14×10^{-4}
W_{FC_1} [kW]	228	
$\eta_{absorption}$ [%]	92.3	
η_{Carnot} [%]	94.9	
$\eta_{overall,ideal}$ [%]	87.6	
η_{ex} [%]	56.9	94.9
$\eta_{overall}$ [%]	50.8	64.9

The temperature at point 2 is found by plotting for the reactants and products streams and arranging both curves as shown in Figure 3.37a. The slope of these curves is $C_{p,mixture}$, the specific heat capacity of the mixture. $C_{p,mixture}$ varies with temperature because the mixture composition, the components' phases, and the C_p of the individual species vary with temperature. ΔH of the reactants varies monotonically with temperature, with a significant gradient in the 1000-1150 K range where most of the reaction occurs. Similarly, the ΔH of the products exhibits a noticeable gradient in the neighborhood of the zinc boiling point (1180 K) due to the heat of vaporization, and a discontinuity at the zinc melting point (692 K) due to the heat of fusion. The intersection of these two curves determines the temperature at the "pinch-point": T_2 = 940 K. Heating the reactants beyond 940 K is not possible because heat cannot flow spontaneously from the colder products to the hotter reactants. The total heat transferred is 135 kW. This recovery amounts to 57% of the sensible and latent heat available in the products. The remainder of the energy is rejected to the surroundings by the quenching. As expected, Table 3.11 indicates that the irreversibilities per Q_{solar} in the reactor and during cooling are reduced by means of the heat exchanger. These improvements increase the process efficiency by 12%.

Closed-cycle scheme with counter-current-flow heat exchanger

Table 3.11 also shows the energy balance calculation when a counter-current-flow heat exchanger is included, i.e. T_1 = 298 K < T_2, T_3 = 1250 K > T_4, and, at the limit, $T_1 = T_4$. Analogous to the parallel-flow, the exit temperatures are found by plotting ΔH = f(T) for the reactants and

products streams and arranging both curves as shown in Figure 3.37b. A pinch point forces the products exit temperature to be no less than 400 K. The exit temperature of the reactants stream is found graphically in Figure 3.37b or analytically by solving equation (3.86). It yields T_3 = 1066 K. Most of the sensible and latent heat available in the hot products, about 225 kW, could in principle be transferred to pre-heat the reactants. The heat recovery factor reaches 95%. In practice, such high recovery efficiency cannot be achieved because of the finite dimensions

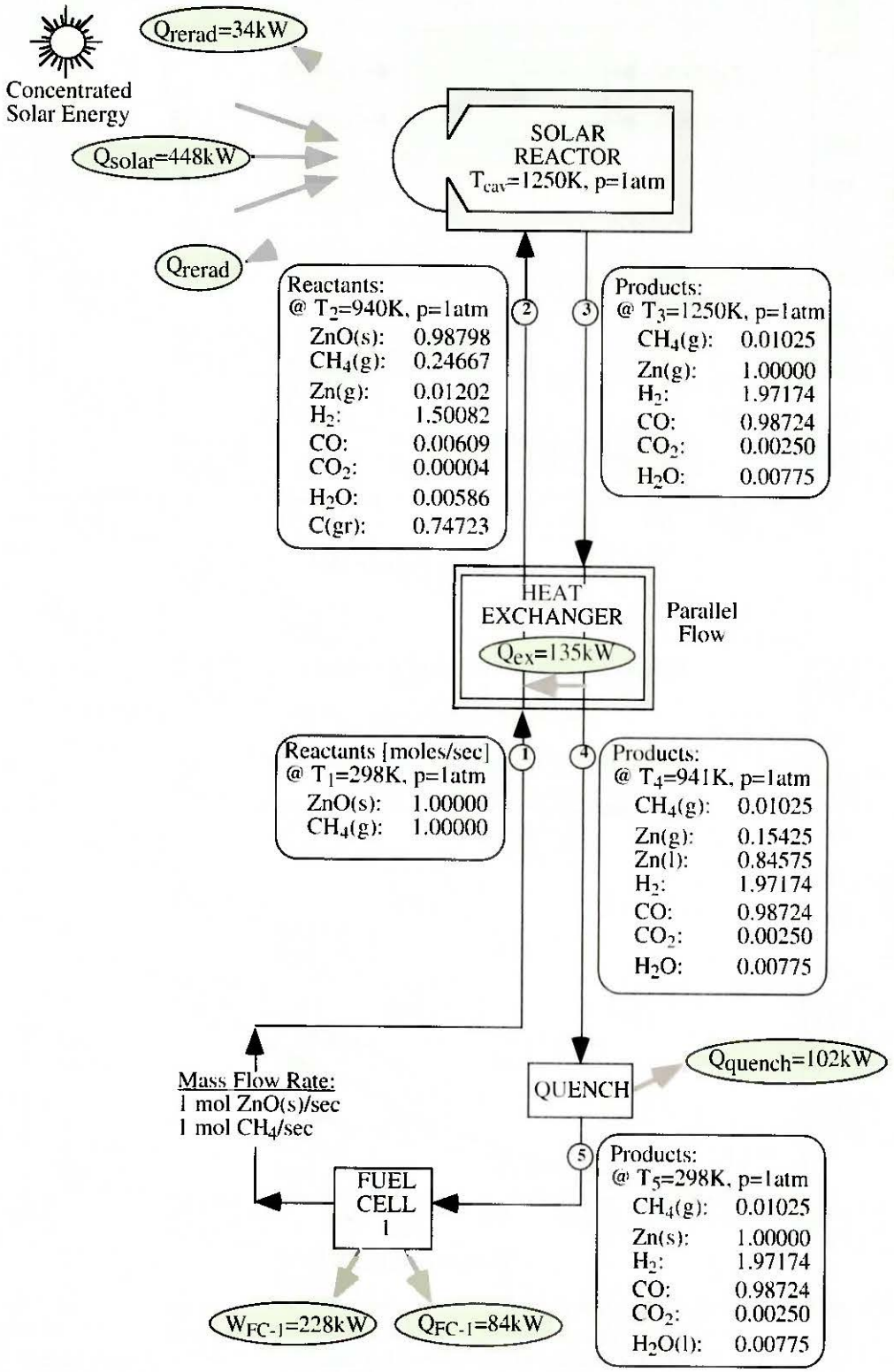

Figure 3.36 Energy balance of the closed-cycle scheme when a parallel flow heat exchanger is employed [Steinfeld *et al.*, 1996a]. The baseline parameters are used.

of the heat exchanger and because the rate of heat transfer approaches zero when ΔT across the counter-current flows is small. Nonetheless, the counter-current flow heat exchanger offers a significantly higher heat recovery factor than that attained for the parallel flow heat exchanger.

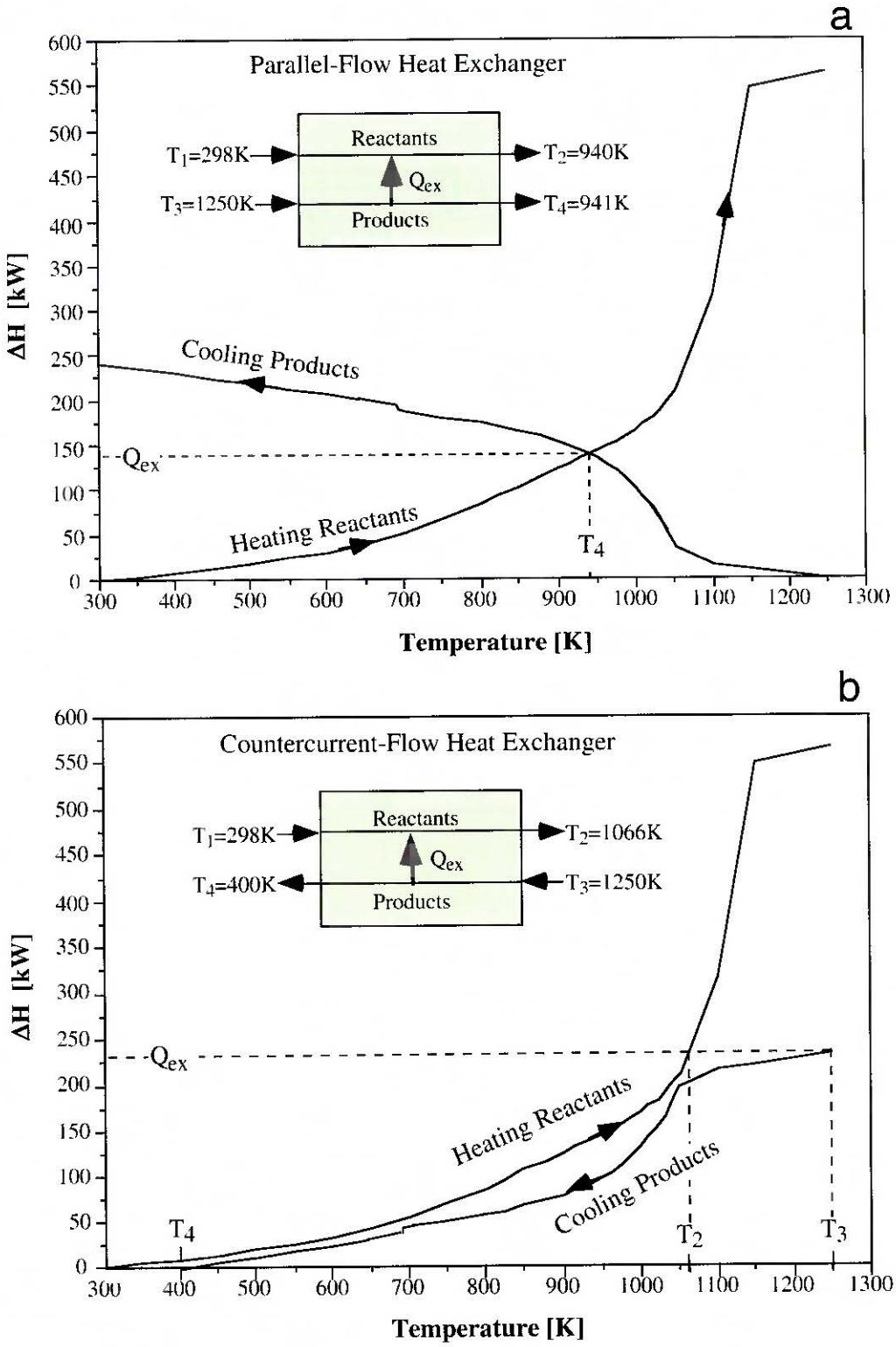

Figure 3.37 Enthalpy change as a function of temperature for the reactants and products [Steinfeld *et al.*, 1996a]. The reactants undergo a change in their chemical equilibrium composition as they are heated. The composition of the products remains constant as they are cooled, except for phase changes. The inlet and outlet temperatures and the heat transferred are shown in a) for the parallel flow heat exchanger and in b) for the counter-current flow heat exchanger.

The overall cycle efficiency is 65%, which is 14% higher than the efficiency obtained for the parallel flow heat exchanger and 26% higher than that obtained without a heat exchanger. The energy balance and species composition for a closed-cycle scheme with a counter-current flow heat exchanger are presented schematically in Figure 3.38.

The effect of the solar concentration on the overall efficiency is shown in Figure 3.39, for the closed-cycle scheme with and without heat exchanger. Obviously, the higher the concentration,

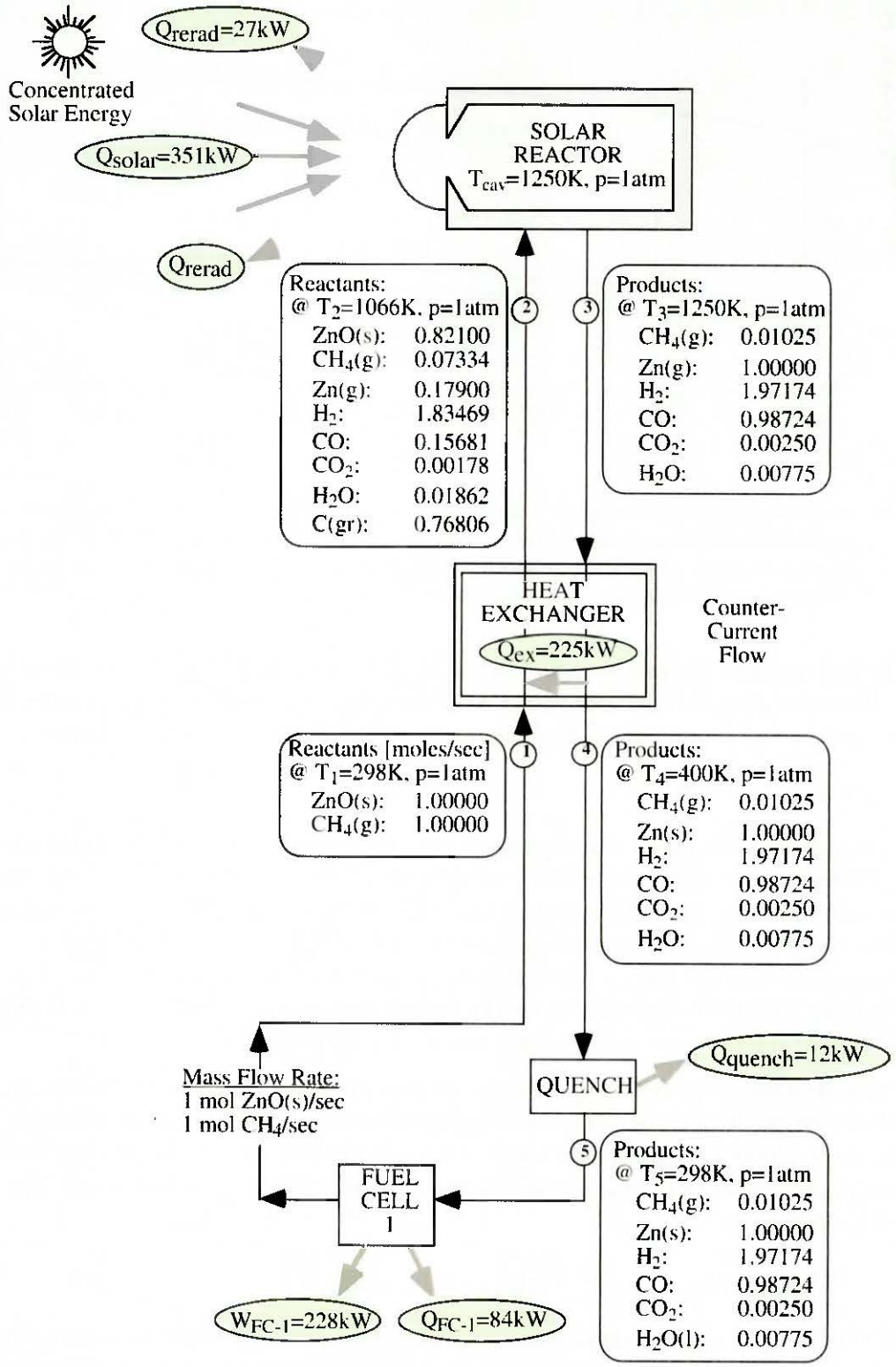

Figure 3.38 Energy balance of the closed-cycle process when a counter-current flow heat exchanger is employed [Steinfeld *et al.*, 1996a].The baseline parameters are used.

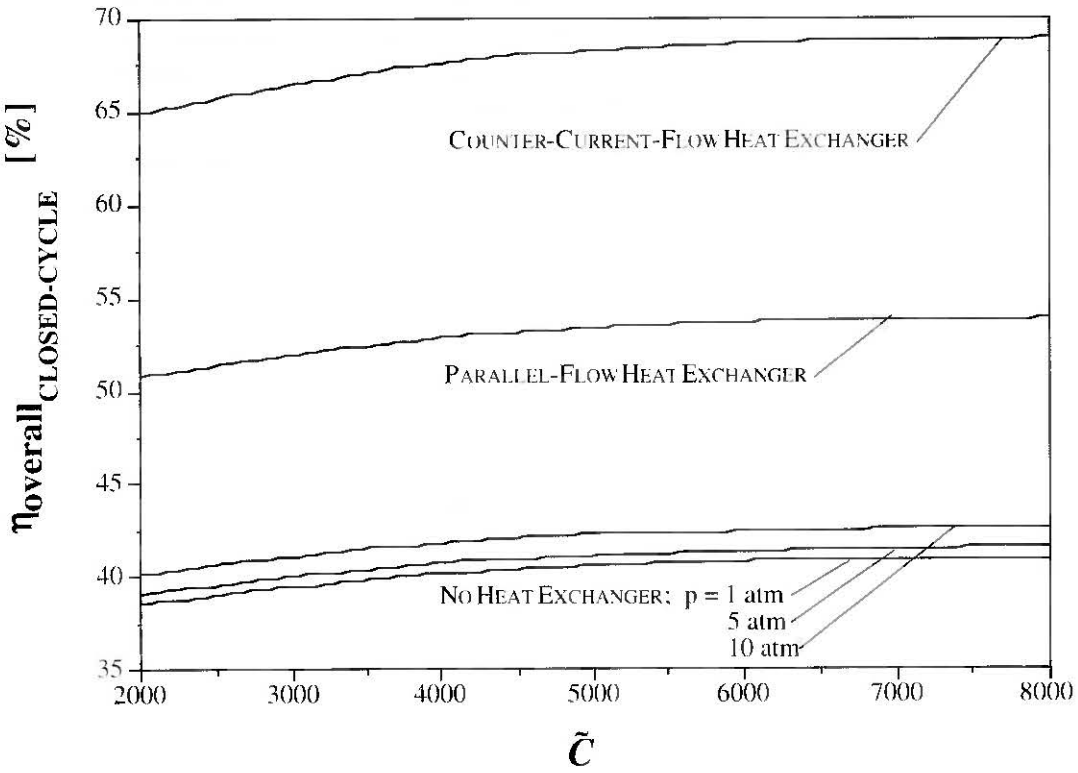

Figure 3.39 Variation of the overall efficiency with solar concentration, for the closed-cycle scheme with and without heat exchanger [Steinfeld *et al.*, 1996a]. The baseline parameters are used. The overall efficiency increases dramatically as a portion of the available sensible heat is recovered, but increasing concentration ratios produce only small improvements in the cycle efficiency.

the smaller the aperture, the less re-radiation losses, and consequently the higher the overall efficiency. However, the cycle efficiency is a weak function of C and doubling or even quadrupling the concentration brings about just a small improvement in the overall efficiency.

Open-cycle scheme

Finally, the open-cycle scheme is analyzed for the baseline case, with and without a heat exchanger. Notice that the chemical products at point 5 in Figure 3.33 do not have the exact stoichiometric composition given by equation (3.1) due to the incomplete CH_4 conversion. (The equilibrium composition at point 5 was given in Figure 3.35, Figure 3.36, Figure 3.38). At this point the products undergo natural phase separation into solid zinc and gas phases. The syngas mixture (having a H_2:CO molar ratio of 1.94) is combusted in the heat engine. Zinc is sent either to the Zn/O_2 fuel cell or to the water-splitter reactor for H_2 production.

Table 3.12 shows the complete energy balance of the open-cycle scheme. Evidently, $\eta_{overall}$ is higher when heat exchangers are employed because the required Q_{solar} is significantly lower. Also superior by about 13% is the efficiency of the scheme that uses Zn directly in a Zn/O_2 fuel cell, as compared to using Zn for splitting water and sending H_2 to a H_2/O_2 fuel cell. The reason is that, on a molar basis,

$$\Delta G|_{Zn(s)+0.5O_2 \rightarrow Zn(s)} > \Delta G|_{H_2+0.5O_2 \rightarrow H_2O(l)} \qquad (3.111)$$

and the Zn/O_2 fuel cell delivers more work than the H_2/O_2 fuel cell. The difference in the work output between the two fuel cells is equal to the difference between the heat rejected plus the heat losses in the exothermic water-splitting reaction, i.e.

$$\underbrace{W_{FC\_2}+Q_{FC\_2}}_{\Delta H|_{Zn(s)+0.5O_2\rightarrow ZnO(s)}} = \underbrace{W_{FC\_3}+Q_{FC\_3}}_{\Delta H|_{H_2+0.5O_2\rightarrow H_2O(l)}} + \underbrace{Q_{WS}}_{\Delta H|_{Zn(s)+H_2O(l)\rightarrow ZnO(s)+H_2}} \quad \textbf{(3.112)}$$

The overall efficiencies for the open-cycle schemes with and without heat exchangers are lower than the corresponding closed-cycle schemes, principally because of the losses incurred in the heat engine. The heat rejected by the heat engine amounts to 550 kW when a 35% engine efficiency is assumed.

Chemical by-products — The chemical products from each open system component are either recycled or discarded. The products of the HEAT ENGINE are H_2O and CO_2, which are discharged to the atmosphere. The product of the FUEL CELL #2 is $ZnO(s)$, which is recycled to the solar reactor. The products of the WATER SPLITTER are $ZnO(s)$ and H_2; $ZnO(s)$ is recycled to the solar reactor while H_2 is directed to the FUEL CELL #3. The product of the FUEL CELL #3 is H_2O, which is vented to the atmosphere. An external source of natural gas is required for supplying CH_4, which, together with $ZnO(s)$, are the feedstock into the solar reactor. The CO_2-emissions from the open-cycle scheme are only those resulting from the combustion of the syngas, expressed in units of specific CO_2 emissions per electricity generation:

$$\text{specific } CO_2 \text{ emissions for the open-cycle} = 0.26 \text{ kg } CO_2 / \text{kWh}_e. \quad \textbf{(3.113)}$$

Table 3.12 Energy balance on the open-cycle scheme with and without a heat exchanger. The baseline configuration is used: $\tilde{C} = 2000$, $I = 900$ W/m^2, $\alpha_{eff} = \varepsilon_{eff} = 1$, $T_1 = 298$ K, $T_3 = 1250$ K, $p = 1$ atm.

	No Heat Exchanger $T_1 = T_2 = 298$ K $T_3 = T_4 = 1250$ K	Parallel Flow Heat Exchanger $T_2 = T_4 = 940$ K	Counter-current Flow Heat Exchanger $T_2 = 1066$ K $T_4 = 400$ K
Q_{solar} [kW]	595	448	351
Q_{rerad} [kW]	46	34	27
$Q_{reactor,net}$ [kW]	549	414	324
Q_{ex} [kW]	0	135	225
Q_{quench} [kW]	237	102	12
Q_{FC_2} [kW]	30		
Q_{FC_3} [kW]	49		
Q_{WS} [kW]	63		
Q_{HE} [kW]	554		
W_{FC_2} [kW]	318		
W_{FC_3} [kW]	236		
W_{HE} [kW]	298		
$\eta_{overall}$ [%] (Zn to Fuel Cell)	41.5	46.0	49.6
$\eta_{overall}$ [%] (H_2 to Fuel Cell)	36.0	39.9	43.1

For comparison, using the *HHV* of methane for generating electricity in a power plant with the same 35% efficiency releases 0.51 kg CO_2/kWh$_e$, i.e. twice as much CO_2 as generated by the proposed solar open-cycle process.

3.4.5.3 Conclusions

The combined *ZnO*-reduction and CH_4-reforming, using solar radiation concentrated 2000 times as the energy source of process heat, could be conducted with maximum closed-cycle efficiencies between 40 and 65%, depending on the heat recovery factor of the heat exchanger. A reactor temperature of 1250K and a pressure of 1 atm. appear to be the optimum operating conditions. Higher temperatures result in higher re-radiation losses while higher pressures result in lower quality chemical products. The open-cycle scheme that extracts work from the products in technically, more readily, feasible processes features maximum overall efficiencies between 36 and 50%, depending on the heat-recovery factor and whether a Zn/O_2 or an H_2/O_2 fuel cell is employed. Major sources of irreversibilities are those associated with the re-radiation losses of the solar reactor and the heat rejected during the quenching.

The proposed thermochemical process combines fossil and solar energies. It helps create a technological link between the current fossil-fuel-based power plants and the future solar chemical plants. The second-law analysis is a useful theoretical tool for assessing maximum achievable efficiencies, for investigating the influence of the operating conditions, and for establishing a base for comparing different thermochemical processes.

Nomenclature

$A_{aperture}$	Area of reactor aperture, m^2
$C_{p,mixture}$	Specific heat capacity of the mixture, kJ mol^{-1} K^{-1}
$\tilde{C}$	Mean flux solar concentration
ΔG	*Gibbs* free energy change, kW
ΔH	Enthalpy change, kW
I	Normal beam insolation, kW/m^2
Irr_{cx}	Irreversibility associated with the heat exchanger, kW K^{-1}
Irr_{quench}	Irreversibility associated with the quenching, kW K^{-1}
$Irr_{reactor}$	Irreversibility associated with the solar reactor, kW K^{-1}
$Q_{absorbed}$	Power absorbed by the solar reactor, kW
$Q_{aperture}$	Incoming solar power intercepted by the reactor aperture, kW
Q_{FC}	Heat rejected to the surroundings by the fuel cell, kW
Q_{HE}	Heat rejected to the surroundings by the heat engine, kW
Q_{quench}	Heat rejected to the surroundings by the quenching process, kW
$Q_{reactor,net}$	Net power absorbed by the solar reactor, kW
Q_{rerad}	Power re-radiated through the reactor aperture, kW
Q_{solar}	Total solar power coming from the concentrator, kW
Q_{WS}	Heat rejected to the surroundings by the water-splitter, kW
ΔS	Entropy change, kW
T_{cav}	Nominal cavity-receiver temperature, K
T_L	Temperature of surroundings, 298 K
T_H	Sun surface temperature, 5800 K

T_{max}	Maximum temperature of the solar cavity-receiver
T_{opt}	Optimal temperature of the solar cavity-receiver for maximum $\eta_{overall,ideal}$
W_{FC}	Work output by the fuel cell, kW
W_{HE}	Work output by the heat engine, kW
α_{eff}	Effective absorptance of the solar cavity-receiver
ε_{eff}	Effective emittance of the solar cavity-receiver
$\eta_{absorption}$	Solar energy absorption efficiency
η_{Carnot}	Efficiency of a *Carnot* heat engine operating between T_H and T_L
η_{coll}	Efficiency of the solar collection system
η_{ex}	Heat recovery factor of the heat exchanger
$\eta_{heat\ engine}$	Efficiency of the heat engine
$\eta_{overall}$	Overall system efficiency
$\eta_{overall,ideal}$	Overall efficiency of an ideal system
σ	*Stefan-Boltzmann* constant, $5.6705 \cdot 10^{-8}$ W m^{-2}K^{-4}

3.5 Solar Cement

The production of cement is a high-temperature and energy-intensive process that releases vast amounts of greenhouse gases. Modern cement plants show a specific CO_2 emission rate of approximately 0.9 kg CO_2 per kg clinker (Figure 3.40). The contribution of the worldwide cement production to the global anthropogenic CO_2 emissions is roughly 5%[10] (Table 3.13). These emissions could be reduced by using solar energy.

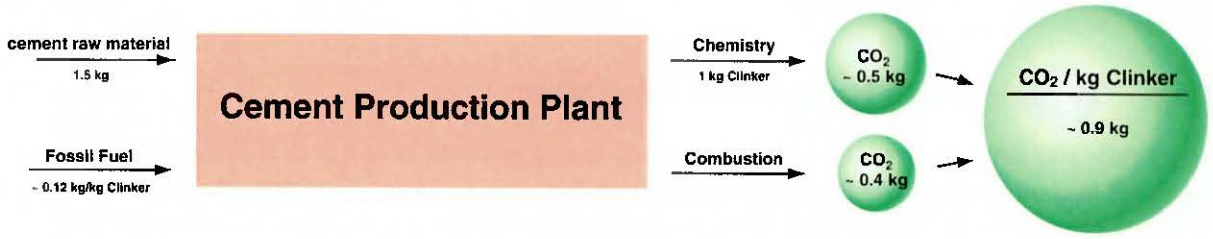

Figure 3.40 Energy flow chart and CO_2 sources of the cement production process

Table 3.13 Cement consumption and related CO_2 emissions

Country	Population 1992 [mill.]	Cement Consumption 1992 [mill. ton]	CO_2 Emissions [mill. ton]
USA	252	76	68
China	1188	308	277
India	865	53	48
Switzerland	7	4	4
World	5500	1237	1113

[10] Assumed global anthropogenic CO_2 Production: 20'000 mill. tons/year

The decomposition of limestone ($CaCO_3$) is the main endothermic step in the cement production process. It is characterized by the equation

$$CaCO_3 \rightarrow CaO + CO_2 \tag{3.114}$$

The dissociation of limestone is thermochemically well known and proceeds at about 1200 K. The reaction is highly endothermic ($\Delta H \approx 477$ kWh/tons of $CaCO_3$) and suffers from no serious back reaction to $CaCO_3$ which is important in regard to the chemical analysis.

The three thermodynamic steps of the cement production process are as follows (Table 3.14):

1. Preheating the ground cement raw material up to 1050 K.
2. Dissociation of the limestone at 1200 K. Limestone is the major ingredient of the cement raw material.
3. Sintering of the dissociated limestone with the accompanied chemical compounds (Fe_2O_3, SiO_2, Al_2O_3) at 1750 K.

As can be seen in Table 3.14, the calcination is a gas/solid reaction, which requires a short particle residence time.

Table 3.14 The three thermodynamic steps of the cement production process

Step	Temperature [K]	Reaction	Time [s]	Energy [kWh/kg Cli]	Energy Source
Preheating	350 to 1050	gas/solid	25	0.16	heat recovery
Calcination	1200	gas/solid	2	0.55	fossil fuel
Sintering	1750	solid/solid	600	0.3	fossil fuel

3.5.1 Technical and Economical Feasibility

To clarify the important technical and economical questions of solar cement plants several meetings and workshops with members of the cement industry were held [Imhof, 1996b; Imhof, 1997a; Imhof, 1997b]. The results of these discussions can be summarized as follows:

1. The application of solar energy to the calcination step is technically feasible, but for economic reasons one needs a 24 hour production process. Thus, a solar assisted cement plant has to be equipped with a fossil fuel fired flash calciner (Hybrid Solar Cement Plant).
2. Based on raw material deposits, market growth and solar insolation (see Figure 3.41), the best locations for installing solar cement plants are presumably found in Jordan, Egypt, Morocco, Mexico, Pakistan, and India.
3. A preliminary economic assessment of HOLDERBANK [Gyurech, 1997] for a large-scale solar cement production plant indicates that the application of solar energy to the cement production process is presently not competitive with conventional methods that make use of fossil fuels as the primary energy source. This problem occurs because of the presently very low fossil fuel prices and relatively high costs for the solar energy concentration (heliostat costs). Therefore, one can expect an increase of product costs up to 10%. However, assuming a heliostat cost of 200 sFr/m^2 and a CO_2 tax of 50 US$/ton CO_2 for CO_2 emissions, no increase of the product cost may be expected. The potential of CO_2 mitigation by a hybrid solar cement plant is approximately 9%.

4. Due to the very high transportation costs (0.1 US$/ton-mile), the average market radius for cement and lime is less than 500km. Consequently, in many rural areas wood is used as the energy source for burning lime. A small scale lime production plant (25 tons lime per day) operated with wood requires a wood plantation area of more than 3 km^2 to guarantee the new generation of trees. Because of the lack of wood fuel, concentrated solar radiation may also be appropriate for burning limestone in sunny rural areas. Although the use of wood is renewable in principle, and arguably CO_2-neutral, in Africa for example the wood energy load is the second largest cause of deforestation, because only one tree is planted for every 20 cut.

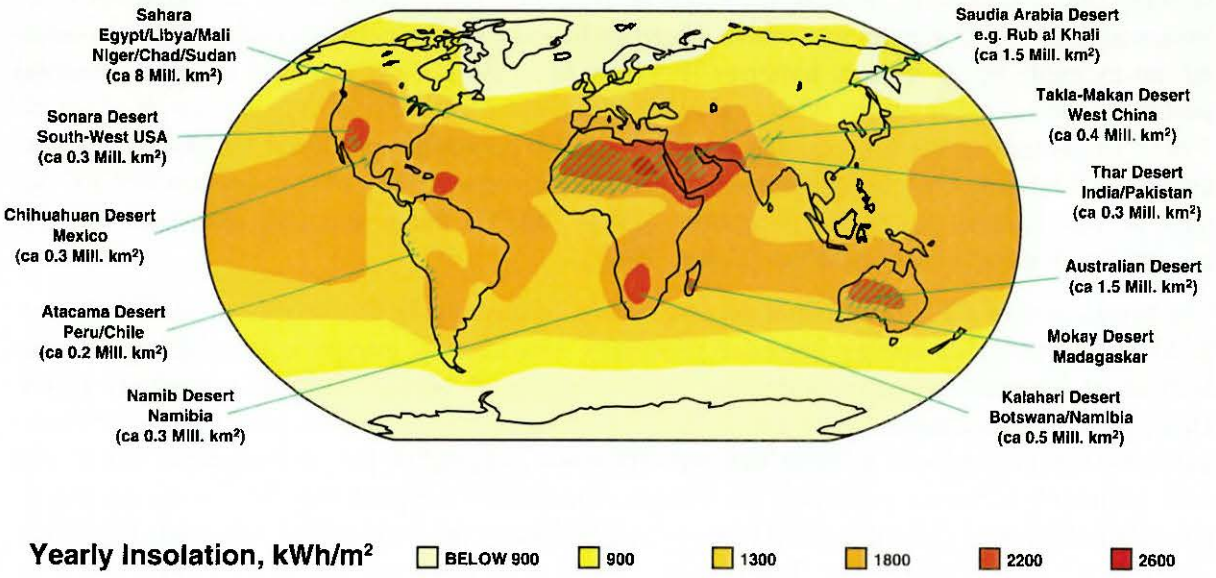

Figure 3.41 Solar Insolation in deserts

3.5.2 Conclusions

It was decided that a pilot plant for the industrial decomposition of limestone should be envisaged. The scope of work for such a P&D project has been defined and a corresponding proposal [Imhof, 1998] has been submitted to different potential sponsors.

Our work regarding the solar cement process was exclusively related to developing a solar reactor for that process. Therefore, the remaining details on this work are found in Chapter 4.

3.6 Decomposition of Hydrocarbons

The solar thermal decomposition of gaseous hydrocarbons and carbon monoxide for producing Catalytic Filamentous Carbon (*CFC*) was investigated within a collaborative project between the Boreskov Institute of Catalysis (*BIC*) and the Paul Scherrer Institute (*PSI*). The chemical feasibility of such a process was shown at *BIC*, where it was carried out under non-transparent conditions. In May 1996 and in September 1997, the process was performed in *PSI*'s solar furnace by direct solar irradiation of the catalyst. The expertise of the *BIC* in preparation, testing and application of metallic catalysts was combined with the expertise of the *PSI* in the design, construction and testing of direct-absorption solar particle reactors. The work was carried out within the framework of the existing *SolarPACES* Program of the International Energy Agency

(*IEA*). The experimental results obtained within this joint *PSI-BIC* project were published in various journals and at international conferences [Kirillov *et al.*, 1996; Steinfeld *et al.*, 1997; Meier *et al.*, 1998a; Meier *et al.*, 1998b].

CFC can be formed by thermal decomposition of hydrocarbons and by *CO* disproportionation in the presence of small catalyst particles containing group VIII metals [Baker, 1989; Likholobov *et al.*, 1995]. A potential application of such a process is the clean conversion of natural and oil tail gases into valuable chemical commodities [Avdeeva, 1995]. The carbon materials produced exhibit unique properties which are of technical interest in various fields [Tibbetts *et al.*, 1986]. *CFC* are used for the reinforcement of composites where high-temperature stability and mechanical strength are required [Calvert, 1992]. They serve as capacitor electrodes for energy storage devices where a high surface area and electrical conductivity are needed, an example being lithium batteries [Frysz *et al.*, 1996]. *CFC* are used in environmental pollution control applications where rapid adsorption/desorption is of importance [Rodriguez, 1993]. In contrast to the high quality graphitic carbon nanotubes produced by electric arc discharge at extremely high temperatures and pressures [Iijima, 1991], the production of *CFC* occurs at significantly lower temperatures (450 to 700°C) using specially prepared catalyst material with metal oxide additives [Baker, 1989].

The production of *CFC* by thermal decomposition of gaseous hydrocarbons or by *CO* disproportionation demands energy-intensive processes. Usually, the energy is supplied by electric heaters or, alternatively, by combusting some portion of the hydrocarbon containing gases. However, internal combustion results in the contamination of the gaseous products while external combustion results in a lower thermal efficiency because of the inefficiencies associated with indirect heat transport via heat exchangers. An attractive approach is the use of concentrated solar radiation as clean source of process heat, avoiding the emission of pollutants [Steinfeld *et al.*, 1997]. Furthermore, the direct solar irradiation of the reactants provides efficient heat transfer directly to the reaction site.

We report on experimental results of this novel chemical application of concentrated solar energy. We studied the influence of the direct solar radiation on the chemical reaction and on the morphology of the produced *CFC*. We determined the carbon mass produced per unit catalyst mass during the reaction time, and the chemical conversion of methane to hydrogen. Furthermore, we examined the solar produced *CFC* samples for their capability to store hydrogen and for their suitability to special electrical and mechanical applications. Experiments were performed under direct solar irradiation using the high-flux solar furnace of the Paul Scherrer Institute (*PSI*) and under similar reaction conditions using an electric furnace with indirect heat transfer at the Boreskov Institute of Catalysis (*BIC*).

3.6.1 Experimental

Reactions

The catalytic decomposition of hydrocarbons proceeds at temperatures above about 450°C when conducted at atmospheric pressure (Baker and Harris, 1978). The general stoichiometric reaction can be represented by:

$$C_nH_m \leftrightarrow nC + \frac{m}{2}H_2 \qquad (3.115)$$

We studied the catalytic decomposition of CH_4 and C_4H_{10} (both in mixtures with H_2 and N_2), and the *CO* disproportionation reaction

$$2CO \leftrightarrow C + CO_2 \qquad (3.116)$$

Catalysts

We used Ni / Al_2O_3 and Co / MgO as catalysts. Both catalysts were prepared by co-precipitation as metal hydroxides from the mixture of their salt solutions. The preparation procedure of the *Ni* catalyst (88 wt% nickel and 12 wt% Al_2O_3) is described elsewhere [Goncharova *et al.*, 1995]. The preparation of the *Co* catalyst (20 wt% cobalt and 80 wt% *MgO*) has previously been described [Khassin *et al.*, 1998].

Reactants

The initial concentrations of the reactants used to produce the *CFC*, namely CO-N_2, CH_4-N_2, CH_4-N_2-H_2, and C_4H_{10}-N_2-H_2 can be calculated from the respective flow rates given in Table 3.15. The catalyst type and the initial catalyst mass m_{cat} are shown for the solar experiments (Exp. *S1* to *S10*) and the corresponding laboratory experiments (Exp. *L1* to *L5*). Furthermore, we indicate the reaction period t_r, the average temperatures T_{av}, and the temperature fluctua-

Table 3.15 Experimental conditions for CFC production in solar furnace (Exp. *S1* to *S10*) and in laboratory (Exp. *L1* to *L5*)

Exp.	Catalyst	m_{cat} [g]	Mean Reactant Flow Rate [m^3/hr]					t_r [min]	T_{av} [°C]	ΔT [°C]
			N_2	H_2	CH_4	C_4H_{10}	CO			
L1	*Co/MgO*[a]	1.05	0.08		0.018			120	550	0
L2	*Co/MgO*	1.11	0.15	0.013	0.018			120	550	0
L3	*Co/MgO*	1.05	0.15				0.012	120	430	0
L4	Ni/Al_2O_3[b]	0.59	0.08				0.021	120	450	0
L5	Ni/Al_2O_3	1.57	0.09				0.024	120	450	0
S1	*Co/MgO*[a]	1.05	0.07		0.018			100	550	±45
S2	*Co/MgO*	1.11	0.10	0.011	0.015			90	550	±60
S3	*Co/MgO*	1.05	0.15				0.018	40	430	±60
S4	Ni/Al_2O_3[b]	0.59	0.10				0.032	70	450	±50
S5	Ni/Al_2O_3	1.57	0.08				0.032	30	450	±50
S6	Ni/SiO_2[c]	0.33	0.08		0.024			30	550	±40
S7	Ni/Al_2O_3	0.47	(a) 0.14 (b) 0.11	(a) 0.016 (b) 0.012	0.018			60	540	±50
S8	Ni/Al_2O_3	1.00	0.10	0.011		0.004		110	470	±50
S9	Ni/Al_2O_3	0.99	0.08	0.009		0.004		50	510	±45
S10	Ni/Al_2O_3	1.00	0.06	0.007		0.003		25	700	±40

a. Co/MgO (20 wt% Co)

b. Ni/Al_2O_3 (88 wt% Ni)

c. New catalyst type: Ni/SiO_2 (96 wt% *Ni*)

tions ΔT that were observed during solar experiments (usually the temperature was constant during laboratory experiments).

Laboratory Experimental Set-up

Laboratory experiments were conducted in an electric furnace at *BIC* using the same catalysts and attempting to reproduce similar operating conditions as those encountered during solar experiments. To achieve high heating rates and constant temperatures, the reactor was placed in an isothermal fluidized bed. Details of the experimental set-up have been reported elsewhere [Kuvshinov *et al.*, 1998].

Solar Experimental Set-up

The solar experiments were conducted in the PSI solar furnace consisting of a sun-tracking heliostat and a stationary primary parabolic concentrator. The experimental set-up has been described in a previous paper [Steinfeld *et al.*, 1997]. Here, we summarize briefly the main features of the solar receiver/reactor. It consisted of a 2 cm diameter quartz tube containing a 5 cm high fluidized bed of inert material (Al_2O_3 grains) and on top of it a 5 mm high layer of fine catalyst granules (Ni/Al_2O_3 or Co/MgO). The inert material did not act as a catalyst support, but rather it was introduced to stabilize the temperature in the reaction zone, prevent sintering and help fluidization. The tubular fluidized bed reactor was uniformly irradiated by concentrated sunlight using a silver-coated secondary reflector. The optical design of this 2-dimensional *CPC* (Compound Parabolic Concentrator) coupled to the involute of the circle formed by the outer wall of the quartz tube has been described elsewhere [Steinfeld *et al.*, 1995a]. The entrance of the *CPC* was positioned at the focal plane of the primary concentrator and re-directed the incident radiation into the vertically placed quartz tube reactor. This concept offered direct heat transfer to the fluidized bed particles, low thermal capacitance, and good thermal shock resistance.

A typical solar experiment consisted of two phases:

1. for the catalyst activation, the fluidized bed was solar-heated to temperatures of about 450 to 500°C under a flow of 10 vol% H_2 and 90 vol% N_2;
2. for the catalyst deactivation, the fluidized bed was subjected to a reacting gas flow according to various process operating conditions (see Table 3.15 for details). For all experiments without H_2 admixture to the reacting gas, the fluidized bed was cooled below 100°C after the catalyst activation phase (10 to 30 minutes) before being re-heated to the desired operating temperature for the catalyst deactivation phase (30 to 120 minutes). The composition of the gaseous products was analyzed by gas chromatography before being released to the atmosphere.

Pressure in the quartz tube reactor was maintained slightly above atmospheric. The fluidized bed was operated under vigorous bubbling conditions and, therefore, likely to be at a uniform temperature. The nominal bed temperature reported here was measured with a thermocouple type-K in an Al_2O_3 protection tube submerged into the bed. It was difficult to maintain a constant fluidized bed temperature by manually controlling the amount of incoming solar power flux (below about 600 suns; 1 sun = 1 kW m^{-2}) with the furnace's venetian-blind shutter. Better isothermal conditions may require an automatic temperature controlled shutter allowing much finer steps for solar power adjustment.

3.6.2 Results and Discussion

3.6.2.1 Carbon Mesostructure

We studied the effect of the catalyst composition and the temperature on the morphology of the carbon deposits produced by the decomposition of gaseous hydrocarbons (CH_4 and C_4H_{10}) and by the CO disproportionation over Ni/Al_2O_3 and Co/MgO catalysts.

After activation of the catalyst particles with hydrogen, the catalytic carbon formation begins with the chemisorption and decomposition of hydrocarbons or CO on the surface of each metal nanoparticle, followed by carbon diffusion through the catalyst nanoparticle and precipitation of carbon in the form of filamentous carbon on the opposite side of the nanoparticle (Baker, 1989). All the produced CFC have an interlayer distance (d_{002}) of 0.34 nm which is characteristic of the graphitic structure of the CFC. The metal particle remains at the tip of the filaments, as seen from high resolution transmission electron micrographs ($HRTEM$) of the CFC products (Figure 3.43).

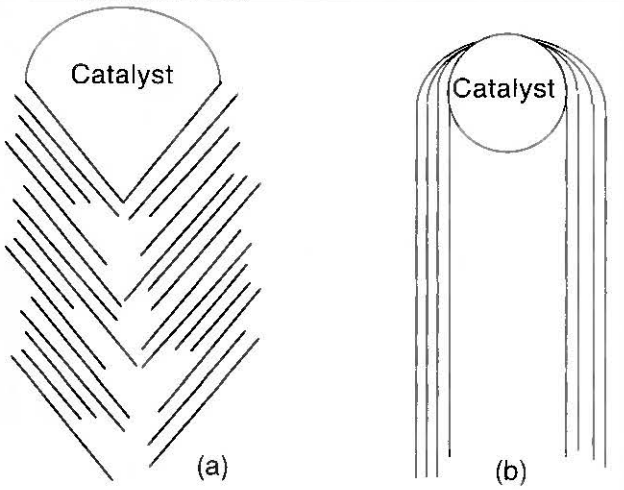

Figure 3.42 Scheme of growth mechanism for (*a*) nanofibers and (*b*) nanotubes [Meier *et al.*, 1998b].

The solar experiments show that two different types of filamentous carbon were obtained, namely nanotubes and nanofibers. The morphology of the produced CFC depends mainly on the catalyst. Ni/Al_2O_3 metal particles essentially form conical nuclei (growth centers) with the tip pointing in the direction of the filament growth. The basal layers of these filaments are always parallel to the surface of the metal particle (Figure 3.42a, Figure 3.43d). Epitactic growth of carbon on the exposed crystallographic planes of the faceted catalyst results in carbon nanofibers or nanorods without a hollow channel that are obtained mainly on the Ni/Al_2O_3 catalyst. In contrast, nanotubes with long, parallel, cylindrical walls containing the catalyst particle inside the hollow core are formed mainly on the rather spherical Co/MgO catalyst (Figure 3.42b, Figure 3.43a).

The size of the produced filaments depends on the size of the catalyst particle. This property gives the opportunity for tailoring catalysts for the production of filaments with specified diameter. The experiments show that the filaments produced with Co/MgO catalyst particles of 6 nm mean diameter are usually smaller than the ones formed on Ni/Al_2O_3 catalyst particles of 27 nm mean diameter. This can be seen most clearly from comparing the Figure 3.43c and Figure 3.43d showing examples of CFC from CH_4+H_2 on Co/MgO and Ni/Al_2O_3 catalyst, respectively.

Another parameter for designing the CFC products is the carbonization agent. For Ni/Al_2O_3 catalyst particles, we observe that the adsorption and the chemical conversion to carbon differs between the CO disproportionation reaction (Figure 3.43b) and the dehydrogenation of hydrocarbons (Figure 3.43d, Figure 3.43f). However, CH_4 and C_4H_{10} both appear to have a similar effect on the formation of CFC on Ni/Al_2O_3 catalyst particles, as seen from the Figure 3.43d and Figure 3.43f. From the present experiments, we observe a tendency to form concentric graphite layers on Co/MgO catalyst when using CH_4 (Figure 3.43e) instead of straight fila-

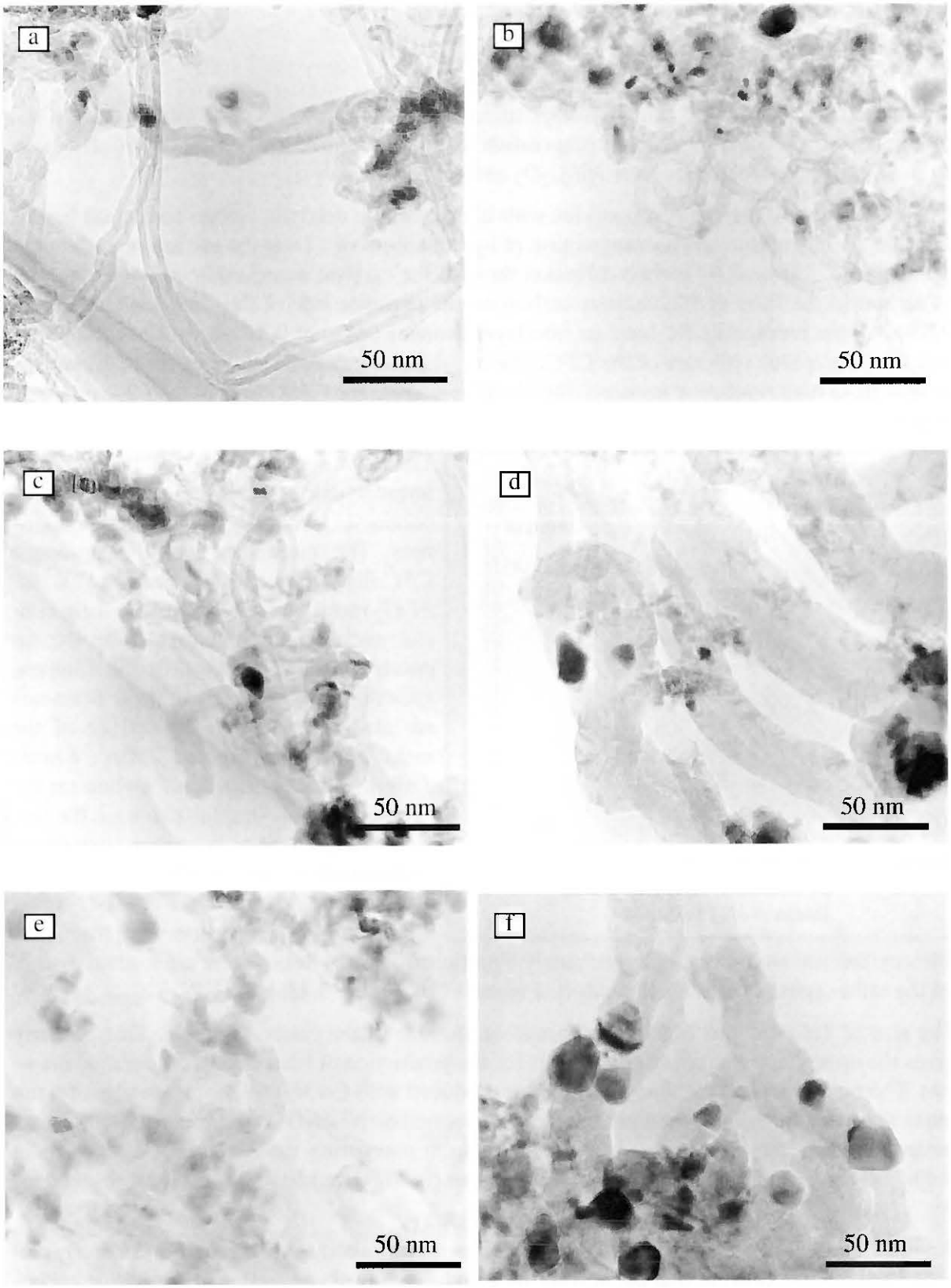

Figure 3.43 HRTEM of different types of *CFC* formed by solar thermal decomposition of hydrocarbons and CO disproportionation: Nanotubes mainly on *Co/MgO* catalyst for (*a*) *CO* (Exp. *S3*), (*c*) $CH_4 + H_2$ (Exp. *S2*) and (e) CH_4 (Exp. *S1*), but also on Ni/Al_2O_3 catalyst for (b) *CO* (Exp. S5). Nanofibers mainly on Ni / Al_2O_3 catalyst for (*d*) $CH_4 + H_2$ (Exp. *S7*) and (*f*) $C_4H_{10} + H_2$ (Exp. *S8*). Magnification 210'000 x [Meier *et al.*, 1998b].

ments when using *CO* (Figure 3.43a), but also on Ni/Al_2O_3 catalyst when using *CO* (Figure 3.43b). The latter observation, however, needs to be confirmed by additional experiments. Some metal particles are even surrounded by layers of carbon which inhibits further formation of filaments (e.g., see Figure 3.43c).

Hydrogen was added to the feed of hydrocarbons in order to avoid rapid deactivation of the catalyst. It has been found earlier in laboratory experiments (Kuvshinov *et al.*, 1998) that hydrogen reacts with the catalyst and that it can influence the shape of the growth centers where the carbon filaments form on Ni/Al_2O_3 catalyst particles. When H_2 was present during the reaction, the formation of faceted growth centers and nanofibers was favored (Figure 3.42a, Figure 3.43d). However, in the absence of H_2, the predicted formation of nanotubes was not confirmed in the solar experiments. In addition, the H_2 content in the reactant mixture did not show any significant effect on the *CFC* formation on *Co/MgO* catalyst (Figure 3.43c, Figure 3.43e).

The storage of hydrogen in layered nanostructures was described in a recent patent [Rodriguez and Baker, 1997]. These authors found that significant amounts of H_2 can be stored in a novel graphitic material produced by decomposing carbon-containing gases over a catalyst. In contrast to these findings, all our solar and laboratory *CFC* samples examined under specific experimental conditions in a specially designed apparatus at *PSI* [Meurant, 1998] did not show any H_2 storage capability [Newson, 1998]. This negative result can be explained by the fact that our *CFC* samples have a very big pore size. H_2 storage may be completely impeded for the nanofibers without a hollow core. In turn, the hollow nanotubes may be closed at least at one side by the catalyst, and thus the access of H_2 is hampered. Furthermore, only single-walled carbon nanotubes are good hydrogen capacitors [Dillon *et al.*, 1997].

Preliminary investigations of a solar produced *CFC* sample (Exp. *S4*) and a similar laboratory sample revealed lattice planes more or less perpendicular to the long axis of the nanofibers which have numerous bends in their structure. These undesirable features imply poor electrical conductivity and tensile strength. In contrast, the solar produced sample of Exp. *S1* (Figure 3.43e) shows lattice planes parallel to the axis of the nanotubes. This is a desirable feature and implies that there is some potential for the solar process [Lewandowski and Fields, 1998]. To be of great technical interest, the tubes must become more uniform in diameter, straight and aligned in arrays [Li *et al.*, 1996].

3.6.2.2 Carbon Texture

We examined the textures of several *CFC* samples obtained in the solar furnace and in the laboratory under the experimental conditions described in Table 3.15. Texture properties of the *CFC* samples obtained in the solar experiments are given in Table 3.16. The specific surface area (*BET* surface area and *T-method* surface area) is about 50 to 170 m^2/g and depends on the chosen experimental conditions. The micropore volume is typically between 0.002 and 0.008 cm^3/g and can even be zero (see Exp. *S2*). Such low micropore volume together with the availability of high mesopore volume is a necessary property of carbon when used as a catalyst support (e.g. catalysts for selective oxidation of hydrocarbons [Rodriguez *et al.*, 1994; Malinovskaja *et al.*, 1975]). The average pore volume ranges between 0.4 and 0.8 cm^3/g and appears to be independent of the experimental conditions. The size of the monolithic carbon crystallites (D_{002}) is 10 nm for nanofibers obtained on the Ni/Al_2O_3 catalyst which is twice as large as the corresponding D_{002} value for nanotubes obtained on the *Co/MgO* catalyst.

Table 3.17 presents texture properties of the carbon samples composed of nanotubes and nanofibers which were obtained from laboratory experiments. The experimental conditions were similar to those for the solar experiments given in Table 3.15, except for the amplitude of the temperature fluctuations which was almost zero when laboratory samples were prepared.

Table 3.16 Texture properties of the samples obtained in the solar experiments (Exp. *S1* to *S5*)

Property	Dimension	Exp. S1	Exp. S2	Exp. S3	Exp. S4	Exp. S5
BET surface area	m^2/g	146.6	99.0	148.1	166.6	150.5
T-method surface area	m^2/g	140.4	100.4	136.3	156.9	135.8
Average pore volume	cm^3/g	0.469	0.485	0.479	0.834	0.428
Micropore volume	cm^3/g	0.0043	0.0	0.0073	0.0059	0.0082
Average pore diameter from *BET* method	nm	13.5	20.8	14.2	20.4	12.3
D_{002} (crystallite size)	nm	-	5	5	10	10

cont'd

Property	Dimension	Exp. S6	Exp. S7	Exp. S8	Exp. S9	Exp. S10
BET surface area	m^2/g	50.7	80.4	108.2	103.1	97.2
T-method surface area	m^2/g	-	-	-	-	-
Average pore volume	cm^3/g	-	-	-	-	-
Micropore volume	cm^3/g	0.0	0.0027	0.0038	0.0061	0.0017
Average pore diameter from *BET* method	nm	23.1	10.9	15.2	17.9	17.1
D_{002} (crystallite size)	nm	-	-	-	-	-

Comparing the texture properties of the solar samples (Table 3.16) and the laboratory samples (Table 3.17), we found no significant influence of the reaction temperature (between 450 and 700°C) on the carbon surface area and the average pore volume. In laboratory experiments, the temperature practically did not affect the carbon texture because the catalytic carbon was produced by maintaining a narrow temperature range. In solar experiments, there is no detectable temperature effect on the carbon texture even for the observed large temperature fluctuations.

In Figure 3.44a, the distribution of the cumulative pore volume in some of the samples obtained in the solar furnace (Exp. *S1* to *S5*) is given according to the conditions listed in Table 3.15. For the most part, the pore diameter ranges from 10 to 100 nm in all experiments. The profiles of

Table 3.17 Texture properties of the samples obtained in the laboratory experiments (Exp. *L1* to *L5*)

Property	Dimension	Exp. L1	Exp. L2	Exp. L3	Exp. L4	Exp. L5
BET surface area	m^2/g	191.3	91.3	237.3	142.7	178.4
T-method surface area	m^2/g	183.7	108.6	230.8	165.8	116.3
Average pore volume	cm^3/g	0,66	0.487	0.635	0.652	0.659
Micropore volume	cm^3/g	0.0057	0.0076	0.0055	0,0094	0.0
Average pore diameter from *BET* method	nm	15.3	20.8	12.5	19.8	34.1
D_{002} (crystallite size)	nm	-	5	5	10	10

the pore volume variations differ insignificantly from one experiment to the other, except for the profile that belongs to the sample obtained during Exp. *S1*. We ascribe the sharp increase in the mesopore volume to the fact that the CH_4 concentration at the inlet was increased by a factor 1.7 compared to Exp. *S2*, the other conditions being the same except for H_2 in Exp. *S2*. Similarly, Figure 3.44b shows the distribution of the cumulative pore surface area in the samples obtained during the solar experiments (Exp. *S1* to *S5*) according to the conditions given in Table 3.15. Here, the profiles do not differ from one experiment to the other, except for the sample of Exp. *S1*.

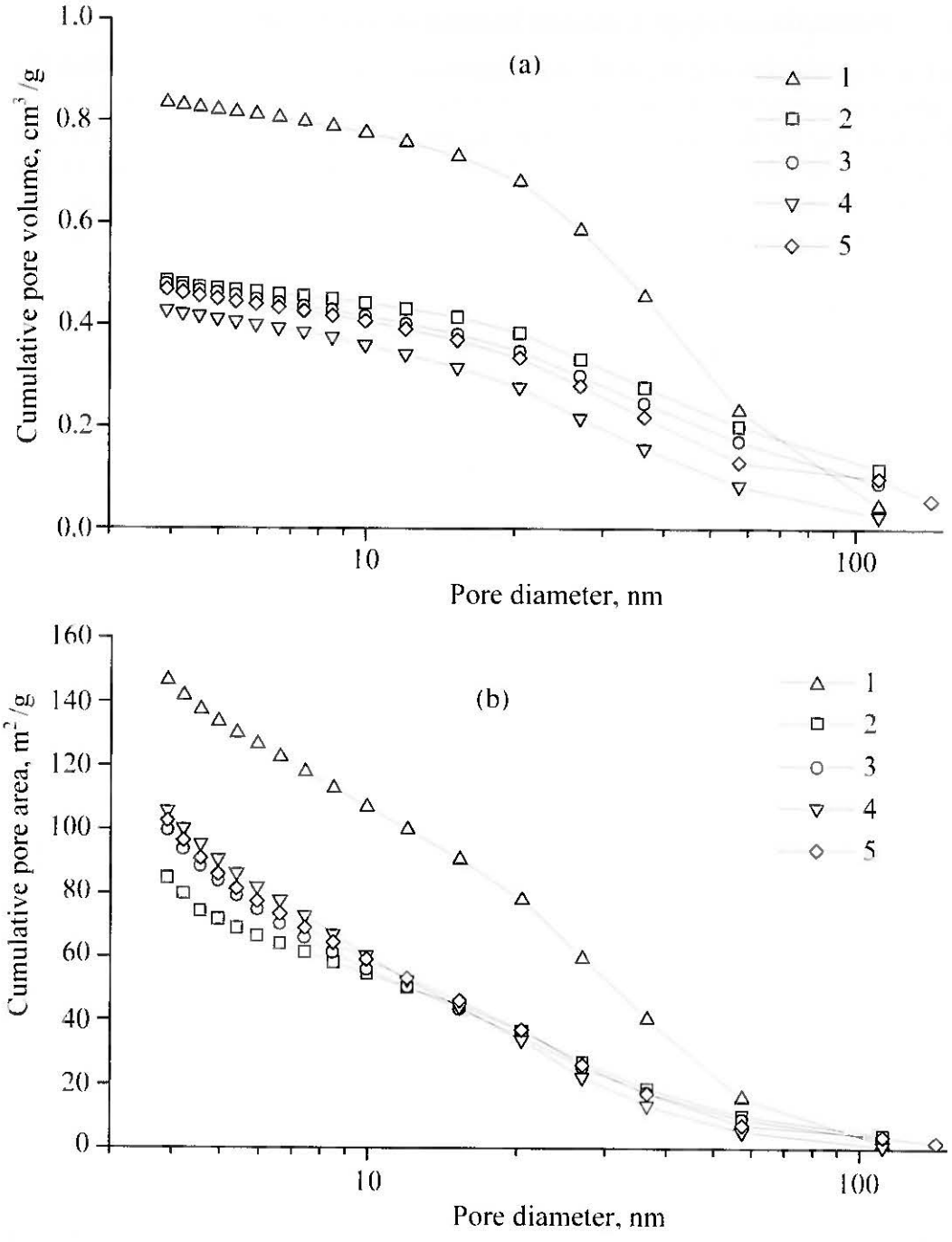

Figure 3.44 Texture properties for CFC samples of solar experiments (Exp. S1 to S5): (*a*) cumulative pore volume and (*b*) cumulative pore area [Meier *et al.*, 1998b]

3.6.2.3 Carbon Yield

The solar experiments were performed using a small scale fluidized-bed solar reactor that was not optimized for high carbon yield. Hence, the carbon deposits on the catalysts were low in solar experiments (1 to 3 gram carbon per gram catalyst within 0.5 to 2 hours before the catalyst was deactivated) compared to laboratory experiments (10 to 20 gram per gram catalyst within 3 to 10 hours before the catalyst reached deactivation conditions). The difference in deactivation time and the lower maximum carbon yield for the solar experiments might be the result of temperature fluctuations and temperature gradients presumably present in the solar reactor. This observation is supported by the corresponding laboratory experiments.

3.6.2.4 Production of H_2 by Catalytic Decomposition of CH_4

The chemical conversion of CH_4 to H_2 was approximately 30% as determined from the outlet gas composition during all relevant solar experiments (Exp. *S1*, *S2*, *S6*, *S7*, see Table 3.15). Figure 3.45 shows the fluidized bed temperature and the chemical conversion from CH_4 to H_2 as determined from the outlet gas composition during a representative solar experiment (Exp. *S7*). For this experimental run, the reacting gas flow initially consisted of 0.018 m^3/hr "pure" (>99.95wt%) CH_4 and 0.016 m^3/hr H_2 in a 10% H_2-N_2 mixture (Table 3.15, Exp. *S7a*). The temperature was kept below 590°C to prevent rapid deactivation of the catalyst. It is observed that small deviations in the temperature were accompanied by deviations in the CH_4 to H_2 conversion rate, indicating a strong temperature dependence of the extent of the reaction. After 30 minutes of experimental operation, the flow of the 10% H_2-N_2 gas mixture was decreased by 25% as can see from the corresponding increase in CH_4 concentration (Table 3.15, Exp. *S7b*). The outlet gas composition showed about 30% chemical conversion from CH_4 to H_2 in a single pass of 0.6 seconds through the 5 cm bed height. Conversion decreased with time as carbon grew over the catalyst particles. This result is consistent with the findings of the solar experi-

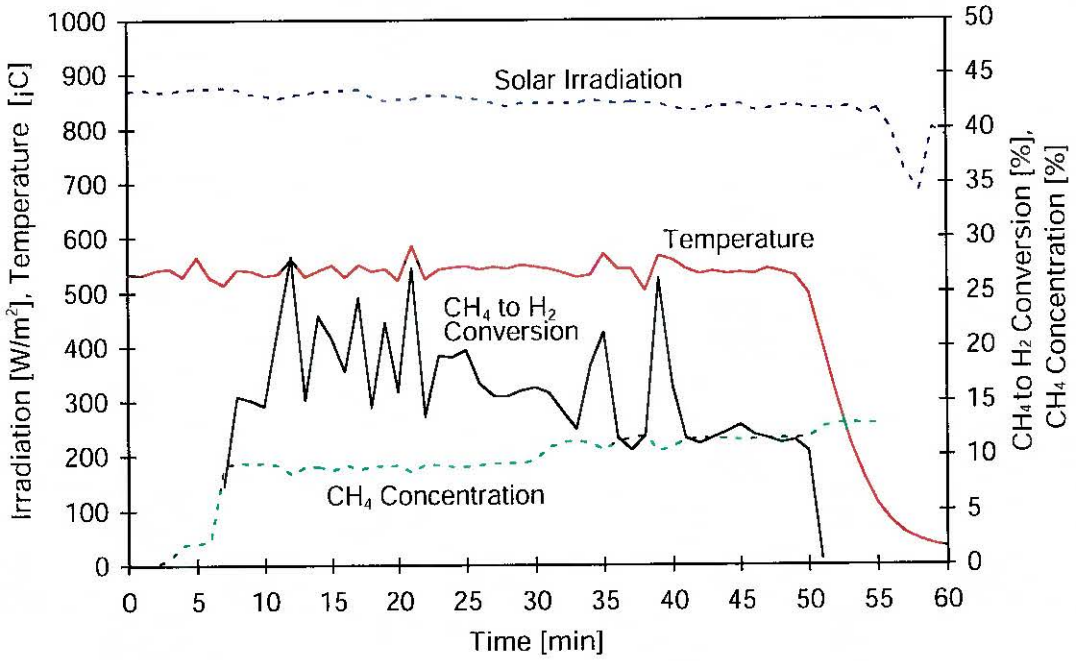

Figure 3.45 H_2 production by solar thermal decomposition of CH_4 (Exp. *S7*). Small deviations in the temperature are accompanied by larger deviations in the chemical conversion of CH_4 to H_2, indicating a strong temperature dependence of the extent of the reaction. This experiment is representative for constant solar irradiation conditions [Meier *et al.*, 1998b].

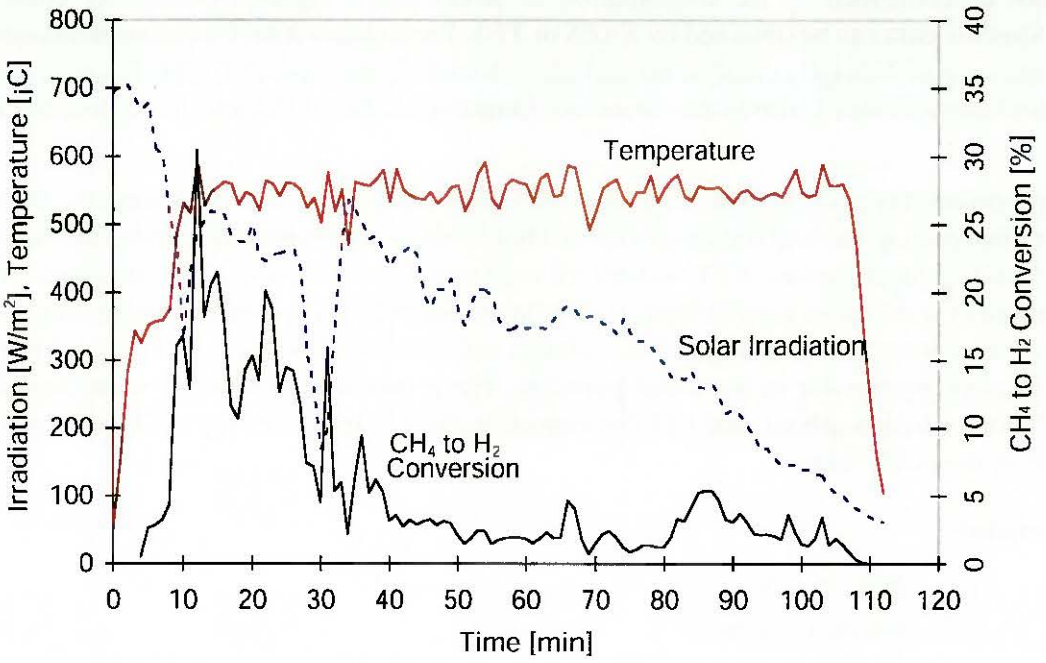

Figure 3.46 H_2 production by solar thermal decomposition of CH_4 (Exp. *S1*). The chemical conversion from CH_4 to H_2 follows the strong temperature variations and decreases rapidly as carbon grows over the catalyst particle. Despite the irregular and decreasing solar irradiation, the temperature was maintained at the 550°C level [Meier *et al.*, 1998b].

mental campaign 1996 reported in a previous paper [Steinfeld *et al.*, 1997]. This particular solar experiment is representative for constant irradiation conditions. In contrast, Figure 3.46 shows a similar experiment but with strong variations of the direct solar irradiation (Exp. *S1*). It was possible to maintain the desired temperature level despite the intermittent solar radiation due to clouds and despite the slowly decreasing solar flux shortly before sunset. The conversion decreased with time as carbon grew over the catalyst.

3.6.3 Conclusions

We investigated the production of Catalytic Filamentous Carbon (*CFC*) by solar thermal decomposition of gaseous hydrocarbons (CH_4 and C_4H_{10}) and by *CO* disproportionation in the presence of small metal catalyst particles. Depending on the catalyst, different types of *CFC*, namely nanotubes and nanofibers, were obtained in the solar experiments. Nanotubes are formed mainly on the *Co/MgO* catalyst for *CO* and $CH_4 + H_2$; nanofibers are formed mainly on Ni/Al_2O_3 catalyst for CH_4, $CH_4 + H_2$, and C_4H_{10}. Laboratory experiments confirm these findings. Typically, the following properties were determined by *BET*: the surface area is about 50 to 170 m^2/g, the micropore volume is between 0.002 and 0.008 cm^3/g, the average pore diameter ranges between 10 and 40 nm, and the pore volume is in the range of 0.4 to 0.8 cm^3/g. From these properties and from the inspection of high resolution transmission electron micrographs (*HRTEM*) we conclude that *CFC* with well defined morphology can be produced using direct solar radiation.

We found that the different catalytic growth mechanisms depend on the type of the metal particles, the exposed crystal surface and the reacting gas. However, the influence of the reaction temperature on the carbon texture and the role of the different reacting gases need further investigation. More research is required to determine the crystallite structure of the metal catalyst particles (monocrystalline, nanocrystalline, or carbide phases?). The formation of carbides

could not be confirmed by the examination of X-ray diffractograms because of coinciding peaks. Specific data can be obtained by *XAFS* or *XPS*. Preliminary *XAFS* measurements confirm that in the case of Ni/Al_2O_3 catalyst no carbide is found. In the case of *Co/MgO* catalyst, however, more complicated features are observed. Ongoing studies will yield more detailed information.

The appropriate choice of the relevant parameters responsible for the *CFC* texture, i.e. the metal catalyst, the reacting gas and the temperature, should allow to produce valuable chemical commodities of technical interest. *CFC* in form of long nanotubes showing graphite layers parallel to the filament walls are of utmost interest. The inner diameter and probably the thickness of the walls may be controlled by the type of the catalyst and its crystallite size, i.e. the size of the *CFC* can be selected by the size of the metal particles. The production of *CFC* by solar thermal decomposition of hydrocarbons and *CO* disproportionation is an interesting challenge for future research in materials science.

Nomenclature

m_{cat}	mass of catalyst, kg
t_r	reaction period, s
T_{av}	average temperature, K
ΔT	temperature fluctuations, K

4 Solar Reactor Development

Conventional solar receivers/reactors for high-temperature applications make use of insulated cavity-type configurations in order to obtain isothermal conditions and efficient solar energy absorption [Steinfeld and Schubnell, 1993; Diver, 1987]. The interior lining of the cavity is often the principal absorbing surface. From there, energy is transferred to the reactor/reactants. However, for operating temperatures above 2000 K under oxidizing atmospheres, ceramic materials of construction are needed for lining the inner walls of the cavity. These materials exhibit large thermal inertia and are not resistant to severe thermal shocks that often occur in solar-driven reactors. These problems prompted us to search for other solar reactor concepts.

The direct-absorption particle reactor, proposed by several authors [Hunt *et al.*, 1986; Hunt and Brown, 1983; Rightley *et al.*, 1992], is based on the absorption of concentrated sunlight directly by a cloud of reacting particles. The advantages of such a concept are threefold:

1. an efficient volumetric absorption is achieved in the particle cloud, where the energy is needed;
2. the highest temperature is attained at the cloud, reducing the thermal load on the reactor walls and the temperature requirement of the materials of construction;
3. a short response time is obtained due to the low thermal capacitance of such a system.

Windows for solar receivers are usually expensive, brittle and require careful mounting. Especially in volumetric reactors with directly irradiated particle flows, the window technology remains an engineering challenge. When possible (if the chemical reaction can be conducted under the presence of air) a windowless reactor is a preferable alternative.

The initial work with solar volumetric reactors involved heating gas suspended particles up to about 1200 K. Because of the relatively low temperature, the reactor could be built from conventional steel alloys. We continued to work at this low temperature, but we also wanted to develop a reactor that would function up to 2500 K. The following sections on volumetric reactors describe our work at developing a high temperature receiver (Section 4.2) and a more modest temperature receiver (Section 4.1). For reactors that operate near 1200 K, we will also describe our work with windowless and closed reactor concepts (Section 4.3).

We also looked at theoretical aspects of reactor design from a modeling perspective using Computational Fluid Dynamics (*CFD*).

CFD is employed in the design and optimization of high-temperature solar chemical reactors where the detailed knowledge of the fluid flow, particle transport, heat transfer and chemical kinetics is needed. *CFD* simulation offers the possibility to calculate velocity, temperature and pressure fields, and particle trajectories, which cannot be measured under the severe radiation flux (above 3000 kW/m^2) and high-temperature (above 1500 K) environment of solar furnace experiments. *CFD* validation is accomplished by comparison with experimental results in cold operating conditions.

We use the general-purpose *CFD* code CFX-4 [CFDS-FLOW3D, 1994; CFX-F3D, 1995; CFX-4, 1997] to simulate the fluid-particle flow and the heat transfer in different solar reactors. Body-fitted multi-block grids are generated. By default, the governing Navier-Stokes equations are solved applying the convenient and usually fast converging "hybrid" differencing scheme. However, the inherent numerical diffusion may lead to solutions that are quantitatively or even qualitatively wrong [Leonard and Drummond, 1995]. Therefore, the second-order accurate and bounded *CCCT* modification of the *QUICK* differencing scheme [Alderton and Wilkes, 1988]

is preferred. The *SIMPLEC* velocity-pressure coupling algorithm [Van Doormal and Raithby, 1984] is used. An improved Rhie-Chow treatment [Rhie and Chow, 1983] along with quadratic extrapolation of pressure at domain boundaries is implemented. The algebraic multigrid (*AMG*) solver is employed for all equations including the pressure correction equation. A re-normalization group (*RNG*) modification of the standard high Reynolds number version of the k-ε turbulence model can be invoked, since the conventional k-ε turbulence model often fails to predict swirling flows correctly [Leschziner, 1994].

4.1 Open Moderate Temperature Volumetric Solar Reactors

Our desire was to continue to develop volumetric reactors that operate in a continuous mode. In cooperation with the company BUEHLER AG, Uzwil, Switzerland we developed an atmospheric open solar receiver containing a particle/gas suspension (we call this the *Pulsar* reactor, see Section 4.1.1). In parallel, the solar *Cyclone* reactor concept was investigated at *PSI* (see Section 4.1.2, [Steinfeld *et al.*, 1992a]. For both projects, the envisaged reaction was the dissociation of limestone by means of concentrated solar light. The *Cyclone* reactors for solar calcination are described in detail in the following Sections 4.1.3 and 4.1.4. A Falling Particle Reactor (*FPR*) concept for the industrial solar calcination is presented in Section 4.1.5.

4.1.1 *Pulsar* Reactor

From a feasibility study [Zimmermann *et al.*, 1988] and the results of a theoretical [Gronen and Unger, 1992] and experimental [Kübler, 1990] investigation, a reverse flow receiver/reactor concept was suggested (Figure 4.1). This reactor consists of a 4 mm wide annular opening in which the particle/gas stream flows towards the front of the reactor where it is reversed and injected into the open reactor zone. The particle cloud then flows towards the back of the reactor forming a conical particle/gas stream. This reactor concept differs from others because a smaller amount of air is drawn into the reactor through the aperture.

1 Annular inlet slit

2 Particle cloud turning part of the receiver

3 Entrance of the solar radiation

4 Inlet air flow for the vortex

5 Central exhaust

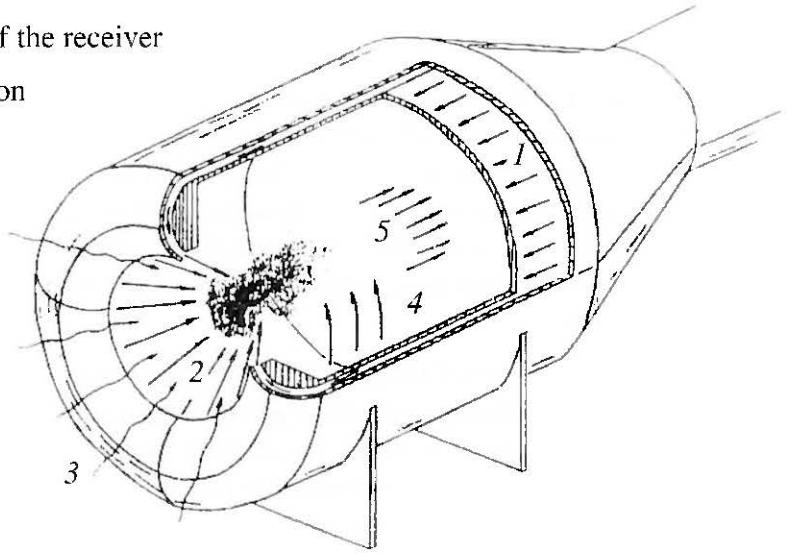

Figure 4.1 Reverse flow concept of the *Pulsar* receiver/reactor

The objective of the solar experiments was the investigation of the reactor concept (Figure 4.1) at an operating temperature below 570 K. This temperature level was selected in order to use ordinary construction material and to study thermodynamic effects like gas expansion, convection and buoyancy. In regard to the *in situ* generation of CO_2 gas which occurs along the dissociation reaction of limestone the dissociation reaction of sodium hydrocarbonate has been selected:

$$2NaHCO_3(s) \rightarrow NaCO_3(s) + CO_2 + H_2O \tag{4.1}$$

This reaction takes place between 380 and 430 K and shows an enthalpy difference of approximately 750 kJ/kg.

4.1.1.1 Reactor Design and Experimental Set-Up

The atmospheric open reverse flow solar reactor depicted in Figure 4.1 has an aperture diameter of 150 mm. The reverse flow was stabilized by a tangentially injected air stream.

The experimental set-up, depicted in Figure 4.2, consisted of a pneumatic conveying system and a suction unit. This unit was used to maintain a static pressure in the aperture of the reactor to prevent particles leaving through the aperture. A central component of the conveying system was the injector which had to accelerate the entrained solid particles entering the reactor. The injector was operated by compressed air (*Roots* blower) and fed from a twin screw feeder. The design parameters are summarized in Table 4.1.

The particle cloud established in the reactor was drawn out of the reactor, moved to the cyclone separator, and then to the ultra-fine filter. To operate the ultra-fine filter, an exhaust unit was required. All these components including the attenuator to move the reactor in or out of focus were conducted by an electronic control system.

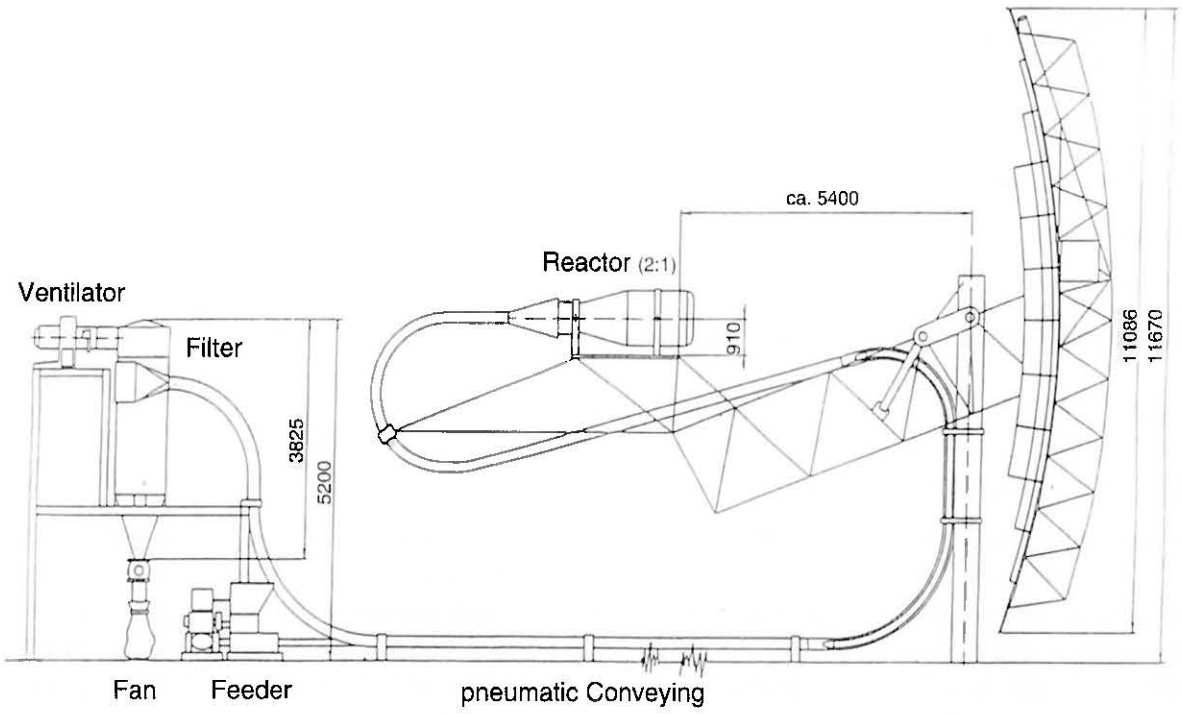

Figure 4.2 Experimental set-up of the *Pulsar* reactor

Table 4.1 Design parameters of the experimental set up for the *Pulsar* reactor

Injector	Gas velocity:	180 m/s	$\varnothing_{Nozzle}$ = 11.5 mm
Screw feeder	Particle mass flow rate:	35 kg/h	
Roots blower	Air mass flow rate:	75 kg/h	@Δp = 280 mbar
Exhaust blower	Air mass flow rate:	148 kg/h	@Δp = 20 mbar
Conveying tube	Length = 30 m		$\varnothing_{Tube}$ = 40 mm
Suction tube	Length = 30 m		$\varnothing_{Tube}$ = 60 mm

The degree of dissociation was found by dissociating the remaining sodium hydrocarbonate in a thermal-gravimetry balance. An indication of the actual degree of dissociation was generated by an infrared extinction coefficient device. All the electronic read-outs like mass flow rates, temperatures, etc. were monitored, stored and processed on a Personal Computer System. After data processing the results can be summarized as follows (Table 4.2) [Nater 1994].

Table 4.2 Summarized experimental results for the *Pulsar* reactor.

Conveying air	$\dot{m}_{air,out}$	75 kg/h
Vortex air	$\dot{m}_{vortex}$	5 kg/h
Exhaust gas flow at reactor exit	$\dot{m}_{exhaust}$	148 kg/h
In situ produced CO_2	$\dot{m}_{CO_2}$	8.4 kg/h
False air mass flow rate	$\dot{m}_{air,aperture}$	60 kg/h
Particle mass flow rate	$\dot{m}_{solid}$	35 kg/h
Loading ratio	μ	0.25
Solar input	P_{solar}	20 kW
Gas temperature after reactor	$T_{reactor}$	165°C
Chemical efficiency	ε	92%
Chemical power	P_{chem}	6.92 kW
Particle residence time in sunlight	$t_{sunlight}$	0.05 s
Particle residence time in reactor zone	$t_{reaction}$	0.20 s

4.1.1.2 Conclusion

It has been demonstrated that a particle cloud can be maintained also in a flow-through reactor based on the reverse flow concept. A very important conclusion is the fact that already at 300°C the amount of air drawn into the reactor to establish a stable particle cloud results in a very negative effect to the reactor efficiency. It is expected that the influence of this air on the reactor efficiency will increase with temperature. The extent of this effect, as found in this experimental investigation, was higher than predicted by a theoretical *CFD* simulation.

4.1.2 *Cyclone* Reactors for Solar Calcination

The decomposition of limestone ($CaCO_3$) has been selected as a model reaction to study solar reactors containing particle/gas suspensions [Steinfeld *et al.*, 1992a]. This reaction, which is the main endothermic step in the cement production process, is characterized by the equation

$$CaCO_3 \rightarrow CaO + CO_2 . \tag{4.2}$$

It is a solid-gas reaction complicated by the fact that reactants and products need to be fed, removed and separated. We have designed a solar receiver-reactor that executes these three operations in a continuous mode, and, in addition, combines the distinctive features of both the cavity-receiver and volumetric-reactor concepts. It is essentially a cyclone gas-particle separator (see Figure 4.3), which has been previously suggested as a solar reactor to conduct gas-solid reactions [Villermaux, 1979, Ambriz *et al.*, 1985]. The conventional cyclone configuration has been modified to let concentrated solar energy enter the cavity through a windowless, atmospheric-open aperture [Imhof, 1990].

At 1170 K and 1 atm., the Gibbs free energy change of the reaction 4.2 is zero [JANAF Tables, 1985]. The total energy required to effect this endothermic transformation is the enthalpy change of the reaction, about 165 kJ/mol. Previous studies on the decarbonation of calcite using solar energy [Badie *et al.*, 1980, Salman and Kraishi, 1988] have shown that the process is technically feasible and a high degree of chemical conversion can be achieved. Preliminary experimentation at our solar furnace, in which samples of $CaCO_3$ powders were exposed to direct high solar fluxes, resulted in complete decomposition to CaO and CO_2 [Durisch *et al.*, 1990]. Various solar reactor types, among them rotary kiln and fluidized beds, have been tested, and thermal efficiencies of about 15 percent were measured [Flamant *et al.*, 1980].

We have shown by simple thermodynamic analysis that if we were to conduct the reaction in the presence of air, which for this specific reaction acts as an inert gas, then the equilibrium is displaced to favor the products CaO and CO_2 [Imhof *et al.*, 1991]. Therefore, atmospheric-open (windowless) reactors can be used. Windows for solar receivers are usually expensive, brittle, require careful mounting, often fail to withstand high solar fluxes/high temperatures, and reduce the solar energy absorption efficiency. When possible, a windowless reactor is certainly a preferable alternative.

In this work we experimentally investigated how to effect the calcination process using the atmospheric-open solar *Cyclone* reactor.

4.1.3 15 kW *Cyclone* Reactor

Two reactor prototypes, of the same configuration but different dimensions, were fabricated. The larger reactor designed for use at the 60 kW McDonnel Douglas dish, has been described in a previous paper [Imhof *et al.*, 1991]. We describe here the smaller reactor prototype, shown schematically in Figure 4.3 for a more detailed diagram see Imhof, 1990). The reactor's main body is a truncated conical cavity, made of DIN-1.4435 steel, 30 cm height, 10 degree cone opening angle, major circular opening of 20 cm diameter, 3 mm thickness. The walls have been insulated with a 12 cm thick layer of *Carborundum Durablanket* (47 percent Al_2O_3, 53 percent SiO_2, max. use temperature 1533 K) and *Wacker Chemie WDS* (65 percent SiO_2, 15 percent FeO, 16 percent TiO_2, max. use temperature, 1123 K).

The remainder of the cavity is formed by two concentric cones that form a conical gap for the gas exhaustion. The upper cone, which is exposed to the direct incoming radiation, is a water-cooled double-wall made of steel, that contains a 6 cm-diameter circular aperture. The front face

has been plasma-coated with a highly reflective aluminum oxide layer, in order to reduce absorption of the spilled radiation and reflect some portion of it into the aperture. The lower cone joins the main body through a concentric cylinder that has a small tangential slot through which the particle/gas stream is been fed. Incoming concentrated solar radiation enters the cavity through the aperture and strikes directly the particles and the cavity walls, undergoes multiple reflections, and is redistributed. Some of this radiation will be absorbed by the insulated walls. As their temperature rises, they will emit more and more diffuse radiation, which undergoes multiple reflections until it is absorbed either by the particles or by the cavity walls, or eventually escapes through the aperture. Other mechanisms of heat transfer include forced convection between the cavity walls and the gas stream, between particles and the gas stream, convection losses through the aperture, and conduction losses through the insulation. In addition, solid particles are swept across the hot reactor walls and are subjected to conduction. Energy transferred to the fluidized $CaCO_3$ particles is used to raise their temperature and to drive their decomposition reaction.

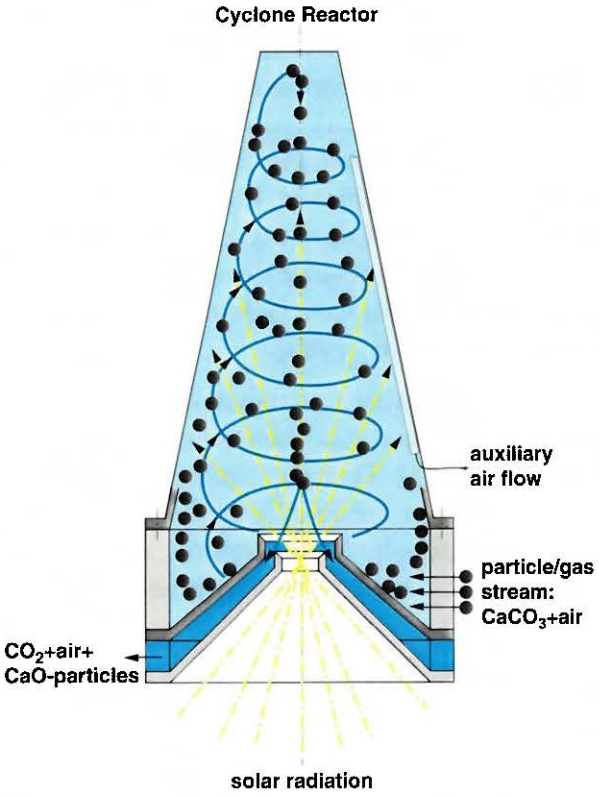

Figure 4.3 Scheme of the Solar *Cyclone* Reactor.

The ability of this cavity-type configuration to capture the incoming concentrated radiation is measured by its apparent absorptance. The apparent absorptance of a cavity is defined as the fraction of energy flux emitted by a blackbody surface stretched across the aperture that is absorbed by the cavity walls [Lin and Sparrow, 1965]. Because of multiple reflections among the cavity walls, the apparent absorptance usually exceeds the surface absorptance of the inner walls. We have calculated the apparent absorptance for our conical cavity using a Monte-Carlo ray-tracing simulation. The incoming radiation entering the cavity-receiver was assumed uniformly distributed over the aperture and to have a directional distribution which is characteristic of our heliostat-concentrator system. We obtained values for the apparent absorptance close to one, even for poorly absorbing surfaces. For example, for wall absorptance of 0.36, which is consistent with reported values of normal total absorptivity of iron for the solar spectrum [Siegel and Howell, 1981], the apparent absorptance is 0.97. In general, the apparent absorptance for diffuse reflecting walls is slightly higher than for specularly reflecting ones.

4.1.3.1 Experimental

The experimental set-up is shown in Figure 4.4. The reactor is positioned horizontally, coaxial with the axis of the solar concentrator. Its aperture lies in the focal plane. (If the reactor is to be run in a vertical position, a 45 degree mirror is to be implemented). Compressed air flows through an injector where $CaCO_3$ is automatically fed with a *Gericke GLD-85* screw-feeder. Particles and air stream enter the cavity through a tangential slot. Inside the cyclone separator the carrier gas (air) forms a vortex with high tangential velocity producing a high centrifugal force to the entrained particles, throwing them to the cavity walls where they swirl in a spiral

path. *CaO* produced is collected and eventually removed at the bottom. CO_2 gas evolved is exhausted together with the air stream through the exhaustion channel. The outlet stream flows through a second cyclone to capture very small particles that did not separate in the reactor. Then the gas is cooled in a heat exchanger and pumped out to the atmosphere. The air/particle leakage through the windowless reactor aperture could be controlled and practically eliminated by the suction unit at the outlet duct.

Type-K thermocouples were placed at various locations inside the cavity walls (but not exposed to the direct irradiation), and on the insulated outer walls. Other parameters measured were pressure, temperature, and volume flow rate of inlet and outlet flow. Power into the cavity was measured optically by an image processing technique [Schubnell *et al.*, 1991]. Every 15 minutes, a water-cooled alumina-coated screen, which closely approximates a *Lambertian* target, was moved to the focal plane and a picture was taken using a *CCD* camera and a 1000 nm narrow-band filter. The procedure lasted 30 seconds. This picture was calibrated by simultaneously measuring the flux density with a *Kendall* point radiometer and processed pixel-by-pixel to obtain the power flux distribution at the focal plane. A similar picture was also taken from the reactor front face to obtain the exact position of the aperture opening relative to the flux contour. Integration of the power flux over the aperture area gave the total power input to the cavity. The *CCD* camera was also used to continuously monitor the position of the reactor at the focal plane. That way we could optimize the positioning in order to intercept the regions of maximum flux intensity. Direct solar irradiation was measured by an *Eppley* pyrheliometer on an *altazimuth* tracking mount. Data acquisition and recording was made via *ACRO* Data Logger, connected to an *IBM-PC*, which allowed real time graphic displaying and verification of the parameters mea-

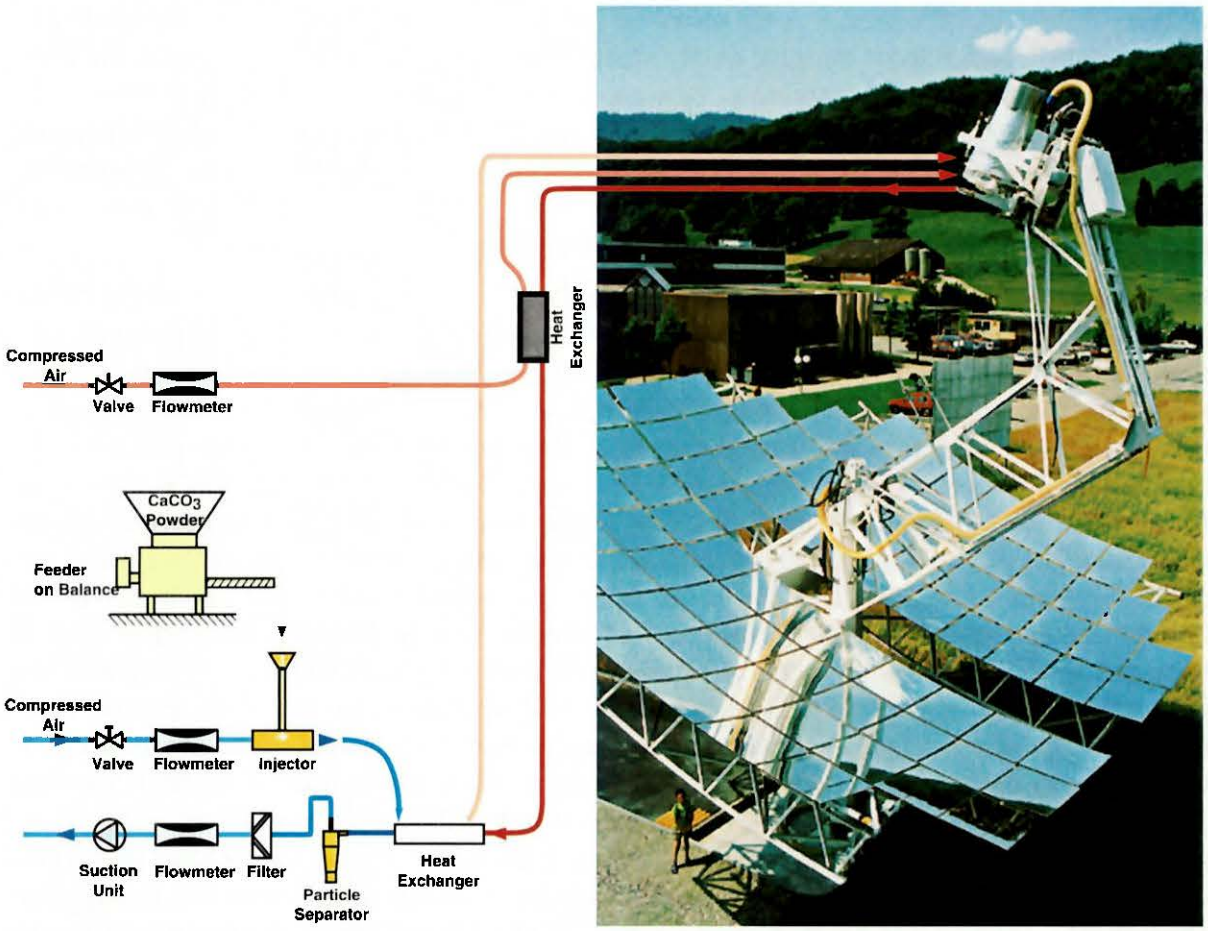

Figure 4.4 Experimental set-up for the solar *Cyclone* reactor (left). The picture shows the 60 kW prototype reactor mounted on the *McDD* dish (right).

sured. The nature of reaction products was determined by X-ray powder diffraction with a *Siemens*-D500 diffractometer. Quantitative results were calculated from thermogravimetric analyses with a *Netzsch* TASC 414/2 thermobalance.

4.1.3.2 Results

We report here results from a representative experiment. Because of the transient characteristics of the experiment, the continuous data measured have been averaged for a period of time under approximate steady-state conditions.

The peak flux concentration ratio observed was 1410 suns (1 sun = 1 kW m^{-2}). The mean flux concentration ratio associated with the aperture, calculated as the average radiation intensity through the aperture divided by the solar intensity, was 1162. The area of the solar image at the focal plane, that received at least 10 W cm^{-2}, was 123.4 cm^2. The area of the aperture was 28.3 cm^2. Integration of the power flux over the image area gave the total power coming from the solar concentrator, 7.36 kW. This is a relatively low value compared to the theoretical maximum power available in the spring season from this collection system [Schubnell *et al.*, 1991]. Losses are due to optical imperfections such as mirror misalignment and not perfectly specularly reflective mirrors, imperfectly matched heliostat and concentrator dish, and shadowing effects from the reactor, photographic screen and peripheral instrumentation. Integration of the power flux over the aperture area gave the input power to the cavity, 3.01 kW. Thus, the aperture was intercepting only 41 percent of the total power available. A larger aperture would certainly intercept more dispersed sunlight. However, the high operating temperatures prompted us to use a smaller aperture to reduce re-radiation losses, which are proportional to $a_p \cdot \varepsilon \cdot \sigma \cdot T^4$, where a_p is the aperture area, ε is the effective emittance of the cavity, σ is the Stefan-Boltzmann constant, and T is the nominal cavity absolute temperature. As a consequence, the aperture size is the result of a compromise between radiation capture and reradiation losses. The high reflective surface of the front face may help redirect some portion of the spilled radiation into the aperture but this amount is negligible since it reflects in a diffuse manner. To some extent, the spillage problem may be made tractable by the use of secondary concentrators which may relax optical tolerances and increase design flexibility.

Inlet air mass flow rate, without particles, was 6 kg/hr. Outlet mass flow rate was varied during experimentation between 6 to 10 kg/hr in order to minimize leakage and convection losses through the aperture. $CaCO_3$ powder from *Fluka Chemika*, with particle size in the 1-5 μm range, were fed at a rate of about 0.6 kg/hr, during intervals of 5 minutes. The loading ratio, i.e. the solid particle mass flow rate over the air mass flow rate, was then 0.1. Inner wall temperatures, under more or less steady-state conditions, ranged between 1200 and 1450 K. Inlet flow temperature was 298 K; maximum outlet flow temperature was 820 K. The temperature of the flow inside the reactor was probably higher, especially in the vicinity of the reactor walls, because the temperature measurement at the outlet duct also included cold, fresh air sucked through the aperture. The power transferred as sensible heat to the particles/air flow was, at least, 1.01 kW. The power absorbed as process heat during the calcination, assuming reaction went to completion, was 0.28 kW. We define energy absorption efficiency of the receiver-reactor as the ratio of the overall energy absorbed, sensible and process heat, to the energy incident underline only on the receiver aperture. The efficiency obtained was 43%; if based on the total energy incident on the focal plane, the efficiency was (0.43)(0.41)=18 percent.The average thermal resistance of the insulation was estimated to be 4 m^2 K W^{-1}. Power lost through the insulation by conduction was about 0.5 kW. Power lost by radiation and convection through the aperture was, from energy balance calculation, 1.23 kW. Of this, about 48 percent was due to reradiation losses. The major source of errors in this heat balance calculation are the calibration

of the *CCD* camera diaphragm vs. the *Kendall* point radiometer, uncertainties in the particle and gas temperatures inside the reactor, and unsteady-state conditions during experimentation. The values reported are believed to be accurate within 10 percent.

A typical experiment lasted about 2 hours; at least 30 minutes were necessary to heat the reactor to 1300 K and obtain steady conditions. Representative samples of particles from two locations were taken for analysis: sample A was taken from the second cyclone separator during experimentation, and sample B was taken from inside the reactor after the reactor was cooled. X-ray diffraction showed the presence of CaO, $Ca(OH)_2$, and $CaCO_3$ in sample A, and only the presence of CaO and $Ca(OH)_2$ in sample B. The formation of $Ca(OH)_2$ is attributed to the hygroscopic characteristics of CaO that reacted with the air humidity. The degree of calcination, defined as moles of $CaCO_3$ decomposed over the moles of $CaCO_3$ in the feed, was determined by thermogravimetric analysis. We obtained between 53 to 94 percent calcination for sample A, and 100 percent calcination for sample B. Evidently, the particles taken from inside the reactor (sample B) had enough residence time to undergo complete decomposition. The particle residence time can, in principle, be adjusted to meet kinetic requirements by changing mass flow rate, loading ratio, and removal rate. The rate of weight loss of the $CaCO_3$ powder used in the solar experiments was studied by thermogravimetric dynamic measurements. The kinetic parameters in the Arrhenius equation were determined by fitting the data to the contracting geometry rate law [Gallagher and Johnson, 1973], given by $dx/dt = k\cdot(1-x)^{0.5}$, where x is the fraction of the solid decomposed at time t, and k is the rate constant. This led to a value of $7.24\cdot10^{-4}$ s^{-1} for the pre-exponential factor A, and 156.8 kJ/mol for the activation energy E_a. According to these numbers, 55 seconds are required to obtain complete conversion at 1300 K. However, a pronounced dependence of the rate constant upon particle size, sample weight, purge gas velocity and heating rate has been reported [Gallagher and Johnson, 1973, Romero *et al.*, 1989]. The mechanism of the reaction was found to be controlled by the transfer of heat to the reaction boundary, and by the diffusion of CO_2 away from it [Hills, 1968]. The heat and mass transport in the solar *Cyclone* reactor experiment was substantially different than that in the thermogravimetric measurements. Therefore, discrepancies are to be expected when evaluating resident time requirements in the solar reactor based on the calculated kinetic parameters.

4.1.3.3 Conclusions

We have designed, fabricated, and tested a solar *Cyclone* reactor to conduct gas-solid reactions. It has a cavity-type configuration which can capture solar radiation efficiently. It provides direct incidence of concentrated sunlight at the reaction site. In addition, heat absorbed by the cavity walls is efficiently being transferred by forced convection to the carrier gas. Reactants are continuously fed; products are being separated and can continuously be removed. It is windowless and therefore restricted to reactions under open-atmospheric conditions. Potential applications of this solar reactor include the thermal decomposition of carbonates and hydroxides of Group IIA elements in the periodic table ($CaCO_3$, $MgCO_3$, $Mg(OH)_2$, $Ca(OH)_2$, etc.), in which the reactant is a solid carbonate or hydroxide and the product consists of a solid oxide and CO_2 or H_2O gas [Wentworth and Chen, 1976]. These reactions have large enthalpy change and therefore are attractive for the purpose of solar thermal energy storage. Other solid-gas reactions of interest, such as coal/biomass gasification, require the use of a window to isolate the products from the oxygen in the atmosphere. We have tested the reactor in the solar furnace with the $CaCO_3$ decomposition reaction at about 1300 K and obtained high degree of calcination. The energy absorption efficiency, based on the energy incident on the receiver aperture was 43 percent.

4.1.4 60 kW *Cyclone* Reactor

Next, a large 60kW Solar *Cyclone* Reactor was built and tested on *PSI*'s parabolic solar concentrator (*McDD* dish) in summer 1995. A counter-current flow heat exchanger was employed to preheat the reactants. The tests were carried out in a continuous mode of operation. The experimental set-up is also depicted in Figure 4.4.

Different kinds of limestones and cement raw mixtures were dissociated. As shown in Table 4.3, the highest degree of calcination[1] of 85% was obtained with a cement raw mixture containing 75% limestone. The related process conditions are summarized in Table 4.4. Figure 4.5 shows the temperature profile during the experiment. The results demonstrate that the decomposition of limestone with solar energy is technically feasible. To match the requirements of the cement production process further development and refinement of the system will have to be done. This was the subject of the performed negotiation with industry.

Table 4.3 Degree of calcination with different types of limestone

Synthetic limestone	≈ 41 to 47%
Natural limestone, white	≈ 38 to 54%
Natural limestone, black	≈ 52 to 58%
Cement raw material	≈ 52 to 85%

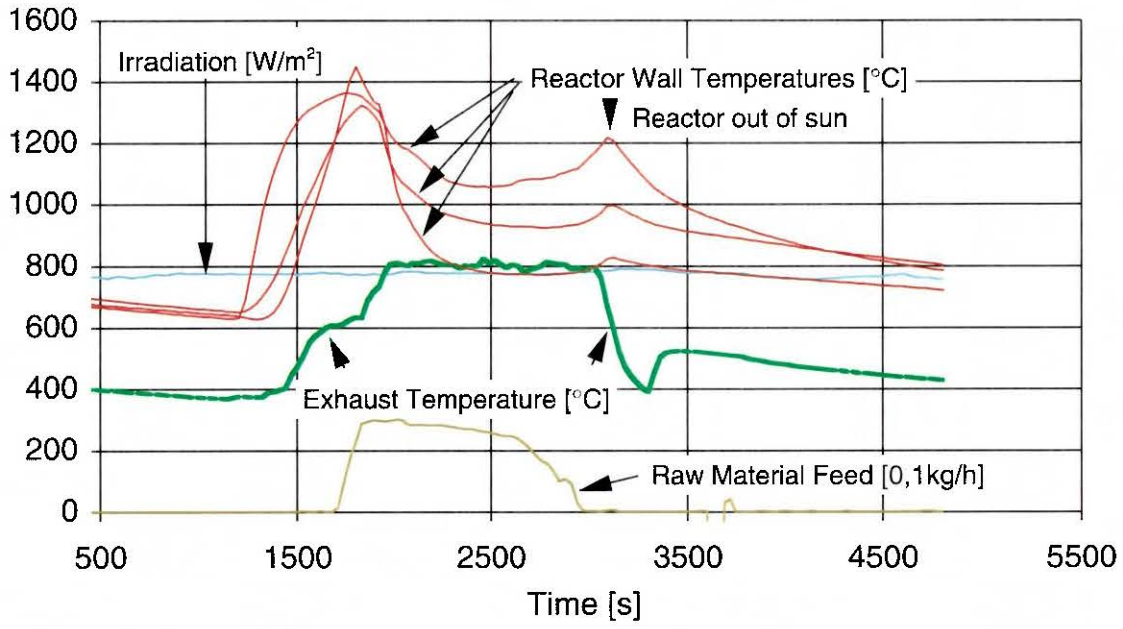

Figure 4.5 The calcination experiment of June 30, 1995 is shown. With the *PSI* raw material a degree of calcination of about 85% is reached

[1] Degree of calcination = 1-(mol $CaCO_3$ in product / mol $CaCO_3$ in inlet)

Table 4.4 Experimental results with cement raw material

Particle feeding rate	≈ 25 kg/h
Inlet air flow rate	≈ 80 kg/h
Outlet air flow rate	≈ 160 kg/h
Solar input power	≈ 54 kW at 800 W/m^2
Degree of calcination	≈ 85%
Chemical conversion efficiency[a]	≈ 15%
Process efficiency[b]	≈ 88%

a. Chemical conversion efficiency = ΔH / Solar-Input

b. Process efficiency = (Sensible heat of air and particles ΔH_r) / Solar-Input

4.1.5 Falling Particle Reactor

To clarify important questions that have a large impact on the design of solar cement plants, task-sharing with related industries was established. The results of these negotiations [Imhof 1996; Imhof 1997a; Imhof 1997b] are as follows:

1. The application of solar energy to the calcination step is technically feasible. In order to perform a round the clock production process a solar assisted cement plant has to be equipped with a fossil fired flash calciner (Figure 4.6).
2. A Hybrid Solar Cement Plant has to be scalable up to the performance level of conventional 3000 tons clinker per day plants, which corresponds to solar input power of 80 to 100 MW.
3. From a technical point of view, the size of an 80 MW solar calcinator, e.g. it's aperture diameter should not exceeded approximately 6 m. In regard to the energy losses through the aperture by reradiation and convection the aperture diameter should be as small as possible.

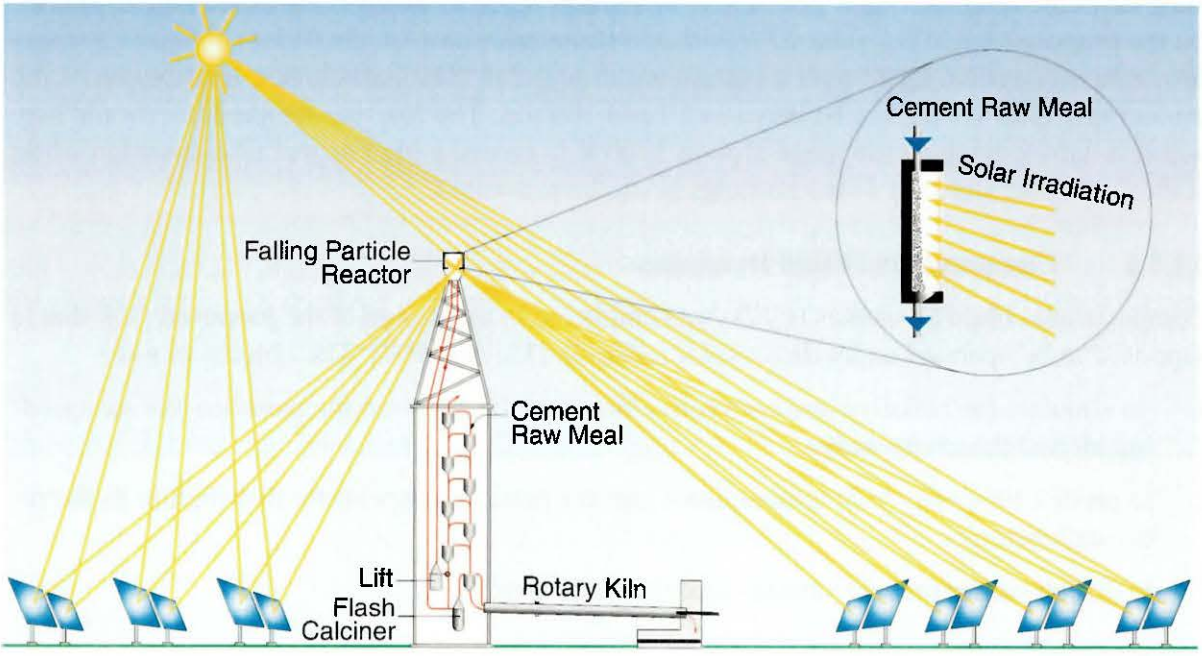

Figure 4.6 Scheme of an Industrial Solar Cement Plant [Meier, 1998].

In this context the achievable solar concentration ratio in a Central Receiver System is a very important question. A theoretical investigation [Steinfeld and Schubnell, 1993] reports that a flux density of approximately 3 MW/m^2 is required for a process temperature of approximately 900°C. An other study [Vant-Hull *et al.*, 1998] came to the conclusion that a high average flux density can be achieved with a properly optimized circular central receiver systems without the use of a terminal concentrator and without a serious increase in the cost/benefit ratio for the system.

4. Large amounts of conveying gases and high convection heat losses are contradictory in regard to a high reactor efficiency [Stine *et al.*, 1988]. Therefore the Falling Particle Receiver/reactor (*FPR*) [Falcone, 1984; Denk, 1996] has been identified by industry as a potential reactor concept for an industrial application (Figure 4.7).

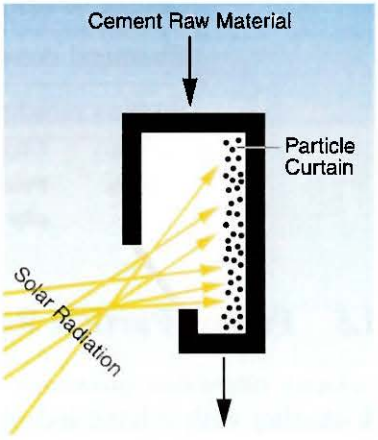

Figure 4.7 Scheme of the Falling Particle Receiver

Regarding the facts mentioned above the *FPR* operated in the face down mode seems to be a promising reactor system to achieve a high reactor efficiency. A face down reactor system has to be installed on top of a tower and requires a pneumatic conveying system to lift up the preheated cement raw material (700°C). Since the raw material preheating system of a modern 3000 Tato[2] cement plant is installed inside of an approximately 80 m high concrete tower, the tower height has to be increased only by about 20 m (Figure 4.6).

Falling Particle Reactor (FPR) Specifications

The reactor dimensions have to match the requirements of the cement industry [Imhof, 1996b] with the specific solar operating conditions. Highly concentrated solar radiation (about 1 MW m^{-2}) is used as the source of process heat for the calcination process. For a typical solar industrial cement plant (3000 Tato cement corresponding to about 100 MW$_{th}$), it was found from energy calculations (neglecting kinetic concerns) that the particle mass flow rate in a *FPR* must be in the order of 2 kg s^{-1} per meter of curtain width to achieve 90% calcination. Hence, for the proposed 1.5 MW$_{th}$ solar *FPR* with an estimated curtain height of 5 m, the particle mass flow rate is about 0.6 kg s^{-1} over a curtain width of 0.3 m. The particle size distribution of the cement raw meal is found to be between 10 and 100 µm. The reaction temperature should stay within a narrow temperature range around 1200 K to ensure a high degree of calcination while at the same time sintering of the particles has to be prevented.

4.1.5.1 Computational Fluid Dynamics

Computational Fluid Dynamics (*CFD*) was employed in the design of the proposed *FPR* that is supposed to be operated under direct solar radiation [Meier, 1998]. The objectives were

1. to simulate the radiative and convective heat transfer between the particles, the surrounding air and the cavity walls;
2. to predict the cavity wall temperatures and the particle temperature distribution in the receiver/reactor;
3. to determine the particle velocity and residence time;

2. Tato: Tagestonnen (German) = Tons per day

4. to estimate the particle volume fraction as a measure of the particle curtain thickness.

The general purpose *CFD* code CFX-4 [CFX-4, 1997] was used. Basic features of this code have been described previously [Meier *et al.*, 1996].

The gas-particle flow and the convective heat transfer in the solar *FPR* are modeled within the CFX-4 SOLVER. Particle heating by radiation is calculated in the CFX-RADIATION model using the Monte Carlo method. The current version of the CFX-4 Lagrangian particle transport model accounts for radiation from the gas phase to and from the particulate phase but does not update the radiation field in response to absorption by or emission from the particles. This is adequate for many applications where the particle density is low. It is also not possible to combine the particle transport model with the chemistry model. Currently, the CFX-4 code is being modified to include both these options, but it has not yet been fully tested to ensure reliable results.

Model Assumptions

Modeling the fluid/particle flow and the combined convective and radiative heat transfer in the proposed *FPR* requires a wide variety of simplifying assumptions. The three-dimensional problem is treated using a body-fitted grid with Cartesian coordinates. Grids with 13'456 cells, 40'386 cells, and 107'648 cells have been used to check the grid-independence of the solution. The standard k-ε turbulence model with the usual turbulence parameters and the 'hybrid' differencing scheme are employed together with the Algebraic Multigrid (*AMG*) solver for the momentum and pressure equations. The buoyancy-driven flow is assumed to be incompressible, such as is usually the case in free or natural convection. Hence, the *Boussinesq* approximation is used. In the current release of the CFX-4 code, the fluid thermal conductivity is constant, but the specific heat can depend on the temperature. In contrast, particles must have a constant specific heat. They are assumed to be spherical. The equations of particle transport have been described elsewhere [Clift *et al.*, 1978]. The drag force, the buoyancy force, and the added mass force exerted on the particles are included in the present *CFD* calculations [CFX-4, 1997]. In the CFX-RADIATION model, the incident solar flux is simulated using the Monte Carlo method. The photons are released from a flat plate representing the aperture plane (either open to the atmosphere or closed with a transparent window) parallel to the particle curtain. Each photon carries some portion of the total energy and starts at a random position and, for isotropic radiation, in random directions. Heating of the system is provided by this "solar" flux impinging uniformly on the front of the particle curtain. Because the direction of the solar radiation incident from the heliostat field is not yet known, two extreme situations are considered: (a) isotropic radiation and (b) directional radiation perpendicular to the aperture plane. No spectral dependence of the incident solar radiation is modeled. The gas is transparent to radiation. In the present work, no chemical reaction is modeled, and thus the CO_2 release from the $CaCO_3$ particles during the calcination process is neglected. In the current version of the CFX-4 code it is not possible to perform a transient calculation of the particle transport equations. Therefore, the *CFD* calculations are steady-state.

The exploratory *CFD* study was accomplished to gain insight into the performance of a *FPR* exposed to concentrated solar radiation. It predicts the air/particle flow and the combined convective and radiative heat transfer in the proposed *FPR*.

Model Input

The *FPR* is designed as a simple rectangular chute with constant 5 m height and 0.36 m width, and variable depth between 0.36 (Figure 4.8b) and 1.08 m (Figure 4.8a). The air/particle inlet slit has a constant width of 0.30 m and a variable depth between 0.004 and 0.012 m. The dis-

tance from this inlet slit to the rear wall is varied between 0.06 and 0.18 m, and the distance to the transparent window is varied accordingly between 0.30 and 0.90 m. An additional air inlet slit is placed between the particle inlet slit and the rear wall. The air/particle outlet region is modeled as an inclined receiving bin, open at one side (see for example Figure 4.8a,b). For symmetry reasons, only half of the *FPR* needs to be modeled, the computational domain being bounded by a wall on one side and a symmetry plane on the other side. The air/particle inlet temperatures are either 300 K (without preheating) or 1000 K (with preheating), the particle mass flow rate is 0.6 kg s^{-1}, and the air/particle inlet velocity is 0.54 m s^{-1} for all considered cases (assuming a bulk density of 690 kg m^{-3}). The pressure is atmospheric. Two different particle fractions are considered: one with a particle size distribution from 10 to 90 µm, the other between 100 and 900 µm. The spherical particles have a density of 2700 kg m^{-3} and a constant specific heat of 1100 J kg^{-1} K^{-1} [Zimmermann *et al.*, 1988]. The solar radiative source is modeled as non-thermal flux varying between 25 and 100 kW m^{-2}. This solar flux is only used for heating the particles because the endothermic chemical reaction is neglected in the present *CFD* study. Diffusely scattering bounding walls with an emissivity of 0.8 are assumed. The walls are not perfectly insulated, thus allowing heat flux to the outside which is at ambient temperature (300 K). The heat transfer coefficient on the outside wall is assumed to be 5 W m^{-2} K^{-1}.

Model Predictions

Important input parameters and results from the *CFD* simulations are summarized in Table 4.5 for all the cases discussed in the subsequent sections. Only the cases with particle sizes between 100 and 900 µm are considered, and the maximum particle velocity $v_{p,down}$ is taken from the particle fraction with diameter 900 µm. For both the *FPR* with window and the *FPR* open to the atmosphere, the maximum downward air velocity $v_{a,down}$, the maximum upward air velocity $v_{a,up}$, and the maximum air and particle temperatures $T_{a,max}$ and $T_{p,max}$ are shown for the different flux and inlet temperature conditions considered in the present study. For each case, the distance between the air/particle inlet slit and the rear wall $D_{inlet,wall}$ is indicated, too.

Table 4.5 Input parameters and results from *CFD* simulations for particle diameters between 100 and 900 µm

Case	Figure	Initial Conditions				Results from *CFD* Simulations					
		Aperture	$D_{inlet/wall}$ [m]	Flux [kW m^{-2}]	T_{in} [K]	$v_{p,down}$ [m s^{-1}]	$v_{a,down}$ [m s^{-1}]	$v_{a,up}$ [m s^{-1}]	$T_{p,max}$ [K]	$T_{a,max}$ [K]	Stable Curtain
1	4.8a 4.9a	open	0.18	0	300	-8.3	-4.1	0	300	300	yes
2	4.10a,b	open	0.18	100	1000	-5.6	-4.1	4.5	1056	1296	no
3		open	0.06	0	300	-8.8	-5.9	0	300	300	yes
4		open	0.06	25	1000	-5.9	-3.4	4.5	1047	1193	no
5		window	0.06	0	300	-7.9	-4.2	2.2	300	300	yes
6	4.8b 4.9b	window	0.06	25	300	-8.0	-3.7	2.4	1003	1015	yes
7	4.11a,b	window	0.06	25	1000	-8.2	-4.8	4.0	1355	1377	yes

In the following, the major trends that can be read from the *CFD* calculations listed in Table 4.5 (and others) will be discussed. First, we consider *CFD* simulations indicating that a stable falling particle curtain can be established under favorable operating conditions. Figure 4.8a shows particle trajectories for an atmospheric open *FPR* operated isothermally at 300 K (Case 1).

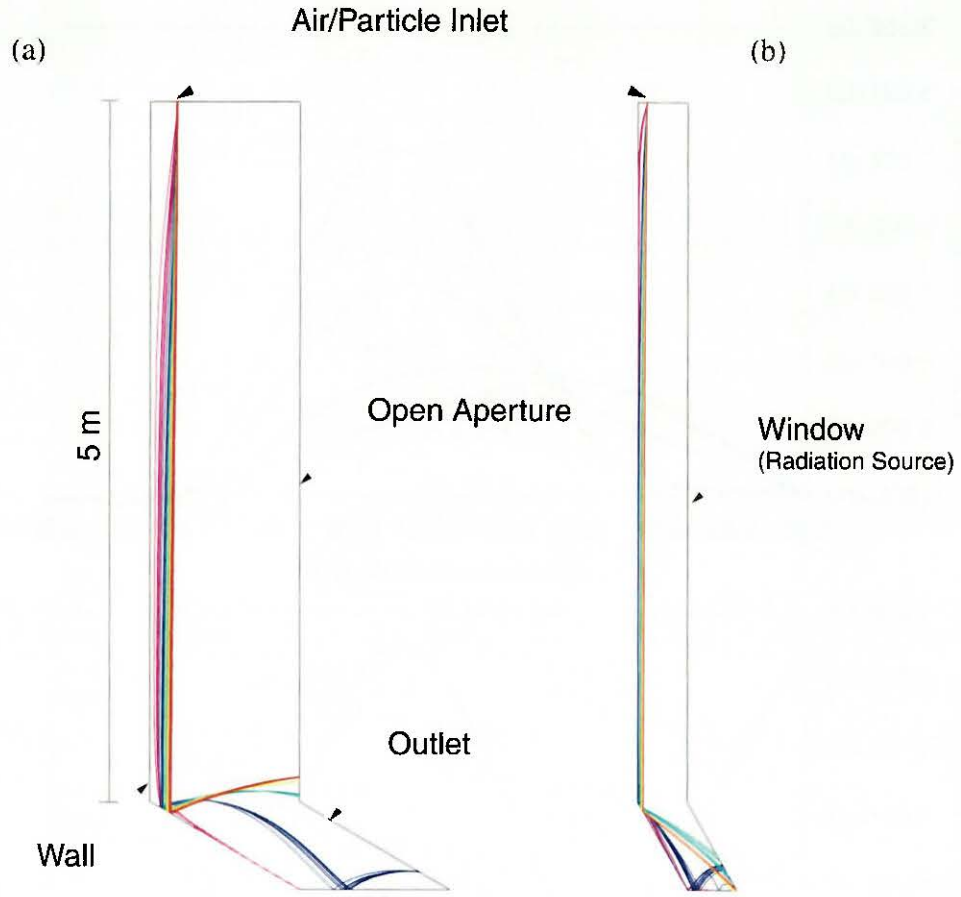

Figure 4.8 *CFD* simulations show particle trajectories forming a stable particle curtain [Meier, 1998]:
(a) for an atmospheric open *FPR* operated under isothermal conditions (Case 1): height 5 m, width 0.36 m, depth 1.08 m, distance between air/particle inlet slit and rear wall 0.18 m; particle inlet slit parallel to rear wall 0.3 m long and 0.012 m wide; particle mass flow rate 0.6 kg s^{-1}, air mass flow rate $2.274 \cdot 10^{-2}$ kg s^{-1}, inlet velocity 0.54 m s^{-1};
(b) for a *FPR* with transparent window (Case 6 with ambient air/particle inlet temperature): height 5 m, width 0.36 m, depth 0.36 m, distance between air/particle inlet slit and rear wall 0.06 m; particle inlet slit parallel to rear wall 0.3 m long and 0.004 m wide; particle mass flow rate 0.6 kg s^{-1}, air mass flow rate $7.578 \cdot 10^{-3}$ kg s^{-1}, inlet velocity 0.54 m s^{-1}, radiative flux 25 kW m^{-2}. Particle diameters: 100, 300, 500, 700, and 900 µm.

Here, the distance between the air/particle inlet and the rear wall is 0.18 m. Decreasing this distance to 0.06 m has no effect on the overall behavior of the *FPR*. For isothermal operating conditions, we observe that a stable particle curtain is formed for both the open *FPR* (Case 3) and the *FPR* using a transparent window (Case 5). Particles entering the cavity at ambient inlet temperature (Case 6) are also falling close to the rear wall and form a stable curtain even if they are heated using a radiative flux of 25 kW m^{-2} (Figure 4.8b). In this case, no particles seem to be entrained by the air flowing along the window up to the top of the cavity. The curtain thickness is approximately equal to the distance between the particle inlet slit and the rear wall. It does not vary much from the top to the bottom, as can be seen from a rough estimate of the particle volume fraction plotted in Figure 4.9a (Case 1 with wall distance 0.18 m) and in Figure 4.9b (Case 3 with wall distance 0.06 m).

Heating the atmospheric open *FPR* with a radiative flux of 100 kW m^{-2} (Case 2) has a negative effect on the particle curtain (Figure 4.10a). Following the trajectories of the particles between 100 and 300 µm diameter, we observe that the lightest particles are carried out of the cavity.

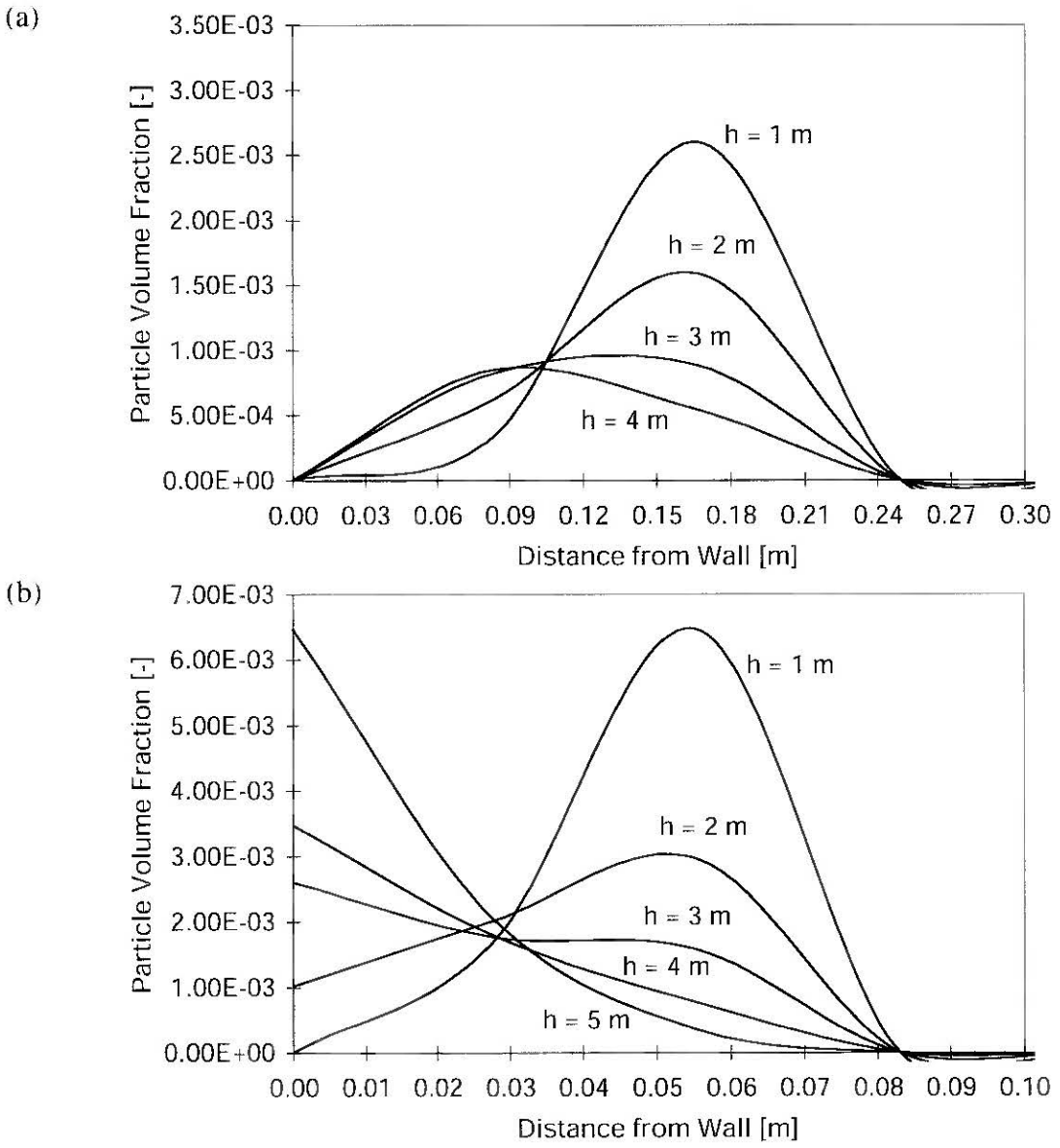

Figure 4.9 Particle volume fraction as a function of the wall distance [Meier, 1998]:
(a) for Case 1 with air/particle inlet slit at 0.18 m from the rear wall;
(b) for Case 3 with air/particle inlet slit at 0.06 m from the rear wall.

This particle outflow is due to convective air currents as seen from the air flow field plotted in Figure 4.10b (enlarged view of the *FPR* top section). The heavier particles are falling down and form a distorted curtain before they are leaving the reactor through the outlet in the inclined receiving bin at the bottom. Moreover, a significant portion of the energy supplied by the radiation source is taken up by the environmental air entering through the open aperture (Figure 4.10b) instead of being absorbed by the particles. A similar behavior is observed for the open *FPR* using a radiative flux of only 25 kW m^{-2} (Case 4). This result is in agreement with experimental findings reported previously for a comparable *FPR* concept [Falcone *et al.*,1985]. The authors of this study state that only particles in the range between 100 and 1000 µm seem to be suited for use in a *FPR*.

In principle, the convective losses and the particle outflow through the open aperture can be controlled by techniques such as air windows or transparent windows. However, in contrast to

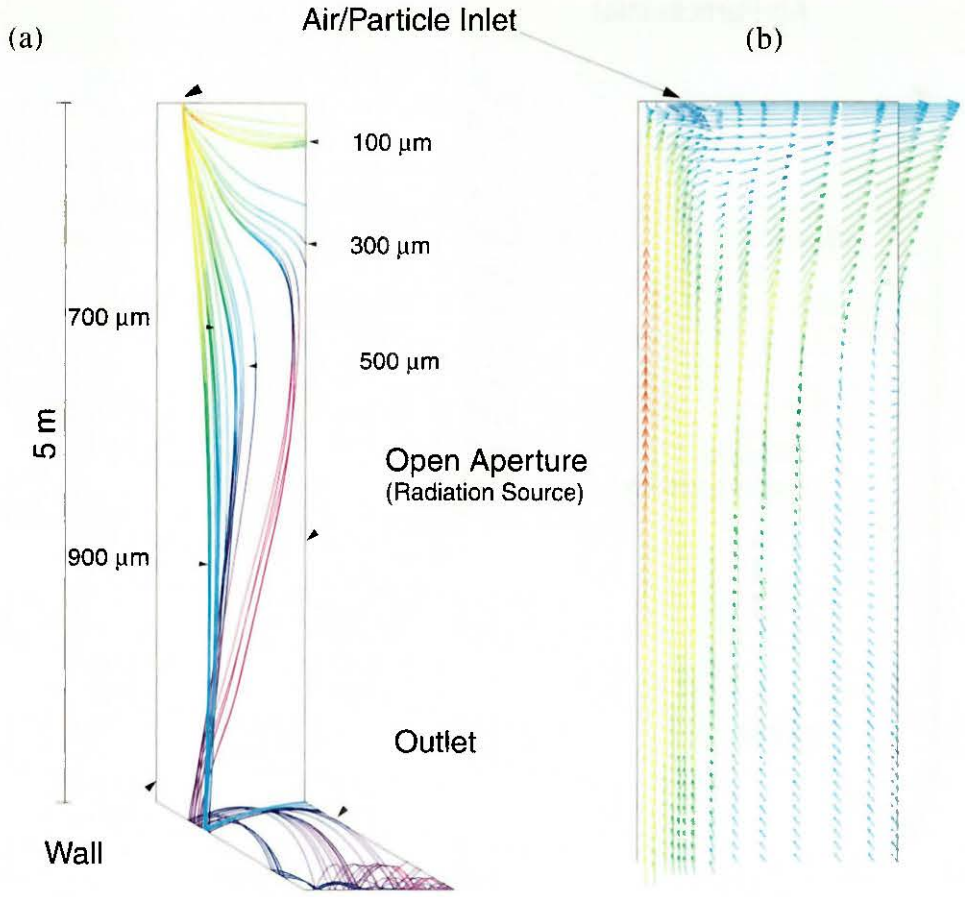

Figure 4.10 *CFD* simulation for an atmospheric open *FPR*, the dimensions given in Figure 4.8a [Meier, 1998]: (a) distorted particle curtain when heated using a radiative flux of 100 kW m^{-2} incident through the aperture (Case 2); particles with diameters less than about 300 µm are carried through the open aperture by (b) convective air currents (enlarged view of the air flow field at the top of the *FPR*).

Case 6 (Figure 4.8b) the *CFD* simulations predict particle uptake by convective air streams along the window (Figure 4.11a) for preheated air/particle inflow (Case 7). This undesired behavior implies additional air streams to keep clean the transparent window which otherwise may crack under the severe high solar flux conditions. Comparing the air flow patterns in the outlet bin, we observe rather laminar air intake for Case 6 and rather turbulent air entrainment and upward acceleration for Case 7 (Figure 4.11b, enlarged bottom section), which corresponds with the maximum upward velocities given in Table 4.5. Hence, there is a higher risk for the particles to be carried up along the transparent window if they are preheated (Case 7) than if they are entering the cavity at ambient temperature (Case 6). From these findings, it seems crucial to design the outflow region properly to avoid the entrainment of the falling particles into the upward air stream when using a window. Suitable mechanical plates will have to be implemented to separate the downward flowing air/particle stream and the upward flowing air current.

One of the most important parameters for characterizing the aerodynamic behavior of the free-falling particle curtain is the particle velocity that defines the particle residence time. Typically, the residence time is between about 1 second for particles of 900 µm diameter and about 1.5 seconds for particles of 100 µm diameter. The cavity temperature distribution is almost uniform in the *FPR* with a transparent window (e.g. Case 7), and thus the mean wall temperatures are close to the mean temperature of the particle curtain.

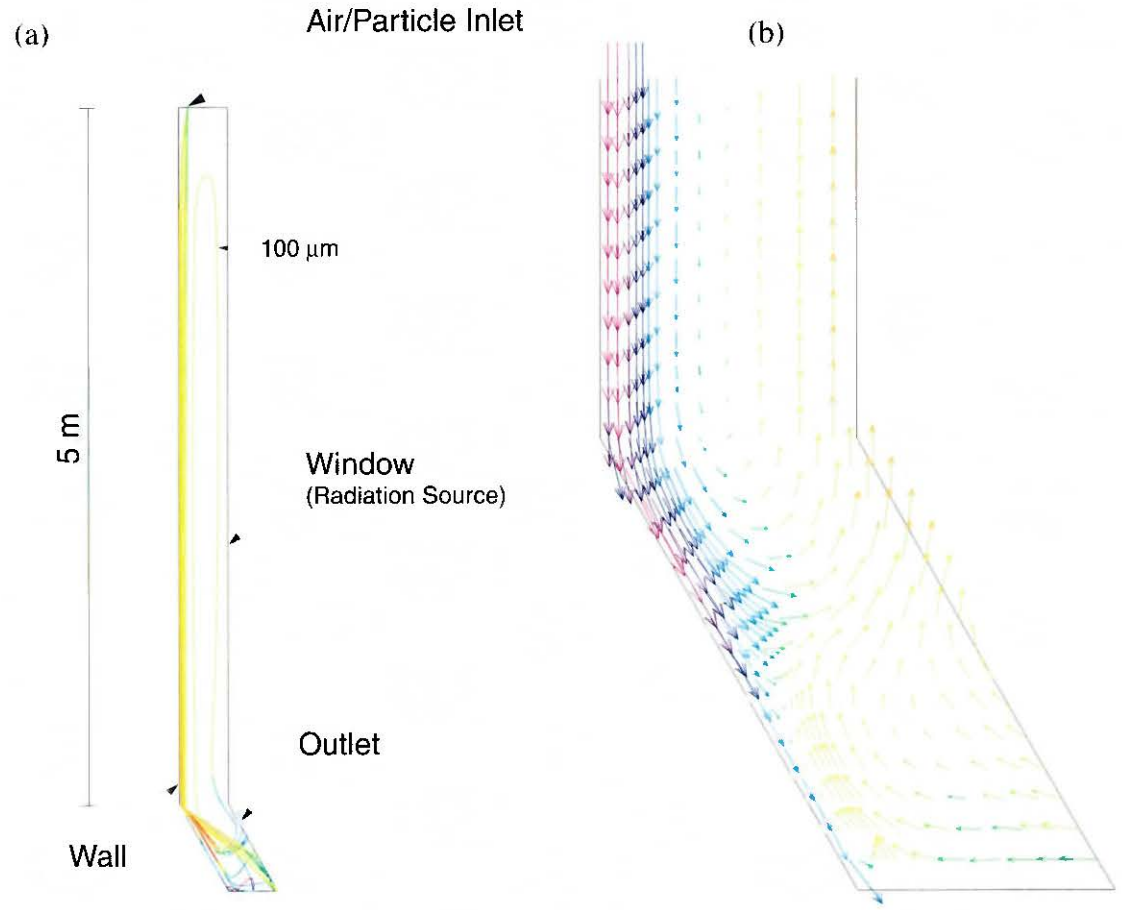

Figure 4.11 *CFD* simulation for a *FPR* with transparent window (Case 7 with preheated air inflow), the dimensions given in Figure 4.8b [Meier, 1998]: (a) Particle trajectories along the rear wall forming a stable curtain, particle recirculation; (b) enlarged view of the bottom region of the *FPR*: vectors representing the air flow field show turbulent entrainment and upward acceleration of air through the open outlet bin and convective air flow along the window up to the top of the cavity.

Model Verification

The *CFD* simulations could not be validated with experimental data because no prototype *FPR* has been built so far. However, the *CFD* results have been checked for grid-independence of the solution and compared with available literature data for a similar *FPR* concept [Hruby, 1986]. The employed assumptions and numerical methods are documented, and the results have been verified with parametric and convergence studies. Usually, the solutions of the *CFD* simulations converged well for the particles with size distribution between 100 and 900 µm. However, for the particles below about 100 µm it was practically not possible to achieve a converged solution, because the calculation started to become numerically unstable and eventually the solution diverged. Furthermore, in most cases the incident solar flux had to be limited to about 25 kW m^{-2} because otherwise the maximum particle temperature exceeded 1400 K creating hot spots and causing numerical problems. However, this is an artifact of the present *CFD* calculations, as the CFX-4 code currently cannot handle chemical reactions in the particle transport model. Thus the energy sink due to the calcination reaction cannot be modeled.

Repetitive *CFD* computations yielded slightly different results even under equal initial and boundary conditions because of the statistical nature of the particle transport model and the

Monte Carlo radiation model used for the *CFD* simulations. Therefore, the computational results must be interpreted with caution. They may not be accurate enough to give exact quantitative flow and temperature fields, but they indicate the overall qualitative trend.

4.1.5.2 Summary of *CFD* Results

We have investigated the performance of a solar Falling Particle Reactor (*FPR*) proposed to be implemented in a pilot and demonstration plant to demonstrate the technical feasibility of the industrial solar calcination. The present study included Computational Fluid Dynamics (*CFD*) modeling of the major aspects of the air/particle flow and the combined convective and radiative heat transfer in such a solar reactor. The *CFD* simulations were exploratory in nature and their aim was to gain insight into the performance of the *FPR* exposed to concentrated solar radiation.

The results of the *CFD* simulations suggest that under favorable conditions a stable operating condition can be established in the *FPR*. However, several areas of uncertainty have been identified. One concerns the particle curtain that may be subject to instabilities under certain conditions. Further investigations are necessary to find out whether these instabilities are inherent to the *FPR* system or whether they are caused by numerical effects. Another critical issue is the residence time of the particles in the *FPR* which may not be sufficiently long to ensure complete calcination of the cement raw meal particles. Inserting suitable mechanical devices such as slopes or steps at the rear wall of the *FPR* could help to reduce the particle acceleration and stabilize the particle curtain. A further problem is the particle containment in an open *FPR* because small particles with a diameter below approximately 300 μm are carried through the aperture by buoyant air currents. In principle, these convective losses can be controlled by techniques such as air windows or transparent windows.

Future work in *CFD* modeling will treat the radiative heat transfer within the *FPR* in more detail. Both the solar spectral dependence and the wavelength dependent particle radiation will be implemented in the *CFD* code. Furthermore, it will be important to include the chemical reaction in the *CFD* model because the release of CO_2 during the calcination process will certainly affect the fluid dynamics inside the solar radiated *FPR*. This forthcoming *CFD* study will give better insight in the performance of the *FPR* exposed to concentrated solar radiation. *CFD* modeling will serve as a design tool in the development of a prototype solar *FPR* that can be operated continuously and has the potential of being scalable for large scale industrial applications.

4.2 Open High Temperature Volumetric Solar Reactors

Even though we want to effect chemical transformations at temperatures near 2500K, we also want to maintain a design philosophy of working with alloy steel, while maintaining all of the design benefits promised by a volumetric reactor. These constraints mean that a temperature gradient of nearly 1000 K is needed between the hot reaction zone and the walls of the reactor. The design must allow for efficient absorption of the solar radiation and allow for effectively use the sensible energy of the carrier gas. This third requirement involves developing a better understanding of the relationship between particle cloud stability and the loading ratio. (The loading ratio is the mass of particles to the mass of carrier gas.)

The research approach was to design, build, and test potential reactors. Besides addressing the design issues described above, this approach gives important hands on experience. In section 2 of this report, one finds a description of our facilities for accomplishing the experimental part of our program.

CFD modeling was employed for the optimization of specific reactor components and their operating conditions. Examples of *CFD* simulations have been described in different publications [Ganz *et al.*, 1996; Meier, 1994; Meier *et al.*, 1996; Meier, 1998a]. In particular a *CFD* study on basic aspects of air flow and convective heat transfer in windowless particle-cloud reactors is summarized in Appendix 8.1(see also [Ganz *et al.*, 1996]).

4.2.1 *JG* Reactor

Our first reactor concept [Ganz *et al.*, 1994] was based on the direct solar energy absorption by a cloud of reacting particles. [Hunt *et al.*, 1986; Rightley *et al.*, 1992]. In initial work, emphasis was placed on finding a means to efficiently absorb the solar radiation. Several reactor concepts were considered, before selecting a central tube reactor [Ganz, 1996]. This reactor concept is illustrated in Figure 4.12 and it is described in detail in the following section. A main design characteristic is that an inlet suspension flows from the back of the reactor to the front, where it becomes exposed to concentrated solar radiation. The hot products exit the reactor through the central tube. This arrangement would enable the hot products to preheat the inlet suspension in a type of counter flow heat exchanger.

Besides efficient absorbing solar radiation, a stable flow pattern is needed for the gas suspension. The major threat to its stability is the buoyancy forces due to the desired temperature gradient within the powder cloud.

4.2.1.1 Reactor Configuration

A schematic diagram of the reactor details is shown in Figure 4.13. Its main body consists of a double-walled cylinder made of steel, 40 cm diameter, 40 cm length. Its front face is water-cooled and plasma-coated with aluminum oxide, and contains a windowless circular aperture of 14 cm diameter. A vortex flow inside the reactor is created by air injected tangentially either via two rows of inlet holes, or through a rotating tube. The vortex flow was our attempt to create a stable particle cloud to counter the destabilizing buoyancy forces set up in the cloud by an impressed temperature gradient.

The two inlet flow options were an important experimental variable. They represented two methods for setting up the vortex flow pattern. It was not clear, *a priori*, which arrangement is best.

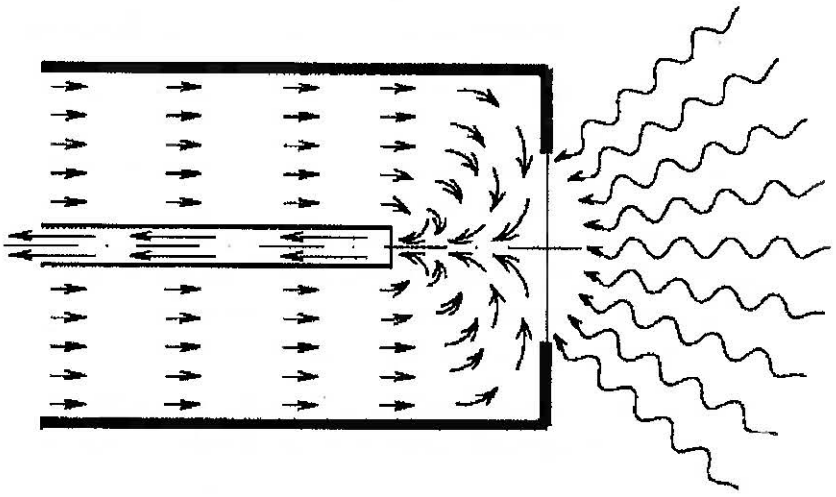

Figure 4.12 Concept of the central tube reactor.

Reactants, in powder form, are conveyed in an air stream and injected into the reactor cavity from the back side. Particles travel to the high-flux zone in a vortex-type flow. Incoming concentrated solar radiation enters the reactor through the aperture and strikes directly on the particles. The particles absorb most of this incident energy, are heated to the reaction temperature and eventually undergo reduction. Finally, particles exit via a water-cooled axial tube where they are quenched to avoid reoxidation. However, this central tube concept can serve as a means for counter flow heat exchange, when quenching is not needed. Some ambient air enters through the windowless aperture and prevents particles from escaping. A radial air jet at the aperture reduces this amount of cold air while producing a more homogeneous cloud inside the reactor.

4.2.1.2 Experimental

A prototype reactor was fabricated and tested at our 15 kW solar furnace. Particles of MnO_2 were utilized as reactants.Table 4.6 shows typical running conditions.

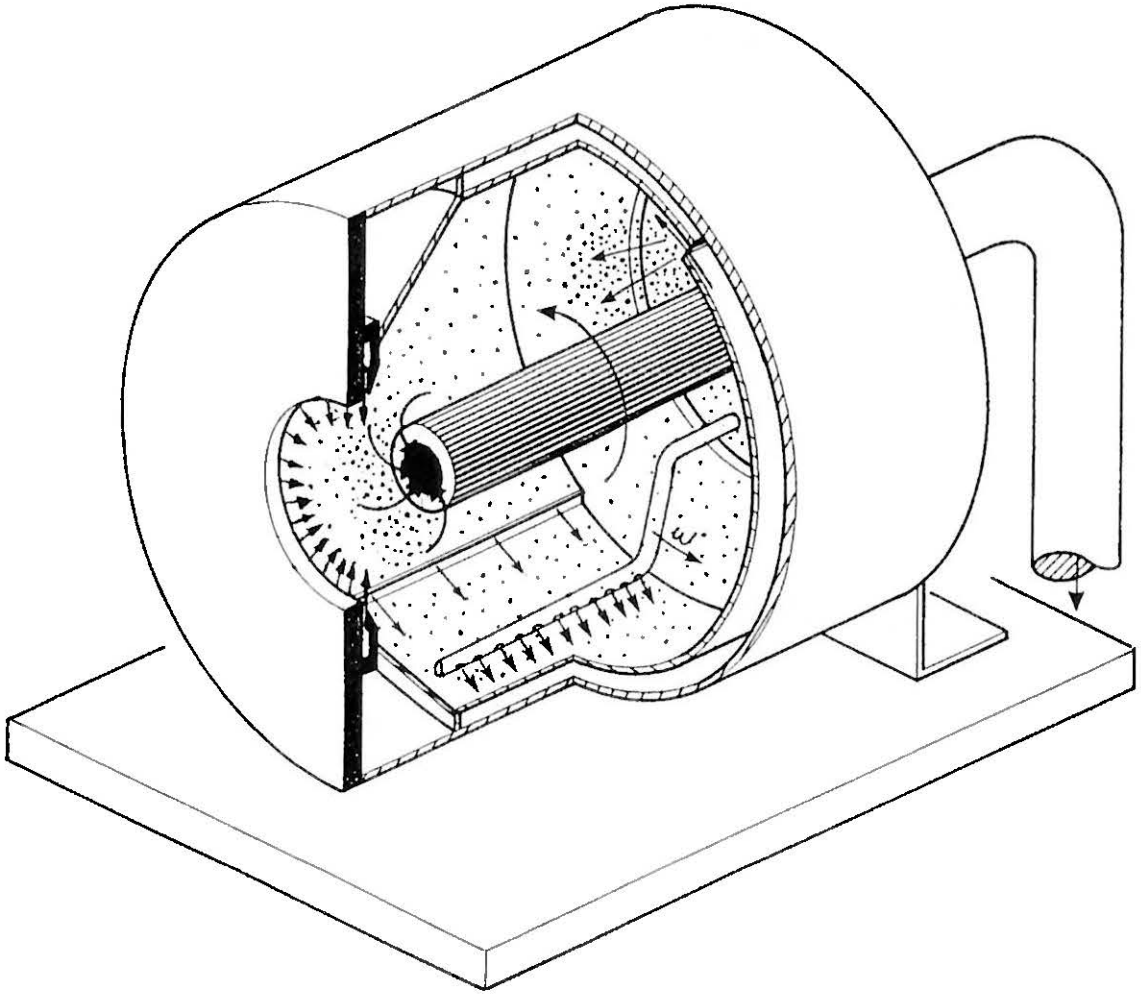

Figure 4.13 Scheme of the *JG* reactor configuration. The outer body is a double-wall cylinder, made of steel. A vortex flow inside the reactor is created by air injected tangential either via two rows of inlet holes, or through a rotating tube. Particles are injected into the reactor from the back side. Sunlight enters the reactor through a water-cooled and windowless aperture. A radial jet at the aperture reduces the amount of air entering through the aperture. The gas particle suspension is withdrawn through a water-cooled copper tube, insulated with ceramic materials.

Table 4.6 Typical running conditions of *JG* reactor experiments.

Reactants	MnO_2
Particle size; median	8.5 μm
Particle feeding rate	1.5 kg/h
Residence time in reaction zone	≈ 0.1 s
Velocity of the rotating tube	≈ 100 rpm
Inlet air flow rate	12 kg/h
Outlet air flow rate	31 kg/h
Inlet air flow temperature	Ambient
Power through aperture	8-9.5 kW
Maximal flux density	2500-4000 kW/m^2

A specially developed particle-feeder is used to uniformly produce a high loading ratio gas-solid suspension, that can be injected into the reactor. At the reactor outlet, the gas-particle mixture flows through a cyclone that separates the particles, followed by a heat exchanger that cools the air stream, a filter, and finally exits through a fan to the atmosphere.

Samples of particles for chemical analysis were taken from the outlet gas-particle flow, from particles sediments inside the reactor, and from particles separated in the cyclone. Samples are taken at different time intervals during experimentation.

Figure 4.14 shows typical time histories of the outlet gas temperatures at the end of the axial tube (after quenching), measured with a thermocouple shielded from direct irradiation. It demonstrates clearly the effect of loading particles into the air flow. The direct absorption of the incoming solar radiation by the particle cloud resulted in an effective heat transfer mechanism.

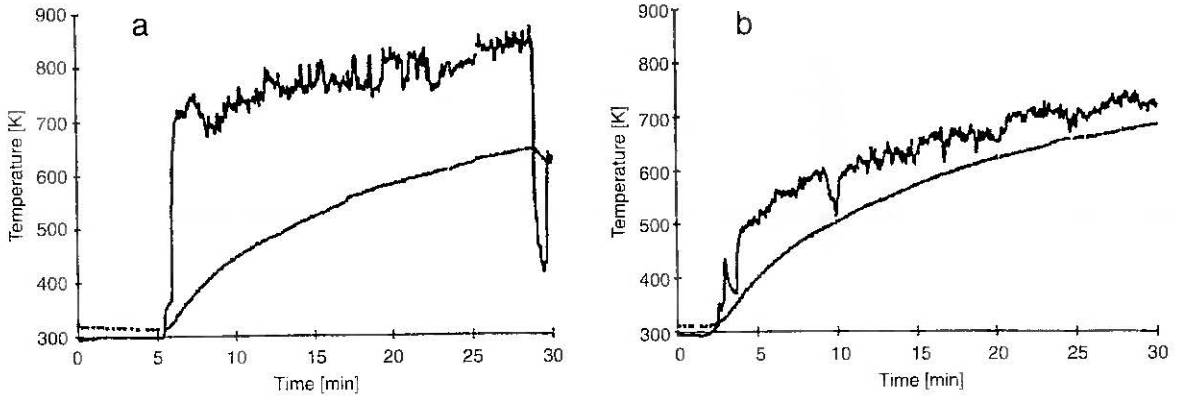

Figure 4.14 Typical temperatures measured during the solar experiments for the *JG* reactor: The upper line is the temperature of the particle suspension at the exit of the water-cooled copper tube. The smoother lower line is the mean reactor wall temperature. The graph at the left corresponds to the reactor configuration without the rotating tube: air enters tangential through two rows of holes at the wall and forms a smooth rotating flow with 1.5 m/s maximum speed. The graph at the right side corresponds to the reactor configuration with the rotating tube: air enters tangential through this rotating tube, with velocities 3 times faster. The turbulent flow obtained for the later case reduces the temperature gradient significantly.

Figure 4.14 also shows the importance of a well organized (not too turbulent) flow to produce a temperature gradient between the cloud and the reactor wall. In Figure 4.14(a) one sees that the temperature gradient is much more significant than that shown in Figure 4.14(b). The former case had less turbulence. Using the degree of reduction as the temperature probe, it is estimated that up to 500 K difference was obtained between the hottest zone in the cloud and the reactor walls.

The two different operating flow conditions (with/without rotating pipe) produce different degrees of reduction. A higher degree of reduction is obtained when air flows through the rotating pipe, although higher temperatures are obtained without the rotating pipe. This result might be due to the different gas-particle mixing conditions (Figure 4.15). The flow, as desired, was stable, but the loading ratio was only 0.04 [Ganz, 1997] and desired ratios should be near 1.

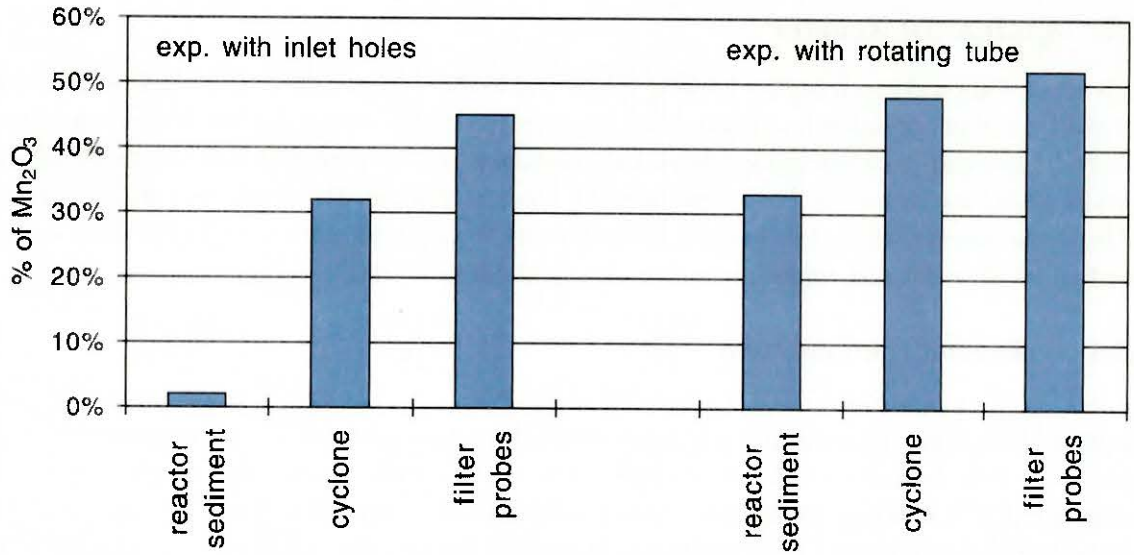

Figure 4.15 Chemical analysis of the different probes taken during the solar experiments with the *JG* reactor shown in Figure 4.14.

Energy balance calculations (Table 4.7) indicate that the reactor is an efficient energy absorber (80% absorption efficiency defined as the ratio of sensible and process heat absorbed to the input power), mostly in the form of sensible heat of carrier gas [Ganz, 1996]. A relatively large amount of air is pumped out in order to prevent particles escaping through the aperture. Improvements are required to reach higher temperatures and chemical conversion yields. Optimization of the design is to be accomplished by further increasing the optical thickness and the particle loading of the cloud, by reducing of the amount of carrier air, and by recovering its sensible heat.

Table 4.7 Energy balance in the *JG* reactor

Power through aperture	100%
Water-cooling of the outlet tube	35%
Sensible heat in the suspension	42%
Chemical conversion	3%
Losses	20%

4.2.1.3 Conclusions

We have designed a direct-absorption solar reactor to conduct high temperature gas-solid reactions. A prototype reactor was fabricated and tested in our solar furnace. Concentrated solar radiation was effectively absorbed by the gas suspension. A temperature gradient up to 500 K was observed between reaction zone and reactor walls as a result of the shielding effect of the particle cloud. Such an effect reduced the thermal load on the reactor walls and the temperature requirements of the reactor materials of construction.

At this juncture we had a reactor made from conventional steel that enabled a particle suspension to efficiently absorb solar radiation, we observed a good temperature gradient, however, more work is needed to develop the desired very high temperatures. Furthermore, the loading ratio is too low. Further research addresses these concerns.

4.2.2 *Sputnic 10* Reactor

A new reactor should reach higher loading ratios and higher temperatures. In addition, it should be proved whether a windowless reactor can be operated with a compound parabolic concentrator (*CPC*) [Welford and Winston, 1989]. Our approach was to continue with an experimental program where we designed, built, and tested a reactor concept. However, we also in parallel with the experimental work, began the *CFD* analysis for proposed reactor concepts. This section describes our new reactor, experimental results, and our *CFD* work.

4.2.2.1 Reactor Configuration

Figure 4.16 shows the *Sputnic 10* reactor. The main body consists of a cylindrical cavity made of heat-resistant steel. It contains a windowless aperture through which concentrated solar radiation enters. Reactants, in powder form (mean particle size about 5 µm), impinge on a cone and are conveyed in a swirling air stream. Particles are directly exposed to the high solar flux. An optional three-dimensional *CPC*, positioned in front of the aperture, increases the incident solar concentration. The radial air jet in the aperture plane helps prevent the particles from leaving the reactor through the open aperture and from damaging the *CPC*. Products exit via a water-cooled axial tube where they are quenched to avoid re-oxidation. This design continues to offer very low thermal capacitance, good thermal shock resistance, and adaptability to direct absorption processes.

The aperture is dimensioned based on the focus characteristic of the solar furnace, the necessary air flow through the aperture (0.12-0.14 kg h^{-1} cm^{-2} aperture), the volume flows and mass flows (see Table 4.8). The chosen diameter is 10 cm because the focal plane is placed about 2 cm inside the reactor. To allow for a *CPC*, an entrance diameter of 8 cm was chosen.

Table 4.8 Volume flows and mass flows for dimensioning the *Sputnic 10* reactor

Gas solid suspension at entrance (air)	30-40 l_N/min
Tangential nozzles (air)	10 l_N/min
Ring-nozzle CPC (air)	10 l_N/min
Ring-nozzle shield (air)	20 l_N/min
Gas-solid suspension outlet (air)	150-180 l_N/min
Particle mass flow rate	1-2 kg/h

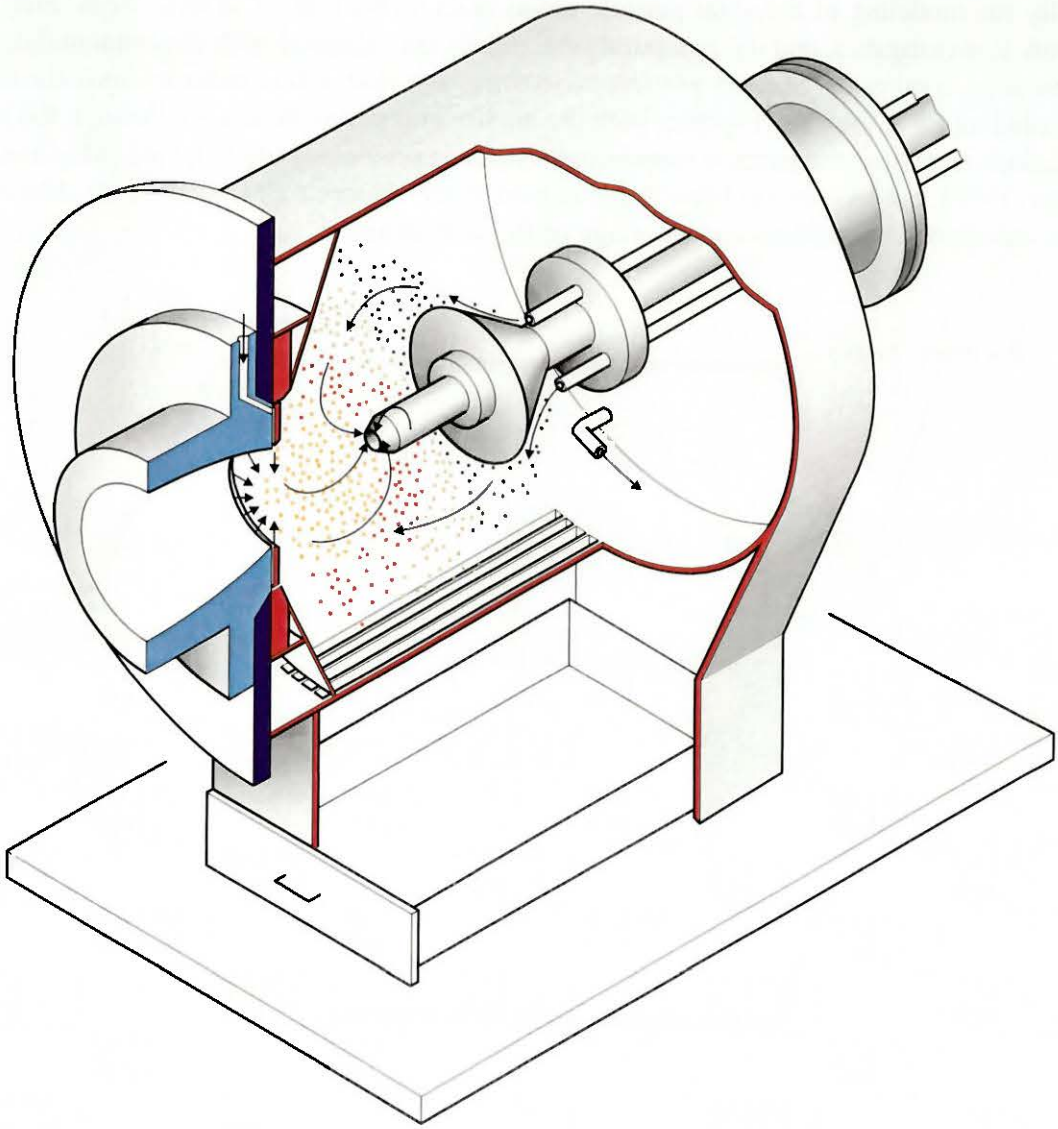

Figure 4.16 Scheme of the high-temperature solar reactor configuration *Sputnic 10*.

The ring-nozzles are dimensioned for a speed of about 10 m/s based on the volume flows from Table 4.8. The resulting gap is 0.1 mm for the ring-nozzle of the shield and 0.2 mm for the ring-nozzle of the *CPC*.

To minimize the heat losses to the central tube, its front surface could be reduced by a factor of 2.5 compared to the one of the *JG* reactor. The inner diameter is dimensioned based on the expected flow. The body of the tube is made of copper and is water cooled.

The reactor has a cylindrical body with a screen on the bottom, so that sedimenting particles fall out of the reactor and the geometry of the reactor chamber is unchanged. In contrast to the *JG* reactor, the gas-solid suspension is injected through three nozzles onto a cone and brought directly to the focus.

4.2.2.2 Computational Fluid Dynamics

We used a general-purpose *CFD* code [CFDS-FLOW3D, 1994] to simulate the fluid flow and heat transfer in the *Sputnic 10* reactor [Meier *et al.*, 1996].

Typically the modeling of the solar particle-cloud reactor proceeds in several steps. First, the fluid flow is investigated, and the computational results are validated with experimental data in cold operating conditions. Second, particle trajectories are observed in order to study the effect of the radial air jet at the *CPC* together with the air streaming into the reactor through the aperture. Radiation exchange in particle suspensions has been previously investigated [Mischler and Steinfeld, 1995], but has not yet been implemented in the present *CFD* calculations. Chemical kinetics was also not considered in this stage of the simulation.

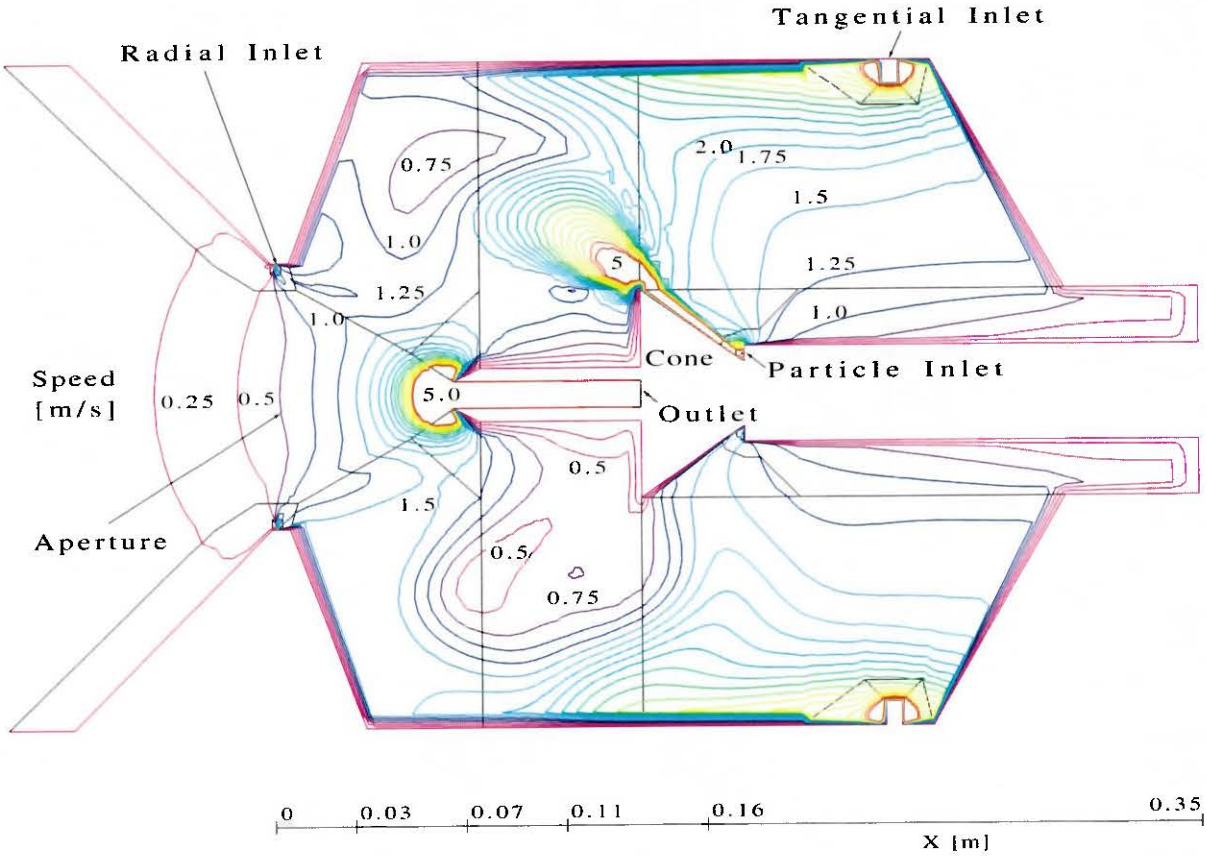

Figure 4.17 3D simulation of the air flow in the solar reactor [Meier *et al.*, 1996]. Boundaries and contour lines of iso-velocity magnitude (interval size 0.25 m/s) are shown. Inlet mass flows: 1) particle inlet: 3.0 kg/hr of air at velocity 122 m/s; 2) tangential inlet: 1.8 kg/hr at velocity 120 m/s; 3) radial inlet: 1.5 kg/hr at velocity 5.7 m/s; 4) aperture inlet: 16.5 kg/hr at mean velocity 0.58 m/s. Dimensions: aperture diameter 0.1 m, insulated outlet pipe: 0.01 m inner diameter, 0.02 m outer diameter. Overall reactor diameter 0.25 m and length 0.35 m. Conical region to the left extends computational domain to allow for monitoring fluid flow through the aperture (Plane X = 0 m).

Fluid Flow

The problem involves calculating the mixing of seven air streams at ambient temperature (300 K), namely the air jets through three small nozzles (1.5 mm diameter) impinging on a cone, the tangential air flows through two small nozzles (1.5 mm diameter) inducing a swirl, the radial air jet through a thin circumferential slit at the aperture (0.2 mm width), and the air flow through the aperture (100 mm diameter). The air is removed by suction through a pipe (10 mm diameter). A minimum number of 100'000 grid cells is required to resolve the small dimensions of the inlets. However, grid-independence of the solution cannot be demonstrated because of the memory and *CPU* time limitations of the workstation. A converged solution was found using the standard k-ε turbulence model and the "hybrid" differencing scheme, but convergence difficulties were encountered applying the *RNG* k-ε model and the *CCCT* differencing scheme.

Figure 4.17 shows a contour plot of the air velocity magnitude in the vertical plane that contains the axis of the cylindrical reactor. The flow specifications are given in the figure captions. The fluid flow calculations are compared with laboratory measurements of the air speed, that is the velocity vector magnitude, which was measured at different spatial locations by means of thermal anemometry. Despite the complex nature of the flow, the three-dimensional simulation describes the main flow patterns and shows a remarkable agreement with the measured data (Figure 4.18) although not all details are resolved correctly. The discrepancies in the aperture

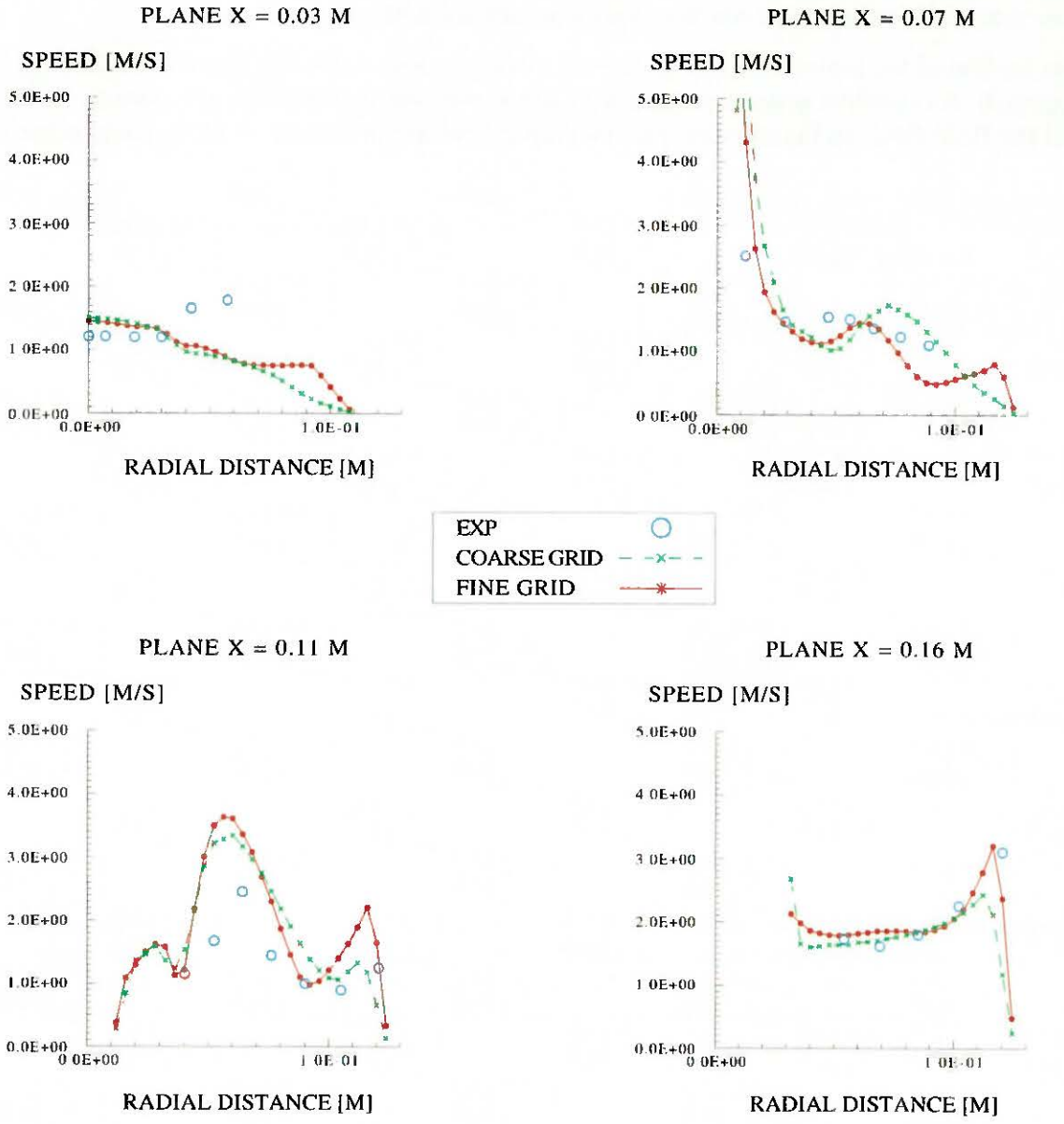

Figure 4.18 Validation of the *CFD* fluid flow calculations with experimental results in cold operating conditions (no *CPC* mounted) [Meier *et al.*, 1996]. For the position of the X planes see Figure 4.17.

region (see plane X = 0.03 m) are presumably due to disturbances in the flow caused by the experimental setup. The jets impinging on the cone appear to carry too much momentum in the forward direction (see plane X = 0.11 m). They do not spread out laterally as it has been observed during experimental operation.

Particle Transport

Air flow entering the cavity through the aperture is required to prevent particles from leaving the reactor and damaging the CPC. However, this additional air has to be heated and removed by suction, which reduces the efficiency of the reactor. Thus, we strive to minimize the amount of additional air. Several flow regimes have been investigated for optimizing the air-particle flow near the aperture and along the reactor walls. Two baseline cases are compared: Case I features 16.5 kg/hr of air streaming through the aperture into the reactor (this is the case discussed in the previous section); and Case II features zero net air flow through the aperture. The mass flow rate of the radial air jet has been kept constant for both cases (1.5 kg/hr).

The motion of the particles in the air flow is modeled using a discrete trajectory (*Lagrangian*) approach. An iterative process is needed to adjust the coupling between the particle transport and the fluid flow. In Figure 4.19, particle trajectories are projected on the vertical plane that

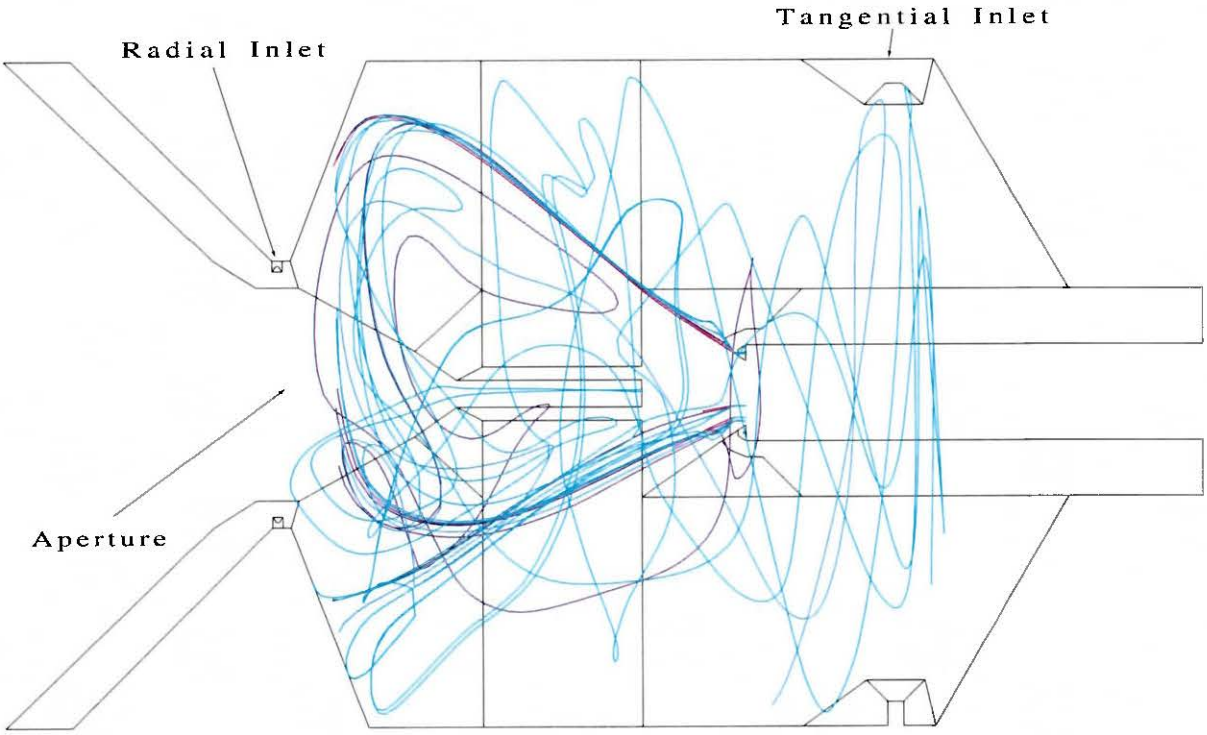

Figure 4.19 Particle transport in the solar chemical reactor [Meier *et al.*, 1996]. Particle trajectories are projected on the vertical plane that contains the axis of the cylindrical reactor. Case I: The radial air jet (1.5 kg/hr at velocity 5.7 m/s) along with the air streaming into the reactor through the aperture (16.5 kg/hr at mean velocity 0.58 m/s) both prevent particles from leaving the reactor. Particle mass flow 2.3 kg/hr, particle size between 1 to 4 μm.

contains the axis of the cylindrical reactor. An example of Case I shows that all particles are redirected by the air streaming into the reactor through the aperture. Some of the particles are moving to the rear of the reactor because of the entrainment by the tangential jets. Case II, however, results in particles escaping through the aperture and damaging the *CPC*.

Heat Transfer

Results of a convective heat transfer simulation are presented in Figure 4.20. We consider Case II (zero net air flow through the aperture into the reactor), neglecting particle transport and radiation heat transfer. The incident solar power is simulated by a 3.3 kW heat source, which is

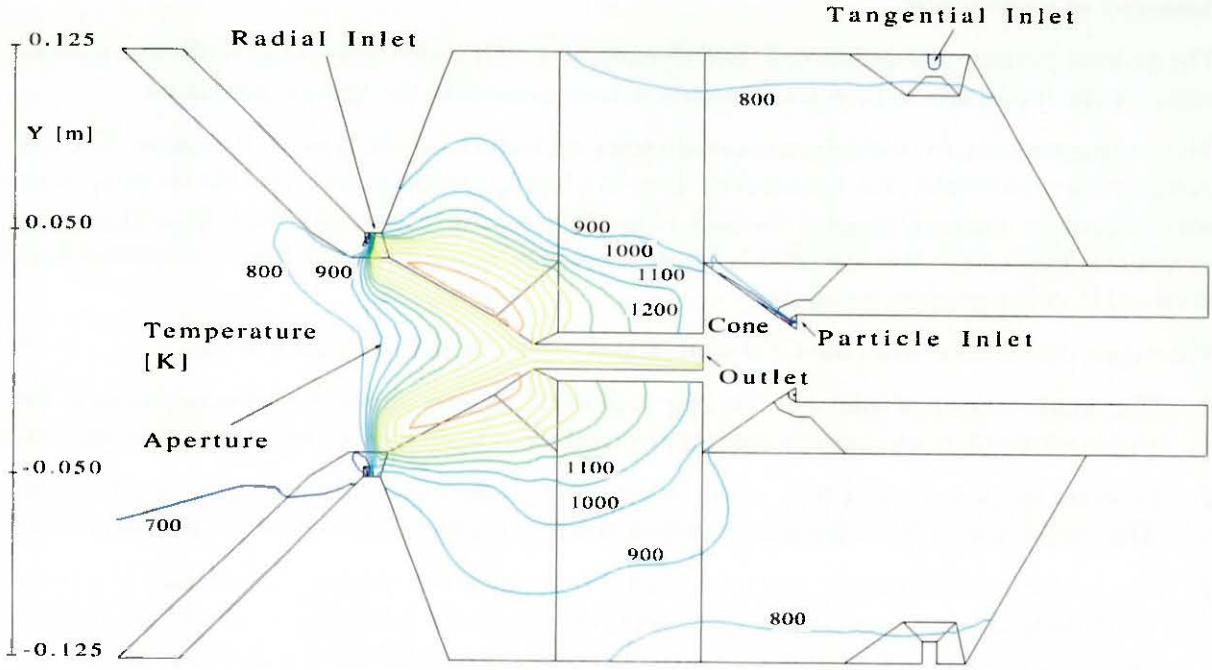

Figure 4.20 3D simulation of heat transfer in the solar chemical reactor [Meier *et al.*, 1996]. Incident solar power is simulated by a 3.3 kW heat source uniformly distributed over the focal region between the aperture and the outlet pipe (6 MW/m^3). Contour lines of iso-temperature (interval size 100 K) are shown for Case II (zero net air flow through the aperture). Adiabatic reactor walls are assumed.

assumed to be uniformly distributed over the focal region between the aperture and the outlet pipe. Maximum temperatures of about 1900 K are reached. The effect of buoyancy is seen from Figure 4.21. The air at the upper edge of the aperture is hotter than that at the lower edge of the aperture and creates a pressure gradient across the aperture. Due to the slight overpressure (about 1 Pa), the convective air flow through the aperture enhances particle outflow. It can be eliminated by injecting (preheated) air through the aperture into the reactor. The air is then further heated to 1700 K and strongly accelerated to 130 m/s before it leaves the reactor through the axial outlet pipe.

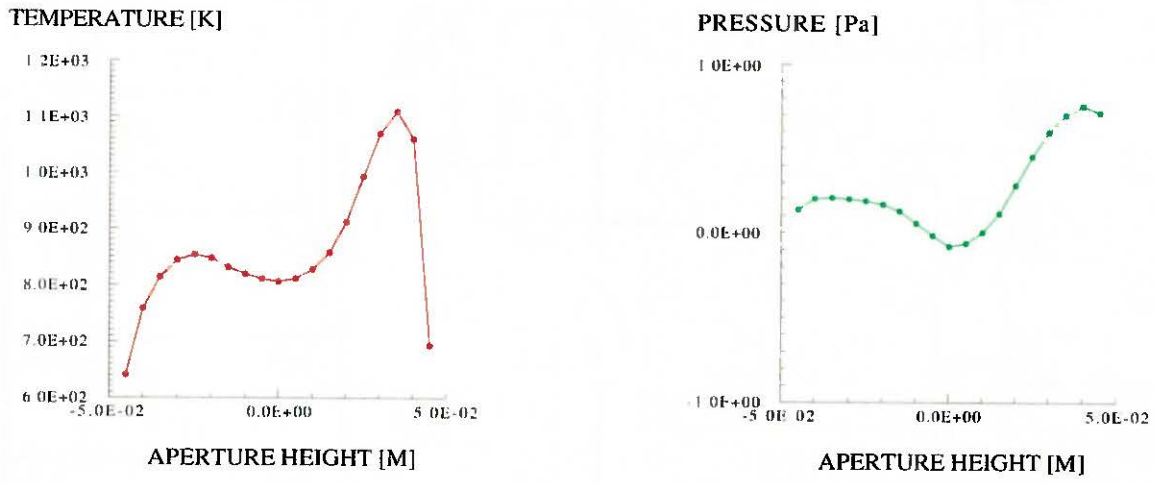

Figure 4.21 Temperature and pressure distribution across the aperture (plane X = 0 m) showing the effect of buoyancy [Meier *et al.*, 1996]. The position along the aperture height is indicated in Figure 4.20 (Y

Summary of CFD results

The general-purpose computational fluid dynamics (*CFD*) code CFDS-FLOW3D was used to simulate the fluid-particle flow and convective heat transfer in the *Sputnic 10* reactor.

The 3-dimensional *CFD* model contained all relevant features of the *Sputnic 10* reactor. The air/particle suspension inlet was modeled as three impinging jets on a cone, and the swirling flow was induced by a tangential jet at the back side of the reactor. Convective heat transfer using a volumetric heat source was simulated. The *CFD* results were validated with experimental data obtained in cold operating conditions.

The major conclusions from the *CFD* simulations of the *Sputnic 10* reactor were:

1. The single tangential inlet near the rear wall of the reactor should be replaced because the single inlet jet leads to particle entrainment and recirculation in the back part of the reactor.
2. Laminar air/particle inlet flow should be considered instead of jets impinging on the cone. This might help to prevent particle outflow and thus minimize the amount of auxiliary flow.
3. The problem of convective air/particle outflow through the aperture is addressed in a basic *CFD* study on open particle-cloud reactors (see Appendix 8.1, [Ganz *et al.*, 1996]) and the optimization of the air flow through the aperture is attempted using a 2-dimensional *CFD* model (see Section 4.2.3 on *Sputnic 50* Reactor).
4. *CFD* shows that it will be necessary to bring air in through the aperture to avoid convective flow out of the reactor.

4.2.2.3 Experimental

Figure 4.22 shows the experimental setup of the *Sputnic 10* reactor. All incoming air flows through mass flow controllers. Quantity and temperatures of cooling water and leaving gas

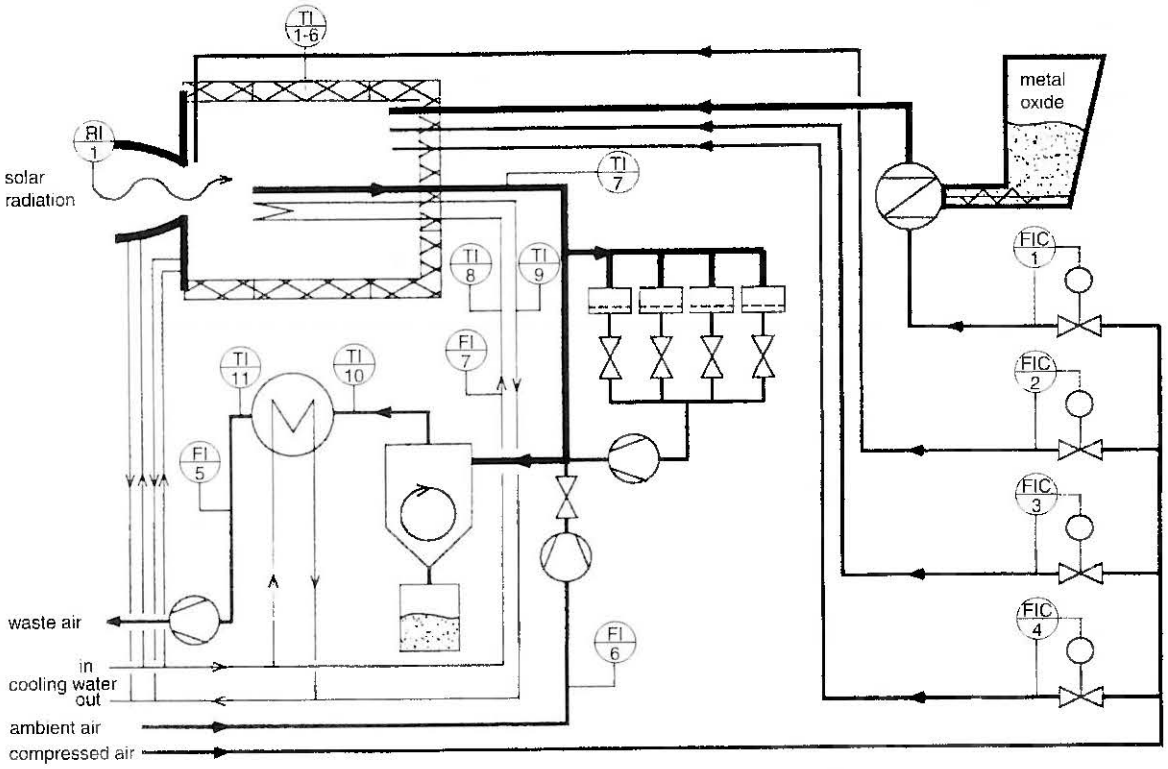

Figure 4.22 Setup of *JG* reactor and *Sputnic 10* reactor.

streams are measured for the energy balance. The metal oxide is introduced by a screw feeder. Together with the carrier gas a rotating brush generates the suspension. The leaving suspension passes a filter battery where samples can be taken. A vacuum pump generates the needed underpressure. The main stream goes on to a cyclone, where the main part of the particles are separated from the gas stream. The gas stream is cooled, passes a filter and is blown to the environment by a ventilator. Table 4.9 shows the standard experimental settings.

Table 4.9 Standard settings for *Sputnic 10* Reactor

Configuration		without *CPC*	with *CPC*
Reactant		MnO_2	MnO_2
Particle size	[µm]	1.22	1.22
Particle mass flow	[kg/h]	1.7 (-> 3.25)	1.7 (-> 3.25)
Carrier gas flow	[l_N/min]	40	40
Tangential gas flow	[l_N/min]	0-35	34
Ring nozzle (aperture)	[l_N/min]	20	30
Total air feed	[l_N/min]	60-95	74
Air leaving	[l_N/min]	250-300	250
Input power	[kW]	10-15	8-10
Max. flux density	[W/cm^2]	250-400	500-650

Table 4.10 shows the energy balance. One sees that nearly 70% of the incoming solar radiation leaves the reactor by re-radiation and convection. Thus we only had 30% of the energy being absorbed by the cloud.

On the other hand, Table 4.11 shows that *Sputnic 10*'s particle cloud reached a maximum temperature significantly higher than that in the *JG* reactor. The maximum suspension temperature was estimated by the fact that we produced Mn_3O_4. The temperature history as measured with thermocouples located at the back of the reactor also showed the temperature difference between *Sputnic 10* and *JG* reactors, respectively. The *JG* and *Sputnic 10* experiments were done under nearly identical conditions.

Table 4.11 also shows that the loading ratio was not increased with *Sputnic 10* although the nozzles were placed much closer to the spot and the mean residence time could be reduced significantly by reducing the volume of the reactor body.

Table 4.10 Energy balance of the *Sputnic 10* reactor.

Power through aperture	100%
Water-cooling of the outlet tube	28%
Sensible heat in the suspension	27%
Chemical conversion	3%
Losses	42%

Table 4.11 Overview of the experimental results.

Reactor	*JG* Reactor		*Sputnic 10* Reactor	
Configuration	Spinning tube	Tangential inlet	Without *CPC*	With *CPC*
Max. suspension temperature [K]	800	900	1150	850
Reached oxidation step to ==> temperature [K]	Mn_2O_3 75% 920	Mn_2O_3 >90% 920	Mn_3O_4 >90% 1260	Mn_3O_4 50% 1260
Loading ratio [-]	0.04	0.04	0.05	0.05

4.2.2.4 Conclusions

The *Sputnic 10* reactor was able to develop a mean gas suspension temperature about 300 K higher than that of the *JG* reactor. However, the conversion of solar energy to sensible and chemical energy was not as efficient as that of the *JG* reactor. We suspect the increase in suspension temperature accounts for the increase in radiant and convective heat loss from the reactor. Although the temperature gradient from the hottest zone in the particle cloud to the wall is a major concern, we were unable to make definitive statements on our success with this aspect of the reactor design in this particular experimental campaign.

The mass loading ratio of the *Sputnic 10* reactor was the essentially the same as that for the *JG* reactor. Thus increasing this value continues to be a major area for research.

Experimental and *CFD* results point to a critical aspect of windowless horizontal reactors: In order to prevent flow out the aperture due to buoyancy forces, a significant amount of additional air must be drawn in through the aperture. This point is critical, because we will need to keep this flow to a minimum, if we hope to have efficient conversion of solar to chemical energy.

4.2.3 *Sputnic 50* Reactor

The *Sputnic 50* reactor was the first step in an up-scaling process (*Solscup* project, see [Ganz, 1997]). The power level of 50 kW is given by our *McDD*-Dish. The reactor is based on the concept of *Sputnic 10*. The main changes are the following: integrated reactant preheating, extinction measurement of the powder cloud, and vortex forming ring nozzle at the aperture (see Figure 4.23)

We preheated the reactants in part with electrical heating elements in order to simulate heat recovery. Our objective was to see the importance of preheating on the gas suspension temperature and the loading ratio without investing time in designing and building traditional equipment.

The extinction coefficient was measured so that we could obtain a value for the cloud's optical thickness. This parameter is needed in modeling radiation transport within the cloud, which is work that we do near the end of our experimental study on the open high temperature volumetric reactors. The extinction coefficient is a function of the loading ratio and temperature, and particle size distribution for a given chemical system. We thus couldn't extract quantitative correlations between this property and our experimental conditions. But we did attempt to establish a feel for how this parameter would change with the feeding rate.

The vortex forming ring of nozzles at the aperture was introduced in order to optimize the flow pattern such that a minimum of ambient air entered the cavity through the aperture. This design feature was suggested by a *CFD* Study.

Again our experimental work is done in parallel with *CFD* work. In this section as in the previous one, our conclusions will be drawn from both sets of information.

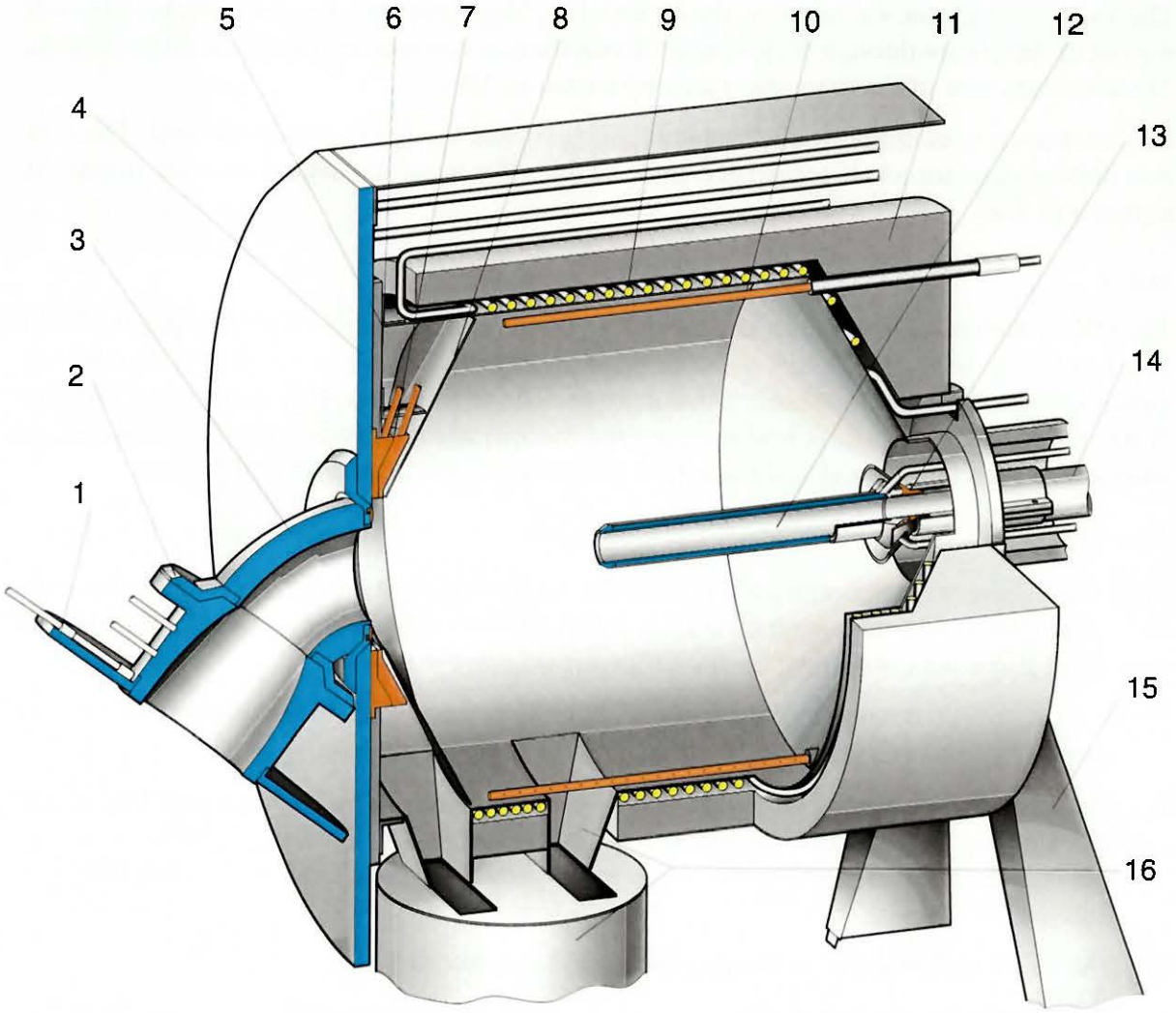

1 *CPC*-shield (copper)
2 *CPC* (aluminum)
3 Torus (aluminum)
4 Shield, water-cooled (copper)
5 Front wall (aluminum)
6 Front ring of nozzles (suction or blowing) (copper)
7 Rear ring of nozzles (copper)
8 Front cone (heat resistant steel)
9 Reactor body with cooling tubes (heat resistant steel)
10 Vortex nozzles (heat resistant steel)
11 Insulation (Ceramic felt and *Al* coat)
12 Central tube tip, water or air cooled (heat resistant steel)
13 Suspension inlet
14 Central tube heat exchanger
15 Reactor carrier
16 Sedimentation outlet and bucket

Figure 4.23 Schematic of *Sputnic 50* with *CPC* and Torus but without equipment for extinction measurement.

4.2.3.1 Reactor Configuration

A schematic of the *Sputnic 50* reactor is shown in Figure 4.23. The most important components are further discussed.

CPC/Torus

The *Sputnic 50* reactor was tested on the *McDD* dish. To avoid agglomerated particles from falling out of the reactor through the aperture the reactor axis was kept horizontal or tilt to the back. The necessary turn of the beam was made by a torus of 50°.

CPC and torus were made from aluminum (*AlMgSi*) that was galvanically silvered. The *CPC* was dimensioned for a half acceptance angle of 44°. The mean theoretical increase in concentration was 2.07.

Shield

The size of the aperture was calculated as it was done for the *Sputnic 10* reactor [Ganz, 1996]. The aim was to reach the highest possible suspension temperatures based on flux distribution, radiation losses and air flow through the aperture. The resulting aperture diameter is 140 mm. Water for cooling the shield is lead once around the aperture to a water bath. This arrangement allows for good cooling next to the aperture with minimal pressure drop in the shield.

Ring of Nozzles

CFD simulations were performed to optimize the air flow through the open aperture and to minimize the amount of cold environmental air inflow. From simple 2-dimensional axisymmetric flow simulations we can summarize the following *qualitative* results.

1. For a given outlet mass flow, the amount of auxiliary gas needed to prevent particle outflow seems to be independent of the configuration of the air/particle inlet.
2. The best results are achieved by suction of environmental air through an outer ring nozzle and blowing in (preheated) air through an inner ring nozzle. Thus the net cold air inflow can be minimized. Therefore, the ring nozzles should be made to allow (preheated) air inflow and air outflow.
3. The radial inlet velocity in the aperture should not exceed 5 m/s.
4. The flow in the aperture is very sensitive to boundary conditions (recirculation zones).
5. The air/particle inlet should be moved towards the front end of the outlet tube to prevent air/particle recirculation at the back of the reactor.

The nozzles shown in Figure 4.23 at position 6 were designed and arranged to incorporate the insight given by the *CFD* analysis. They are mounted to the inner side of the shield to influence the flow in the aperture region. The ring nozzle has two planes. The outer plane allows to either bring in preheated air or exhaust. At the inner plane, air can be blown in radially at 25° or 45° angles. The nozzle width is either 0.5 or 1 mm. The configuration with 25° / 0.5 mm was found to work best.

Reactor Body

The reactor body is made of heat resistant steel of 1.5 mm thickness. It is wrapped with cooling tubes. The temperature of the body is monitored by 16 thermocouples. The wall temperature is limited to 1300 K by blowing air through the cooling tubes. This heated air can be used in the outer ring nozzle.

Vortex Nozzles

To generate a vortex with low velocities and to avoid excess turbulence in the reactor, two rows of nozzles are placed along the cylindrical reactor wall.

Central Tube

The central tube consists of three separable pieces: (1) central tube tip; (2) dispersion cone, combined with dispersion nozzle ring; (3) heat exchanger. The dispersion nozzle ring is removable. One tube is the inlet of the cooling media (water or air). The second is the outlet. The third gives us the opportunity to bring in air in the outlet stream.

The heat exchanger projects out the backside of the reactor. To minimize the thermal losses it is insulated. To reach even higher temperatures, the incoming reactants are preheated with an electrical heater. The inlet tube wall can be heated up to 870 K.

In the central tube, suspension temperatures are measured with thermocouples. The temperature values have to be corrected because the thermocouples are in radiation exchange with the wall. Figure 4.24 shows the correction values. One sees that the suspension temperature can be up to 140 K higher than the temperature of the thermocouple.

Because of the complexity of the heat exchange between thermocouple and the suspension we can't quantify the accuracy of the correction term. To be conservative we use uncorrected temperatures. Thus, we are sure the temperatures are higher than the measured value.

To investigate the suspension temperature at the entrance of the central tube tip we need to know the heat exchange coefficient between suspension and wall. This problem is too complex to be solved by an easy theoretical calculation. Theories and material properties are missing. For this reason the Nusselt number is investigated experimentally by measurements in the central tube.

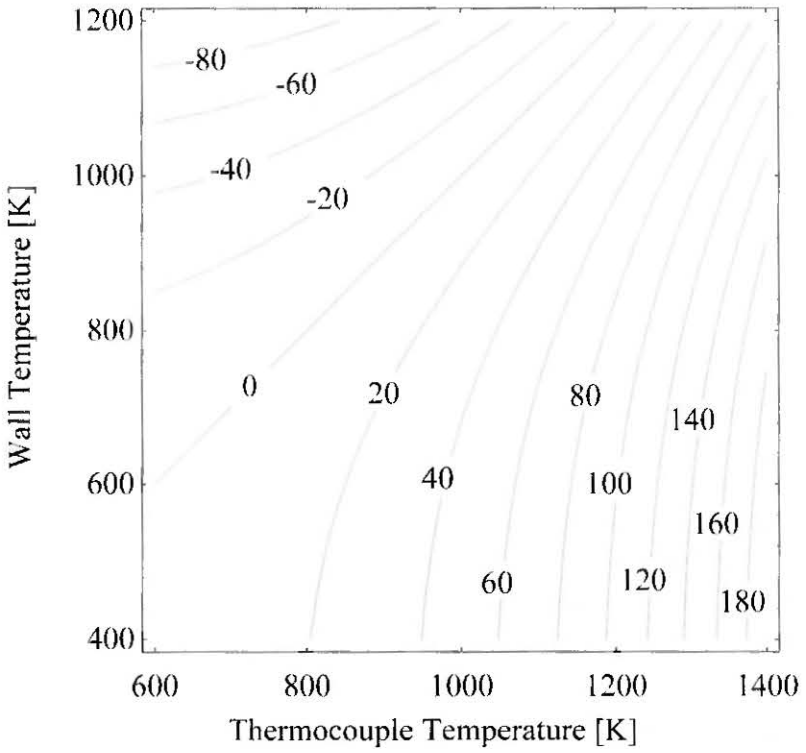

Figure 4.24 Temperature correction caused by radiation exchange with the walls for $K_{SO} = 5.1\ 10^{-11}$ [Ganz, 1997].

The results were compared with the theory of heat transfer for pure gas streams and parametrized.

The experimental Nusselt numbers were in every case lower than the ones calculated by the turbulent theory (Nu≈30) although according to the Reynolds numbers a turbulent flow is expected. It is likely that the particles act as a turbulence damper. The measured Nusselt numbers in the range of 10 to 15 match quite well the ones of the laminar theory of about 13. The calculated temperature drop of the suspension from the central tube entrance to the first thermocouple is about 110 K.

The highest temperature of a thermocouple reached about 1360 K. With the thermocouple correction of about 140 K and the compensation of the suspension cooling in the central tube of about 110 K we can expect that a maximal temperature of 1600 K is reached in the suspension. This matches well with the reduction degree of the iron oxide.

Extinction Measurement

The optical density can be characterized by the extinction coefficient. The equipment required to make this measurement was attached to the reactor.

4.2.3.2 Experimental

For the experiments MnO_2 powder was used. In some experiments we added 10 wt% of Fe_2O_3 as a temperature indicator in the range of 1600 K. We present the results in each of the main topical areas of interest: energy balance, estimate of maximum powder cloud temperature, loading ratio, and commentary on the flow stability.

Energy Balance

The energy balance for the case when the reactor walls were water cooled is shown in Figure 4.25. This experiment enabled us to measure all of the energy distribution within the flows. We use it to illustrate that 50% of the energy went to the wall of the reactor. We estimate radiation losses out the aperture to be 10%. This 10% is the quantity of energy that was not present in any of the flows. Figure 4.26 shows the energy balance for the case in which the reactor walls were air cooled. About 60% of the incoming solar radiation is absorbed in the particle cloud. The figure shows how this energy is distributed. For example, the energy transported away from the reaction zone by ambient air entering the cavity through the aperture represented about 15 to 20% of the incoming radiation. The sensible energy in the particles represented about 3%. We estimate the chemical energy within the particles to be about 3%. It is also interesting to note that the convection losses from the cavity wall represent about 40% of the energy loss of the incoming radiation. (We assumed that about 10% of the energy leaves the aperture as emitted radiation from a black body cavity at the temperature of the powder cloud.)

Estimate of Maximum Powder Cloud Temperature

As mentioned earlier, it is not easy to measure the temperature of the particle cloud. Our approach was to make corrected thermocouple measurements of the exiting gas temperature and also make judgements about the maximum temperature based on the chemical transformations that occurred within the reactor, namely the conversion of MnO_2 and Fe_2O_3 to lower oxidation states.

A typical experiment for the air cooled reactor shows that the maximum temperature in the cloud was between 1400 and 1600 K. The measured thermocouple temperature was 1400 K, but the chemistry indicates that we were near 1600 K. The combination of the flux density, power

input, and flow rates were similar to those of the *Sputnic 10* experiments. Thus we can say that we improved the design of the reactor in the sense that we increased by about 200-400 K the maximum powder cloud temperature in going from *Sputnic 10* to *Sputnic 50*. It is difficult to point to a particular design feature responsible for this change. It is conceivable that scaling fac-

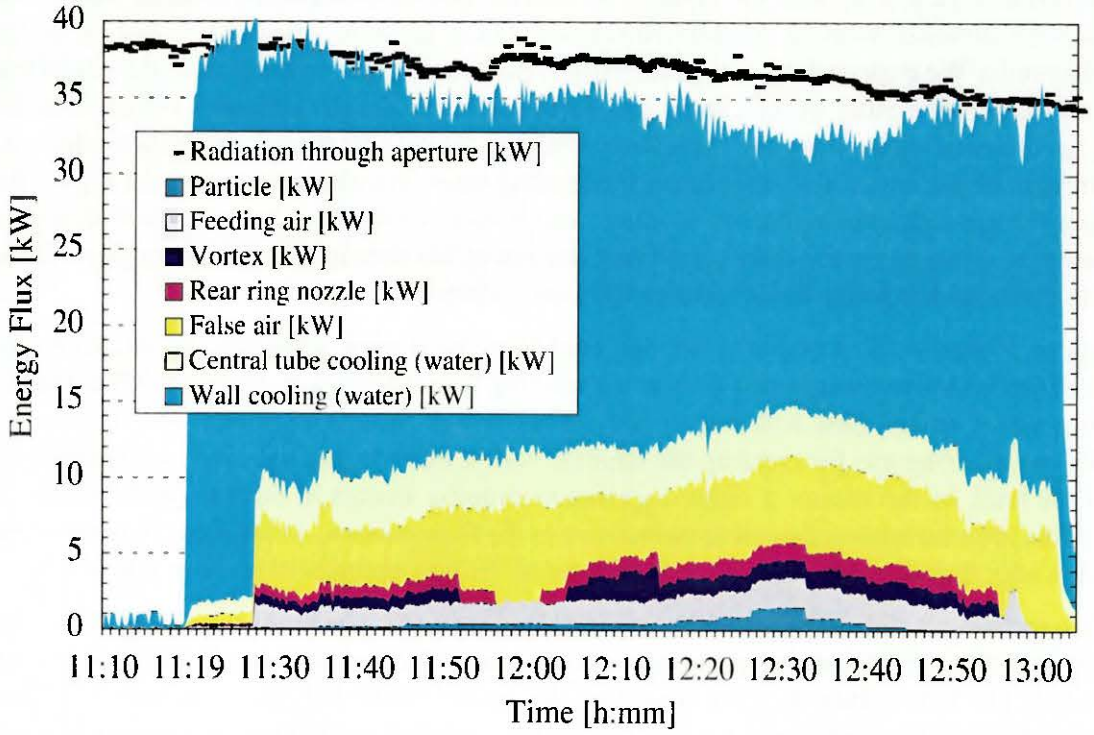

Figure 4.25 Energy balance for experiment #13. The Reactor walls were water cooled. to about 400 K.

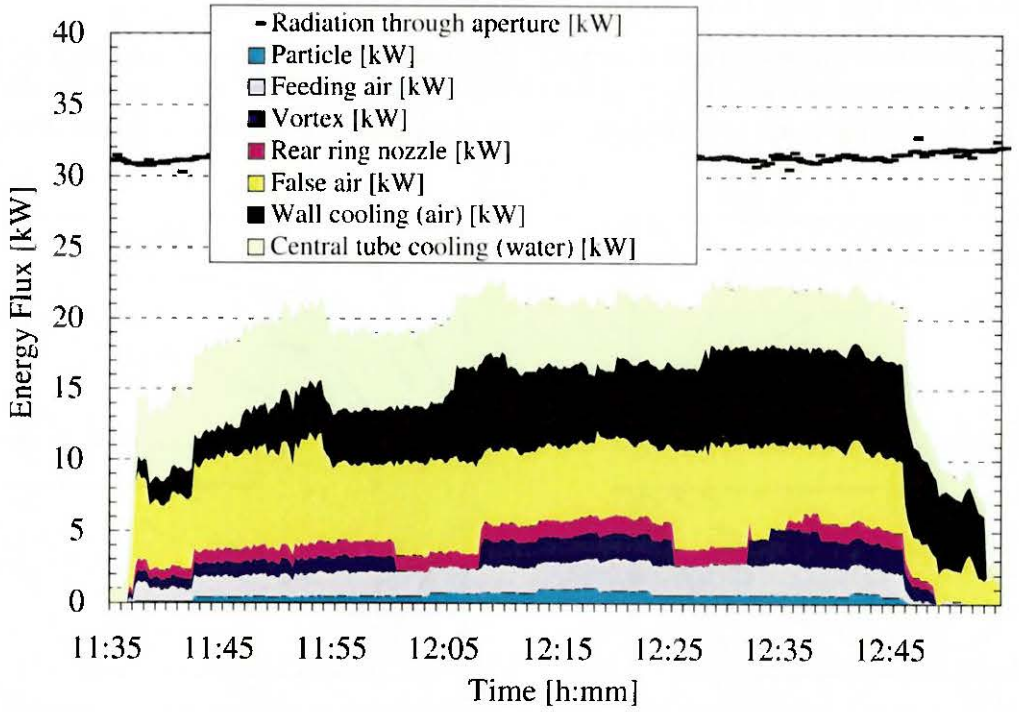

Figure 4.26 Energy balance for experiment #11. The Reactor walls were air cooled to about 1200 K.

tors alone are responsible for the improvement. It is quite clear, however, that even though we improved the maximum temperature, it is far below the desired value near 2500 K.

Loading ratio and flow stability

A major research objective with the *Sputnic 50* reactor was to increase the loading ratio from that which we obtained with the *Sputnic 10* reactor. There are many parameters that influence the loading ratio. We expected the size of the vortex flow regime in comparison to the axial flow pattern and the temperature of the carrier gas, to be the main design variables influencing the loading ratio. Specifically, from our experience with the *Sputnic 10* reactor, we believe the lower the strength of the vortex flow the higher the loading ratio. We also expect that the higher the carrier gas temperature, the higher the loading ratio [Ganz, 1996]. This hypothesis with regard to temperature is based on the assumption that the lower the density of the carrier gas and the higher its viscosity the better the loading ratio [Ganz, 1996].

Referring to Figure 4.23 at position 10, one sees that the design attempted to minimize the strength of the vortex by using a row of nozzles running from the back to the front of the reactor for setting up the vortex flow within the cavity. This design feature minimizes the impulse required by the entering gas for creating the desired vortex flow; if one uses only one nozzle located at the back of the reactor a rather significant impulse occurs in the gas as the vortex is created. This impulse adds undesirable turbulence to the flow pattern. At position 14 in the same figure, one sees that the inlet suspension is preheated. (It was preheated to about 800 K.)

These design features did enable us to increase the loading ratio. The highest ratio was 0.3. This result occurred in an experiment that lasted for 30 minutes. The estimated maximum cloud temperature was just below 1600 K. (The solar flux was only 750 W m^{-2}). It is important to note, that during this run the sedimentation was higher than normal, indicating that the suspension was not able to hold all of the particles. In a typical experiment, with low sedimentation, we reached a loading ratio of 0.1 to 0.2. These results indicated that from the point of view of the loading ratio, the *Sputnic 50* reactor was an improvement over all previous reactors. However, as mentioned earlier the desired loading ratio is between 1 and 2.

Our experimental observations suggest a complex relationship between the desired high loading ratio and the desired high temperature gradient within the cloud. Figure 4.27 (a) shows the desired flow pattern and (b) is the undesired one, because in pattern (a) the flow is essentially plug

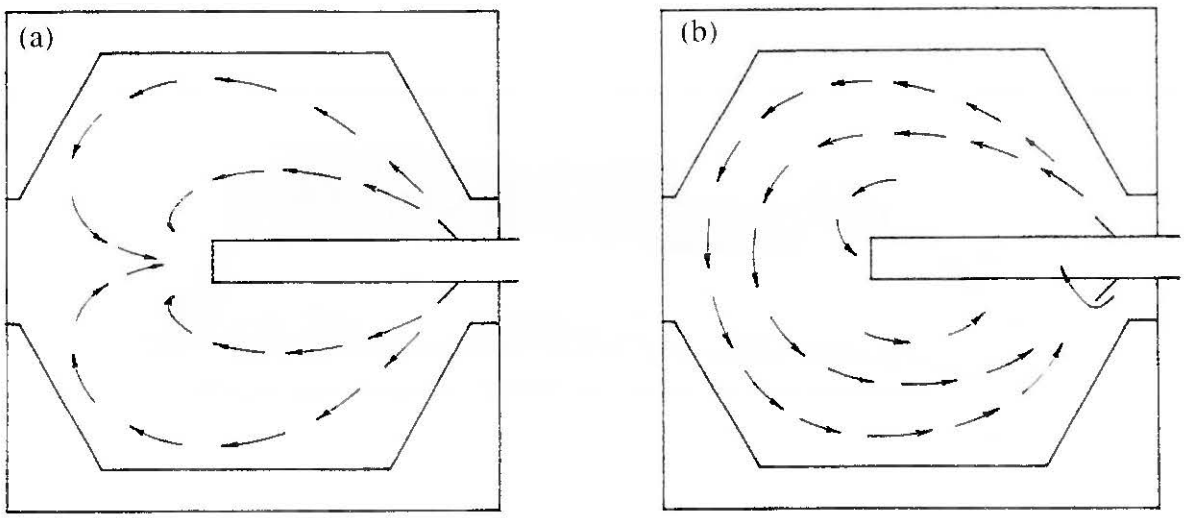

Figure 4.27 The two flow states in the *Sputnic* reactor
a) the desired axisymmetric "plug" flow; b) the undesired "well-stirred" flow

flow. Hydrodynamic plug flow is required if one is to set up a strong temperature gradient in the cavity. Unfortunately flow pattern (b), that of a well stirred reactor appears to be more stable. Also this flow pattern was the one where we had the highest loading ratio.

4.2.3.3 Modeling Volumetric Gas-Particle Solar Reactors

The results and a discussion of the residence time distribution measurements as well as the complete details of a numerical radiation heat transfer and fluid flow model [Mayer, 1996] can be found in Appendix 8.2ff. Here is a summary of this work.

The numerical simulation with a newly developed computer program, called KOMBIMODELL, allows one to investigate the absorption behavior of a radiated powder cloud in an ideal solar reactor. Even though significant simplifications were made with regard to radiant transport and fluid flow, the calculated results are in good agreement with solar experimental results.

The experimental results lie between the simulated results of a model composed of two zones, plug flow plus perfectly stirred, and the model results of a purely stirred flow reactor. From this observation, we conclude that our reactor design led to strong back mixing in the flow field. Furthermore, the two extreme cases of the model, an ideal sink flow reactor and an ideal well stirred reactor, bracket the essential upper and lower reactor performance characteristics.

The model was used to conduct a sensitivity analysis. The investigation illustrated the importance of the loading ratio, air flow rate, solar power, and wall losses on the temperature field and the distribution of the absorbed energy. The temperature field and the energy distribution were greatly influenced by the optical thickness of the powder cloud and the radius of the sink flow field. As the sink flow radius is increased, the extinction characteristics of the cloud become most important on obtaining the maximum temperature. Furthermore, for a stirred reactor the increase of the optical thickness has little effect on the temperature difference between the wall and the hot zone within the cloud. In contrast, the presence of a relatively small sink flow can lead to large improvements in the advantages of direct solar radiation within the cloud. For example, a small sink flow can lead to good shadowing of the reactor wall, which improves the desired temperature difference. Furthermore, with increasing optical thickness, the difference between a well stirred reactor and a sink flow reactor grows.

Surprisingly as the reactor dimensions increase from a certain minimum size the influence of the sink flow radius decreases. But for a well stirred reactor, which has bad absorption behavior, high losses at the wall occur due to the increased surface area at the wall as the reactor size is increased.

Residence time measurements gave us important information on the flow behavior. We conducted such experiments in cold experiments without particles. They showed that the flow pattern within our reactor is a combination of an ideal well stirred reactor and that of an ideal plug flow reactor. Experimental work revealed that the flow in the area of the centre exit tube is essentially plug flow. This result confirms that we are justified in using a flow model that is well stirred in the outer ring near the cavity walls and plug flow near the centre of the cavity.

The numerical model showed that the flow of air through the aperture of the reactor was divided into the plug flow zone and the stirred zone before exiting the reactor. By increasing the vortex flow a larger portion of the flow through the aperture went into the plug flow zone.

4.2.3.4 Conclusions

Solar experiments confirmed that volumetric gas-particle reactors with a vertical aperture need extra air inflow to prevent particles from escaping through the windowless aperture, or to keep

clean a window or a *CPC*. The amount of extra air can be expressed as the mass flow per aperture area, which is found to vary between 0.3 and 0.6 kg s^{-1} m^{-2} in reactors without a *CPC* and up to 1.1-1.8 kg s^{-1} m^{-2} in the presence of a *CPC*. The values are higher for reactors with a *CPC* because these reflecting surfaces are very sensitive to particle deposition. Similar to the reactor configuration with a *CPC*, windows in the aperture have the disadvantage of high extra gas flow to keep them clean, although they may be indispensable to eliminate the wind sensitivity of open reactors or to control the gaseous atmosphere.

Such basic aspects of air flow and convective heat transfer in windowless particle-cloud reactors have been studied using Computational Fluid Dynamics (*CFD*), see Appendix 8.1 [Ganz *et al.*, 1996].

4.2.4 *Sputnic 10(97)* Reactor

The series of volumetric gas/particle reactors, called *Sputnic 10* and *Sputnic 50*, respectively, that were designed, built and subsequently tested at *PSI*'s solar facilities [Ganz, 1996; Ganz *et al.*, 1996], gave experimental results that were encouraging from the viewpoint of process technology. However, temperatures and loading ratio required to efficiently conduct the desired chemistry has not been achieved.

Theoretical investigations indicated that the flow regime in the reaction zone is critical: It should be dominated by plug-flow behavior. Experimental investigations, however, revealed that well-stirred flow conditions prevailed in the reaction zone in both *Sputnic 10* and *Sputnic 50* reactors [Mayer, 1996]. Thus reactor walls are exposed to high temperatures and they have to be cooled to prevent overheating. Substantial heat losses are the consequence. Flow analysis using *CFD* showed that the thermal efficiency is further decreased by heating up environmental air that enters the reactor through the aperture.

To address these problems and to build a better performing reactor, a new reactor concept was developed, called *Sputnic 10(97)*, see Figure 4.28. The dominant feature of the new design is a central outlet for the gas/particle suspension in front of the reactor aperture. In addition, the reactor is equipped with a new suspension chamber that should help to obtain a laminar flow in the reaction zone. To efficiently cool the product, the reactor is equipped with a water-spray quench unit (position 2).

4.2.4.1 Experimental

The metal oxide to be reduced was pure MnO_2 (manganese(IV)oxide) with a mean particle size of 0.5 µm. Particle feeding rate was 3 kg h^{-1}. Air was used as a carrier gas with flow rates between 40 and 120 l_N min^{-1} at position 6. The outlet gas flow rate (at position 1) ranged from 500 to 800 l_N min^{-1}. The gas/particle suspension was preheated to a temperature of 600 to 700 K (measured at position 6). The solar input varied between 10 and 15 kW, the measured mean flux density was 140 to 190 W cm^{-2}.

To investigate the influence of the suspension mass flow on the reactor wall temperature, the mass flow of the suspension was varied and the response of the wall temperature was recorded. The results of three experiments (#1 to #3) are shown in Figure 4.29. They clearly revealed a correlation between the suspension mass flow, expressed as carrier gas flow, and the resultant maximum wall temperature T_{max}: Increasing the mass flow reduced T_{max}. This is consistent with a reduced heat transfer to the reactor wall and indicates that the suspension directly absorbed a significant fraction of the incoming radiation. Chemical analysis of the products provided no evidence that an increased mass flow had an impact on the particle temperatures. *MnO* (besides Mn_3O_4) was formed in each experiment, indicating that with all three flow rates (see

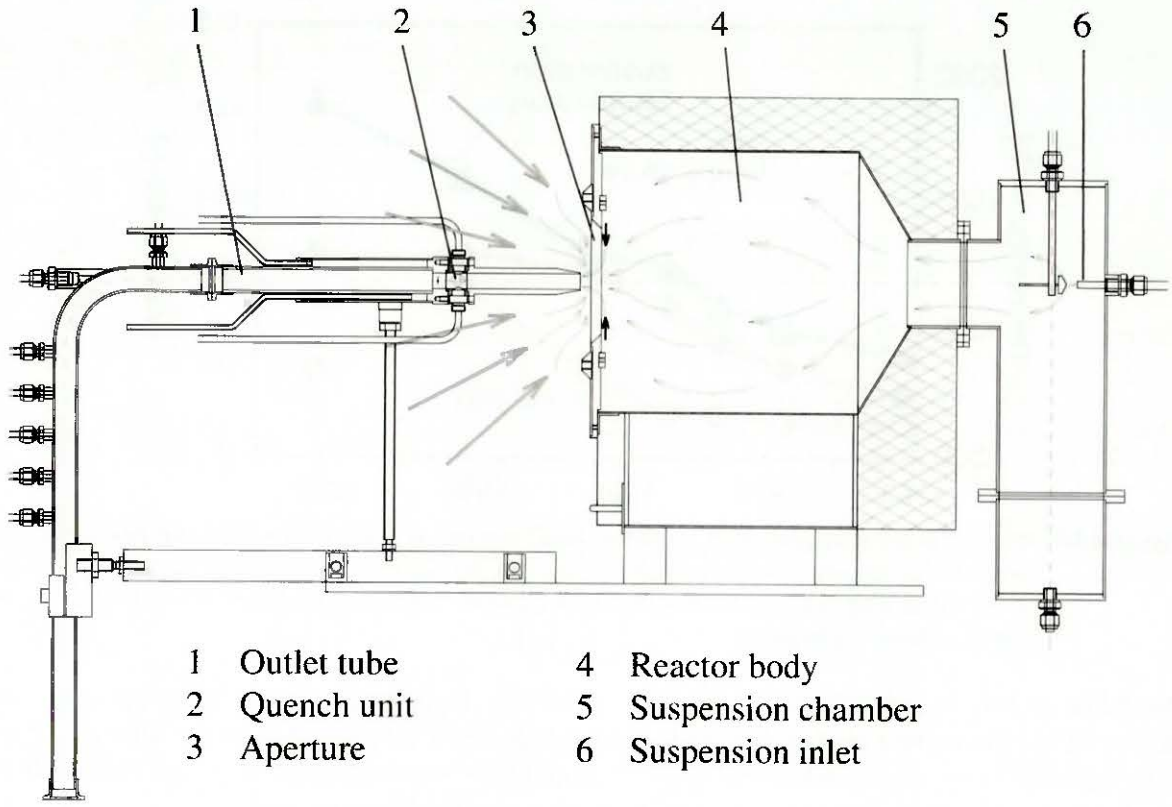

Figure 4.28 Schematic drawing of the *Sputnic 10(97)* reactor with the central outlet in front of the aperture.

Figure 4.29) at least a fraction of the particles reached the reduction temperature of about 1840 K.

An important issue to be addressed with the *Sputnic 10(97)* reactor was the amount of environmental air that enters the reactor through the aperture. By flowing through the reaction zone it is heated up and thus, lowers the amount of heat available to the chemical reaction. Although it has an auxiliary function, namely to prevent particles from escaping the reactor, its amount

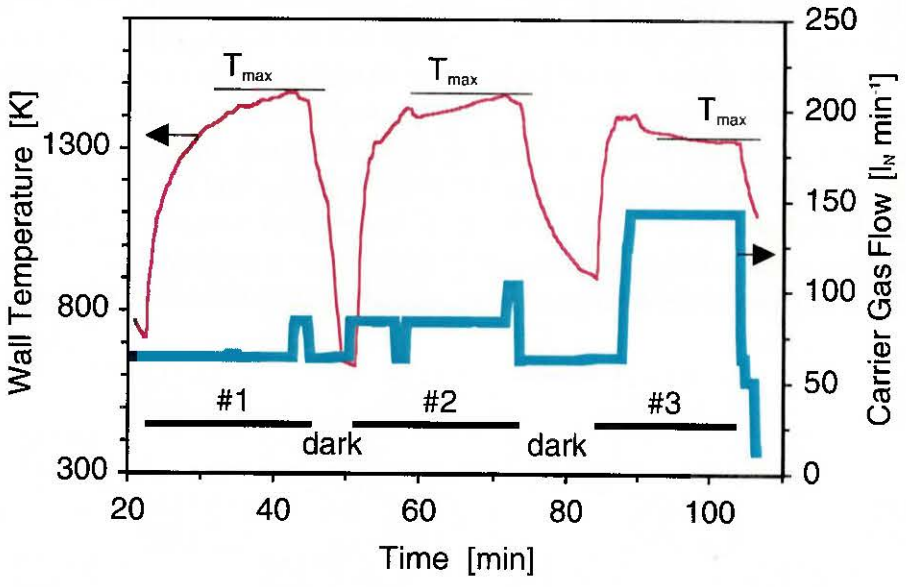

Figure 4.29 Correlation between the carrier gas flow and the reactor wall temperatures.

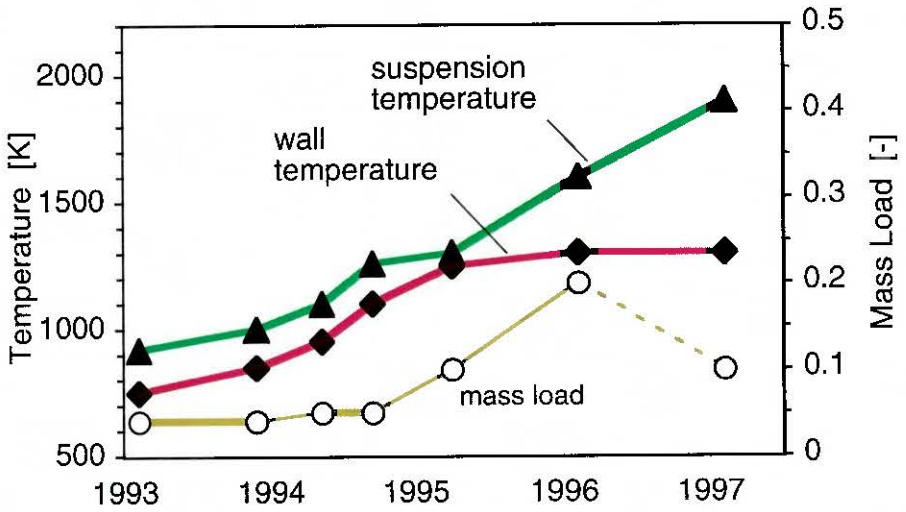

Figure 4.30 Progress in the development of "powder-cloud" reactors at *PSI* between 1993 and 1997. N.B. Enhancement of the mass load was not an objective of the experiments with the last reactor generation (1997), though better understanding the limiting factors of the mass loading will be crucial for a successful technical application.

should be as low as possible. With the outlet centrally positioned in front of the aperture, the inflow of environmental air could be reduced by a factor of 10 compared to the *Sputnic 10* reactor with the same reactor body, but with the outlet tube inside the reactor [Ganz, 1996]. It is, to our knowledge, the lowest value yet recorded for powder cloud reactors.

Positioning of the outlet tube in front of the aperture is also beneficial if product quenching is required. Cold environmental air can be used to quench the hot gas/particle suspension right after passing the reaction zone. If necessary, the outlet tube can be supplemented in a straightforward way with a more efficient quench unit, e.g. with a water-spray quench unit (Figure 4.28, position 2).

4.2.4.2 Conclusions

"Powder cloud" reactors represent potential solutions for solar high-temperature processes. To date we have achieved temperatures near 1850 K in reactors made from conventional steel. To our knowledge this is the highest temperature achieved in a solar powder cloud reactor. No failure occurred during more than 50 hours of operation and more than 100 temperature changes (start/stop). With the new reactor design the thermal efficiency of the reactor could be increased and for the first time *MnO* (besides Mn_3O_4) could be prepared in a powder cloud reactor. However more research is needed to establish the maximum loading ratio and also to elevate the cloud temperature. More fundamental work is needed to understand the complex flow and heat transfer situation so that one can create the optimal design. For example, the *CFD* study in Appendix 8.1 suggests that a face-down reactor is better than a horizontal reactor. Figure 4.30 shows the progress in developing powder cloud reactors at *PSI* between 1993 and 1997 [Ganz *et al.*, 1997].

4.3 Closed Moderate Temperature Volumetric Solar Reactor

4.3.1 *SynMet* Reactor

SynMet is a solar chemical reactor designed specifically for the co-production of metallic *Zn* and syngas starting from *ZnO* and natural gas (*NG*) [Steinfeld *et al.*, 1998b]. It is shown schematically in Figure 4.31. It consists of an insulated cylindrical cavity (#1), that contains a circular, windowed, aperture (#2) to let in concentrated solar energy. Particles of *ZnO*, conveyed in a flow of *NG*, are continuously injected into the reactor's cavity via a tangential inlet port (#3) located at the back of the cavity. Inside the reactor's cavity, the gas-particle stream forms a vortex flow that progresses towards the front following a helical path. The chemical products, *Zn* vapor and syngas, continuously exit the cavity via a tangential outlet port (#4) located at the front of the cavity, behind the aperture. The window (#5) is actively cooled and kept clear of particles by means of an auxiliary flow of gas (#6) that is injected tangentially and radially at the window and aperture planes, respectively.

Heat Transfer

With this arrangement, the *ZnO* particles are directly exposed to the high-flux irradiation. Such concept provides efficient radiation heat transfer to the reaction site where the energy is needed.

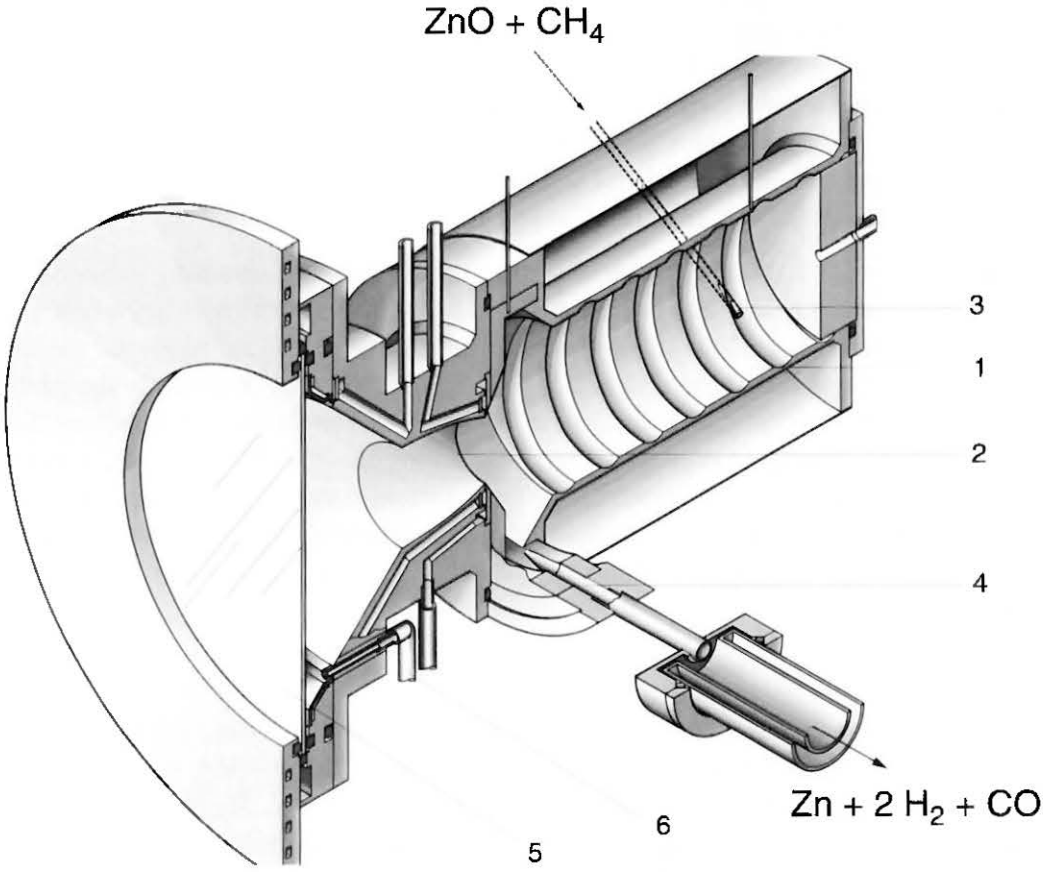

Figure 4.31 Schematic configuration of the *SynMet* solar chemical reactor for the co-production of *Zn* and syngas [Steinfeld *et al.*, 1998b]. 1 cavity; 2 aperture; 3 inlet port for reactants; 4 outlet port for products; 5 window; 6 auxiliary gas flow. The particles of *ZnO* are directly exposed to high-flux irradiation, providing efficient heat transfer directly to the reaction site. Energy absorbed by the reactants is used to raise their temperatures to the range 1200-1600 K and to drive the simultaneous reduction of *ZnO* and reforming of *NG*. The chemical products exiting the reactor are *Zn* vapor and syngas.

by-passing the limitations imposed by indirect heat transport via heat exchangers. Some of the incoming irradiation undergoes multiple scattering among the particles and multiple reflections within the cavity walls, until it is absorbed by the particles and cavity walls. Other mechanisms of heat transfer to the reactants include infrared radiation by the hot particles and cavity walls, forced convection between the cavity walls and the gas stream, and conduction to *ZnO* particles that are swept across the hot reactor walls. Vortex (and cyclone) reactors have proven to be efficient devices for the transfer of heat to flows laden with particles [Szekeley and Carr, 1966]. Energy absorbed by the reactants is used to raise their temperature to above about 1200 K and to drive reaction equation (3.73).

4.3.1.1 Reactor Engineering Design of *SynMet*

Reactor Geometry

The reactor features a cavity-type receiver geometry. It is basically an insulated enclosure designed to effectively capture incident solar radiation entering through a small opening (the *aperture*). Because of multiple internal reflections, the fraction of the incoming energy absorbed by the cavity exceeds the surface absorptance of the inner walls. Such an effect, called the cavity effect, can be expressed by the apparent absorptance, defined as the fraction of energy flux emitted by a blackbody surface stretched across the cavity opening that is absorbed by the cavity walls. The apparent absorptance has been calculated for cylindrical, conical and spherical geometries having diffuse and specularly reflecting inner walls [Lin and Sparrow, 1965; Siegel and Howell, 1992; Steinfeld, 1991]. The larger the ratio of cavity diameter or depth to aperture diameter, the closer the cavity-receiver approaches a blackbody absorber. For example, for a cylindrical cavity having the same relative dimensions as the *SynMet* (ratio of cavity diameter to aperture diameter = 1.7, ratio of cavity depth to aperture diameter = 2), the apparent absorptance is greater than 0.979 for surface absorptance greater than 0.5.

It is important to note that the apparent absorptance is calculated assuming a *Lambertian* directional distribution of the incident radiation. In reality, the power flux distribution will depend on the optics of the concentrator. It is also assumed that the medium inside the cavity does not participate in the radiation exchange, but, in reality, the reactants (especially the particles), absorb, emit and scatter radiation. Nevertheless, Monte-Carlo ray tracing simulations have shown that the apparent absorptance of a cavity-receiver is only weakly affected by the directional distribution of the incident power [Steinfeld, 1991; Steinfeld, 1993b]. As the incoming rays undergo multiple isotropic scattering among particles and multiple diffuse reflections within the inner walls, the apparent absorptance becomes less and less dependent on the direction of the incident rays.

Reactor Sizing

At temperatures above about 1000 K, the net power absorbed by the cavity-receiver is diminished mostly by radiative losses through the aperture. Thus, the aperture size is the most important dimension for determining the amount of power in and out. The solar energy absorption efficiency of a cavity-receiver, $\eta_{absorption}$, accounts for this phenomenon. It is defined as the net rate at which energy is being absorbed divided by the solar power coming from the concentrator. For a perfectly insulated cavity receiver (no convection or conduction heat losses), it is given by [Fletcher and Moen, 1977]

$$\eta_{absorption} = \frac{\alpha Q_{aperture} - \varepsilon A_{aperture} \sigma T^4}{Q_{solar}} \tag{4.3}$$

The first term in the numerator denotes the total power absorbed and the second term denotes the re-radiation losses; their difference yields the net power absorbed by the reactor. The incoming solar power is determined by the normal beam insolation, by the collector area, and by taking into account for the optical imperfections of the collection system (e.g., reflectivity, specularity, tracking errors). The capability of the collection system to concentrate solar energy is often expressed in terms of its mean flux concentration ratio over an aperture, normalized with respect to the incident normal beam insolation as follows:

$$\tilde{C} = \frac{Q_{aperture}}{I \cdot A_{aperture}} \tag{4.4}$$

Solar concentration ratios of 1000 are technically feasible in large scale solar collection facilities using present central-receiver and heliostat technology [Winter *et al.*, 1991]. They can be further increased by improving the optical precision of the heliostat field or by using non-imaging secondary reflectors (e.g. compound parabolic concentrators, often referred to as *CPC* [Welford and Winston, 1989]). Higher concentration would allow for smaller apertures to intercept the same amount of energy, thus reducing re-radiation losses. Although larger apertures intercept more sunlight reflected from imperfect and imperfectly matched heliostats and concentrators, they also re-radiate more energy. Therefore, the optimum aperture size for maximum $\eta_{absorption}$ results from a compromise between maximizing radiation capture and minimizing re-radiation losses. It is determined by solving [Steinfeld and Schubnell, 1993]

$$\frac{\partial \eta_{absorption}}{\partial r_{aperture}} = 0 \tag{4.5}$$

For imaging solar concentrators, for which the incident flux-density distribution at the focal plane is close to Gaussian (with maximum flux density F_{peak} and radial standard deviation μ), and further assuming a blackbody cavity-receiver ($\alpha = \varepsilon = 1$), yields the optimum aperture radius

$$r_{opt} = \sqrt{-2\mu^2 \ln \frac{\sigma T^4}{F_{peak}}} \tag{4.6}$$

that serves to guide the determination of the aperture size for maximum efficiency. For example, for a reactor operating at 1400 K and for a solar flux input having the optical characteristics of *PSI*'s solar furnace ($F_{peak} \approx 2500$ kW/m^2 and $\mu \approx 2.5$ cm, which are representative for 75% of full power load), the optimum aperture radius is 5.5 cm. An alternative approach is to determine the size of the aperture so that it intercepts a given incident solar power. Assuming again a Gaussian power flux distribution, the radius of the aperture becomes

$$r = \sqrt{-2\mu^2 \ln \frac{1 - Q_{aperture}}{2\pi\mu^2 F_{peak}}} \tag{4.7}$$

For example, for a desired input power of 5 kW using *PSI*'s small solar furnace, the aperture diameter should be about 6 cm.

Given the total power input, the aperture size, and the operating temperature, one can estimate the power lost by re-radiation and the net power absorbed by the reactants. The mass flow rates of the reactants result from matching the net power absorbed with the enthalpy of the reaction

$$Q_{reactor,net} = \dot{m}\Delta H\big|_{\text{reactants @ } (T_1, p) \rightarrow \text{products @ } (T_2, p)} \tag{4.8}$$

Table 4.12 shows the enthalpy change of the reaction as a function of the total pressure p; the reactants are 1 mol ZnO and 1 mol CH_4, fed at 298 K, and the products are in thermodynamic equilibrium at 1250 K and at 1350 K [Reynolds, 1986].

Table 4.12 Enthalpy change for $ZnO + CH_4$ @ 298 K $\rightarrow$ products @ 1250K, 1350 K

	$T = 1250$ K				$T = 1350$ K
	$p = 1$ atm.	$p = 3$ atm.	$p = 5$ atm.	$p = 10$ atm.	$p = 10$ atm.
ΔH [kJ]	549	545	541	449	554

Once the mass flow rates are determined, the dimensions of the cavity-receiver are estimated so that the residence time of the reactants inside the reactor chamber is sufficient for the complete reaction (or for a desired reaction extent), as imposed by the kinetics of the reaction. If the reactants are only partially reacted after one pass, they can eventually be recirculated back to the reactor until they are fully reacted.

Flow Visualization and Computational Fluid Dynamics (CFD)

The reactor design evolved from an initial proposal as a result of flow-visualization experiments and *CFD* simulations carried out in various geometries and flow configurations. Clear *Plexiglas* models were built for the purpose of visualizing the flow patterns in cold conditions. The initial design had an axial outlet flow and did not perform satisfactorily because of particle sedimentation inside the cavity chamber as well as deposit of dust at the window and *CPC*. The sedimentation could be minimized to some acceptable levels by having instead tangential inlet and outlet ports at the cavity's back and front respectively, thus creating a stable vortex flow that is able to carry particles along a helical path, regardless of the orientation relative to gravity. In order to increase the residence time of particles inside the reactor chamber and to augment heat transfer between reactants and reactor walls, a spiral groove was machined to guide the particles into a tight helical path rather than the natural coarse helical path. Such a feature was applied with success in a vortex reactor for the ablative pyrolysis of biomass [Diebold and Scahill, 1997]. A pitch of 3 cm for a reactor tube diameter of 10 cm was found to function properly for fine ZnO powder (0.5-2 μm particles) within a wide range of inlet velocities. The window and *CPC* were kept clear of particles with the help of auxiliary gas flows (not laden with particles) injected through tangential and radial ports located strategically at the window and aperture planes, respectively (see Figure 4.31).

CFD simulations were employed to calculate the velocity field and particle trajectories for different geometries and flow boundary conditions. The *Navier-Stokes* equations were solved by applying the hybrid differencing schemes and the k-ε turbulence model [Meier *et al.*,1996]. The motion of the particles in the gas flow was modeled using a discrete trajectory (*Langrangian*) approach. Optimization was accomplished for minimizing the auxiliary flow while keeping the window and *CPC* clear of particles. Figure 4.32 shows the results of a 3-dimensional calculation of the isothermal gas flow. It is observed that, near the axis, the vortex flow moves in the positive direction (from left to right), primarily as a result of the auxiliary window flow, while close to the walls the vortex flow moves in the opposite direction (from right to left) as a result of the main gas/particle stream that progresses towards the front following a helical path. This helical path is illustrated by the particle trajectories in Figure 4.33. Larger (and heavier) particles follow a tighter spiral path, while the smaller (and lighter) particles follow closer the gas flow streamlines. For the given gas and particles mass flow rates, no particles escape through the aperture.

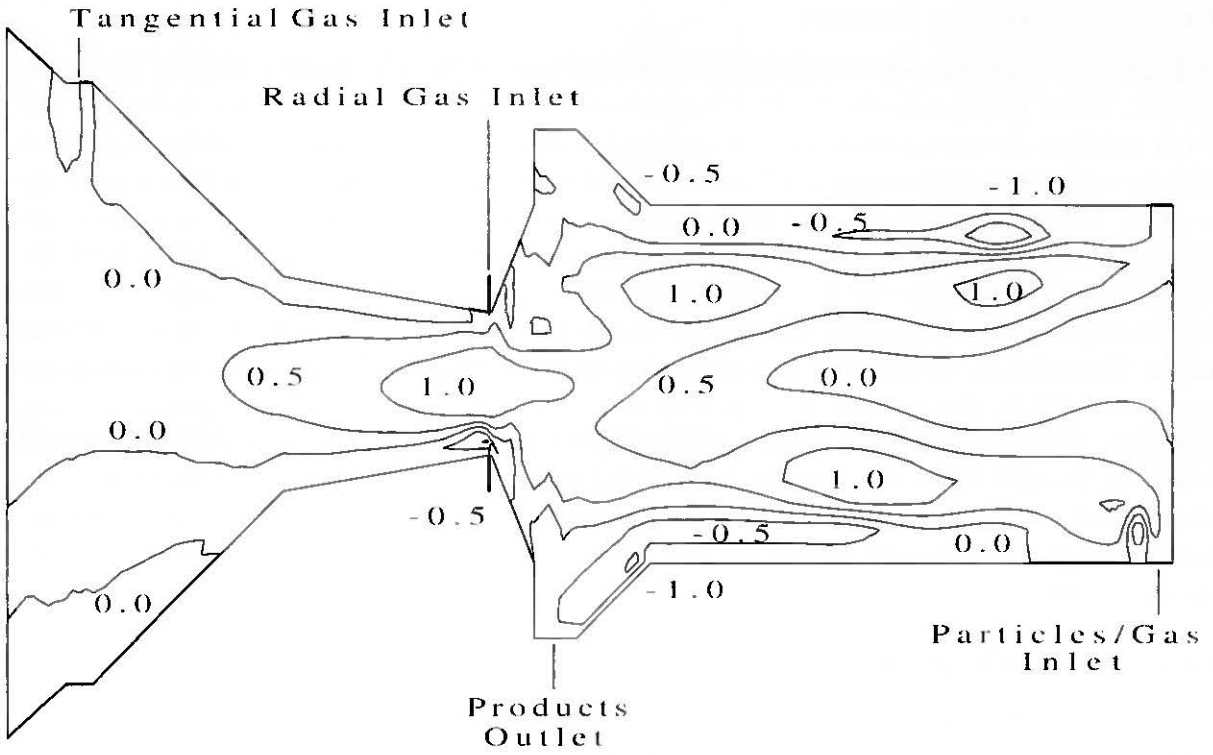

Figure 4.32 Wall boundaries and contour lines are shown for constant velocity (interval size 0.5 m/s) for the axial velocity component [Steinfeld *et al.*, 1998b]. Parameters: the main flow at the back inlet port = 27.8 l_n/min; the radial jet flow at the aperture = 13.9 l_n/min; the tangential flow at the window = 9.3 l_n/min; particle mass flow rate = 8.4 g/min. Positive values are for the direction from left to right.

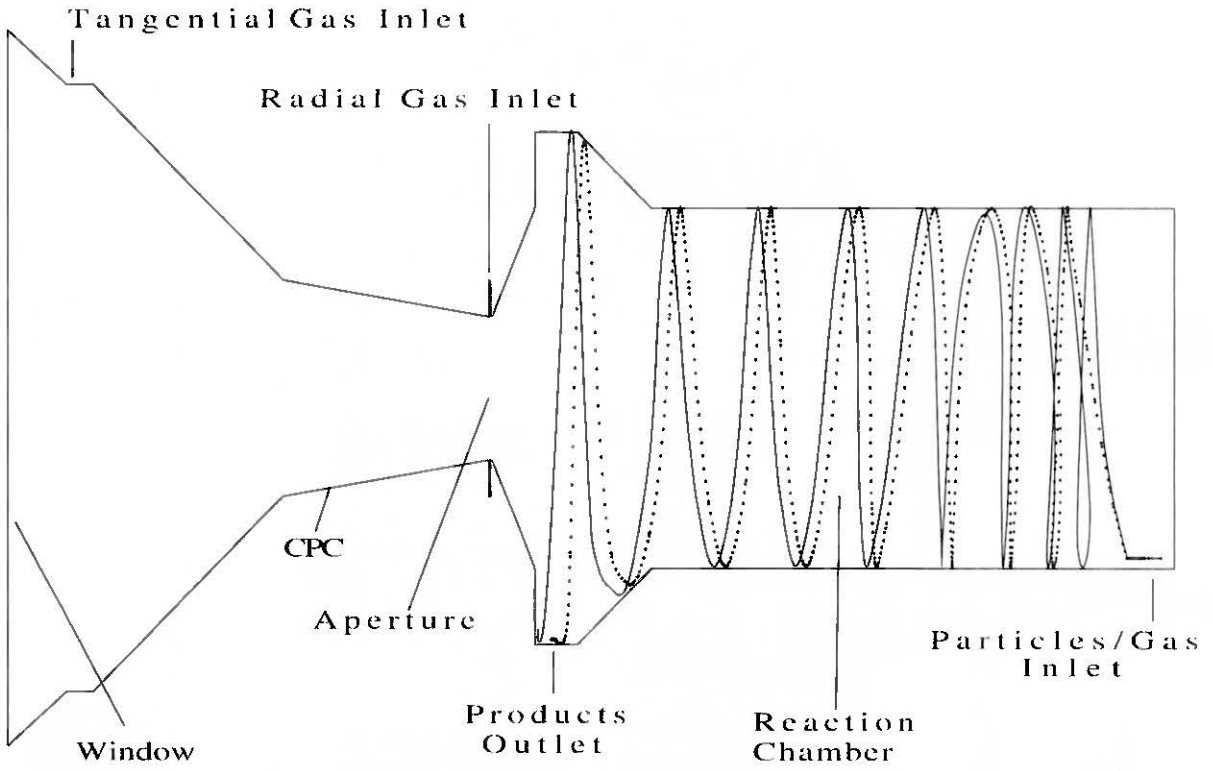

Figure 4.33 Boundaries and particle trajectories projected on the vertical plane that contains the reactor axis [Steinfeld *et al.*, 1998b]. Parameters are the same as in Figure 4.32. The full line refers to a particle diameter of 10.5 μm and the dotted line to 14.3 μm.

Fabrication of Reactor Prototype

A 5-kW prototype was fabricated and is shown in Figure 4.34. The cavity body is a 10-cm diameter, 20-cm length cylinder made of heat-resistant steel alloy (m.p.=1670 K). In front of the 6-cm aperture, the cavity-receiver was equipped with a diverging conical aluminum funnel so that the window could be mounted 7 cm in front of the focal plane where the radiation intensity is about 10 times smaller and dust deposition is unlikely to occur. The window is a 24-cm diameter, 0.3-cm thick clear fused quartz disc. It has a nominal transmissivity of 0.94 in the 0.26-3.6 μm wavelength range, but its transmissivity drops to 0.20 in the 2.5-3.6 μm range. Thus, the quartz may absorb a substantial fraction of the infrared radiation emitted by the reactor in that range. Nevertheless, the physical and thermal properties of quartz should permit its continuous use up to 1300 K. The window is suspended in 3 o-rings that permit thermal expansion in any direction, and is mounted in a water-cooled copper ring that also serves as a shield for spilled radiation. In some of the experiments, we incorporated a water-cooled, diamond-machined aluminum CPC, which augmented the flux concentration by a factor of 2. Thus, for a given input power, the aperture size was reduced by half, and consequently, the re-radiation losses were reduced by half.

4.3.1.2 Solar Experimental Program

Solar experimentation was conducted at the *PSI*'s high-flux solar furnaces (see Chapter 2). The 1997 experimental campaign was conducted at the smaller solar furnace which is capable of delivering peak flux concentrations of up to 3000 suns (1 sun = 1 kW/m^2). The 1998 experimental

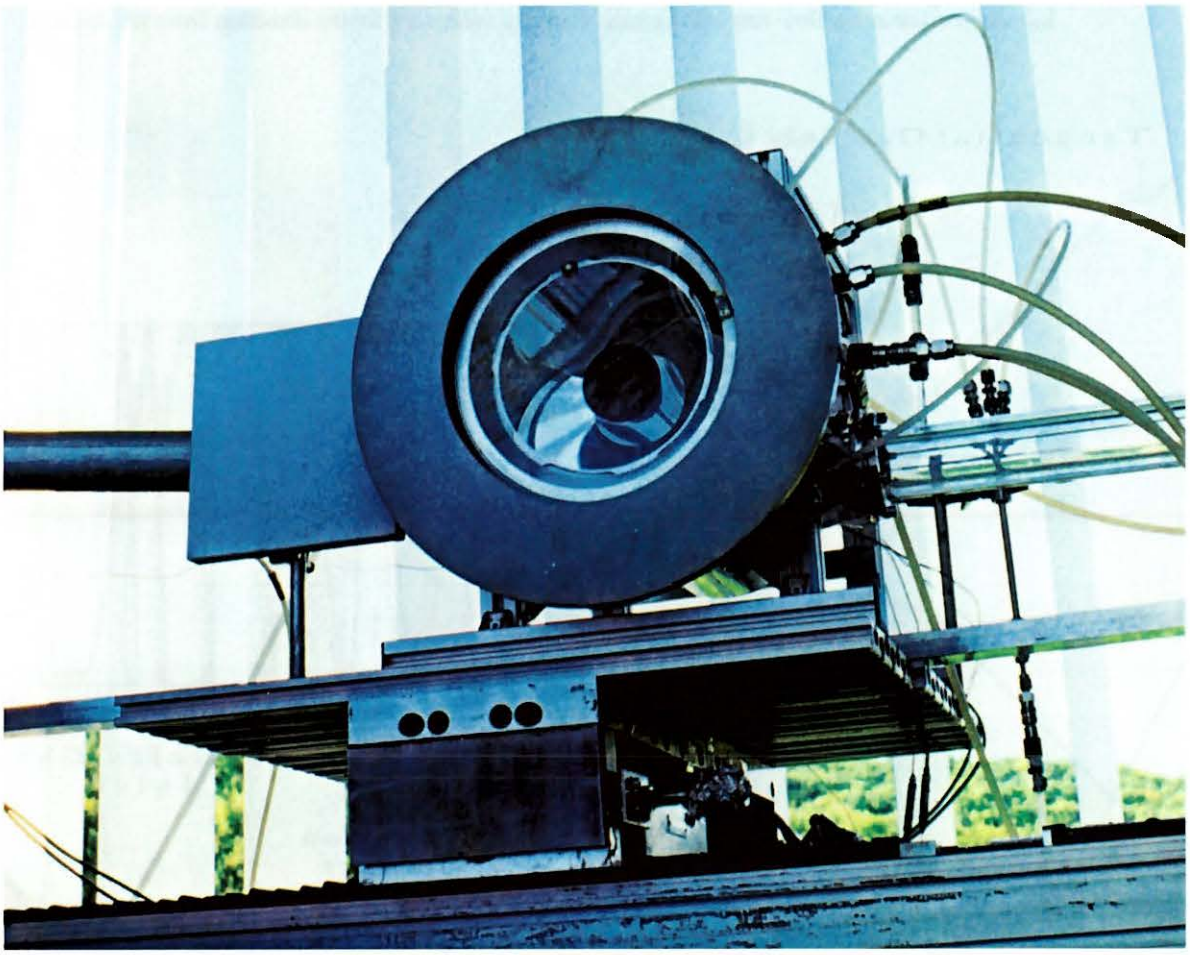

Figure 4.34 *SynMet* reactor: 5 kW prototype solar reactor tested at *PSI* solar furnace

campaign was conducted at the new solar furnace which delivers peak solar concentration exceeding 5000 suns.

The complete experimental reactor system, including the peripheral components and the measuring and control instrumentation, is shown schematically in Figure 4.35. *ZnO* particles are fed mechanically into the main gas stream by means of a spiral-type feeder, just before injection into the reactor. Gas mass flow rates and concentration of CH_4 in *Ar* are electronically controlled. Both gas and particles are injected at ambient temperature and at slightly above atmospheric pressure. If preferred, the main gas stream can be pre-heated electrically to simulate heat exchange with the exiting hot products. Reactor wall temperatures are measured with thermocouples type-K inserted in the wall and not exposed to the direct irradiation. Pressure inside the reactor is also electronically monitored and its value is limited by a pressure release safety valve. Reaction products exiting the reactor flow through a 1 m long water-cooled *Pyrex* condenser, where some portion of the *Zn* condenses. Downstream, a battery of filters collects the remaining particles, derived either from *Zn* condensation, *Zn* re-oxidation, or unreacted *ZnO*. The composition of the product gases is quantitatively analyzed by gas chromatography. The nature of the solid products collected at the condenser and at the filters is analyzed by X-ray powder diffraction. The amount of *Zn* produced is determined by reacting the solid products with *HCl* and measuring the volume of hydrogen evolved. The accuracy of such technique is ±6%.

Preliminary Solar Experimental Results

ZnO powder (Alfa Nr. 85113) with a mean particle size of 0.4 μm was fed at a rate of about 5 g/min. Inlet gas flow rate, for various concentrations of CH_4 in *Ar*, was in the 15-20 l_n/min^3 range; the auxiliary flow without particles was in the range of 20-30 l_n/min. The loading ratio

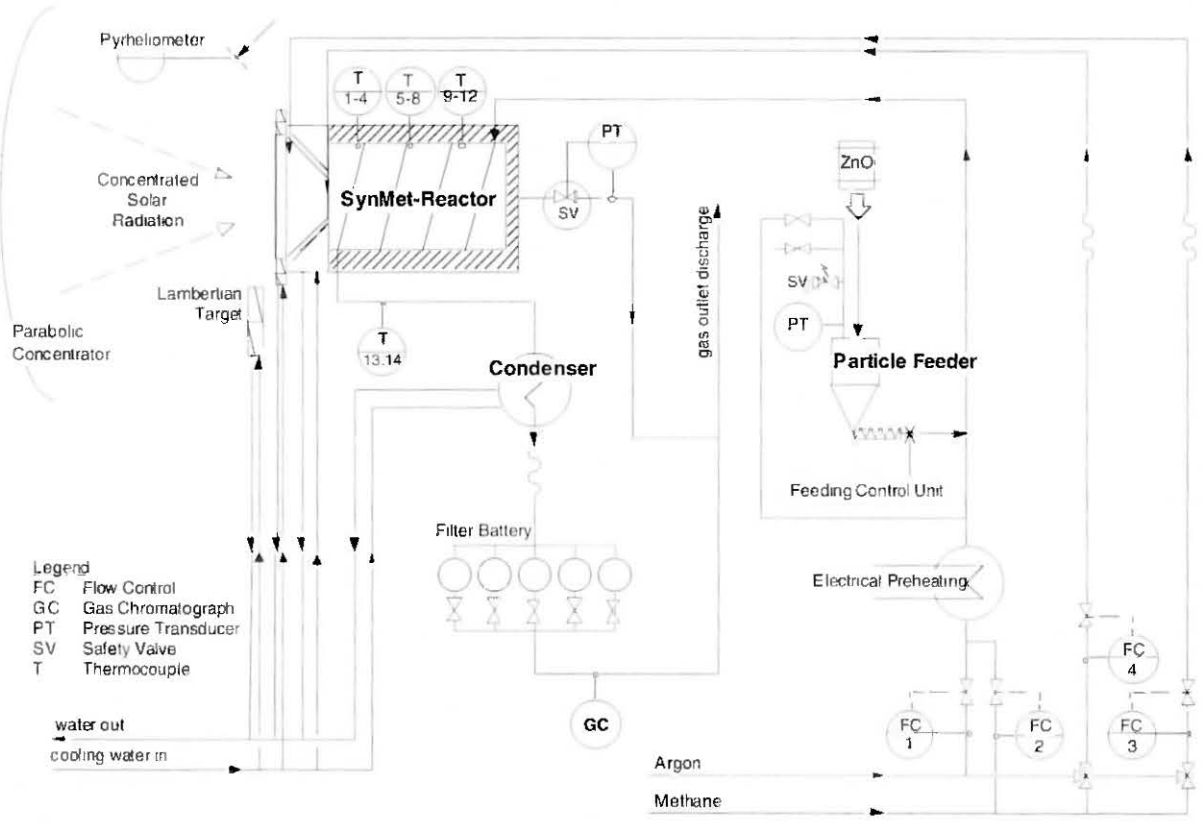

Figure 4.35 *SynMet* reactor: Flow sheet diagram of the complete experimental set-up [Steinfeld *et al.*, 1998b]. The reactor operates in a continuous mode; the reactant mass flow rates and inlet solar power are controlled.

of particles to gas was kept below the stoichiometric ratio [as given by equation (3.73)] to avoid plugging or sedimentation, and to protect the window from particle deposition. Excess methane was between 5 and 25 times more than the stoichiometric amount. During a typical experiment, the reactor was solar-heated to the desired temperature under a flow of Ar or N_2 and then isothermally subjected to the reacting flow. The reactor was exposed to peak solar fluxes of about 2,000 suns; higher flux intensities were possible but were avoided to prevent overheating. Maximum reactor wall temperatures, under approximate steady-state conditions, ranged between 1000-1600 K and were measured typically at the center top. As soon as particles were injected into the hot reactor, wall temperatures dropped by about 100-150 degrees, as a result of the endothermic reaction and of the shielding effect of the particles. The particles of ZnO were forced to the walls by the centrifugal force and were efficiently heated by contact with the hot walls (besides being heated by direct absorption, as described in the *Heat Transfer* paragraph of Section 4.3.1). Wall temperatures were not uniform; close to the aperture, where the main and cold auxiliary flows are mixed, temperatures were typically 100-250 degrees lower than those at the center top. A more uniform temperature distribution may be obtained by pre-heating both flows. Temperatures were controlled indirectly by controlling the amount of incoming power flux with the furnace's shutter. Zn vapor exiting the reactor was distilled in the water-cooled condenser.

The chemical conversion of ZnO to Zn obtained is shown in Table 4.13; the maximum reactor wall temperature, the CH_4 concentration of the inlet gas, the main inlet mass flow rate and its inlet temperature are also indicated. As expected, best results were obtained at higher temperatures, higher CH_4 concentrations, and when the reactants were pre-heated. The main differences between the 1997 and 1998 test campaigns are the inlet mass flow rate and the ZnO-feeding. As the inlet flow decreases, the residence time of the reactants at the hot reaction zone increases, leading to much higher zinc yields and approaching complete conversion. An additional consequence of reducing the inlet flow is that large ZnO particles which often result from agglomeration of poorly dispersed small particles are not conveyed and deposit on the reactor's cavity. These sediments eventually react and the product gases are finally transported out of the reactor. In contrast, when using 15-20 l_n/min, even large agglomerations of ZnO particles are conveyed and eventually leave the reactor before achieving complete reduction.

Zinc vapor exits the reactor in a reducing atmosphere of H_2, CO, and unreacted CH_4. Zinc is separated from the gas phase by condensation on the cold surface of the condenser. Zinc lost by re-oxidation during condensation is negligible. The implications of this simple observation are remarkable when one contemplates the conventional carbothermic smelting process, wherein coke serves as both reducing agent and primary energy source. There, coke is supplied in much excess of what is needed for reducing ZnO (about 4-6 times more), because it is burned internally to supply for the process heat [Graf, 1996]. Thus, zinc vapor is produced together with CO_2, and as the gases are cooled and zinc condenses, it can react immediately with CO_2. Industrially, the re-oxidation of zinc by CO_2 is avoided by using lead-spray condensers, in which a shower of 400 tons of molten lead are needed to separate 1 ton of zinc from the gas phase [Weidenkaff *et al.*, 1998]. The proposed solar process eliminates the need for Pb condensers.

Several solar runs were conducted without CH_4, in which reaction (3.43) was tested using 100% Ar or N_2 in the carrier gas. The results of these runs are also shown in Table 4.13 (see for "0" in the "*%CH4-Ar*" column). In the absence of a reducing agent, $ZnO(s)$ dissociates to $Zn(g)$ and O_2 and some portion of the zinc is subjected to re-oxidation during condensation. Higher zinc yields are obtained when using higher dilution of inert gas, but at the expense of reducing the energy efficiency [Palumbo *et al.*, 1998]. By studying the morphology of the solid products us-

3. l_n means liters at normal conditions; mass flow rates are calculated at 273 K and 1 atm.

Table 4.13 *SynMet*: Results from the solar experimental campaigns of 1997 and 1998. Indicated are: maximum wall temperature (T_{max}), methane concentration in the inlet gas, main inlet mass flow rate and inlet temperature, and zinc yield obtained.

	T_{max} [K]	CH_4-Ar [%]	Main Flow [l_n/min]	Inlet Temp. [K]	Zn yield[a] [%]
1997 Solar Test Campaign	1000	100	15-20	300	0.9
	1050	10	15-20	300	7.5
	1150	4	15-20	300	17.3
	1175	22	15-20	300	32.2
	1200	10	15-20	300	9.9
	1200	10	15-20	300	10.0
	1200	24	15-20	300	36.1
	1230	100	15-20	300	40.3
	1250	10	15-20	300	15.3
	1250	100	15-20	300	43.4
	1260	10	15-20	300	15.6
	1280	10	15-20	300	26.1
	1350	10	15-20	300	54.6
	1410	100	15-20	300	78.0
	1473	0	15-20	300	9.5[b]
	1550	10	15-20	800	85.0
	1600	10	15-20	800	90.0
1998 Solar Test Campaign	1223	10	5	773	98.8
	1273	10	5	773	98.8
	1273	10	5	723	100
	1273	10	5	300	99.5
	1323	10	5	693	95.7
	1373	10	5	773	99.4
	1373	10	5	753	100
	1373	10	12	300	80.0
	1373	0	5	773	95.5[c]
	1423	10	5	300	98.5
	1473	10	10	693	86.0
	1473	10	3	773	100
	1473	0	15	300	16.9[b]
	1473	0	5	733	96.4[b]
	1273-1600	10	5	773	100

a. Chemical conversion (or zinc yield) is defined as the amount of zinc produced in the solar furnace divided by the maximum amount of zinc that would have been recovered if the reaction had gone to completion. Representative product samples are taken from the material collected in the condenser and are analyzed by X-ray diffraction and by measuring the volume of hydrogen evolved when reacted with HCl. The accuracy of such technique is 6%.

b. 100% Ar in main and auxiliary flows; total 45 l_N/min

c. 100% N_2 in main and auxiliary flows; total 45 l_N/min

ing scanning electron microscopy it is possible to distinguish between *ZnO* particles formed by zinc re-oxidation and *ZnO* particles from unreacted reactants [Weidenkaff *et al.*, 1998]. For the runs of 1998 without CH_4, all of the *ZnO* collected in the condenser derived from the re-oxidation of zinc.

Scanning electron micrographs (S.E.M.) were obtained from the reactants and the products for the solar run using 10% CH_4-*Ar* and at a maximum wall temperature of 1280 K. Figure 4.36 shows *ZnO* powder used as reactant; particles underwent partial sintering while being dried for 2 hours at 873 K. Figure 4.37 shows the products collected at the water-cooled condenser where the average *Zn* yield obtained was 26.1%. It is observed that *Zn* grew in plane layers, resulting from the condensation of *Zn* vapor when coming in contact with the cold surface. Figure 4.38shows the products collected in the form of aerosol at the filter downstream from the condenser, where the average *Zn* yield was 30%. The spherical particles of 1-4 μm resulted from the condensation of *Zn* vapor and contain more than 70% *Zn* (as determined by Energy Dispersive X-ray spectroscopy, *EDX*). The remaining particles are mostly unreacted *ZnO* that were carried away by the gas flow.

Some observations about windows and CPCs

The window worked well during the course of the experiment. But, while trying to minimize the auxiliary flows, some Zn vapor would diffuse to the front, condense at the window, and decrease its transmissivity. Windowed reactors offer the advantage of direct irradiation of the reactants. However, windows that operate in the presence of severe atmospheres such as particles and condensing vapors require aerodynamic protecting flows. Unless such auxiliary flows serve also the function of reactants in gas-solid reactions, the energy conversion efficiency will be significantly decreased due to the energy requirement for separation and re-circulation processes. For example, for the $ZnO + CH_4$ reaction, methane should be used to protect the window. Another gas-solid reaction for which *SynMet* may find application is the solar gasification of car-

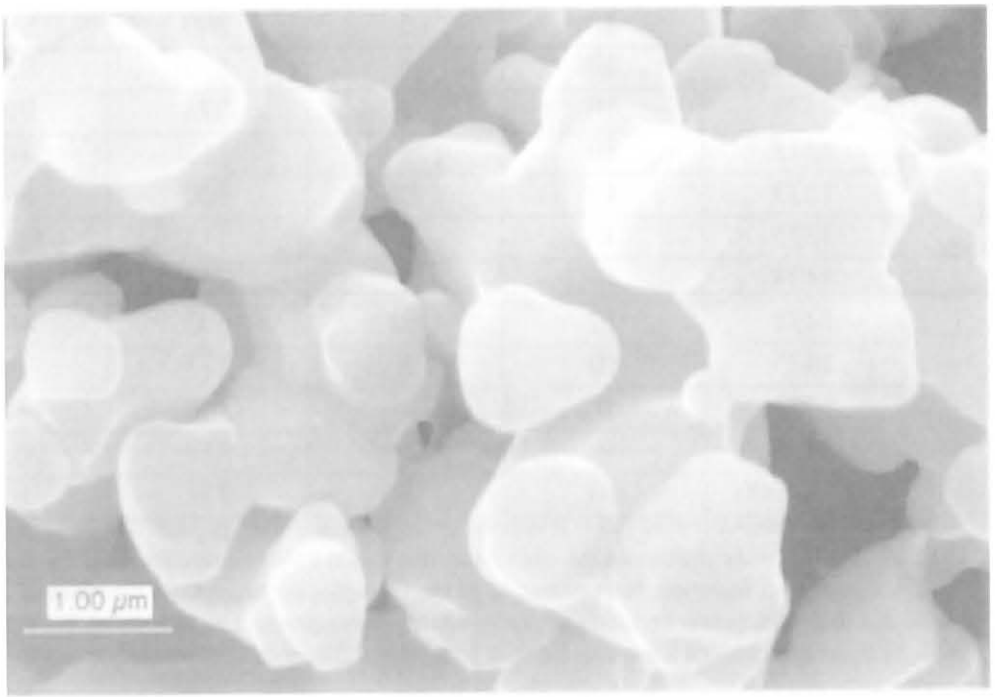

Figure 4.36 S.E.M. of the reactant *ZnO* powder (Alfa Nr. 85113) after drying for 2 hours at 873 K [Steinfeld *et al.*, 1998b].

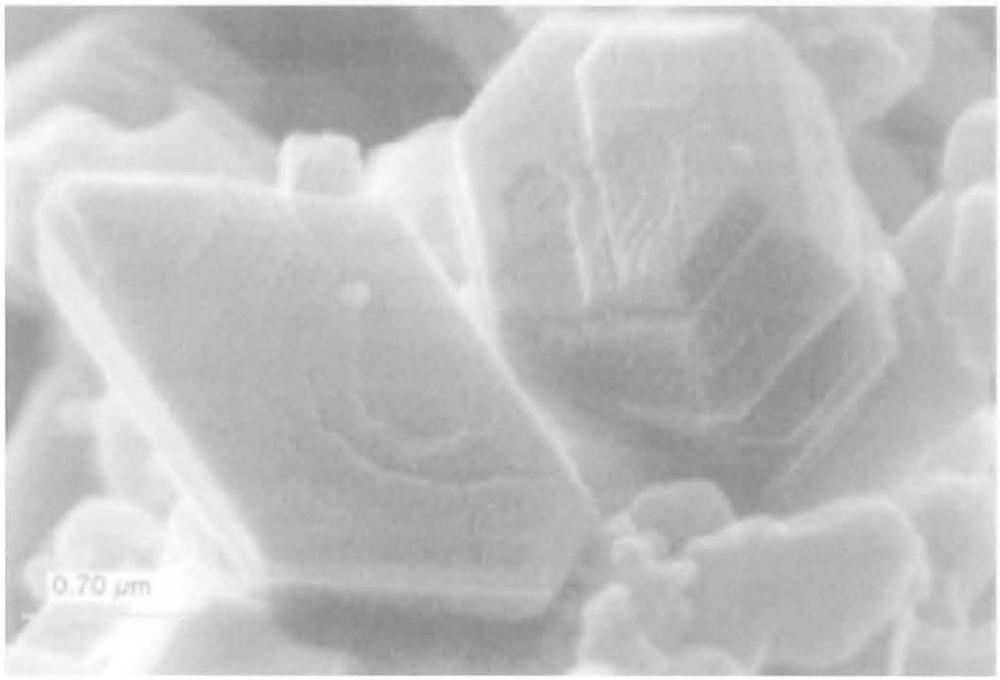

Figure 4.37 S.E.M. of products collected at the water-cooled condenser [Steinfeld *et al.*, 1998b]. *Zn* grew in plane layers as a result of the condensation of *Zn* vapor.

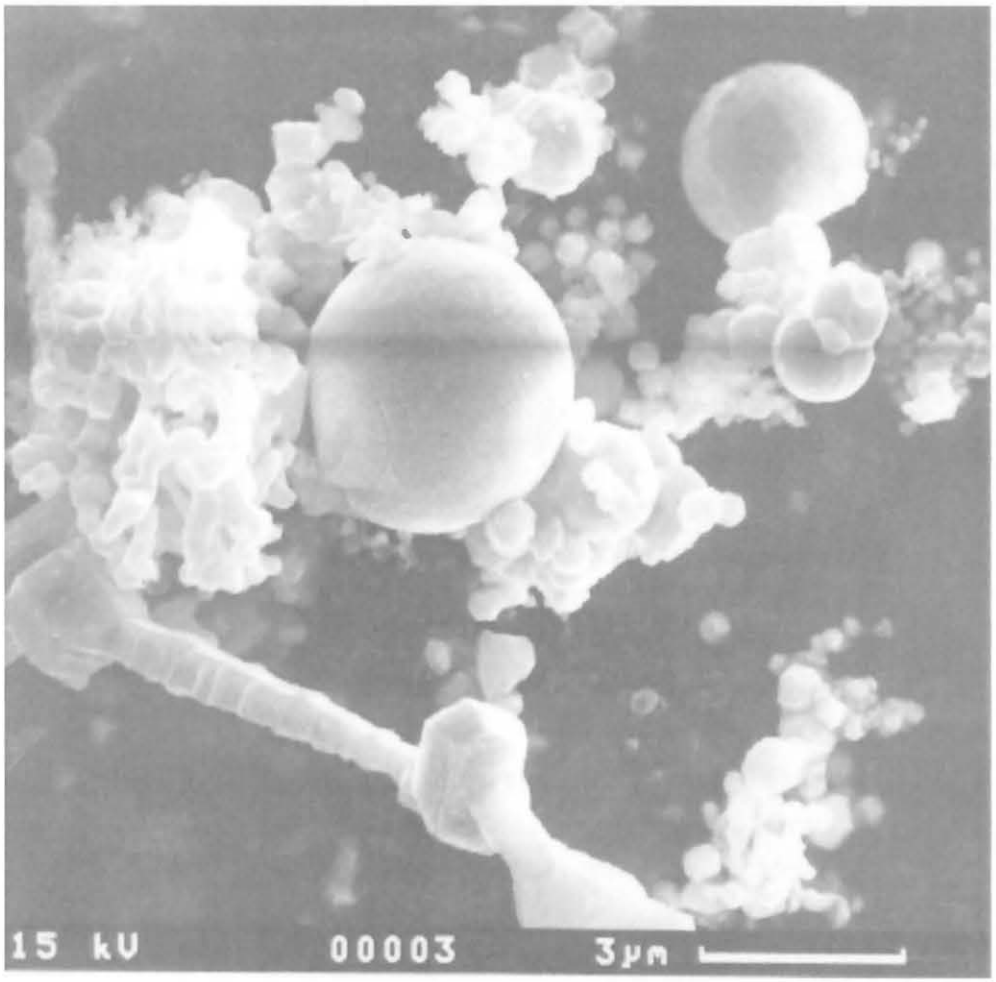

Figure 4.38 S.E.M. of products collected at the filter downstream from the condenser [Steinfeld *et al.*, 1998b]. The large spherical particles (of 1-4 µm) resulted from condensation and solidification of *Zn* vapor. The remaining particles are mostly unreacted *ZnO*.

bonaceous materials (e.g., coal and biomass). For gasification processes using steam as the gasifying agent, it would be preferable to use steam for protecting the window. The same problem affects the implementation of *CPCs* in severe gas-solid reacting environments. Since the concentrated light exits the *CPC* with a view angle of 180°, the *CPC* exit should be positioned exactly at the aperture plane. In this critical zone, *ZnO* particles or *Zn* vapor may be deposited and cause deterioration of the *CPC* reflectivity. Similar to the window protection, the *CPC* can also be protected by having an auxiliary flow that prevents dust deposition but, unless such a flow acts as a reactant, it will affect the reactor efficiency significantly. The use of *CPCs* and windows in gas-particle environments should be further investigated.

4.3.1.3 Concluding Remarks

We have presented the engineering design of a solar chemical reactor for conducting the simultaneous *ZnO*-reduction and CH_4-reforming. The vortex flow configuration was proven to be an efficient reactor concept for the transfer of heat to gas flows laden with particles and for conducting fast gas-solid thermochemical processes. First tests conducted in a solar furnace using a small scale reactor prototype yielded up to 90% chemical conversion to *Zn* in a single pass. Technical feasibility for the proposed solar process has been demonstrated. There is still room for improvement and optimization.

The use of high-temperature solar process heat for the co-production of zinc and synthesis gas offers the possibility of reducing greenhouse-gas and other pollutant emissions produced in conventional fossil-fuel-based processes. Furthermore, it provides an efficient conversion path of solar energy into storable and transportable chemical fuels.

Present market prices for *Zn* are about 1000 US$/mt. The cost of this valuable metal is directly tied to the cost of the energy required to produce it: assuming an energy consumption of 35-50 GJ/mt when produced electrolytically and a power cost of 0.05 US$/kWh, the cost of the energy represents between 40-70% of the value of *Zn*. The cost of solar producing *Zn* from *ZnO* would have to be compared with the economics of conventional fossil-fuel-based processes. Once the cost of energy will account for the environmental externalities from burning fossil fuels (e.g. depletion, CO_2 mitigation, and pollution abatement), solar energy will become a favorable competitive long term prospect.

Nomenclature

$A_{aperture}$	Area of reactor aperture, m^2
$\tilde{C}$	Mean flux solar concentration
ΔH	Enthalpy change, kW
F_{peak}	Peak solar flux intensity, kW/m^2
I	Normal beam insolation, kW/m^2
p	Pressure, atm.
$Q_{aperture}$	Incoming solar power intercepted by $A_{aperture}$, kW
$Q_{reactor,net}$	Net power absorbed by the solar reactor, kW
Q_{solar}	Total solar power coming from the concentrator, kW
$T_{reactor}$	Nominal cavity-receiver temperature, K
$r_{aperture}$	Radius of reactor aperture, m
r_{opt}	Optimum radius of reactor aperture for maximum $\eta_{absorption}$, m
α, ε	Apparent absorptance and emittance of the solar cavity-receiver

$\eta_{absorption}$	Solar energy absorption efficiency
μ	Radial standard deviation of Gaussian flux distribution, m
σ	Stefan-Boltzmann constant, $5.6705 \cdot 10^{-8}$ W m^{-2} K^{-4}

5 Conclusions

The results of this research bring fundamental knowledge applicable to the development of process technology for effecting solar thermal chemical transformations. The very specific details are found within each section of the report. Here we outline the major conclusion themes from the study.

Although at this time it is still controversial which metal oxide is best for storing sunlight in a uniquely solar process, the *Zn/ZnO* solar quench process from a process technology point of view has emerged as one with high potential. Unlike with the iron oxide system, the chemistry of the *ZnO* system is such that one can quench the products without necessarily compromising the viability of the process. A quench process requires a device to remove the sensible energy from the hot products. Such a device can be a cold surface, a device that cools by diluting the products with a gas, or a combination of these two ideas. By contrast, for the iron oxide system the chemistry is such that a quench will not be permitted if the process leading to a solar fuel is to be viable. After the product gas and liquid phases are in-situ separated, this chemical system will require heat exchangers that can transfer thermal energy at the high temperature of the products to the reactants throughout the process. Material problems and problems associated with matching heat exchanger flow conditions to avoid pinch points can make this type of device inherently more complex than a quenching device. The quench will not be easy for the *Zn/ZnO* process, but the device for doing it could be less complex than a system of heat exchangers.

The *Zn/ZnO* quench process has some inherent simplicity *vis-à-vis* solar processes using other oxide systems. But there are some very critical concerns that need to be addressed in future research. First, the quench will need to lead to high *Zn* yields and the quench medium will need to be economical. Specifically, if an inert gas is needed to effect the quench, it will be necessary to find an economical path for separating O_2 from the gas. Secondly, the reactor will require a window. This feature imposed by the chemistry of the reaction complicates the process engineering. Thirdly, one must envision the reactor that would interface the decomposition of *ZnO* to concentrated sunlight.

The research effort greatly advanced our understanding of the fundamentals for designing such solar chemical reactors. Firstly, we learned to use *CFD* as a tool for making design decisions. This numerical work enabled us to see how a given design concept will influence gas-particle flow paths and velocities. This information is critical if one is to optimize the thermal performance of a reactor. For example, our *CFD* work illustrated the critical conditions when excess air would flow through the aperture of an open to air reactor, thereby lowering its efficiency. Secondly, it is clear that the chemistry of a potential solar decomposition reaction places important constraints on the reactor designed to effect the chemical transformation. Chemical thermodynamics and kinetics of the decomposition and reverse reaction determine the reactor's operating temperature and pressure; they determine whether a quench or in-situ separation is needed; they indicate whether or not the reactor can be open to atmospheric air; and they reveal the maximum thermal efficiency for a process that would use a specific ideal reactor concept.

The thermal efficiency of a solar chemical plant is determined in part by the interrelationship between the flux intensity of the solar furnace, the chemical kinetics of the reaction, and the method by which the reactants are fed to and extracted from the reactor. Future reactor designs need to be developed in concert with numerical models of the reactor that couple the kinetics of a chemical reaction to the energy and mass balance equations. This next step in modeling adds to the extensive work we have done in *CFD*.

Besides chemistry boundary conditions, the reactor design must respect the transient nature of solar energy. This requirement means that the reactor should be made from conventional reliable materials. And the reactor needs to be able to handle thermal shocks while enabling reactants to quickly come to the reaction temperature. We call these mechanical engineering design constraints. Our work over the past several years in this regard focused on developing technically feasible high temperature reactors for generic metal oxide reactions. We developed reactors into which micro size reactants are fed in a gas stream forming a powder cloud. Concentrated solar radiation directly heated the particles enabling a fast reaction while the reactor walls remained at reduced temperatures. Our latest windowless reactor prototype operated for more than 50 hours while experiencing more than a hundred transients. Parts of the particle cloud reached temperatures near 1900 K.

Some of the volumetric reactor concepts described in Chapter 4 and the in-situ product separation reactor described in Section 3.2 are examples of reactor designs where we attempted to meet the chemistry and mechanical engineering boundary conditions.

An example of a volumetric reactor respecting these design boundary conditions is the closed moderate temperature reactor for effecting a $ZnO + CH_4$ reaction. It is a continuous flow reactor made from conventional materials. It has good thermal response to transients. The products exiting the reactor were rich in Zn and H_2. Future work will need to focus on keeping the window clean with a minimum flow of CH_4. High flows mean high convection heat losses at the surface of the window. It will be necessary to learn to operate the reactor near the stoichiometric ZnO/CH_4 ratio without the presence of an inert gas. Thus an experimental program will need to establish how close one can obtain the particle cloud density that gives this stoichiometric ratio. In addition, the mass flow rate must be matched to the solar flux input such that one obtains high conversion efficiencies at the desired operating temperature.

Our work with the solar calcination process gave us valuable experience in attempting to cooperate with industry. We began to approach some of the constraints and concerns industry can have with respect to turning a conventional fossil fuel process into a hybrid solar process. This knowledge base is a building block from which the Solar Technology Section at *PSI* will learn to transfer its ideas and technology to society.

In summary, the research has identified the fundamentals for designing a solar thermal chemical reactor, it identified future reactor development work, and it has suggested promising solar processes for either moderate or high temperature applications. Furthermore, the research program has given individuals the valuable experience of working with concentrated solar energy, experience that is invaluable to one trying to create the new technology.

6 Publications from this Project

6.1 Peer-Reviewed Journals

1992

Steinfeld A., Imhof A., Mischler D., "Experimental Investigation of an Atmospheric-Open Cyclone Solar Reactor for Solid-Gas Thermochemical Reactions", *Journal of Solar Energy Engineering* **114**, pp. 171-174, 1992.

1993

Steinfeld A., "Radiative Transfer in a Diffusely/Specularly Reflecting Spherical Cavity Containing a Gray Medium", *Wärme und Stoffübertragung* **28**, pp. 65-68, 1993.

Steinfeld A., Schubnell M., "Optimum Aperture Size and Operating Temperature of a Solar Cavity-Receiver", *Solar Energy* **50**, No. 1, pp. 19-25, 1993.

Steinfeld A., Kuhn P., Karni J., "High Temperature Solar Thermochemistry: Production of Iron and Synthesis Gas by Fe_3O_4-Reduction with Methane", *Energy - The International Journal* **18** (3), pp. 239-249, 1993.

1994

Steinfeld A., Bombach R., Haueter P., Hemmerling B., Kreutner W., Thompson G., Wuillemin D., "Experimental Set-Up of a Laser Diagnostics System for an High-Temperature Solar Receiver-Reactor", *Journal of Solar Energy Engineering* **116**, pp. 206-211, 1994.

Steinfeld A., Thompson G., "Solar Combined Thermochemical Processes for CO_2 Mitigation in the Iron, Cement, and Syngas Industries", *Energy - The International Journal* **19**, (10), pp. 1077-1081, 1994.

1995

Mischler D., Steinfeld A., "Nonisothermal Nongray Absorbing-Emitting-Scattering Suspension of Fe_3O_4-Particles Under Concentrated Solar Irradiation", *Journal of Heat Transfer* **117** (2), pp. 346-354, 1995.

Murray J. P., Steinfeld A., Fletcher E. A., "Metals, Nitrides, and Carbides Via Solar Carbothermal Reduction of Metals Oxides", *Energy - The International Journal* **20** (7), pp. 695-704, 1995.

Steinfeld A., Frei A., Kuhn P., Wuillemin D., "Solarthermal Production of Zinc and Syngas Via Combined ZnO-Reduction and CH_4-Reforming Processes", *International Journal of Hydrogen Energy* **20** (10), pp. 793-804, 1995.

Steinfeld A., Frei A., Kuhn P., "Thermoanalysis of the Combined Fe_3O_4-Reduction and CH_4-Reforming Processes", *Metallurgical and Materials Transactions* **26B**, pp. 509-515, 1995.

Tamaura Y., Steinfeld A., Kuhn P., Ehrensberger K., "Production of Solar Hydrogen by a Novel, 2-Step, Water-Splitting Thermochemical Cycle", *Energy - The International Journal* **20** (4), pp. 325-330, 1995.

1996

Meier A., Ganz J., Steinfeld A., "Modeling of a Novel High-Temperature Solar Chemical Reactor", *Chemical Engineering Science* **51** (11), pp. 3181-3186, 1996.

Steinfeld A., Kuhn P., Tamaura Y., "CH_4-Utilization and CO_2-Mitigation in the Metallurgical Industry via Solar Thermochemistry", *Energy Conversion and Management* **37**, pp. 1327-1332, 1996.

Steinfeld A., Larson C., Palumbo R., Foley M., "Thermodynamic Analysis of the Co-Production of Zinc and Synthesis Gas Using Solar Process Heat", *Energy - The International Journal* **21** (3), pp. 205-222, 1996.

Tsuji M., Wada Y., Tamaura Y., Steinfeld A., Kuhn P., Palumbo R., "Coal Gasification Using the ZnO/Zn Redox System", *Energy and Fuel* **10**, pp. 225-228, 1996.

1997

Ehrensberger K., Palumbo R., Larson C., Steinfeld A., "Production of Carbon from CO_2 with Iron Oxides and High-Temperature Solar Energy", *Industrial & Engineering Chemistry Research* **36**, pp. 645-648, 1997.

Steinfeld A., "High-Temperature Solar Chemistry for CO_2 Mitigation in the Extractive Metallurgical Industry", *Energy - The International Journal* **22** (2/3), pp. 311-316, 1997.

Steinfeld A., Kirillov V., Kuvshinov G., Mogilnykh Y., Reller A., "Production of Filamentous Carbon and Hydrogen By Solarthermal Catalytic Cracking of Methane", *Chemical Engineering Science* **52**, pp. 3599-3603, 1997.

Tamaura Y., Wada Y., Yoshida T., Tsuji M., Ehrensberger K., Steinfeld A., "The Coal/Fe_3O_4 System for Mixing of Solar and Fossil Energies", *Energy - The International Journal*, **22** (2/3), pp. 337-342, 1997.

Weidenkaff A., Nüesch P., Wokaun A., Reller, A., "Mechanistic studies of the water-splitting reaction for producing solar hydrogen", *Solid State Ionics* **101**, pp. 915-922, 1997.

1998

Haueter P., Seitz T., Steinfeld A., "A New High-Flux Solar Furnace for High-Temperature Thermochemical Research", *Journal of Solar Energy Engineering*, submitted 1998.

Meier A., Kirillov V.A., Kuvshinov G.G., Mogilnykh Yu.I., Reller A., Steinfeld A., Weidenkaff A., 1998b, "Solar Thermal Decomposition of Hydrocarbons and Carbon Monoxide for the Production of Catalytic Filamentous Carbon", *Proc. 15th International Symposium on Chemical Reaction Engineering*, Newport Beach, California, 13-16 September 1998, *Chem. Eng. Sci.*, in press 1999.

Meier A., 1998c, "A Predictive Model for a Falling Particle Receiver/Reactor Exposed to Concentrated Sunlight", *Proc. 15th International Symposium on Chemical Reaction Engineering*, Newport Beach, California, 13-16 September 1998; *Chem. Eng. Sci.*, in press 1999.

Palumbo R., Lédé J., Boutin O., Elorza Ricart E., Steinfeld A., Möller S., Weidenkaff A., Fletcher E. A., Bielicki J., "The Production of Zn from ZnO in a Single Step High Temperature Solar Decomposition Process", *Chemical Engineering Science* **53**, pp. 2503-2518, 1998.

Steinfeld A., Kuhn P., Reller A., Palumbo R., Murray J., Tamaura Y., "Solar-Processed Metals as Clean Energy Carriers and Water-Splitters", *International Journal of Hydrogen Energy* **23**, No. 9, pp. 767-774, 1998.

Steinfeld A., Brack M., Meier A., Weidenkaff A., Wuillemin D., "A Solar Chemical Reactor for the Co-Production of Zinc and Synthesis Gas", *Energy - The International Journal*, **23**, pp. 803-814, 1998.

Steinfeld A., Spiewak I., "Economic Evaluation of the Solar Thermal Co-Production of Zinc and Synthesis Gas", *Energy Conversion and Management* **39**, No. 15, pp. 1513-1518, 1998.

Steinfeld A., Sanders S., Palumbo R., "Design Aspects of Solar Thermochemical Engineering", *Solar Energy*, in press 1999.

Steinfeld A., Weidenkaff A., M. Brack, Möller S., Palumbo R., "Solar Thermal Production of Zinc: Program Strategy and Status of Research", High Temperature Material Processes, in press 1999.

Weidenkaff A., Steinfeld A., Wokaun, A., Eichler B., Reller A., 1998, "The Direct Solar Thermal Dissociation of Zinc oxide: Condensation and Crystallization of Zinc in the Presence of Oxygen", *Solar Energy*, in press 1999.

6.2 Conference Proceedings, Reports, and Posters

1992

Steinfeld A., Imhof A., Fletcher E. A., "High Temperature Solar Receivers with Internal Infrared Mirrors", *Proc. 6th Int. Symp. Solar Thermal Concentrating Technologies*, Vol. I, pp. 501-510, Mojacar, Spain, Sept. 28-Oct. 2, 1992.

Steinfeld A., Schubnell M., "Maximizing the Energy Conversion Efficiency of a Solar Cavity-Receiver", *Proc. 6th Int. Symp. Solar Thermal Concentrating Technologies*, Vol. I, pp. 491-500, Mojacar, Spain, Sept. 28-Oct. 2, 1992.

Steinfeld A, Kuhn P., "Direct Irradiation of Fe_3O_4-Particles Fluidized in Methane", *Solar Engineering 1993 - Proc. ASME International Solar Energy Conference*, pp. 19-24, Washington D.C., USA, April 22-28, 1993, and *PSI General Energy Technology Newsletter*, pp. 29-28, 1992.

1993

Steinfeld A., "Solar Thermal Reduction of Metal Oxides Without Discharge of Pollutants to the Environment", *C&E'93 - Proc. International Symposium on CO_2 Fixation and Efficient Utilization of Energy*, pp. 123-132, Tokyo, Japan, Nov. 29-Dec. 1, 1993.

Thompson G., Bombach R., Haueter P., Hemmerling B., Kreutner W., Steinfeld A., Wuillemin D., "*In situ* Laser Diagnostics of Solar Chemical Reactions using Coherent Anti-Stokes Raman Spectroscopy (CARS)", *Solar Engineering 1994 - Proc. ASME International Solar Energy Conference*, pp. 67-72, San Francisco, March 27-30, 1994, and *PSI General Energy Technology Newsletter*, pp. 31-33, 1993.

1994

Bombach R., Haueter P., Hemmerling B., Kreutner W., Steinfeld A., Thompson G., Wuillemin D., "CARS Measurements in a Solar Heated Reactor", *13th European CARS Workshop* (Poster Session), Paris, March 21-22, 1994.

Bombach R., Haueter P., Hemmerling B., Kreutner W., Steinfeld A., Thompson G., Wuillemin D., "Laserdiagnostik in einem solarchemischen Reaktor", *Proc. 9. Internationales Sonnenforum*, pp. 1346-1351, Stuttgart, 28 June - 1 July, 1994.

Funken K., Lüpfert E., Kuhn P., Steinfeld A., Wuillemin D., "High-temperature oxidation of micron to sub-micron sized carbon particles under high flux solar conditions", *Proc. 7th Int. Symp. Solar Thermal Concentrating Technologies*, Vol. 3, pp. 694-706, Moscow, Sept. 26-30, 1994.

Ganz J., Haueter P., Steinfeld A., Wuillemin D., "A Novel Volumetric Solar Reactor for Metal Oxides Reduction", *Proc. 7th Int. Symp. Solar Thermal Concentrating Technologies*, Vol. 4, pp. 826-832, Moscow, Sept. 26-30, 1994.

Kuhn P., Steinfeld A., Reller A., "Solar thermal production of basic chemicals: possibilities, potentials, and applications", *Proc. 7th Int. Symp. Solar Thermal Concentrating Technologies*, Vol. 3, pp. 557-565, Moscow, Sept. 26-30, 1994.

Meier A., "Computational Fluid Dynamics Simulation of High-Temperature Solar Chemical Reactors", *PSI Annual Report 1994 — Annex V*, pp. 35-37, 1994

Mischler D., Steinfeld A., "Improved Monte Carlo Simulation Using Bi-Cubic Bezier Splines", *Proc. 1st Joint Conference of International Simulation Societies*, pp. 226-229, Zürich, Aug. 22-25, 1994.

Murray J. P., Steinfeld A., "Solarthermal Production of Nitrides by Carbothermal Reduction of Metal Oxides in N_2-atmosphere" (Best Paper Award), *Solar Engineering 1994 - Proc. ASME International Solar Energy Conference*, pp. 59-66, San Francisco, March 27-30, 1994.

Nater E., "PULSAR-Warmphase, Abschlussbericht", 26. Aug. 1994, Bühler AG, Uzwil (DS-514 476), 1994

Steinfeld A., Brack M., Ganz J., Haueter P., Imhof A., Meier A., Mischler D., Nater E., Seitz T., Schwartz A., Wuillemin D., "Particle-Cloud Reactor Development for High-Temperature Solar Chemistry", *Proc. 7th Int. Symp. Solar Thermal Concentrating Technologies*, Vol. 4, pp. 888-895, Moscow, Sept. 26-30, 1994.

Steinfeld A., Bombach R., Hemmerling B., Kreutner W., Thompson G., "The Potential of In-Situ Laser Diagnostics for Solar Energy Research", *Proc. 7th Int. Symp. Solar Thermal Concentrating Technologies*, Vol. 4, pp. 1009-1013, Moscow, Sept. 26-30, 1994.

Steinfeld A., Kuhn P., "Solar-Processed Zinc as Clean Energy Carrier", *PSI Annual Report 1994 — Annex V*, pp. 33-34, 1994.

Steinfeld A., "Direct Absorption Chemical Processes", *International Energy Agency - Solar-PACES Annual Report*, pp. 62-65, 1994.

Tamaura Y., Steinfeld A., Kuhn P., Ehrensberger K., "A Novel 2-step Water-Splitting Thermochemical Cycle for Solar Energy Conversion", *PSI Annual Report 1994 - Annex V*, pp. 30-32, 1994.

1995

Kuhn P., Ehrensberger K., Steiner E., Steinfeld A., "An Overview on PSI's High-Temperature Solar Chemistry Research", *Solar Engineering 1995 - Proc. ASME International Solar Energy Conference*, pp. 375-380, Hawaii, March 19-24, 1995.

Kuhn P., Steinfeld A., Tamaura Y., "Two-Step H_2O-Splitting Solar Thermochemical Cycles based on Metal Oxides Redox Systems", *Proc. International Conference of the IEA Greenhouse Gas R&D Programme "Greenhouse Gases: Mitigation Options"* (Poster Session), London, UK, 22-25 August 1995.

Kuhn P., Steinfeld A., Reller A., "Solar Thermal Production of Basic Chemicals", *Solar World Congress* (Poster Session), Harare, Zimbabwe, 11-15 Sept., 1995.

Mischler D., Steinfeld A., "Monte Carlo Radiative Transfer Analysis of Particle Clouds" *PSI Annual Report - Annex V*, pp. 35-38, 1995.

Tamaura Y., Sano T., Tsuji M., Steinfeld A., Kuhn P., Ehrensberger K., "Ferrites for Solar Energy Conversion into Hydrogen Energy", *Proc. International Conference of the IEA Greenhouse Gas R&D Programme "Greenhouse Gases: Mitigation Options"* (Poster Session), London, UK, 22-25 August 1995.

Wada Y., Trianto A., Yamamoto T., Tsuji M., Tamaura Y., Steinfeld A., Ehrensberger K., Kuhn P., "Coal/Fe_3O_4 System for Mixing of Solar and Fossil Energies", *C&E'95 - Proc. 2nd International Symposium on CO_2 Fixation and Efficient Utilization of Energy* (Poster Session), Tokyo, Japan, Oct. 23-25, 1995.

1996

Ganz J., Meier A., Mischler D., Tschudi H.R., "Properties of volumetric gas-particle solar reactors", *Proc. 8th Int. Symp. On Solar Thermal Concentrating Technologies*, Köln, Germany, October 6-11, 1996.

Meier A., Ganz J., Steinfeld A., "Modeling of a Novel High-Temperature Solar Chemical Reactor", *14th International Symposium on Chemical Reaction Engineering* (Poster Session), Brugge, Belgium, 5-8 May, 1996.

Imhof A., "Decomposition of Limestone in a Solar Reactor", *Proc. World Renewable Energy Congress*, Denver, Co, USA, June 15-21, 1996.

Imhof A., "Decarbonization of Limestone with Solar Energy", *8th International Symposium on Solar Thermal Concentrating Technologies*, Köln, Germany, October 6-11, 1996.

Imhof A., "Entsäuerung von Kalkpulver in einem Solarreaktor", *XV. Kongress der internationalen Konferenz für industrielle Energiewirtschaft*, Leipzig, Germany, September 23-25, 1996.

Imhof A., "Decarbonization of Limestone with Solar Energy", *EuroSun 96*, Freiburg, Germany, September 16-19, 1996

Imhof A., *et al.*, Protokoll des ersten Workshop "Industrielle Solarkalzinierung", PSI, 3./4. Oktober 1996.

Kirillov V., Kuvshinov G., Reller A., Steinfeld A., "Production of Filamentous Carbon and H_2 by Solarthermal Catalytic Cracking of CH_4", *PSI Annual Report 1996*, p. 12-13

Steinfeld A., "Solar-Processed Chemical Fuels as Clean Energy Carriers", *Greenhouse Issues*, Vol. 27, 1996.

Steinfeld A., "Solar-Processed Metals: Energy Vectors of the 21st Century", *The 3rd. Sabin Conference on Energy and The Environment,* Weizmann Institute, Israel, Nov. 26, 1996.

Steinfeld A., Palumbo R., Lédé J., Tamaura Y., Reller A., "The Solar Thermal Reduction of Metal Oxides", *Proc. 8th Int. Symp. on Solar Thermal Concentrating Technologies*, Vol. 3, pp. 1231-1234, Cologne, Oct. 6-11, 1996.

Steinfeld A., Kuhn P., Reller A., Palumbo R., Murray J., Tamaura Y., "Solar-processed metals as clean energy carriers and water-splitters", *Hydrogen Energy Progress XI*, 1996, pp. 601-609.

Tamaura Y., Tsuji M., Ehrensberger K., Steinfeld A., "The Solar-Driven Coal/Fe_3O_4 Redox System", *Proc. 7th International Conference on Ferrites*, Bordeaux, France, Sept. 3-6, 1996.

Tamaura Y., Steinfeld A., "Combined Coal Gasification and Fe_3O_4-Reduction Using High-Temperature Solar Process Heat", *Proc. 8th Int. Symp. on Solar Thermal Concentrating Technologies*, Vol. 3, pp. 1235-1240, Cologne, Oct. 6-11, 1996.

1997

Ganz J., Schelling Th., Sturzenegger M., "A new design for volumetric gas/particle reactors for the solar thermal reduction of metal oxides", *PSI Annual Report 1997 - Annex V*, pp. 8-9, 1997.

Imhof A., *et al.*, Protokoll des zweiten Workshop "Industrielle Solarkalzinierung", PSI, 4. Juni 1997.

Imhof A., *et al.*, Protokoll des dritten Workshop "Industrielle Solarkalzinierung", PSI, 12. August 1997.

Möller S., Steinfeld A., Palumbo R.D., "Solarthermal Production of Zinc from Zinc Oxide", *International Symposium on Solar Chemistry* (Poster Session), Switzerland, Oct. 6-8, 1997.

Palumbo R., Steinfeld A., M, "ZnO in a High-Temperature Solar Decomposition Process", *PSI Annual Report - Annex V*, pp. 4-5, 1997.

Steinfeld A., Kesselring P., "Solar High-Temperature Technology" *1er Symposium Chaud*, pp. 47-75, Yverdon-les-Bains, March 12, 1997.

Steinfeld A., Brack M., Meier A., Palumbo R., Weidenkaff A., Wuillemin D., "Chemical Storage and Transport of Solar Energy", *International Symposium on Solar Chemistry* (Poster Session), Switzerland, Oct. 6-8, 1997.

Steinfeld A., Brack M., Meier A., Weidenkaff A., Wuillemin D., "A Solar Chemical Reactor for the Co-Production of Zinc and Syngas", *PSI Annual Report - Annex V*, pp. 6-7, 1997.

Weidenkaff A., Steinfeld A., Wokaun A., Auer P., Reller A., "The Direct Solar Thermal Dissociation of ZnO: Condensation and Crystallization of Zinc in the Presence of Oxygen", *VIth European Conference on Solid State Chemistry* (Poster Session), Zürich, Sept. 17-20, 1997; *International Symposium on Solar Chemistry* (Poster Session), Switzerland, Oct. 6-8, 1997.

Weidenkaff A., Steinfeld A., Wokaun A., Reller A., "The Solar Thermal Production of Zn from ZnO", *Gordon Research Conference on Solid State Chemistry*, Queen's College, Oxford UK, Sept 21-26, 1997.

1998

Boogmann P., Lippunder L., Zuberbuehler H. J., "Vergleich der herkömmlichen mit der solaren Zinkherstellung", *Semesterarbeit*, ETH Zürich, 1998.

Imhof A., "Proposal for a pilot and demonstration plant for a 1.5 MW_{th} solar calciner" (German title: "Antrag für ein Energieforschungs- und Technologietransferprojekt: Entwicklung und Untersuchung eines industriellen Solarkalzinators sowie Aufbau einer 100 kW Hochfluss-Turmanlage zur Demonstration der solaren Dissoziation von Zementrohmehl", under revision 1998).

Meier A., Kirillov V.A., Kuvshinov G.G., Mogilnykh Yu.I., Reller A., Steinfeld A., Weidenkaff A., "Solar Thermal Decomposition of Hydrocarbons and Carbon Monoxide for the Production of Catalytic Filamentous Carbon", *15th International Symposium on Chemical Reaction Engineering* (Poster Session), Newport Beach, California, 13-16 September 1998.

Meier A., "A Predictive Model for a Falling Particle Receiver/Reactor Exposed to Concentrated Sunlight", *15th International Symposium on Chemical Reaction Engineering* (Poster Session), Newport Beach, California, 13-16 September 1998.

Meier A., Kirillov V.A., Kuvshinov G.G., Mogilnykh Yu.I., Weidenkaff A., Steinfeld A., "Production of Catalytic Filamentous Carbon by Solar Thermal Decomposition of Hydrocarbons", *Proc. 9th International Symposium on Solar Thermal Concentrating Technologies*, Odeillo, France, June 22-26, 1998.

Vant-Hull L., Izygon M. E., Imhof A., "Optimization of Central Receiver Fields to Interface with Applications Requiring High Flux Density Receivers", *9th International Symposium on Solar Thermal Concentrating Technologies*, Odeillo, France, June 22-26, 1998.

6.3 Magazines and Newsletters

1997

Imhof A., Steinfeld A., Wokaun A.: "Die Sonne als Kalkbrenner", *Partnerschaften für die Zukunft - Die Entwicklungszusammenarbeit der ETH Zürich*, pp. 30-31, 1997.

Meier A., "Modeling Solar Chemical Reactors", *CFD Fluid Engineering Solutions - CFX Update* No. 14, p. 13, 1997.

Steinfeld A., Palumbo R., "Fuels from Sunlight and Water", *Sun at Work in Europe*, Vol. 12, No. 2, pp. 8-10, 1997, and in *World Development Aid & Joint Venture Finance - Energy Sources & Supply*, ed. A. J. Fairclough, Kensington Publications Ltd., UK, pp. 300-303, 1998.

1998

Meier, A., Steinfeld A., "Solarchemie - Technologie fürs 21. Jahrhundert", *Schweizerische Technische Zeitschrift - STZ Technik Aktuell*, Vol. 4, pp. 28-31, 1998.

Steinfeld A., Meier A., Palumbo R., "Brennstoffe aus Sonnenlicht und Wasser", *Sonnenenergie*, Vol. 3, pp. 12-15, 1998.

6.4 Dissertations and Diploma Theses

1995

Mischler D., 1995, "Strahlungsübertragung in Partikelwolken. Numerische und experimentelle Untersuchungen an Eisenoxid-Systemen im Hinblick auf eine chemische Speicherung von Sonnenenergie", *Dissertation,* PSI/ETH, Zürich, Nr. 11218.

1996

Ganz J., 1996, "Entwicklung von Gas-Feststoff-Reaktoren zur solarthermischen Metalloxidreduktion", *Dissertation,* PSI/ETH, Zürich, Nr. 11634.

Möller S., 1996, "Untersuchung der solarthermischen Dissoziation von ZnO zu Zn und O_2 in einem Sonnenofen zur Speicherung von Sonnenenergie", *Diplomarbeit,* Universität Dortmund, Germany.

6.5 Patents

1992

Imhof A., Zimmermann R., Marugg Ch., Kübler I., "Fensterloser Pulverwolkenreaktor für Solarchemie", Europäische Patentanmeldung "Pulsar" TZ 017, No. 92105191.8, October 21, 1992; US Patent Application No. 07/866323, 1992

1998

Steinfeld A., "Process for the reduction of metal oxides", Australia, No. 59435/98, March 20, 1998.

6.6 Conferences and Workshops

(partially sponsored by BFE)

1995

International Workshop on High-Temperature Solar Chemistry, PSI, Switzerland, August 17, 1995 (60 participants).

1996

1. Workshop "*Industrielle Solarkalzinierung*", 3./4. Oktober 1996.

1997

2. Workshop "*Industrielle Solarkalzinierung*", 4. Juni 1997.

3. Workshop "*Industrielle Solarkalzinierung*", 12. August 1997.

International Symposium on High-Temperature Solar Chemistry, PSI, Switzerland, October 6-8, 1997 (160 participants).

6.7 Press Releases

SEDOS/PSI: "Zement aus Sonnenenergie" (September 1996).

Radio DRS: "Einsatz der Solarenergie bei der Zement- und Wasserstoffproduktion" (13. Nov. 1996).

Frankfurter Allgemeine Zeitung: "Bauen mit Sonne" (20. 5. 1997).

Radio DRS, Fernsehen DRS, and 40 newspapers: "Inauguration of the new solar furnace" (October 6, 1997).

7 References

Ambriz J. J., Romero-Paredes H., Quintana J., 1985, Solar Chemical Reactors, *Proc. 7th Int. Conf. on Alternative Energy Sources*, Miami, USA, pp. 177-187

Abdelrahman M., Fumeaux P., Suter P., 1979, Study of Solid-Gas-Suspensions Used for Direct Absorption of Concentrated Solar Radiation, *Solar Energy* **22**, pp. 45-48

Abrahamson D., 1992, *Nature* **356**, 484

Alderton J.H., Wilkes N.S., 1988, Report AERE-R 13234, Harwell, UK

Andersson B., Sletnes J. O., 1977, *Acta Cryst.* **A33**, 268-276

Anthrop D.F., Searcy A.W., 1964, Sublimation and Thermodynamic Properties of Zinc Oxide. *Journal Physical Chemistry*, **68,** 2335-2342

Avdeeva L.B., Kuvshinov G.G., Goncharova O.V., Mogilnykh Yu.I., Likholobov V.A., 1995, Environmentally friendly production of new carbon materials from natural and oil tail gases, *Proc. 1st World Congress Environmental Catalysis, Pisa, Italy*, pp. 459-462

Badie J. M., Bonet C., Faure M., Flamant G., Foro R., Hernandez D., 1980, Decarbonation of calcite and phosphate rock in solar chemical reactors, *Chem. Eng. Sci.* **35**, pp. 413-420 (1980)

Baker R.T.K., Harris P.S., 1978, *Chemistry and physics of carbon Volume 14*, pp. 83-165, Marcel Decker Inc., New York

Baker R.T.K., 1989, *Carbon* **27**(3), 315-323

Barin I., 1993, *Thermochemical Data of Pure Substances, 2nd ed.*, Weinheim: VCH, 1690

Barret D., 1972, *Ind. Eng. Chem. Process Des. Develop.* **11**, pp. 415-420

Bilgen E., Ducarroir M., Foex M., Sibieude F., Trombe, F., 1977, Use of Solar Energy for Direct and Two-Step Water Decomposition Cycles. *Int. J. Hydrogen Energy*, **2,** 251-257

Birkle, 1994, *Messtechnik im Umweltschutz*, Vorlesungsskript, Universität Karlsruhe

Blake D., 1995, Bibliography of Work on the Photocatalytic Removal of Hazardous Compounds from Water and Air. National Renewable Energy Laboratory, NREL/TP-473-20300, Golden, CO, USA

Böhmer M., Cheza C., 1991, The Ceramic Foil Volumetric Receiver, *Solar Energy Materials* **24**, 182-191

Bohren, F. C., Huffman, D. R., 1983, Absorption and Scattering of Light by Small Particles, John Wiley & Sons, Inc., N.Y., USA., Appendix A: BHMIE subroutine, pp. 477-482

Boutin O., 1996, Dissociation Thérmique, Suivie de Trempe, de l'oxyde de zinc. *Diplôme d'Etudes Approfondies*, LSGC-ENSIC, Nancy-France

Braunschweig N., 1997, Ausmessung und Bewertung eines solaren Radiometers zur Messung konzentrierter Solarstrahlung, *Studienarbeit* PSI / TU Berlin

Brewer L., Mastick D.F., 1951, The Stability of Diatomic Gaseous Oxides. *Journal Chemical Physics*. **19,** 834-843

Bronstien L.N., Semendjajew, 1991, *Taschenbuch der Mathematik*, B.G. Teubner, Stuttgart

Brown H.E., 1976, Zinc Oxide Properties and Applications, International Lead Zinc Organisation, New York, *Zinc: The Metal, Its Alloys and Compounds*, Edited by C.H. Mathewson

Buck R., Muir J. F., Hogan R. E., Skocypec R. D., 1991, Carbon Dioxide Reforming of Methane in a Solar Volumetric Receiver/Reactor: the Caesar Project. *Solar Energy Materials* **24**, 449-463

Calvert P., 1992, *Nature* **357**, 365

Canadas L., Salvador L., Ollero P., 1990, Radiative Heat-Transfer Model in the Interior of a Pulverized Coal Furnace, *Ind. Eng. Chem. Res.* **29**, pp. 669-675

CFDS-FLOW3D, 1994, *Release 3.3: User Manual*, AEA Technology, Harwell, UK (June 1994)

CFX-F3D, 1995, *Release 4.1: User Manual*, AEA Technology, Harwell, UK (October 1995)

CFX-4, 1997, *Release 4.2: User Manual*, AEA Technology, Harwell, UK (December 1997)

Chase Jr. M. W., *et al.* 1985, *JANAF Thermochemical Tables, Third ed. Part 1*, American. Institute of Physics, New York, NY 10017, USA, p.15

Clift R., Grace J.R., Weber M.E., *Bubbles, Drops and Particles*, Academic Press, London

Collares-Pereira *et al.*, 1995, *Proc. SPIE*, 2538, p.131-135

Coughlin J. P., 1954, Heats and Free Energies of Formation of Inorganic Oxides, *National Bur. Mines Bull.* **542,** Pittsburgh, PA, USA

Davis C. G., McFarlin J. F., Pratt H. R., 1982, *Ironmaking and Steelmaking* **9**, 93

De Laquil P., 1994, Status of Solar Tower Development. *Proceedings 7th Int. Symp. Solar Thermal Concentrating Technologies*, pp. 59-71, Moscow, Russia

Denk Th., 1996, The Falling-Particle-Receiver (FPR), *Proc. 8th Int. Symp. Solar Thermal Concentrating Technologies*, Köln, Germany, October 6-11, 1996

Diebold J., Scahill J.W., 1997, *Developments in Thermochemical Biomass Conversion*, Banff, Canada, pp. 242-252

Dillon A.C., Jones K.M., Bekkedahl T.A., 1997, *Nature* **386**, 377-379

Diver R. B., 1987, Receiver/Reactor Concepts for Thermochemical Transport of Solar Energy, *J. Solar Energy Engineering* **109**, 199-204

Duncan D. A., Dirksen H. A., 1980, SERI/TR-98326-1, Boulder, CO, USA

Durisch W., Kuhn P., Maurer H., Wochele J., 1990, Some physical and chemical experiments under concentrated solar radiation, *5th Symp. Solar High Temp. Technologies*, Davos, Switzerland

Edwards D. K., Glassen L. K., Hauser, W. C., Tuchscher, J. S., 1967, Radiation Heat Transfer in Nonisothermal Nongray Gases, *J. Heat Transfer* **89**, pp. 219-229

Ehrensberger K., Frei A., Kuhn P., Oswald H. R., Hug P., 1995, Comparative Experimental Investigations of the Water-splitting Reaction with Iron Oxide $Fe_{1-y}O$ and Iron Manganese Oxides $(Fe_xMn_{1-x})_{1-y}O$. *Solid State Ionics* **78**, 151-160

Ehrensberger K., Palumbo R., Larson C., Steinfeld A., 1997, Production of Carbon from CO_2 with Iron Oxides and High-Temperature Solar Energy. *Industrial & Engineering Chemistry Research* **36,** 645-648

Eicher H., 1985, Chemische Speicherung von Sonnenenergie, *Ph.D. Thesis*, Universität Basel

Eichler B., Zude F., Fan W., Trautmann N., Herrmann G., 1992, Volatilization and Deposition of Ruthenium Oxides in a Temperature Gradient Tube. *Radiochimica Acta* **56**, 133-140

Encyclopedia of Chemical Technology, 1985, 3rd edition, John Wiley & Sons, New York, **24,** pp. 807-854

Engeln-Muellges G., Reutter F., 1987, *Numerische Mathematik für Ingenieure*, B.I. Wissenschaftsverlag, Zurich, pp. 339-347

Estermann A., Widmer P., 1997, Ermittlung und Eichung einer Methode zur schnellen Bestimmung des Zinkgehaltes in Zn/ZnO Mischungen, Semesterarbeit

Evans G., Houf W., Greif R., Crowe C., 1987, Gas-Particle Flow Within a High Temperature Solar Cavity Receiver Including Radiation Heat Transfer, *J. Solar Energy Engineering* **109**, pp. 134-142

Falcone P.K., 1984, Technical Review of the Solid Particle Receiver Program, January 25-26, 1984, SANDIA National Laboratories, Livermore, *Report SAND84-8229*

Falcone P.K., Noring J.E., Hruby J.M., 1985, Assessment of a Solid Particle Receiver for a High Temperature Solar Central Receiver System, SANDIA National Laboratories, Livermore, *Report SAND85-8208*, p. 30

Flagan R.C., Seinfeld J.H., 1988, *Fundamentals of Air Pollution Engineering*, Prentice Hall

Flamant G., Hernandez D., Bonet C., Traverse J., 1980, Experimental Aspects of the Thermochemical Conversion of Solar Energy: Decarbonation of $CaCO_3$. *Solar Energy* **24**, 385-395

Flamant G., Gauthier D., Boudhari C., Flitris Y., 1988, A 50 kW Fluidized Bed High Temperature Solar Receiver: Heat Transfer Analysis. *Solar Energy Engineering* **110**, 313-320

Fletcher E.A., Moen R.L., 1977, *Science*, **197**, 1050

Fletcher E. A., 1983, *J. Minnesota Academy of Science* **49**, 30

Fletcher E. A., Noring J.E., 1983, High Temperature Solar Electrothermal Processing — Zinc from Zinc Oxide. *Energy*, **8,** 247-254

Fletcher E.A., MacDonald F. J., Kunnerth D., 1985, High Temperature Solar Electrothermal Processing II. Zinc from Zinc Oxide. *Energy*, **10,** 1255-1272

Fletcher E.A., 1997, A Message to the 2nd International Symposium on CO_2 Fixation and Efficient Utilisation of Energy. *Energy*, **22,** 107-108

Frysz Ch.A., Shui X., Chung D.D.L., 1996, *Journal of Power Sources* **58**, 41-54

Gallagher P. K., Johnson D. W., 1973, The effects of sample size and heating rate on the kinetics of the thermal decomposition of $CaCO_3$, *Thermochimica Acta* **6**, pp. 67-83

Ganz J., Haueter P., Steinfeld A., Wuillemin D., 1994, *Proc. 7th Int. Symp. Solar Thermal Concentrating Technologies*, **4**, pp. 826-832, Moscow, Russia (Sept. 26-30, 1994)

Ganz J., 1996, Entwicklung von Gas-Feststoff-Reaktoren zur solarthermischen Metalloxidreduktion, *PSI/Diss. ETH* Nr. 11634

Ganz J., Meier A., Mischler D., Tschudi H.R., 1996, Properties of volumetric gas-particle solar reactors, *Proc. 8th Int. Symp. On Solar Thermal Concentrating Technologies*, Köln, Germany

Ganz J., 1997, Solscup – Scale Up eines Solarreaktors: Schlussbericht, *PSI Internal Report*

Ganz J., Schelling Th., Sturzenegger M., 1997, A new design for volumetric gas/particle reactors for the solar thermal reduction of metal oxides, *PSI Annual Report 1997 - Annex V*, pp. 8-9

Ghosh D., Roy, A.K., Ghosh, A., 1986, *Transactions Iron Steel Inst. Jpn.* **26**, pp. 186-193

Goedecke R., 1974, Untersuchung des Verweilzeit- und Kontaktzeitverhaltens des Anströmgases in Wirbelbett-Reaktoren bei verschiedenen Temperaturen, *Dissertation*, TU Hannover

Goncharova O.V., Avdeeva, L.B., Fenelonov, L.B. *et al.*, 1995, *Kinet. Katal.* **36**, 293-298

Gordon S., McBride J. B., 1976, Computer Program for Calculation of Complex Chemical Equilibrium Composition, Rocket Performance, Incident and Reflected Shocks, And Chapman-Jouguet Detonations, NASA SP-273, NASA Lewis Research Center, Cleveland[1]

Grasse W., Becker M., Finnstroem B., 1987, *Solar Energy for High Temperature Technology and Applications*, DFVLR, Cologne, Germany

Gretz J., Korf W., Lyons R., 1991, *Int. J. Hydrogen Energy* **16**, 691

Gronen, Unger, 1992, Partikelströmung PULSAR, T.O.R.-Engineering; D-Köln

Grunze M., Hirschwald W., 1974, *J. Vac. Sci. Technol.* **11**, pp. 424-428

Grunze M., 1981, Reduction and Chlorination of ZnO, pp. 432-447, in *Current Topics in Materials Sciences* **7**, Ed. E. Kaldis, North-Holland Publishing Co.

Guger C.E., Manning F. S., 1971, *Metallurgical Transactions* **2**, pp. 3083-3090

Gupta R. P., Wall T. F., Truelove J. S., 1983, Radiative scatter by fly ash in pulverized-coal-fired furnaces: application of the Monte Carlo method to anisotropic scatter, *Int. J. Heat Mass Transfer* **26**, pp. 1649-1660

Gyurech M., 1997, Einfluss der solaren Kalzinierung auf die Energiebilanz, die Qualität und die Wirtschaftlichkeit des Klinkerbrennens, Holderbank Management und Beratung AG, Bericht PT 97/14289/D

Haas L. A., Nigro J. C., Zahl R. K., 1985, Bureau of Mines Report RI-8997, U. S. Department of Interior, Minneapolis, MN

Hasiguti R.R., Yumoto H., Kuriyama Y., 1981, Thin layer VLS growth, its cessation and morphologies of Cd crystals with Bi impurities. *Journal of Crystal Growth* **52**, 135-140

Hassmann K., Kühne H.M., 1993, *Int. J. Hydrogen Energy* **18**, 635-640

Haueter P., Seitz T., Steinfeld A., 1998, A New High-Flux Solar Furnace for High-Temperature Thermochemical Research, *Journal of Solar Energy Engineering*, submitted 1998.

1. A *PC*-version devised by T. Kappauf, M. Pipho, and E. Whitby for E. A. Fletcher at the University of Minnesota was used in this study

Heaslet M. A., Warming R. F., 1965, Radiative Transport and Wall Temperature Slip in an Planar Medium, *Int. J. Heat Mass Transfer* **8**, pp. 979-994

Hills A. W. D., 1968, The mechanism of the thermal decomposition of calcium carbonate, *Chemical Engineering Science* **23**, pp. 297-320

Hirschwald W., Stolze F., 1972, Kinetics of the Thermal Dissociation of Zinc Oxide. *Zeitschrift Physikalische Chemie Neue Folge*, **77**, 21-42

Houf W. G., Greif R., 1987, Radiant Transfer in a Solar Absorbing Particle Laden Flow, *Chemical Engineering Communications* **51**, pp. 153-165

Howell J. R., Perlmutter M, 1964, Monte Carlo Solution of Thermal Transfer Through Radiant Media Between Gray Walls, *J. Heat Transfer* **86C**, pp. 116-122

Hruby J.M., 1986, A technical feasibility study of a solid particle solar central receiver for high temperature applications, *Report SAND-86-8211*, SANDIA National Laboratories, Livermore, USA

Hsia H. M., Love T. J., 1967, Radiative Heat Transfer Between Parallel Plates Separated by a Nonisothermal Medium with Anisotropic Scattering, *J. Heat Transfer* **89C**, pp. 197-204

Hunt A. J., Brown C. T., 1983, Solar Test Results of an Advanced Direct Absorption high Temperature Gas Receiver (SPHER), *Proc. ISES Solar World Congress*, Perth, Australia, Aug. 15-19, **2**, pp. 959-962

Hunt A. J., Ayer J., Hull P., Miller F., Noring J. E., Worth D., 1986, Solar Radiant Heating of Gas-Particle Mixtures. Lawrence Berkeley Laboratory LBL-22743, University of California, Berkeley, CA 94720, USA

Hunt A. J., Ayer J., Hull P., Miller F., Noring J. E., Worth D., 1987, Solar Radiant Heating of Gas-Particle Mixtures, Lawrence Berkeley Laboratory, University of California LBL-22743, Berkeley, CA 94720.

Hutchings K. M., Hawkins R. J., Smith J. D., 1988, *Ironmaking and Steelmaking* **15**, pp. 121-126

Huwyler S., Seifritz W., 1975, *Nature* **255**, 188

Iijima S., 1991, *Nature* **354**, 56

Imhof A., 1990, The cyclone reactor—An atmospheric open solar reactor, *5th Symp. Solar High Temp. Technologies*, Davos, Switzerland.

Imhof A., Suter C., Steinfeld A., 1991, Solar Thermal Decomposition of $CaCO_3$ on an Atmospheric-open Cyclone Reactor, *Proc. Biennial Congress of the ISES 91*, Denver, USA, **2**, pp. 2091-2096

Imhof A., 1996a, Decarbonization of Limestone with Solar Energy, *Proc. 8th Int. Symp. On Solar Thermal Concentrating Technologies*, Köln, Germany, October 6-11, 1996

Imhof A., 1996b, Protokoll des ersten Workshop "*Industrielle Solarkalzinierung*", 3. / 4. Oktober 1996

Imhof A., 1997a, Protokoll des zweiten Workshop "*Industrielle Solarkalzinierung*", 4. Juni 1997

Imhof A., 1997b, Protokoll des dritten Workshop "*Industrielle Solarkalzinierung*", 12. August 1997

Imhof A., 1998, Proposal for a pilot and demonstration plant for a 1.5 MW_{th} solar calciner (German title: Antrag für ein Energieforschungs- und Technologietransferprojekt: Entwicklung und Untersuchung eines industriellen Solarkalzinators sowie Aufbau einer 100 kW Hochfluss-Turmanlage zur Demonstration der solaren Dissoziation von Zementrohmehl, currently under revision)

Ingel G., Levy M., Gordon J., 1992, Oil-Shale Gasification by Concentrated Sunlight: An Open-Loop Solar Chemical Heat Pipe. *Energy - The International Journal* **17**, 1189-1197

Iwanaga H., Fujii M., Ichihara M., Takeuchi S. 1994, Some evidence for the octa-twin model of tetrapod ZnO particles. *Journal of Crystal Growth* **141**, 234-238

Jakubith M., 1991, *Chemische Verfahrenstechnik: Einführung in Reaktionstechnik und Grundoperationen*, VCH, Weinheim

JANAF Thermochemical Tables, 1985, National Bureau of Standards, 3rd ed., Washington, D.C., USA

Kappauf T., Murray J. P., Palumbo R. D., Diver R. B., Fletcher E. A., 1985, Hydrogen and Sulfur from Hydrogen Sulfide - IV. Quenching the Effluent from a Solar Furnace. *Energy - The International Journal* **10**, 1119-1137

Kashireninov O.E., Kuznetsov V.A., Repka L. F., 1978, Kinetics of the Gas-phase Reactions of Zinc and Cadmium with Molecular Oxygen. *Russian Journal Physical Chemistry*, **52**, 107

Kashireninov O.E., Manelis G.B., Repka, L.F., 1982, Recalculation of the Kinetic Constants for the Oxidation of Alkaline-earth Metal Vapours. *Russian Journal Physical Chemistry*, **56**, 630-631

Khassin A.A., Yuriewa T.M., Zaikovskii V.I. *et al.*, 1998, *Kinet. Catal.* **39**, 1-11

Kim T. K., Menart J. A., Lee H. S., 1991, Nongray Radiative Gas Analysis Using the S-N Discrete Ordinates Method. *J. Heat Transfer* **113**, pp. 946-952.

Kirillov V., Kuvshinov G., Reller A., Steinfeld A., 1996, Production of Filamentous Carbon and H_2 by Solarthermal Catalytic Cracking of CH_4, *PSI Annual Report 1996 - Annex V*, pp. 12-13

Klimas P. C., Diver R. B., Chavez J., 1991, United States Department of Energy Solar Receiver Development. *Solar Energy Materials* **24**, 136-150

Koenigsdorff R., 1994, Direkteinkopplung konzentrierter Solarstrahlung in eine zirkulierende Wirbelschicht, *VDI-Fortschrittsberichte Reihe 6*, Nr.301, VDI-Verlag

Kola R., 1985, *Proceedings of the International Symposium on Extractive Metallurgy of Zinc*, Tokyo, 14-16 October 1985, pp. 573-596

Koumoto K., Yanagida H., Mizuta S., 1980, Evaporation of Zinc Oxide from Spinel Solid Solutions in Vacuum. *Journal American Ceramic Society*, **63**, 17-20

Kreetz H., 1996, Entwicklung und Konstruktion eines solaren Radiometers zur Messung der Leistung am Solarkonzentrator des Paul Scherrer Instituts, *Studienarbeit* PSI / TU Berlin

Kübler I., 1990, PULSAR-Zwischenbericht 1990, Fa. Bühler AG Uzwil (Schweiz)

Kuhn P., Ehrensberger K., Steiner E., Steinfeld A., 1995, An Overview on PSI's High-Temperature Solar Chemistry Research. In *Solar Engineering 1995 - Proceedings ASME International Solar Energy Conference*, Hawaii, USA, pp. 375-380

Kumar S., Tien C. L., 1990, Analysis of Combined Radiation and Convection in a Particulate-Laden Liquid Film, *J. Solar Energy Engineering*, **112**, pp. 293-300

Kuvshinov G.G., Mogylnik Yu.I., Kuvshinov D.G. *et al.*, 1998, *Carbon* **36** (1-2), 87-97

Hellwege K. H., ed. 1982, *Landolt-Boernstein Numerical Data and Functional Relationships in Science and Technology*, New Series, Springer-Verlag, Berlin, **17g**, p. 543

Lapicque F., 1983, Mise en Oeuvre de Réactions Chimiques a très Haute Température dans un Ecoulement a Travers une Zone soumise a une Forte Concentration d'Energie. Application à la Thermolyse de L'Eau. *Ph.D Thesis*, LSGC-INPL, Nancy, France

Lapicque F., Lédé J., Tironneau P., Villermeaux J., 1985, A Solar Reactor for High-Temperature Gas Phase Reactions (Water and Carbon Dioxide Thermolysis and Nitric Oxide Synthesis). *Solar Energy*, **35**, 153-166

Lédé J., Villermaux J., 1993, Comportement thermique et chimique de particules solides subissant une réaction de décomposition endothermique sous l'action d'un flux de chaleur externe. *Can. J. Chem. Eng.*, **71**, 209-217

Lédé J., 1994, Reaction temperature of solid particles undergoing an endothermic volatilisation. Application to the fast pyrolysis of biomass. *Biomass Bioenergy*, **7**, 49-60

Leonard B. P., Drummond J. E., 1995, *Int. j. numer. methods fluids*, **20**, 421-442

Leschziner M. A., 1994, *Computational Fluid Dynamics '94*, pp. 33-46

Levenspiel O., 1972, *Chemical Reaction Engineering*, 2nd ed., John Wiley & Sons, Inc., New York

Levy M., Rubin R., Rosin H., Levitan R., 1992, Methane Reforming by Direct Solar Irradiation of the Catalyst, *Energy - The International Journal* **17**, 749-750

Lewandowski A., Fields C., 1998, NREL, private communication

Lewis L. A., Cameron, A. M., 1995, Oxidation Kinetics of Zinc Vapor in CO:CO_2 Mixtures: Part I. Comparison with Past Literature. *Metallurgical Materials Transactions*, **26B**, 911-918

Li W.Z., Xie S.S., Qian B.H. *et al.*, 1996, *Science* **274**, 1701-1703

Likholobov V.A., Fenelov V.B., Okkel L.G. *et al.*, 1995, *React. Kinet. Catal. Lett.* **54** (2), 381-411

Lin H. S., Sparrow E. M., 1965, Radiant Interchange among curved specularly reflecting surfaces—Application to cylindrical and conicalcavities, *Transactions of the ASME Journal of Heat Transfer*, pp. 299-307

Malinovskaja O.A., Beskov V.S., Slin'ko M.G., 1975, Simulation of catalyst processes on the pore granules. *Nauka*, Novosibirsk, 264

Mayer R., 1996, Simulation von solaren Gas-Feststoff-Reaktoren und Vergleich mit Messungen, *Diplomarbeit*, PSI Villigen, Switzerland

Meier A., 1994, Computational Fluid Dynamics Simulation of High-Temperature Solar Chemical Reactors, *PSI Annual Report 1994 - Annex V*, pp. 35-37

Meier A., Ganz J., Steinfeld A., 1996, Modeling of a Novel High-Temperature Solar Chemical Reactor, *Chemical Engineering Science*, **51** (11), pp. 3181-3186

Meier A., Kirillov V.A., Kuvshinov G.G., Mogilnykh Yu.I., Weidenkaff A., Steinfeld A., 1998a, Production of Catalytic Filamentous Carbon by Solar Thermal Decomposition of Hydrocarbons, *Proc. 9th International Symposium on Solar Thermal Concentrating Technologies*, Odeillo, France, 22-26 June 1998, in press

Meier A., Kirillov V.A., Kuvshinov G.G., Mogilnykh Yu.I., Reller A., Steinfeld A., Weidenkaff A., 1998b, Solar Thermal Decomposition of Hydrocarbons and Carbon Monoxide for the Production of Catalytic Filamentous Carbon, *Proc. 15th International Symposium on Chemical Reaction Engineering*, Newport Beach, California, 13-16 September 1998; *Chem. Eng. Sci.*, in press

Meier A., 1998, A Predictive Model for a Falling Particle Receiver/Reactor Exposed to Concentrated Sunlight, *Proc. 15th International Symposium on Chemical Reaction Engineering*, Newport Beach, California, 13-16 September 1998; *Chem. Eng. Sci.*, in press

Mengüc M. P., Viskanta R., 1986, An Assessment of Spectral Radiative Heat Transfer Predictions For a Pulverized Coal-Fired Furnace, *Heat Transfer-1986* **2**, pp. 815-820.

Meurant B., 1998, PSI internal report

Millar J., Palumbo R. D., Rouanet, A., Pichlin G., 1997, The Production of ZnO in a Two-Step Solar Process Utilising FeO and Fe_3O_4. *Energy*, **22**, 301-309

Miller F., Koenigsdorff R., 1991, Theoretical Analysis of a High-Temperature Small-Particle Solar Receiver, *Solar Energy Materials* **24**, pp. 210-221

Mischler D., 1995, Strahlungsübertragung in Partikelwolken. Numerische und experimentelle Untersuchungen an Eisenoxid-Systemen im Hinblick auf eine chemische Speicherung von Sonnenenergie, *PSI/Diss. ETH* Nr. 11218

Mischler D., Steinfeld A., 1995, *J. Heat Transfer* **117**, 346-353

Modest M., Azad F., 1980, The Influence and Treatment of Mie-Anisotropic Scattering in Radiative Heat Transfer, *J. Heat Transfer* **102**, pp. 92-98

Moore W. J., Williams E. L., 1959, Decomposition of Zinc Oxide by Zinc Vapour. *Journal Physical Chemistry*, **63**, 1516-1517

Möller S., 1996, Untersuchung der solarthermischen Dissoziation von ZnO zu Zn und O_2 in einem Sonnenofen zur Speicherung von Sonnenenergie, *Diplomarbeit*, Universität Dortmund, Germany

Murray J. P., Steinfeld A., 1994, Solarthermal Production of Nitrides by Carbothermal Reduction of Metal Oxides in N_2-atmosphere, *Solar Engineering 1994 - Proc. ASME International Solar Energy Conference*, pp. 59-66, San Francisco, March 27-30, 1994

Murray J. P., Steinfeld A., Fletcher E. A., 1995, Metals, Nitrides, and Carbides Via Solar Carbothermal Reduction of Metals Oxides, *Energy - The International Journal*, **20** (7), pp. 695-704

Nakamura T., 1977, Hydrogen Production From Water Utilizing Solar Heat at High Temperatures. *Solar Energy* **19**, 467-475

Nater E., 1994, PULSAR-Warmphase, Abschlussbericht, 26. Aug. 1994, Bühler AG, Uzwil (DS-514 476)

Neumann G., 1981, Non-stoichiometry and defect structure. In: *Current topics in Materials Science*, edited by Kaldis, E.North-Holland, pp. 154-168

Newson E., 1998, PSI, private communication

Nüesch P., 1996, *Diplomarbeit*, University of Zurich, Switzerland

Palumbo R. D., 1987, An Exploratory Study of High Temperature Solar Electrothermal Processes which Produce Zn from ZnO and Mg from MgO, *Ph.D. Thesis*, University of Minnesota

Palumbo R. D., Fletcher, E. A., 1988, High Temperature Solar Electro-Thermal Processing — III. Zinc from Zinc Oxide at 1200-1675 K using a Non-Consumable Anode. *Energy*, **13,** 319-332

Palumbo R. D., Campbell M. B., Grafe, T. H., 1992, High Temperature Solar Thermal Processing Zn(s) and CO from ZnO(s) and C(gr) using Ti_2O_3 (s) and TiO_2 (s). *Energy*, **17,** 179-190

Palumbo R. D., Rouanet A., Pichelin G., 1995, The Solar Thermal Decomposition of TiO_2 at Temperatures above 2200 K and its use in the Production of Zn from ZnO. *Energy*, **20,** 857-868

Palumbo R., Lédé J., Boutin O., Elorza Ricart E., Steinfeld A., Möller S., Weidenkaff A., Fletcher E. A., Bielicki J., 1998, The Production of Zn from ZnO in a Single Step High Temperature Solar Decomposition Process, *Chemical Engineering Science* **53**, pp. 2503-2518

Pankratz L. B., 1982, *Thermodynamic Properties of Elements and Oxides*. U.S. Department of the Interior Bureau of Mines, Bulletin **672**

Parks D. J., Scholl K. L., Fletcher E. A., 1988, A Study of the use of Y_2O_3 doped ZrO_2 Membranes for Solar Electrothermal and Solar Thermal Separations. *Energy* **13,** 121-136

Pippel W., 1978, *Verweilzeitanalyse in technologischen Srömungssystemen*, Akademie-Verlag, Berlin

Reynolds W.C., 1986, The Element Potential Method for Chemical Equilibrium Analysis, Stanford University, Palo Alto, CA., Private Communication

Rhie C. M., Chow W. L., 1983, *AIAA JI* **21**, pp. 1527-1532

Ries H., Schubnell M., 1990, The optics of a two-stage solar furnace, *Solar Energy Materials* **21**, pp. 213-217

Rightley M. J., Matthews L., Mulholland G., 1992, Experimental Characterization of the Heat Transfer in a Free-Falling-Particle Receiver. *Solar Energy* **48**, 363-374

Rizzuti L., Yue P., 1983, The Measurement of Light Transmission Through An Irradiated Fluidized Bed. *Chemical Engineering Science* **38**, 1241-1249

Rodier D. D., 1995, Meeting the Challenges to the Zinc Industry. *Proceedings of the International Symposium on the Extraction and Application of Zinc and Lead*, Sendia, Japan, pp. 15-47

Rodriguez N.M., 1993, *J. Mater. Res.* **8** (12), 3233-3250

Rodriguez N.M., Kim, M-S., Baker, R.T.K., 1994, *J. Phys. Chem.* **98**, 13108-13111

Rodriguez N.M., Baker R.T.K., 1997, US Patent No. 5,653,951, publ.5.8.97

Romero A., Garcia E., Beneitez C., 1989, Effects of sample weight, particle size, purge gas and crystalline structure on the observed kinetic parameters of calcium carbonate decomposition, *Thermochimica Acta* **143**, pp. 339-345

Ruprecht P., Baerns M., 1971, *Chemie-Ing. Techn.* **43**, pp. 894-902

Salas-Morales J. C., Evans, J. W., 1994, Further studies of a zinc-air cell employing a packed bed anode Part III: Improvements in cell design. *J. Applied Electrochemistry*, **24**, 858-862

Salman, O. A., Kraishi N., 1988, Thermal decomposition of limestone and gypsum by solar energy, *Solar Energy* **41**, pp. 305-308

Sasse C., 1992, Bestimmung der optischen Eigenschaften von Partikeln für solarbeheizte Wirbelschichten, *Dissertation* Universität Karlsruhe und Forschungsbericht DLR 92-15

Sasse C., Ingel G., 1993, *Solar Energy Materials and Solar Cells* **31**, pp. 61-73

Schubnell M., Keller J., Imhof A., 1991, Flux density distribution in the focal region of a solar concentrator system, *ASME Journal of Solar Energy Engineering* **113**, pp. 112-116

Secco E. A., 1960, Decomposition of Zinc Oxide. *Can. J. of Chemistry*, **38**, 596-601

Sibieude F., Ducarroir M., Tofighi A., Ambriz J., 1982, High Temperature Experiments with a Solar Furnace: The Decomposition of Fe_3O_4, Mn_3O_4, CdO. *Int. J. Hydrogen Energy* **7**, 79-88

Siegel R., Howell J. R., 1981, *Thermal Radiation Heat Transfer*, 2nd. edition, Hemisphere Publishing Co., Belmont, CA., Appendix D

Siegel R., Howell J. R., 1992, *Thermal Radiation Heat Transfer*, 3rd ed., Hemisphere Publishing Corp., Washington DC, USA

Sparrow E. M., Cess R. D., 1966, *Radiation Heat Transfer*, Wadsworth Publishing Company, Belmont, CA

Steiner E., 1997, Internal Report, Paul Scherrer Institute, CH-5232 Villigen, Switzerland

Steinfeld A., 1991, Apparent Absorptance for Diffusely and Specularly Reflecting Spherical Cavities, *International Journal of Heat Mass Transfer*, **34** (7), 1895-1897

Steinfeld A., Fletcher E. A., 1991, Theoretical and Experimental Investigation of the Carbothermic Reduction of Fe_2O_3 Using Solar Energy, *Energy - The International Journal*, **16** (7), 1011-1019

Steinfeld A., Schubnell M., 1992, Maximizing the Energy Conversion Efficiency of a Solar Cavity-Receiver, *Proc. 6th Int. Symp. Solar Thermal Concentrating Technologies*, **1**, pp. 491-500, Mojacar, Spain (Sept. 28-Oct. 2, 1992)

Steinfeld A., Imhof A., Mischler D., 1992a, Experimental Investigation of an Atmospheric-Open Cyclone Solar Reactor for Solid-Gas Thermochemical Reactions. *Journal of Solar Energy Engineering* **114**, 171-174

Steinfeld A., Imhof A., Fletcher E. A., 1992b, High Temperature Solar Receivers with Internal Infrared Mirrors, *Proc. 6th Int. Symp. Solar Thermal Concentrating Technologies*, **1**, pp. 501-510, Mojacar Spain, (Sept. 28-Oct. 2, 1992)

Steinfeld A., 1993a, Solar Thermal Reduction of Metal Oxides Without Discharge of Pollutants to the Environment, *C&E'93 - Proc. International Symposium on CO_2 Fixation and Efficient Utilization of Energy*, pp. 123-132, Tokyo, Japan, (Nov. 29-Dec. 1, 1993)

Steinfeld A., 1993b, Radiative Transfer in a Diffusely/Specularly Reflecting Spherical Cavity Containing a Gray Medium, *Wärme und Stoffübertragung* **28**, pp. 65-68

Steinfeld A., Schubnell M., 1993, Optimum Aperture Size and Operating Temperature of a Solar Cavity-Receiver, Solar Energy **50** (1), pp. 19-25

Steinfeld A., Kuhn P., Karni J., 1993, High Temperature Solar Thermochemistry: Production of Iron and Synthesis Gas by Fe_3O_4-Reduction with Methane. *Energy - The International Journal* **18**, 239-249

Steinfeld A., Brack M., Ganz J., Haueter P., Imhof A., Meier A., Mischler D., Nater E., Seitz T., Schwarz A., Wuillemin D., 1994, Particle-Cloud Reactor Development for High-Temperature Solar Chemistry. In *Proceedings 7th Int. Symp. Solar Thermal Concentrating Technologies*, **4**, pp. 888-895, Moscow, Russia

Steinfeld A., Thompson G., 1994, Solar Combined Thermochemical Processes for CO_2 Mitigation in the Iron, Cement, and Syngas Industries, *Energy - The International Journal* **19**, 1077

Steinfeld A., Frei A., Kuhn P., Wuillemin D., 1995a, Solar Thermal Production of Zinc and Syngas Via Combined ZnO-Reduction and CH_4-Reforming Process. *Int. J. Hydrogen Energy*, **20,** 793-804

Steinfeld A., Frei A., Kuhn P., 1995b, Thermoanalysis of the Combined Fe_3O_4-Reduction and CH_4-Reforming Processes, *Metallurgical and Materials Transactions*, **26B**, pp. 509-515, 1995

Steinfeld A., Larson C., Palumbo R., Foley M., 1996a, Thermodynamic Analysis of the Co-Production of Zinc and Synthesis Gas Using Solar Process Heat. *Energy - The International Journal* **21**, 205-222

Steinfeld A., Kuhn P., Tamaura Y., 1996b, CH_4-Utilization and CO_2-Mitigation in the Metallurgical Industry via Solar Thermochemistry, *Energy Conversion and Management*, **37**, pp. 1327-1332

Steinfeld A., Kuhn P., Reller A., Palumbo R., Murray J., Tamaura Y., 1996c, Solar-processed metals as clean energy carriers and water-splitters, *Hydrogen Energy Progress XI*, 601-609

Steinfeld A., 1997, High-Temperature Solar Chemistry for CO_2 Mitigation in the Extractive Metallurgical Industry, *Energy - The International Journal*, **22** (2/3), pp. 311-316

Steinfeld A., Kirillov V., Kuvshinov G., Mogilnykh Y., Reller A., 1997, Production of Filamentous Carbon and Hydrogen by Solarthermal Catalytic Cracking of Methane. *Chemical Engineering Science* **52**, 3599-3603

Steinfeld A., Kuhn P., Reller A., Palumbo R., Murray J., Tamaura Y., 1998a, Solar-Processed Metals as Clean Energy Carriers and Water-Splitters, *International Journal of Hydrogen Energy*, **23** (9), pp. 767-774

Steinfeld A., Brack M., Meier A., Weidenkaff A., Wuillemin D., 1998b, A Solar Chemical Reactor for the Co-Production of Zinc and Synthesis Gas, *Energy - The International Journal*, **23** (10), pp. 803-814

Steinfeld A., Sanders S., Palumbo R., 1998c, Design Aspects of Solar Thermochemical Engineering, *Solar Energy*, in press

Steinfeld A., Spiewak I., 1998, Economic Evaluation of the Solar Thermal Co-Production of Zinc and Synthesis Gas, *Energy Conversion and Management*, **39** (15), pp. 1513-1518

Stine W. B., McDonald C. G., 1988, Cavity Receiver Heat Losses Measurements; *Proceedings of ASME Solar Energy Conference*, Denver

Stølen S., Glöckner R., Grønvold F., 1996, *Thermochimica Acta* **256**, 91-106

Stull D.R., Prophet H., 1971, *JANAF Thermochemical Tables, 2nd Ed.*, NSRDS-NBS 37 U.S. Government Printing Office, Washington D.C. 20402

Sundstrom D. W., De Michiell, R. L., 1971, Quenching Processes for High Temperature Chemical Reactions. *Ind. Eng. Chem. Process Des. Develop.*, **10**, 114-122

Szekely J., Carr R., 1966, *Chemical Engineering Science*, **21**, 1119

Tamaura Y., Steinfeld A., Kuhn P., Ehrensberger K., 1995, Production of Solar Hydrogen by a Novel, 2-Step, Water-Splitting Thermochemical Cycle. *Energy - The International Journal* **20**, 325-330

Tibbetts G.G., Endo M., Beetz C.P., 1986, *SAMPE Journal* **22**, 30-35

Tien C. L., Drolen B. L., 1987, Thermal Radiation in Particulate Media with Dependent and Independent Scattering, *A. Rev. Numer. Fluid Mech. Heat Transfer* **1**, pp. 1-32

Tofighi A., Sibieude F., 1980, Note on the Condensation of the Vapor Phase above a Melt of Iron Oxide in a Solar Parabolic Concentrator. *Int. J. Hydrogen Energy* **5**, 375-381

Tofighi A., 1982, Contribution a l'étude de la décomposition des oxydes de fer au foyer d'un four solaire, *Ph.D. Thesis*, L'Institut National Polytechnique de Toulouse, Toulouse, France

Tofighi A., Sibieude F., 1984, Dissociation of Magnetite in a Solar Furnace for Hydrogen Production. Tentative Production Evaluation of a 1000 kW Concentrator From Small Scale (2 kW) Experimental Results. *Int. J. Hydrogen Energy* **9**, 293-296

Ullmann's Encyclopedia of Industrial Chemistry, 1988, W. Gerhartz ed., VCH Verlag, Weinheim, Germany

Usiskin C. M., Sparrow E. M., 1960, Thermal Radiation Between Parallel Plates Separated by an Absorbing-Emitting Nonisothermal Gas, *Int. J. Heat Mass Transfer* **1**, pp. 28-36

Van Doormal J. P, Raithby G. D., 1984, *Numer. Heat Transfer* **7**, pp. 147-163

Vant-Hull L.L., Izygon M. E., Imhof A., 1998, Optimization of Central Receiver Fields to Interface with Applications Requiring High Flux Density Receivers, *9th International Symposium on Solar Thermal Concentrating Technologies*, Odeillo, France, June 22-26, 1998

VDI-Wärmeatlas, 1991, 6. Auflage, VDI-Verlag

Villermaux J., 1979, Les réacteurs chimiques solaires, *Entropie* **85**, pp. 25-31

Villermaux J., Antoine B., Lédé J., Soulignac F., 1986, A new model for thermal volatilisation of solid particles undergoing fast pyrolysis. *Chem. Eng. Sci.*, **41**, 151-157

Villermaux J., 1995, *Génie de la réaction chimique. Conception et fonctionnement des réacteurs*. Tec & Doc–Lavoisier

Watson L. R., Thiem T. L., Dressler R. A., Salter R. H., Murad E., 1993, High Temperature Mass Spectrometric Studies of the Bond Energies of Gas-Phase ZnO, NiO, and CuO. *Journal Physical Chemistry*, **97,** 5577-5580

Wang K. Y., Yuen W. W., 1987, Rapid Heating of Gas/Small Particle Mixture, *J. Solar Energy Engineering* **109**, pp. 143-149

Wang Z., Harris R., 1993. Morphology of zinc deposited from mixed gas streams at reduced pressures. *Materials Characterization* **30**, pp. 155-173

Weidenkaff A., Nüesch P., Wokaun A., Reller, A., 1997, Mechanistic studies of the water-splitting reaction for producing solar hydrogen. *Solid State Ionics* **101**, pp. 915-922

Weidenkaff A., Steinfeld A., Wokaun A., Eichler B., Reller A., 1998, The Direct Solar Thermal Dissociation of Zinc oxide: Condensation and Crystallisation of Zinc in the Presence of Oxygen, *Solar Energy*, in press

Welford W. T., Winston R., 1989, *High Collection Nonimaging Optics*, Academic Press, San Diego, USA

Wentworth W. E., Chen E., 1976, Simple thermal decomposition reactions for storage of solar thermal energy, *Solar Energy* **18**, pp. 205-214

Winter C.J., Sizmann R.L., Vant-Hull L.L., 1991, *Solar Power Plants*, Springer-Verlag, Berlin

Yamada Y., Cartigny J. D., Tien C. L., 1986, Radiative Transfer with Dependent Scattering by Particles: Part 2-Experimental Investigation, *J. Heat Transfer* **108**, pp. 614-618

Yuen W. W., Ma A., 1992, Evaluation of Total Emittance of an Isothermal Nongray Absorbing, Scattering Gas-Particle Mixture Based on the Concept of Absorption Mean Beam Length, J. Heat Transfer, **114**, pp. 653-658

Zaltash A., Myler C., Klinzing G. E., 1988, Stability Analysis of Gas-Solid Transport with Electrostatics, *J. of Pipelines* **7**, pp. 85-100

Zimmermann R., Marugg Ch., 1988, PULSAR; Eine Machbarkeitsstudie für einen Pulverreaktor für solarchemische Untersuchungen; Fa. Bühler AG, Uzwil Schweiz, 10. Aug. 1988

8 Appendix

8.1 Properties of Volumetric Gas-Particle Solar Reactors

To study basic aspects of air flow and convective heat transfer in windowless particle-cloud re-

Table 8.1 Summary of case studies for *CFD* simulations.

Case	A	B	C	D	E
Figure	8.2	8.2	8.3	8.3	8.4
Orientation of the reactor	horizontal with vertical aperture				vertical with horizontal aperture at the bottom
Swirl	no		5 revolutions per second		no
Heat source	5.3 kW (4 MW/m^3)				
Inlet mass flow	28.3 kg/hr air				
Mass flow through the aperture	0	equal to inlet mass flow	0	equal to inlet mass flow	0

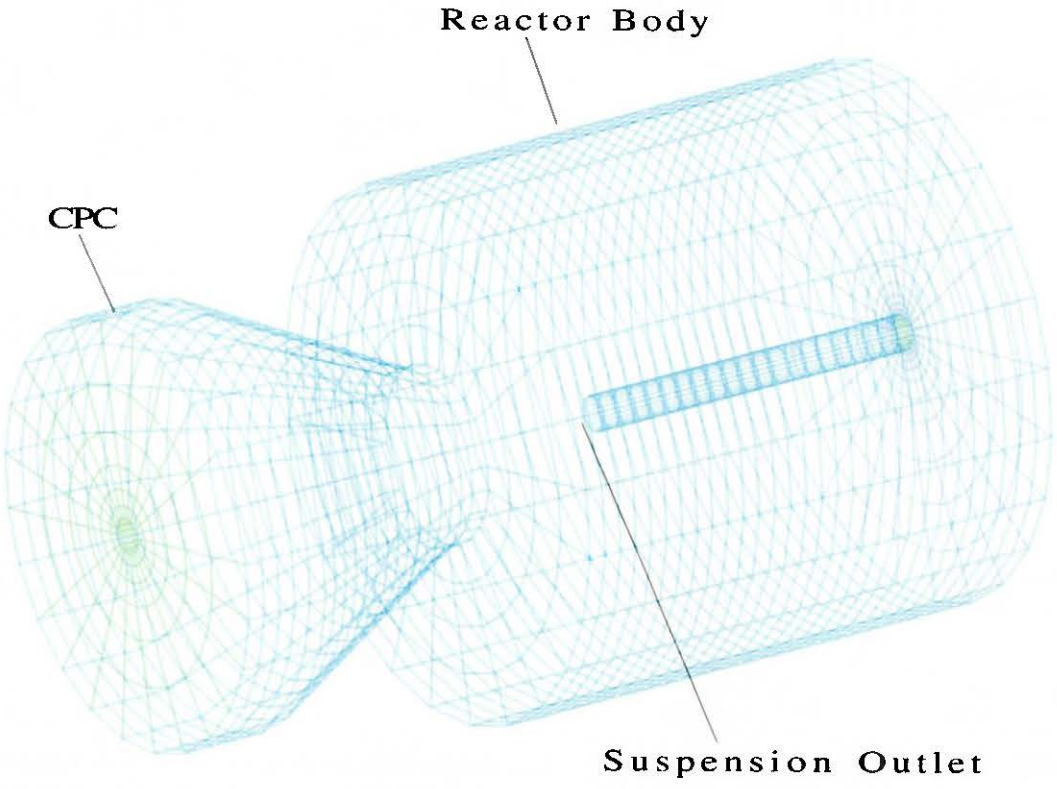

Figure 8.1 Simplified model reactor showing the three-dimensional grid used for the numerical simulation [Ganz *et al.*, 1996]. Dimensions: aperture diameter 0.1 m, suspension outlet pipe diameter 0.02 m. Cylindrical reactor body with diameter 0.3 m and length 0.3 m. Conical region to the left represents CPC and extends computational domain to allow for monitoring air flow through the aperture.

actors [Ganz *et al.*, 1996] we used the general purpose computational fluid dynamics (*CFD*) code *CFX-F3D* [CFX-F3D, 1995]. The simulations were performed for a simplified model reactor, neglecting particle transport and radiation heat transfer (Figure 8.1). This axisymmetric reactor consists of a cylindrical cavity, containing the circular aperture at the front wall. The air enters the reactor through the back wall and is heated in the focal region between the aperture and the axial outlet pipe. Outside the aperture, a conical region representing the *CPC* extends the computational domain to allow for monitoring air flow through the aperture.

Two different reactor concepts are considered: one is the horizontal reactor with vertical aperture; the other is the vertical reactor with horizontal aperture at the bottom, i.e. the so-called face-down reactor. For each of these reactor concepts, two baseline cases are compared: the first case features zero net air flow through the aperture; in the second case, the amount of additional air streaming through the aperture into the reactor is set equal to the air mass flow rate through the inlet boundary. Furthermore, for these two cases, the effect of both perpendicular and swirling air inlet flows is investigated. A summary of all cases considered for the present study is given in Table 8.1. The incident solar power is simulated by a 5.3 kW volumetric heat source (4 MW/m) distributed in half sphere shells, assuming the input power to decrease linearly away from the center of the aperture. Adiabatic reactor walls are assumed. The inlet mass flow

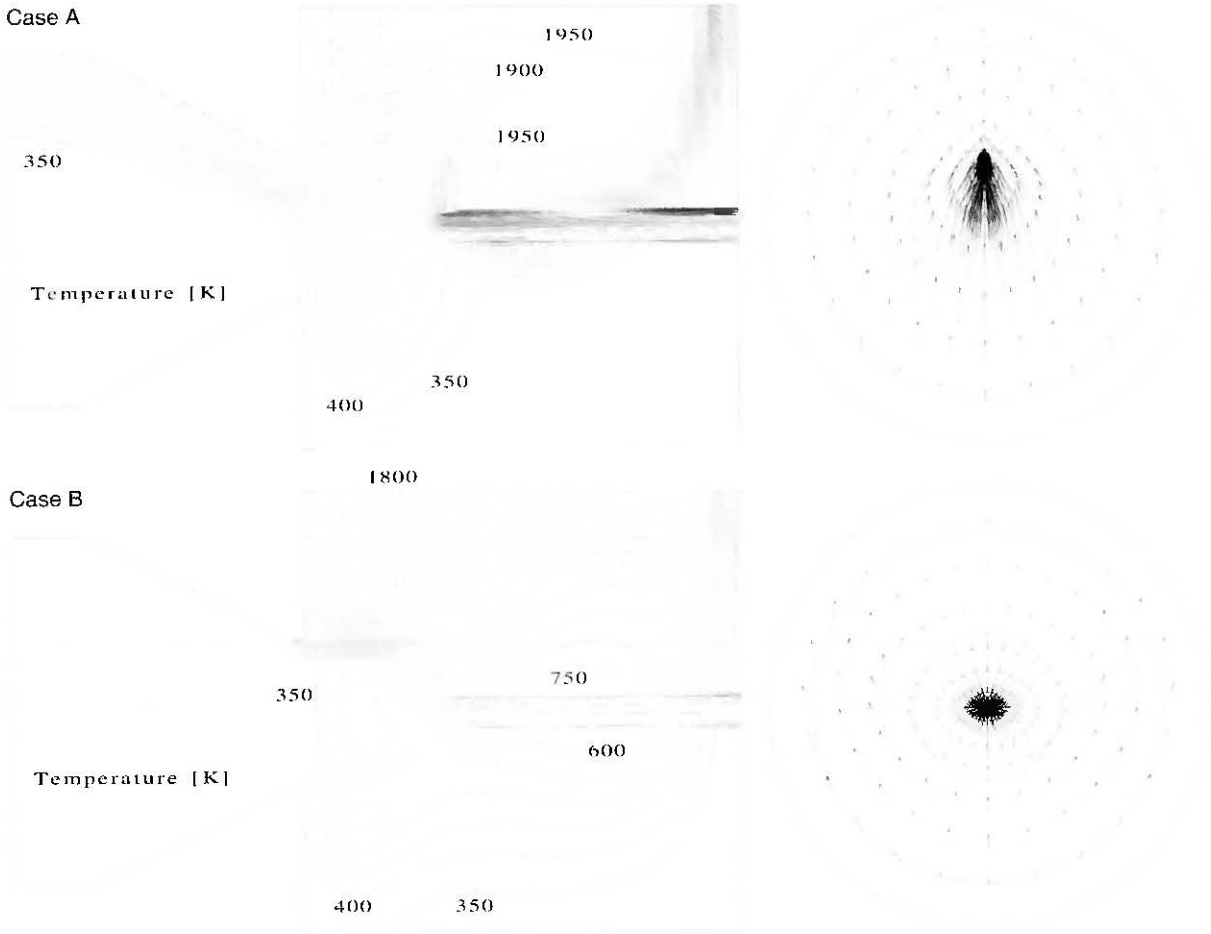

Figure 8.2 3D simulation of air flow and convective heat transfer in the horizontal model reactor without swirl, for Case A and Case B, respectively [Ganz *et al.*, 1996]. Temperature distribution is shown as contour lines of iso-temperature (interval size 50 K) for the vertical plane that contains the axis of the cylindrical reactor; air flow field is indicated by velocity vectors in a plane normal to the axis and half-way between the aperture and the outlet pipe. Boundary conditions are given in Table 8.1. For the dimensions see Figure 8.1.

through the back wall is 28.3 kg/hr of air with normal velocity 0.1 m/s; in the cases with swirl, the angular velocity is 5 revolutions per second.

Figure 8.2 shows the effect of buoyancy on the air flow field and temperature distribution for the horizontal reactor with vertical aperture; in this case, no swirl is applied. The density of the heated air inside the reactor is lower than the ambient air density. This causes convective outflow of the hot air through the upper part of the aperture, as can be seen for Case A (zero net air flow through the aperture into the reactor). The air outflow can be eliminated by suction of (preferably preheated) air through the aperture into the reactor (Case B). For both cases, the hottest region in the reactor is found at the upper wall of the cylindrical cavity. This results in thermal stresses for the wall material which cannot be tolerated. In addition, most of the air bypasses this hot zone and leaves the reactor without participating in a potential reaction.

Inducing a swirl at the air inlet boundary significantly influences the flow field and temperature distribution in the horizontal model reactor (Figure 8.3). The thermal convection is suppressed, and the air flow is stabilized producing a hot, torus-like zone in the focal region of the reactor. For Case C (zero net air flow through the aperture into the reactor), convective outflow of the hot air through the upper part of the aperture still occurs, similar to Case A. In Case D, most of the air flow entering the reactor at the back wall is streaming through the hot zone. In contrast

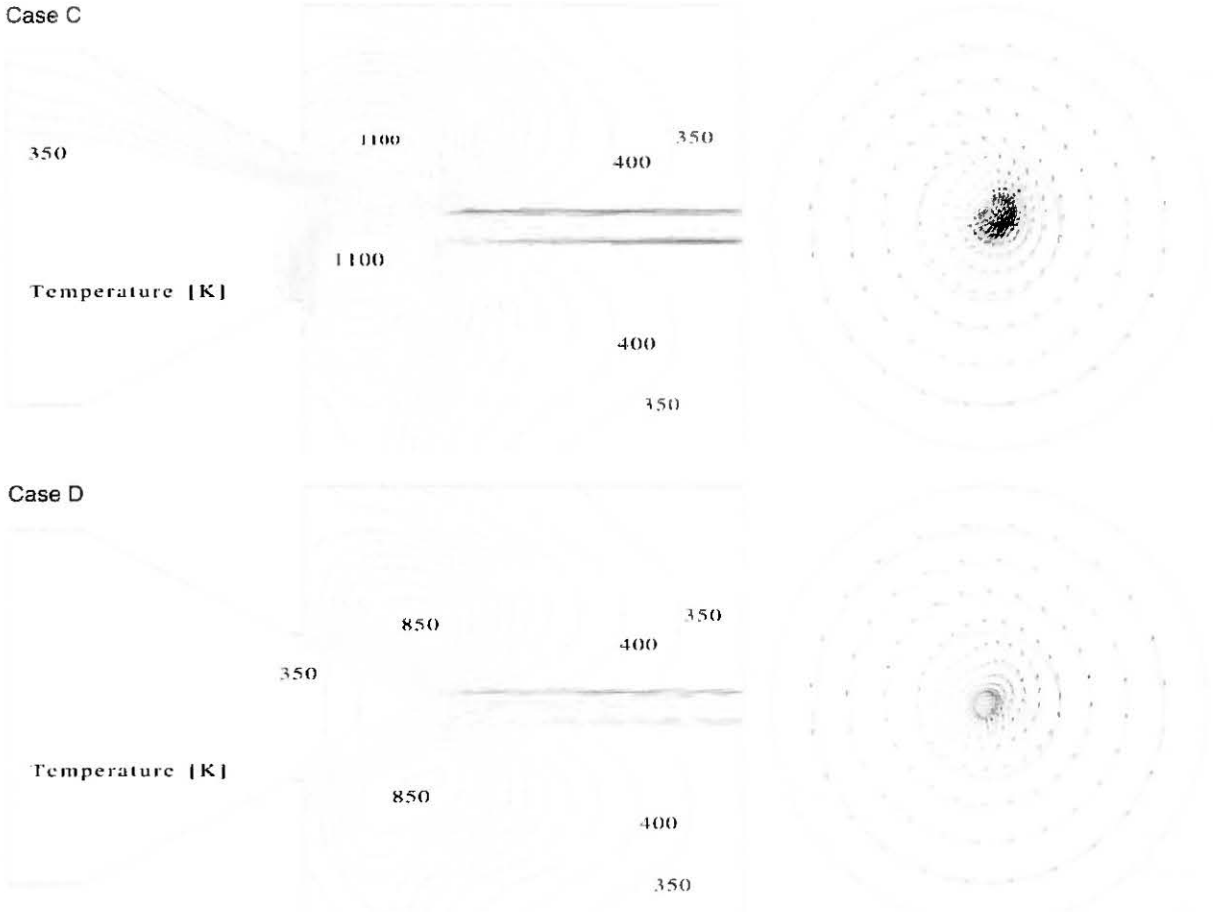

Figure 8.3 3D simulation of air flow and convective heat transfer in the horizontal model reactor with swirl, for Case C and Case D, respectively [Ganz *et al.*, 1996]. Temperature distribution is shown as contour lines of iso-temperature (interval size 50 K) for the vertical plane that contains the axis of the cylindrical reactor; air flow field is indicated by velocity vectors in a plane normal to the axis and halfway between the aperture and the outlet pipe. Boundary conditions are given in Table 8.1. For the dimensions see Figure 8.1.

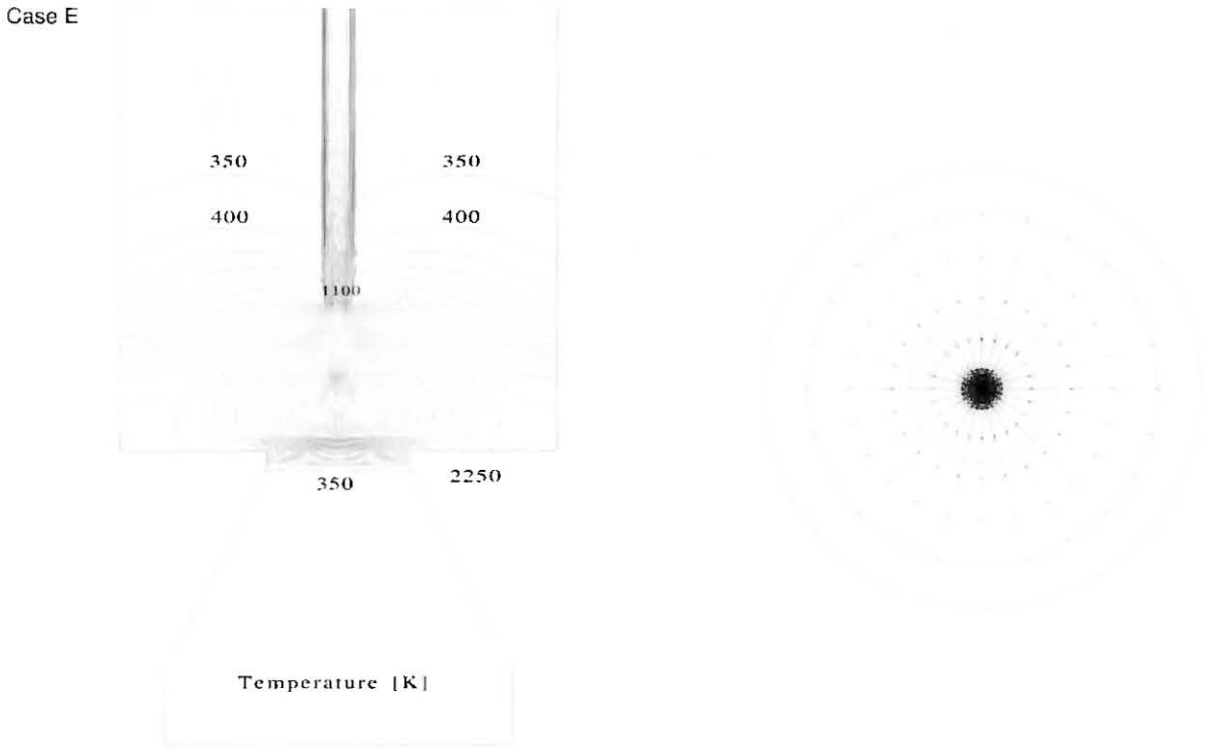

Figure 8.4 3D simulation of air flow and convective heat transfer in the vertical face-down model reactor for Case E without swirl [Ganz *et al.*, 1996]. Temperature distribution is shown as contour lines of isotemperature (interval size 50 K) for the vertical plane that contains the axis of the cylindrical reactor; air flow field is indicated by velocity vectors in a plane normal to the axis and half-way between the aperture and the outlet pipe. Boundary conditions are given in Table 8.1. For the dimensions seeFigure 8.1 .

to case B, a large amount of air is heated. Consequently, the maximum temperatures achieved are considerably lower in the case with swirling flow. Mixing with the cold extra air suction flow through the aperture only takes place at the suspension outlet. In spite of these advantages, highly swirling flows should be avoided because they enhance particle sedimentation.

For the vertical reactor with horizontal aperture at the bottom (face-down reactor), the density distribution of the atmosphere in the aperture region leads to a stable situation. Almost no air outflow occurs through the aperture (Case E, Figure 8.4). However, only part of the main air flow passes through the focal zone of the reactor. A considerable amount of the air flows directly into the outlet pipe. Furthermore, large agglomerates may fall through the downward oriented aperture and damage mirrors positioned below the reactor.

Summary of CFD Results

The general-purpose *CFD* code *CFX-F3D* was used to simulate the air flow and convective heat transfer in a model solar reactor. We have shown that horizontal reactors with open vertical aperture tend to suffer from convective air outflow, which can only be eliminated by sucking a considerable amount of extra air flow into the reactor. The thermal convection can be suppressed by imposing a vortex-like motion to the air flow field. For vertical open face-down reactors, no convective air outflow occurs, and hardly no additional air has to flow through the aperture.

8.2 Messung der Verweilzeitverteilungen

Dieses Kapitel enthält einen Auszug aus einer Diplomarbeit, die im Rahmen des vorliegenden Projekts am *PSI* angefertigt wurde [Mayer, 1996].

8.2.1 Theoretische Grundlagen

Zur Untersuchung von durchströmten Reaktoren wird häufig die Methode der Verweilzeitanalyse benutzt, die eine integrale Beschreibung des Systems liefert [Pippel, 1978]. Dabei muß unterschieden werden zwischen der Verteilungsdichte und der Summenverteilung der Verweilzeit im Reaktor. Die Verteilungsdichte $q(t)$ ist der Anteil der Elemente $dZ(t)$ vom Gesamtkollektiv Z_0, deren Verweilzeit im Zeitintervall zwischen t und $t+dt$ liegt [Jakubith, 1991]:

$$q(t) = \frac{dZ(t)}{Z_0 \cdot dt} \tag{8.1}$$

Die Definition der Summenverteilung $Q(t)$, die den Anteil der Elemente angibt, die eine kleinere Verweilzeit haben als t, lautet:

$$Q(t) = \frac{Z(t)}{Z_0} = \int_0^t q(t)) \tag{8.2}$$

Die mittlere Verweilzeit τ ist allgemein definiert als erstes Moment der Verteilung $q(t)$ [Bronstien and Semendjajew, 1991; Goedecke, 1974]:

$$\tau = \int_0^\infty t \cdot q(t) dt \tag{8.3}$$

Für ideale Reaktoren können die Verteilungsdichtekurven aus den differentiellen Massenbilanzgleichungen berechnet werden, die Summenkurven ergeben sich dann durch Integration [Jakubith, 1991]. Beim idealen Rührkessel erhält man folgende Gleichungen mit der mittleren Verweilzeit τ_{RK} als Parameter, die angibt, nach welcher Zeit $Q(t)$ den Wert *1-1/e* erreicht:

$$q(t) = \frac{1}{\tau_{RK}} \exp\left(-\frac{t}{\tau_{RK}}\right) \tag{8.4}$$

$$Q(t) = 1 - \exp\left(-\frac{t}{\tau_{RK}}\right) \tag{8.5}$$

Betrachtet man eine ideale Verdrängungsströmung, so bekommt man einen Diracschen Stoßimpuls bzw. eine ideale Sprungfunktion zur Zeit t_{VS}, d.h. alle Elemente haben die gleiche Verweilzeit. Die Abbildung 8.5 und Abbildung 8.6 stellen die Verweilzeitverteilungen für den idealen Rührkessel und die ideale Verdrängungsströmung dar.

Kombiniert man diese beiden idealen Modellreaktoren durch Reihen- oder Parallelschaltung miteinander, so erhält man die in Abbildung 8.7 gezeigten Verweilzeitsummenverteilungen. Während es im ersten Fall ausreicht, die beiden charakteristischen Zeiten, t_{VS} für die Verdrängungströmung und τ_{RK} für den Rührkessel, anzugeben, benötigt man im zweiten Fall auch noch die Aufteilung des Volumenstroms auf die beiden Reaktoren (Anteil des Rührkessels a_{RK}). Die Gleichung für die Summenverteilung bei Reihenschaltung lautet:

$$Q(t) = 1 - \exp\left(-\frac{t - t_{VS}}{\tau_{RK}}\right) \tag{8.6}$$

Für eine Parallelschaltung ergibt sich:

$$Q(t) = a_{RK}\left(1 - \exp\left(-\frac{t}{\tau_{RK}}\right)\right) \qquad \text{für } 0 < t < t_{VS} \tag{8.7}$$

$$Q(t) = 1 - a_{RK} \cdot \exp\left(-\frac{t}{\tau_{RK}}\right) \qquad \text{für } t \geq t_{VS} \tag{8.8}$$

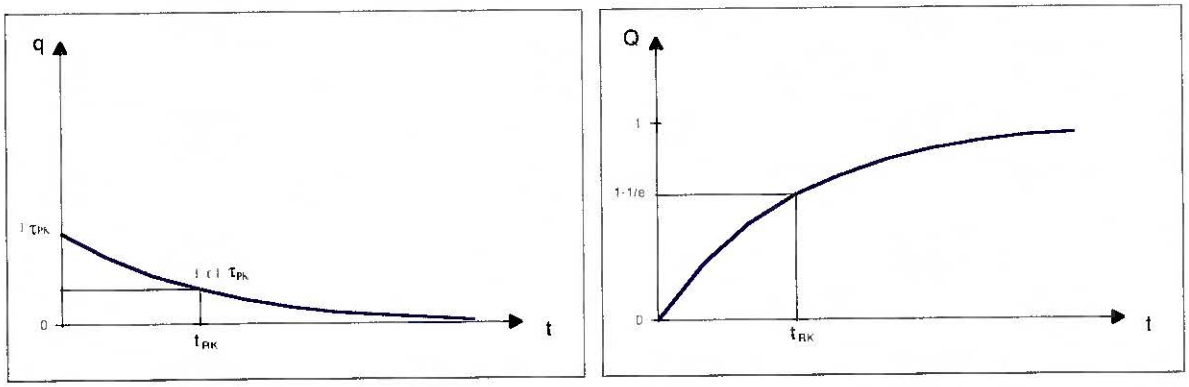

Abbildung 8.5 Dichte und Summenkurven der Verweilzeitverteilung eines idealen Rührkessels

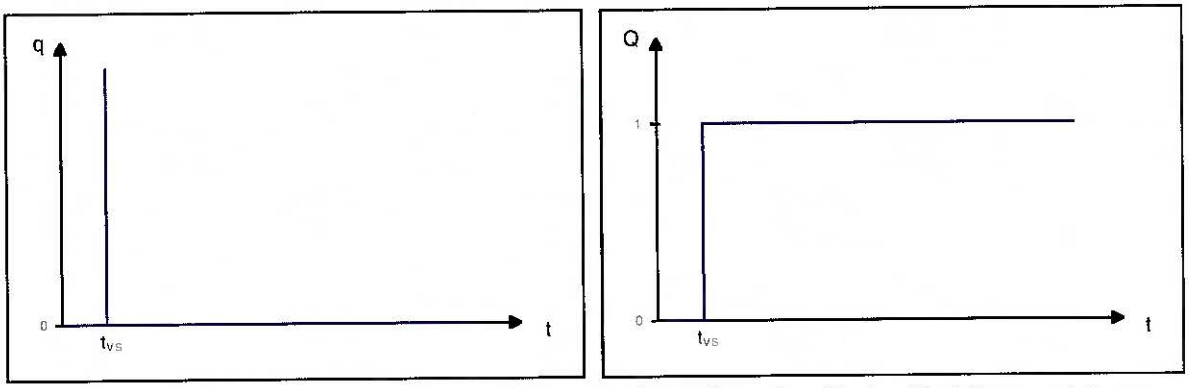

Abbildung 8.6 Dichte- und Summenkurven der Verweilzeitverteilung einer idealen Verdrängungsströmung

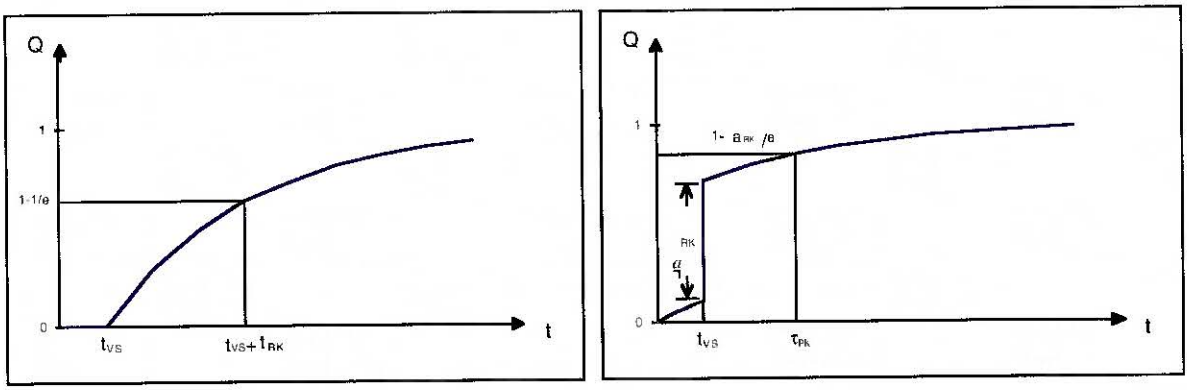

Abbildung 8.7 Verweilzeitsummenverteilung bei Reihenschaltung (links) und Parallelschaltung (rechts) von idealem Rührkessel (Anteil a_{RK}) und idealer Verdrängungsströmung (Anteil $1\text{-}a_{RK}$)

8.2.2 Aufbau der Meßapparatur

Möchte man Verweilzeitverteilungen messen, so muß man das Medium am Reaktoreintritt zu einem genau bekannten Zeitpunkt markieren, ohne die Strömung nennenswert zu stören, und die Konzentration der Markierungssubstanz am Reaktoraustritt kontinuierlich messen. Arbeitet man mit einen Stoßimpuls der Markierungssubstanz, mißt man die Verteilungsdichte, bei einem Verdrängungsimpuls (Sprungfunktion), erhält man die Summenverteilung der Verweilzeit. In dieser Arbeit wird die Methode des Verdrängungsimpulses verwendet.

Bei der direkten Bestimmung der Partikelverweilzeiten ist sowohl das Erzeugung der Sprungfunktion durch schnelles, störungsfreies Umschalten zwischen zwei fesstoffbeladenen Gasströmen als auch die genaue Messung der Partikelkonzentration im Abluftstrom äußerst problematisch. Messungen der optischen Dichte der Suspension lassen nur ungenaue Rückschlüsse auf die Beladung zu [Birkle,1994], was zu großen Fehlern führen kann.

Allerdings ist die Differenzgeschwindigkeit zwischen Partikeln und Gas bei so feinen Pulvern (Durchmesser von 0,1 bis 10 µm) sehr gering. Nach [Flagan und Seinfeld, 1988] ergibt sich für kugelförmige Partikeln mit einem Durchmesser von 1µm und einer Dichte von 5 g/cm^3 (Fe_3O_4) eine stationäre Sinkgeschwindigkeit in atmosphärischer Luft von 0,2 mm/s. Die modifizierte Hinkle-Korrelation [Zaltash *et al.*, 1988] wurde für den pneumatischen Transport feiner Pulver entwickelt und berücksichtigt auch nicht-stationäre Effekte. Sie gibt die Differenz zwischen Partikel- und Gasgeschwindigkeit an, gilt allerdings ab d_p= 20 µm. Bei einem Partikeldurchmesser von 20 µm und den obengenannten Bedingungen ist die berechnete Differenz bereits nur noch 1%.

Es reicht daher aus, die Verweilzeitverteilungen des Trägergases ohne Partikeln zu bestimmen, da der so zu erwartende Fehler geringer ist als bei direkter Messung der Partikelverweilzeit.

Für die Gasverweilzeitmessungen wird CO_2 als Markierungssubstanz verwendet und die Konzentration im Absaugrohr kontinuierlich mit einem Massenspektrometer (BALZERS MS-Cube mit Quadrupol-Analysator) bestimmt. Um ein auswertbares Signal zu erhalten, ohne die Dichte und Viskosität des strömenden Gases zu stark zu verändern, wird im zu markierenden Gasstrom soviel Luft durch CO_2 ersetzt, daß es 4% des abgesaugten Volumenstroms entspricht. Daraus folgt , daß beim 10 kW-Reaktor 10 l_N /min und beim 50 kW-Reaktor 20 l_N /min CO_2 eingesetzt werden. Das Schema des Versuchsaufbaus ist in Abbildung 8.8 dargestellt.

Die als Eingangssignal benötigte Sprungfunktion wird mit Hilfe von vier Magnetventilen realisiert, die über ein Relais mit einem Tastschalter synchron umgeschaltet werden können. Zunächst strömt reine Druckluft durch den Reaktor, während die markierte Luft - ein Teil des Volumenstroms ist durch CO_2 ersetzt - in die Umgebung geblasen wird. Beim Umschalten der Ventile wird der reine Luftstrom in die Umgebung und der markierte Luftstrom in den Reaktor geleitet. Der Zeitpunkt des Umschaltens wird vom Massenspektrometer parallel zur Konzentrationsmessung aufgezeichnet. Die Volumenströme der Düsen werden von Durchflußreglern gesteuert und der abgesaugte Gasstrom wird mit einem V-Konus gemessen und über einen Frequenzumformer am Gebläse konstant gehalten.

Die Probenahme für die Konzentrationsmessung erfolgt kontinuierlich über die Quarzglas-kapillare des Massenspektrometers, wobei die Meßwerte jeweils über 20 ms gemittelt werden. Die Totzeit zwischen zwei Meßwerten beträgt 15 ms, d.h. es wird alle 35 ms ein Meßwert ausgegeben. Das Meßprinzip des Massenspektrometers beruht darauf, daß die von der Vakuumpumpe angesaugten Gasmoleküle ionisiert und in einem Magnetfeld abgelenkt werden. Je nach Masse beschreiben sie eine Flugbahn mit entsprechendem Radius. Der Detektor, auf den die ionisi-

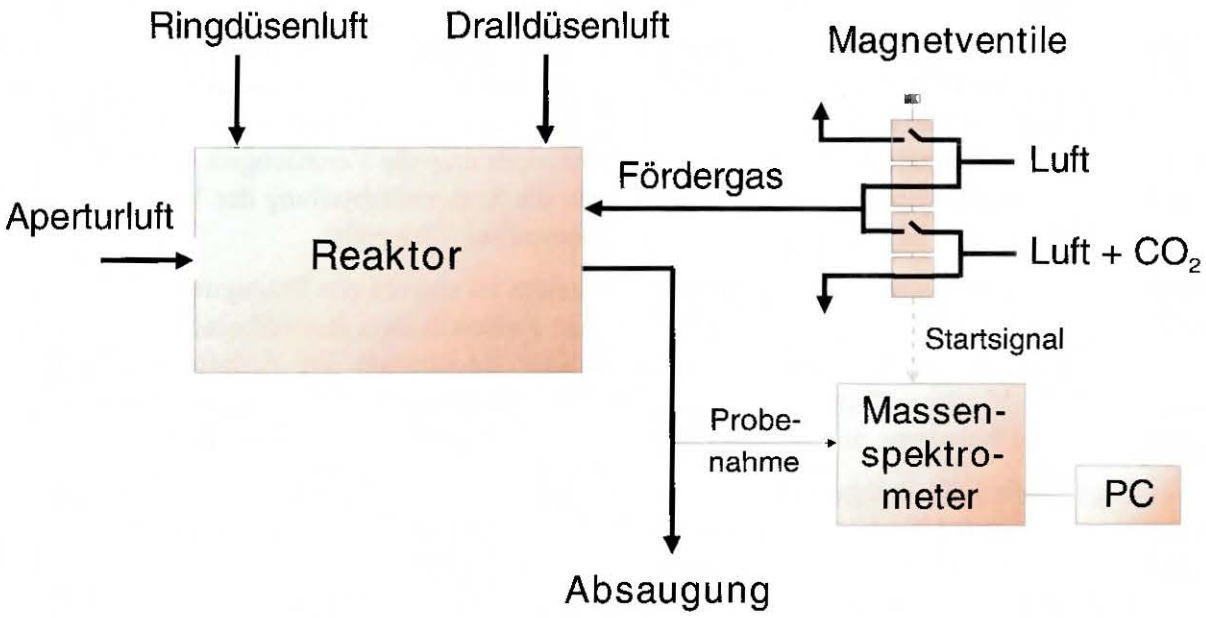

Abbildung 8.8 Schema des Versuchsaufbaus zur Verweilzeitmessung

erten Moleküle auftreffen, mißt nun den bei bestimmten Radien fließenden Strom. So kann zu jeder Molekülmasse der Molanteil im Gas bestimmt werden.

Beim Versuchsaufbau wurde darauf geachtet, daß sowohl die Umschaltventile als auch die Stelle der Probenahme möglichst nahe am Reaktor liegen, um die durch Leitungen bedingte Totzeit möglichst gering zu halten. Für die Datenerfassung steht ein PC zur Verfügung, der auch das Massenspektrometer steuert.

8.2.3 Durchführung der Experimente

Untersucht werden die beiden in Kapitel 4 (Abschnitte 4.2.2 und 4.2.3) beschriebenen Reaktoren, die für 10 bzw. 50 kW eingestrahlte Leistung ausgelegt sind. Zunächst werden die Eingangssignale nach dem Umschalten bestimmt, indem der Verlauf der CO_2-Konzentration direkt am Reaktoreintritt gemessen wird. In den Meßreihen wird jeweils der Volumenstrom der Dralldüsen variiert, wobei die Ringspaltdüse einmal ein- und einmal ausgeschaltet ist. Bei den Versuchen mit Ringdüsenluft wird eine zusätzliche Versuchsreihe durchgeführt, bei der anstatt der Förderluft die Ringdüsenluft markiert wird. So kann der Einfluß der Falschluft durch die Apertur auf die Strömung im Reaktor bestimmt werden unter der Annahme, daß sie sich mit der Ringdüsenluft gleichmäßig mischt. Die Volumenströme sind in Tabelle 8.2 dargestellt.

Tabelle 8.2 Volumenströme bei den Versuchen (Normaleinstellungen unterstrichen)

		10 kW - Reaktor	50 kW - Reaktor
Förderluftstrom	[l_N/min]	40	150
Luftstrom der Dralldüsen	[l_N/min]	0 / 10 / 15 / **25**	0 / 25 / **50** / 75
Luftstrom der Ringdüse	[l_N/min]	0 / **20**	0 / **50**
Abgesaugter Luftstrom	[l_N/min]	250	500
CO_2 - Markierungsstrom	[l_N/min]	10	20

Zusätzlich werden noch Verweilzeitverteilungen für den 10 kW-Reaktor bei Normaleinstellungen mit der Meßkapillare als Sonde im Reaktorinnenraum gemessen. Dadurch kann man Aussagen über die Inhomogenität der Strömung machen. Alle Versuche werden mehrfach bei gleichen Einstellungen wiederholt, um die Reproduzierbarkeit zu überprüfen. Die Versuchsdauer beträgt beim 10 kW-Reaktor 35 s (1000 Zyklen) und beim 50 kW-Reaktor 52.5 s (1500 Zyklen).

8.2.4 Auswertung und Diskussion der Ergebnisse

8.2.4.1 Allgemeines

Zunächst werden die Konzentrationsverläufe bezüglich der Differenz zwischen der Grundhöhe und der mittleren Endhöhe des Signals normiert. So erhält man eine erste Summenverteilung, aus der die Totzeit des Versuchs $t_{tot,aus}$ abgelesen werden kann. Diese setzt sich zusammen aus der Totzeit des Meßsystems (einschließlich der Leitungen) t_{tot} und der Verweilzeit der Verdrängungsströmung t_{VS} im Reaktor. Um Fehler bei der Bestimmung weiterer Parameter zu vermeiden, werden die Kurven nun geglättet [Pippel, 1978]), in dem jeweils über 0.35 s (10 Meßwerte) gemittelt wird. Mit dem Datenauswertungsprogramm DeltaGraph Pro3 wird für jede Versuchseinstellung eine mathematische Funktion an die gemittelten Ausgangssignale aller Einzelversuche angepaßt. Die Ausgleichsfunktion entspricht der Summenverteilung der Verweilzeit für eine Ersatzschaltung, wie sie in Abbildung 8.14 dargestellt ist:

$$Q(t) = 1 - \exp\left(-\frac{t - t_{tot,aus}}{\tau_{aus}}\right) \qquad \text{bei Markierung der Förderluft)} \qquad \textbf{(8.9)}$$

$$Q(t) = 1 - a_{RK} \cdot \exp-\frac{t - t_{tot,aus}}{\tau_{aus}} \qquad \text{bei Markierung der Ringdüsenluft)} \qquad \textbf{(8.10)}$$

Der Anpassungsparameter ist die mittlere Verweilzeit τ_{aus} der Rührkesselzone, die so bestimmt wird. Die Verweilzeit $t_{tot,aus}$ wird entsprechend den vorher abgelesenen Werten vorgegeben.

Systematische Fehler wie die Totzeit der Zuleitungen und des Meßsystems t_{tot} sowie die endliche Dauer des Sprungimpulses, d.h. die Abweichung von einer idealen Sprungfunktion, werden erst nach der Auswertung der experimentell ermittelten Antwortfunktionen korrigiert [Pippel, 1978]. In den gezeigten Diagrammen sind die Kurven bereits normiert, geglättet und um die Totzeit des Systems t_{tot} korrigiert.

8.2.4.2 Auswertung der Eingangssignale

Die Diagramme in Abbildung 8.9 zeigen die normierten Konzentrationsverläufe der Eingangssignale für den 10 kW- und den 50 kW-Reaktor.

Die Totzeit des Systems bis zum Reaktoreinlaß läßt sich direkt aus den Meßwerten bestim-men. Gemittelt über die Einzelversuche beträgt sie für die Versuchsanordnung beim 10 kW-Reaktor 1.65 s und beim 50 kW-Reaktor 1.1 s. Berücksichtigt man nun noch die Verweilzeit in den Leitungen, berechnet aus der Geometrie und den Volumenströmen, erhält man die Totzeiten des gesamten Systems t_{tot} (Tabelle 8.3).

Da das Umschalten der Magnetventile keine ideale Sprungfunktion ergibt, sondern eine endliche Zeit dauert, wird auch für die Eingangssignale die mittlere Verweilzeit τ_{ein} bestimmt, mit der die entsprechenden Werte der Ausgangssignale τ_{aus} korrigiert werden müssen, um die wirkliche Verweilzeit in der Rührkesselzone τ_{RK} zu erhalten [Pippel, 1978]):

Tabelle 8.3 Totzeit des Systems t_{tot} und mittlere Verweilzeit des Eingangssignals τ_{ein}

	10 kW-Reaktor	50 kW-Reaktor
Totzeit des Systems t_{tot}	1,7 s	1,2 s
Mittlere Verweilzeit τ_{ein}	0,2 s	0,2 s

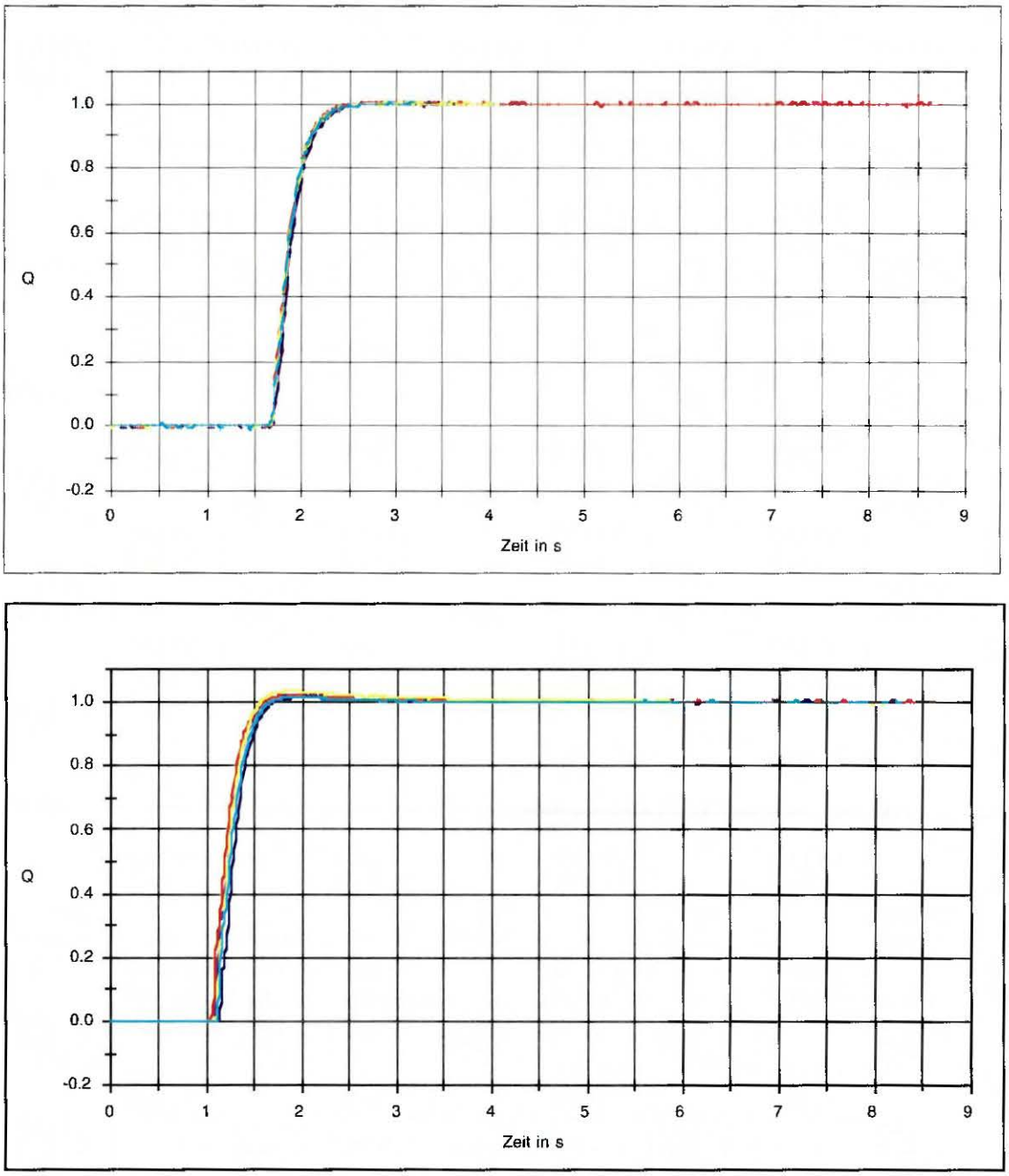

Abbildung 8.9 Eingangssignale von jeweils 5 Einzelversuchen für den 10 kW- (oben) und den 50 kW-Reaktor (unten)

$$\tau_{RK} = \tau_{aus} - \tau_{ein} \tag{8.11}$$

Berechnet wird τ_{ein} nach der Definition (Gl. 3-5), umgeschrieben als Summengleichung:

$$\tau_{ein} = \sum_{0}^{n} t \cdot q(t) \cdot \Delta t \tag{8.12}$$

8.2.4.3 Auswertung und Diskussion der Versuche bei Normaleinstellung

Die Abbildung 8.10 und Abbildung 8.11 zeigen die geglätteten Konzentrationsverläufe und die daran angepaßten Kurven für die Ausgangssignale der beiden Reaktoren bei Normaleinstellung und Markierung der Förderluft. Zum Vergleich ist auch das jeweilige Eingangssignal mit darg-

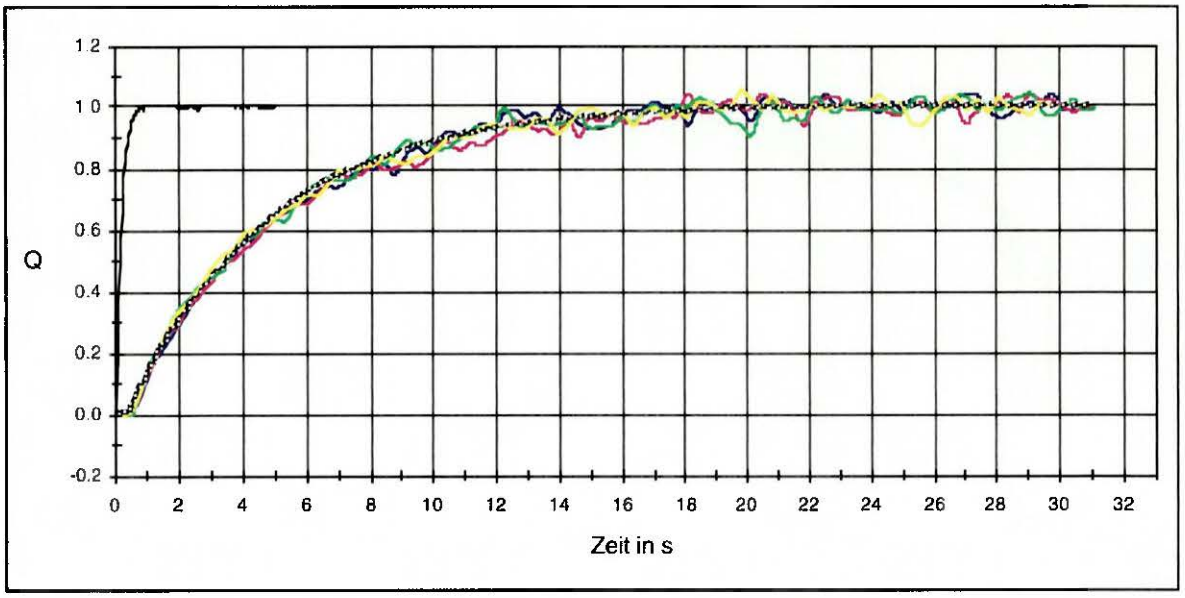

Abbildung 8.10 Geglättete Verläufe und angepaßte Kurve für den 10 kW-Reaktor bei Markierung der Förderluft (4 Experimente)

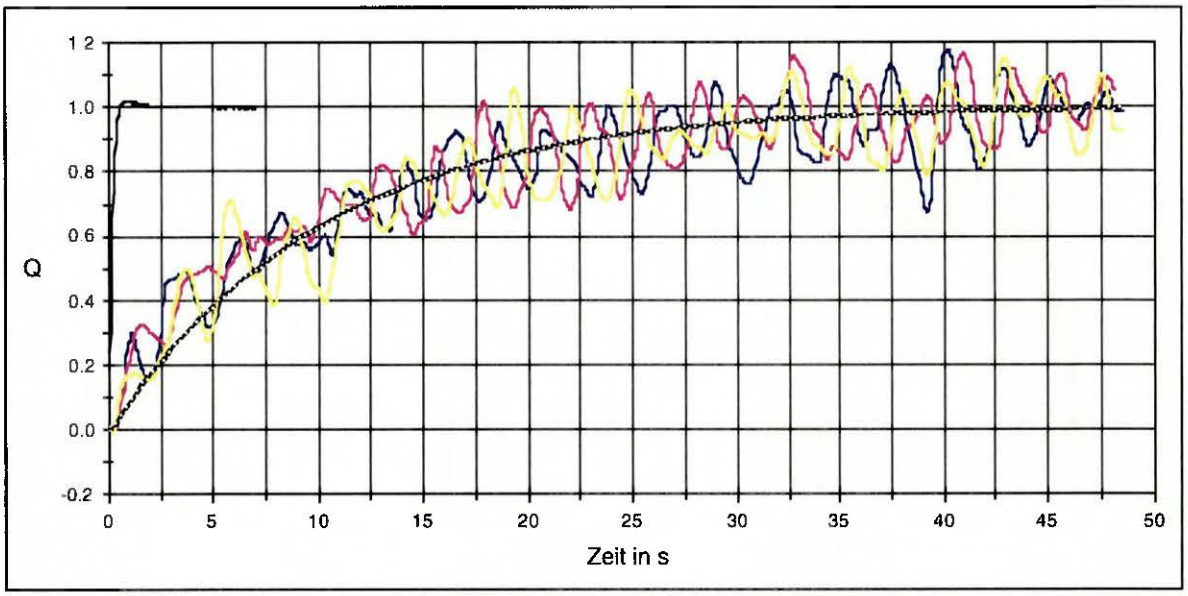

Abbildung 8.11 Geglättete Verläufe und angepaßte Kurve für den 50 kW-Reaktor bei Markierung der Förderluft (3 Experimente)

estellt.. Auf die Schwankungen der Signale, die beim großen Reaktor wesentlich stärker sind, wird in Kapitel 8.2.4.4 näher eingegangen.

Es zeigt sich, daß die Experimente gut reproduzierbar sind und sich die Strömung bezüglich der Förderluft mit einer Reihenschaltung aus Verdrängungsströmung und Rührkessel beschreiben läßt. Dazu sind, wie in Kapitel 8.2.1 gezeigt wurde, zunächst nur zwei Parameter nötig, die aus den Meßwerten bzw. durch die Anpassung gewonnen werden können. Berücksichtigt man die Totzeit des Systems t_{tot} und die Nichtidealität des Sprungimpulses τ_{ein}, so erhält man die in Tabelle 8.4 angegebenen Werte für die Verweilzeiten in den beiden Zonen.

Betrachtet man nun die in den Abbildung 8.12 und Abbildung 8.13 dargestellten Kurven, die Versuche zeigen, bei denen die Ringdüsenluft und somit die Aperturluft markiert wurde, so fällt der steile Anstieg zu Beginn auf. Er deutet darauf hin, daß eine Bypass-Strömung existiert, die

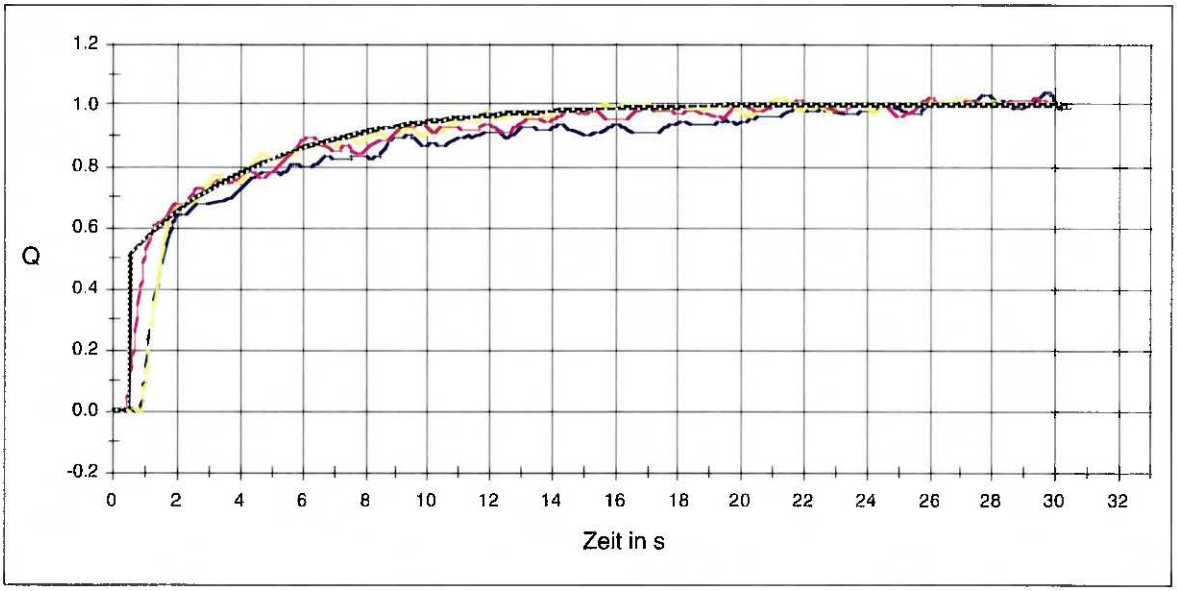

Abbildung 8.12 Geglättete Verläufe und angepaßte Kurve für den 10 kW-Reaktor bei Markierung der Ringdüsenluft (3 Experimente)

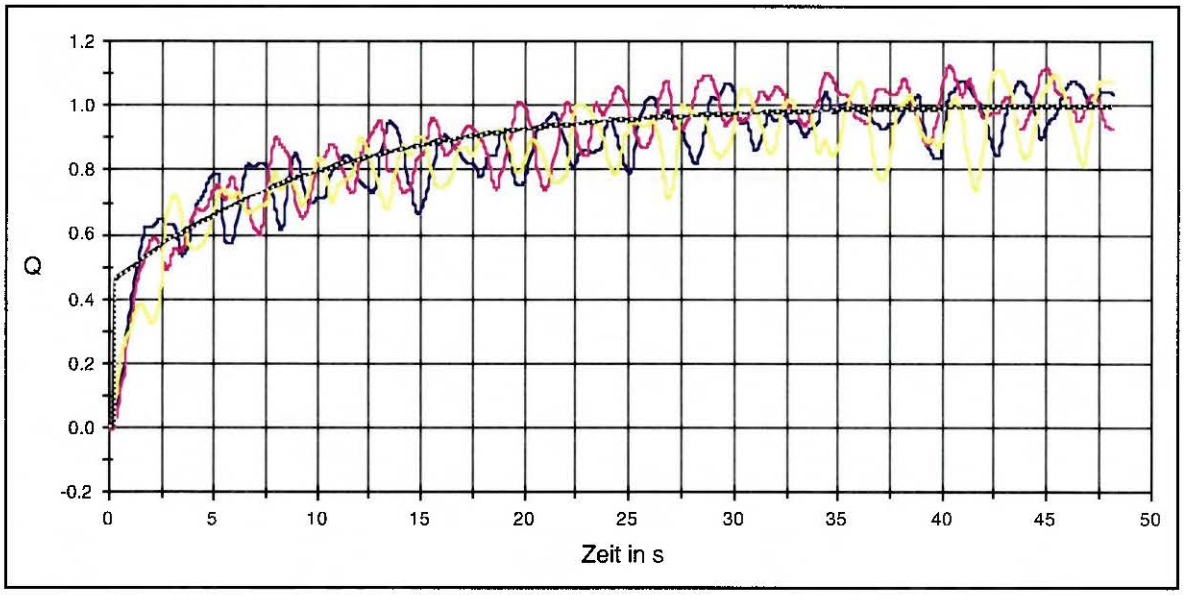

Abbildung 8.13 Geglättete Verläufe und angepaßte Kurve für den 50 kW-Reaktor bei Markierung der Ringdüsenluft (3 Experimente)

sehr schnell in die Absaugung gelangt, und sich nur ein Teil der Aperturluft mit der Förderluft im Reaktor mischt.

Der anschließende Kurvenverlauf kann mit einer Rührkesselfunktion nach Gleichung (8.10) beschrieben werden. Bei der Auswertung stellt sich heraus, daß bis auf wenige Ausnahmen die gleichen Parameterwerte t_{VS} und τ_{RK} wie bei Markierung der Förderluft zur Anpassung verwendet werden können. Die Verteilung der Aperturluft auf die beiden Ströme (Anteil a_{RK}) wird grafisch bestimmt.

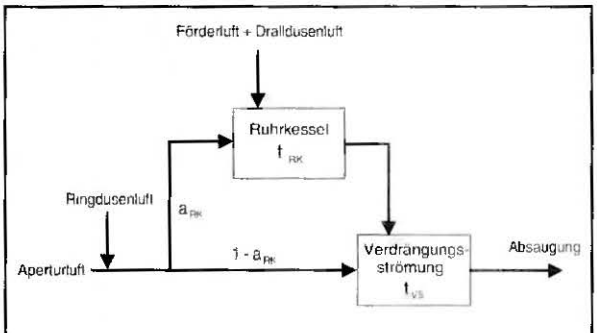

Abbildung 8.14 Ersatzschaltung aus Rührkessel und Verdrängungsströmungszone

Somit ist es möglich, das Verweilzeitverhalten des Reaktors mit der in Abbildung 8.14 gezeigten Ersatzschaltung zu beschreiben. Die Förderluft strömt zunächst durch die Rührkesselzone und dann durch die im Bereich der Absaugung liegende Verdrängungsströmungszone. Die Aperturluft mischt sich zum Teil mit der Förderluft im Rührkessel, der andere Teil geht direkt in die Verdrängungsströmungszone. Das Volumen der beiden Zonen in diesem Modell kann aus den Verweilzeiten und den Volumenströmen (umgerechnet auf 20°C) berechnet werden (Tabelle 8.4). Das von der Förderluft nicht genutzte Volumen V_{tot} ist die Differenz zum Reaktorvolumen (Tab. 2.1).

Daß die Verweilzeitanalyse nur eine integrale Beschreibung des Systems ermöglicht, zeigen die am 10 kW-Reaktor bei Normaleinstellung durchgeführten Sondenversuche. Hierbei wird die CO_2-Konzentration nicht am Ende des Absaugrohres gemessen, sondern direkt im Reaktor. Dazu wird die Meßkapillare in eine Halterung gespannt, die in Polarkoordinaten verdreht werden kann. Markiert wird die Förderluft. Die Abbildung 8.15 zeigt die Ergebnisse für eine vertikale Ebene im Abstand von 10mm vor der Absaugspitze. Gemessen wird auf einem Radius von 70 mm jeweils oben, unten, rechts und links (von der Apertur aus gesehen).

Es zeigt sich, daß die Strömung im Reaktor sehr inhomogen ist. Die Kurven, die unten bzw. rechts aufgenommen wurden, erreichen gar nicht den erwarteten Endwert. Das läßt darauf schließen, daß die Aperturluft vor allem unten einströmt und dann durch die Rotation nach rechts gedrückt wird. Somit wird in diesen Bereichen die markierte Förderluft verdünnt. Im oberen Bereich des Reaktors liegt die CO_2-Konzentration dagegen etwas über der in der Absaugung gemessenen, da hier vor allem die markierte Förderluft strömt. Die Totzeit entfällt bei allen

Tabelle 8.4 Mittlere Verweilzeiten, Rührkesselanteil der Aperturluft und Volumen der Zonen in der Ersatzschaltung

	10 kW-Reaktor	50 kW-Reaktor
Verweilzeit in der Verdrängungsströmungszone t_{VS}	0,45 s	0,25 s
Mittlere Verweilzeit im Rührkessel τ_{RK}	4,3 s	9,8 s
Rührkesselanteil der Aperturluft a_{RK}	0,5	0,55
Volumen der Verdrängungsströmungszone V_{VS}	2,0 l	2,3 l
Volumen der Rührkesselzone V_{RK}	12,0 l	64,0 l
Nicht genutztes Volumen V_{tot}	0,8 l	8,7 l

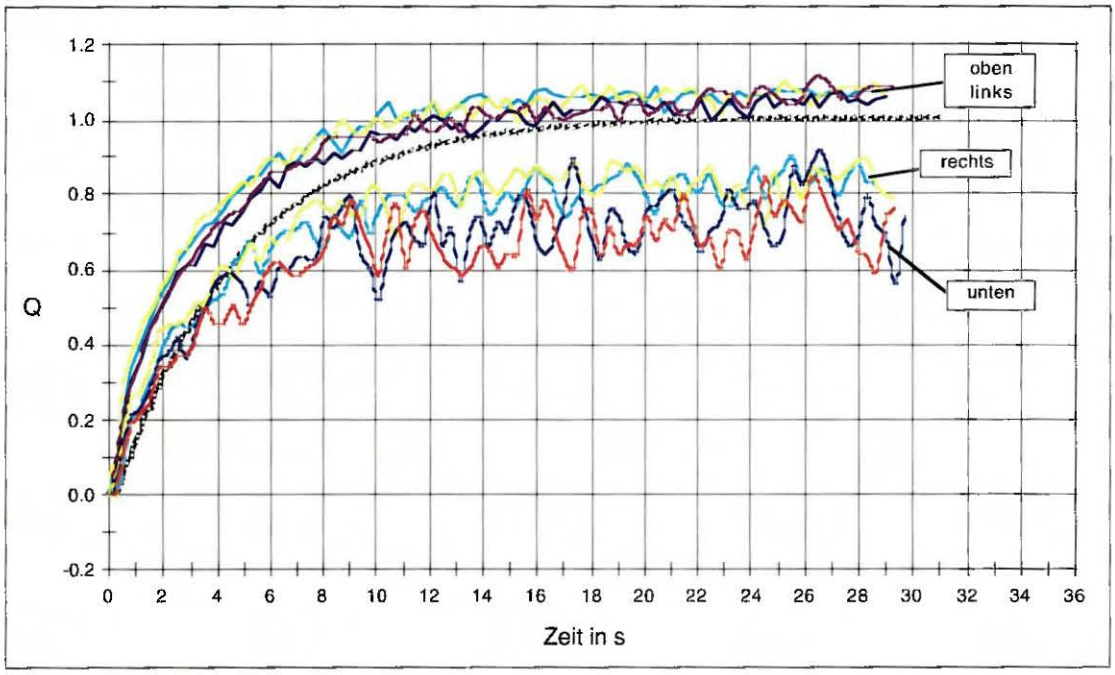

Abbildung 8.15 Geglätteter Kurvenverlauf der Sondenversuche (Abstand von der Absaugspitze 10 mm, auf einem Radius von 70 mm) und als Vergleich die Ausgleichskurve des normalen Versuchs

Sondenversuchen fast vollständig. Das bestätigt die Annahme, daß der Verdrängungsströmungsanteil vor allem durch die Strömung im Absaugbereich verursacht wird.

8.2.4.4 Auswertung und Diskussion der Versuchsreihen

Um den Einfluß der Wirbelstärke und der Ringspaltluft auf das Verweilzeitverhalten bestimmen zu können, werden die Volumenströme der Dralldüsen gemäß Tabelle 8.2 variiert, wobei die Ringdüse einmal eingeschaltet ist und einmal nicht.

Versuchsreihen mit eingeschalteter Ringdüse

In Tabelle 8.5 und Tabelle 8.6 sind die Ergebnisse der Versuchsreihe mit eingeschalteter Ringdüse für den 10 kW- und den 50 kW-Reaktor zusammengestellt.

Die Verweilzeit in der Verdrängungsströmungszone t_{VS} weist bei beiden Reaktoren mit zunehmender Wirbelströmung steigende Tendenz auf. Die Unterschiede sind ebenso wie die absoluten Werte sehr gering. Beim 50 kW-Reaktor läßt sich der Versuch ohne Wirbelströmung schwer auswerten, da die Kurve einen schleichenden Anstieg hat. Das Volumen der Verdrängungsströmungszone verhält sich analog zur Verweilzeit t_{VS}, da der gesamte Gasstrom durch diese Zone geht.

Tabelle 8.5 Ergebnisse für den 10 kW-Reaktor bei eingeschalteter Ringdüse (20 l_N/min)

Volumenstrom der Dralldüsen	0 l_N/min	10 l_N/min	15 l_N/min	25 l_N/min
t_{VS}	0,3 s	0,35 s	0,4 s	0,45 s
τ_{RK}	3,3 s	3,1 s	3,3 s	4,3 s
a_{RK}	1	1	0,8	0,5
V_{VS}	1,2 l	1,6 l	1,7 l	2,0 l
V_{RK}	14,8 l	13,9 l	11,6 l	12,0 l

Tabelle 8.6 Ergebnisse für den 50 kW-Reaktor bei eingeschalteter Ringdüse (50 l_N/min)
(bei zwei Werten ist der erste für markierte Förderluft und der zweite für markierte Ringdüsenluft)

Volumenstrom der Dralldüsen	0 l_N/min	25 l_N/min	50 l_N/min	75 l_N/min
t_{VS}	0,9 / 0,2 s	0,15 s	0,25 s	0,3 s
τ_{RK}	10,8 s	8,3 / 10,3 s	9,8 s	9,3 s
a_{RK}	0,65	0,6	0,55	0,55
V_{VS}	- / 1,8 l	1,3 l	2,3 l	2,7 l
V_{RK}	73,0 l	55,0 / 68,2 l	64,0 l	62,6 l
V_{tot}	- / 0,2 l	18,7 / 5,5 l	8,7 l	9,7 l

Deutlich ist, daß der Anteil a_{RK} der Aperturluft, der sich mit der Förderluft in der Rührkesselzone mischt, bei Erhöhung des Dralldüsenstroms abnimmt. D.h. es wird immer mehr Falschluft direkt in die Absaugung geleitet. Die mittlere Verweilzeit in der Rührkesselzone τ_{RK} ist deshalb nicht allein entscheidend für die Größe dieser Zone. Bei den Versuchen am 10 kW-Reaktor (Tabelle 8.5) nimmt τ_{RK} bei stärkerer Wirbelströmung leicht zu, trotzdem wird die Rührkesselzone kleiner, da der Volumenstrom abnimmt. Beim 50 kW-Reaktor (Tabelle 8.6) sinkt die mittlere Verweilzeit τ_{RK} innerhalb der Versuchsreihe. Die Versuche mit einem Dralldüsenstrom von 25 l_N/min ergeben bei der Anpassung der Summen-verteilungen für die beiden Fälle (Förderluft bzw. Ringdüsenluft markiert) nicht den gleichen Parameter. Das Volumen der Rührkesselzone nimmt stark ab, gleichzeitig steigt das von der Förderluft nicht genutzte Volumen. Die Größe des Totvolumens ist allerdings mit einiger Unsicherheit behaftet, da das freie Reaktorvolumen nicht genau bestimmt werden kann.

In beiden Versuchsreihen treten Schwingungen des Ausgangsignals auf, deren Amplitude mit steigender Drallströmung zunimmt. Eine Frequenzanalyse (*Fast Fourier Transformation*) einzelner Versuche am 50 kW-Reaktor ergibt, daß auch die Frequenz der Schwingungen ansteigt. Mit einem Kugelanemometer werden bei ausgeschalteter Absaugung für verschiedene Dralldüsenströme die Tangentialgeschwindigkeiten auf einem mittleren Radius im Reaktor gemessen. Die daraus folgenden Zeiten für eine Wirbelumdrehung liegen in der Größenordnung der entsprechenden mit der Frequenzanalyse ermittelten Schwingungsdauern.

Versuchsreihen mit ausgeschalteter Ringdüse

Bei den Versuchen am 50 kW-Reaktor nimmt die Amplitude der Schwingungen mit steigendem Dralldüsenstrom stark zu. In beiden Versuchsreihen liegen sie deutlich über den Schwankungsamplituden, die bei eingeschalteter Ringdüse auftreten. D.h. die Saugwirkung der Ringdüsenluft führt zu einer besseren Vermischung der einzelnen Ströme. Zusätzlich bestätigt wird das durch die Versuchsreihe am 50 kW-Reaktor. Hier zeigt sich ein starker Anstieg zu Beginn, der darauf hindeutet, daß bei ausgeschalteter Ringdüse nur ein Teil der Förderluft durch die Rührkesselzone strömt, während der andere Teil über eine Bypass-Strömung sehr schnell in die Absaugung gelangt. Dieser Anteil nimmt bei steigender Wirbelströmung durch deren Mischwirkung leicht ab. Beim 10 kW-Reaktor kann das Phänomen der Aufteilung der Förderluft nicht beobachtet werden.

Tabelle 8.7 und Tabelle 8.8 zeigen die ermittelten Verweilzeiten für die Versuche mit ausgeschalteter Ringdüse. Bei den Versuchen am 10 kW-Reaktor steigt die mittlere Verweil-zeit in der Rührkesselzone τ_{RK} mit zunehmender Drallströmung. Da es hier nicht möglich ist, die Aperturluft zu markieren, können keine Aussagen über die Aufteilung der Falschluft gemacht wer-

Tabelle 8.7 Ergebnisse für den 10 kW-Reaktor bei ausgeschalteter Ringdüse

Volumenstrom der Dralldüsen	0 l_N/min	10 l_N/min	25 l_N/min
t_{VS}	0,4 s	0,3 s	0,4 s
τ_{RK}	3,3 s	3,7 s	4,9 s

Tabelle 8.8 Ergebnisse für den 50 kW-Reaktor bei ausgeschalteter Ringdüse

Volumenstrom der Dralldüsen	0 l_N/min	25 l_N/min	50 l_N/min	75 l_N/min
t_{VS}	0,15 s	0,1 s	0,2 s	0,25 s
τ_{RK}	11,8 s	13,3 s	11,3 s	13,3 s
a_{RK} (Förderluft)	0,7	0,7	0,8	0,8

den. Bei den übrigen Verweilzeiten ist keine deutliche Tendenz zu erkennen. Fast alle Werte liegen über denen aus den entsprechenden Versuchen mit eingeschalteter Ringdüse. Das kann durch die fehlende Saugwirkung der Ringspaltluft erklärt werden, die auch zur erwähnten Inhomogenität der Strömung führt.

8.2.4.5 Fehlerabschätzung

Neben den bekannten systematischen Fehlern, die korrigiert werden können, treten noch weitere Fehlerquellen und Unsicherheiten auf. Im folgenden werden deren Auswirkungen abgeschätzt.

Die Volumenströme durch die Düsen sind mit einem relativen Fehler von 1 % behaftet, der abgesaugte Luftstrom ist auf 3 % genau. Für die Massenspektrometer-Daten ist der maximale Fehler der Grundhöhe kleiner als 1 %, bei der mittleren Endhöhe des Signals beträgt er 2 %. Durch die Auswertung der gemessenen Verweilzeitverteilungen ergeben sich zusätzliche Fehler. So ist die Ableseungenauigkeit für die Totzeit $t_{tot,aus}$ 0,05 s , für die Verweilzeit in der Verdrängungsströmungszone t_{VS} folgt dann eine Ungenauigkeit von 0,1 s . Bei der Bestimmung der mittleren Verweilzeit in der Rührkesselzone τ_{RK} liegt die Unsicherheit im Bereich von 0,3 s . Besonders hoch ist der Fehler des Rührkesselanteil a_{RK} der Aperturluft. Er schwankt sehr stark von Versuch zu Versuch und beträgt teilweise bis zu 10 %. Die beschrieben Fehler wirken sich vor allem auf die absoluten Werte der interessierenden Größen aus; besonders die Ablesefehler beeinflussen den Trend zwischen den verschiedenen Betriebseinstellungen nur wenig.

8.3 Modellierung der Strahlung und Strömung im Reaktor

8.3.1 Theoretische Grundlagen

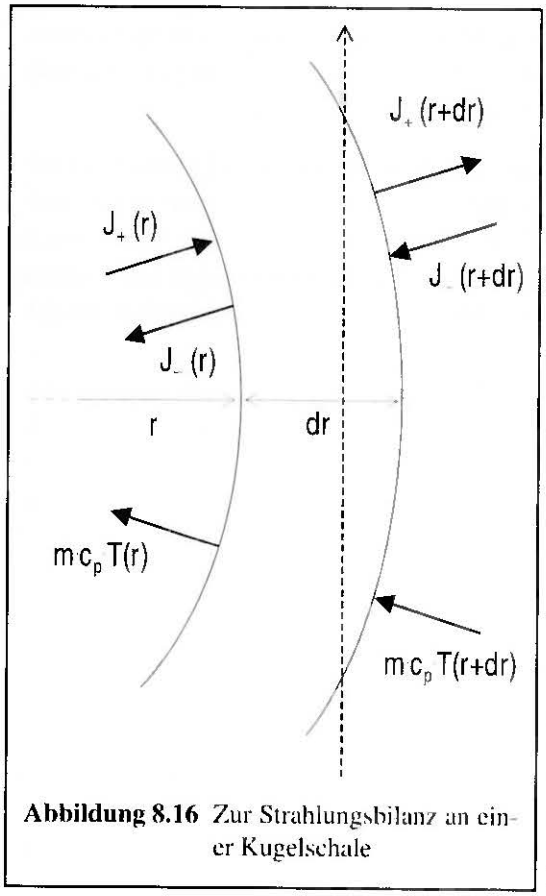

Abbildung 8.16 Zur Strahlungsbilanz an einer Kugelschale

Allgemein läßt sich die Ausbreitung der Strahlung in einphasigen Medien mit der Strahlungstransportgleichung beschreiben [Siegel and Howell, 1992]. Diese Bilanzgleichung gibt die Änderung pro Weglänge der vom Ort und vom betrachteten Raumwinkel abhängigen Intensität der Strahlung an. Berücksichtigt werden neben der Absorption und Streuung der Primärstrahlung auch die Temperaturstrahlung des Mediums und der in die betrachtete Raumrichtung einfallende Anteil der gestreuten Strahlung. Da alle Größen wellenlängenabhängig sind, muß der Strahlungstransport für jede Wellenlänge getrennt berechnet werden. Meist wird aber vereinfachend ein graues Medium angenommen und mit über alle Wellenlängenbereiche integrierten Größen gerechnet.

Untersuchungen von [Sasse, 1992] haben gezeigt, daß Partikelwolken in Luft als quasi-homogenes Medium angesehen werden können, wenn die Streuvorgänge an den einzelnen Partikeln voneinander unabhängig sind. Diese Unabhängigkeit ist erfüllt, solange das Verhältnis von Partikeldurchmesser zu mittlerer Wellenlänge nicht kleiner als eins ist [Siegel and Howell, 1992]. D.h. die Strahlungstransportgleichung kann auch auf die interessierenden Gas-Feststoffpartikel-Gemische angewandt werden, lediglich im infraroten Bereich ist bei sehr kleinen Partikeln mit Ungenauigkeiten zu rechnen [Koenigsdorff, 1994]).

Die Strahlungstransportgleichung ist im allgemeinen nicht analytisch lösbar, daher müssen zur Berechnung von Strahlungsfeldern vereinfachende Annahmen gemacht werden. Weitverbreitet sind die sogenannten Fluß-Modelle. Hierbei wird der gesamte Raumwinkel an jedem Ort in mehrere diskrete Raumrichtungen aufgeteilt. Die Strahlungsintensität wird für jede Raumrichtung als isotrop angenommen oder über den entsprechenden Raumwinkel integriert. Dadurch läßt sich die Strahlungstransportgleichung in einen Satz von gekoppelten linearen Differentialgleichungen überführen [Koenigsdorff, 1994]. Zusätzlich kann die oben erwähnte Vereinfachung getroffen werden, daß die optischen Eigenschaften unabhängig von der Wellenlänge sind (graues Medium).

Das einfachste dieser Fluß-Modelle ist das Zwei-Fluß-Modell nach Schuster und Schwarzschild [Siegel and Howell, 1992], bei dem der gesamte Raumwinkel an jedem Ort in zwei Halbräume aufgeteilt wird, deren Trennebene senkrecht zur Ortsachse steht, die die Hauptausbreitungsrichtung der Strahlung angibt. Durch Integration über die beiden Halbräume wird das Strahlungsfeld auf einen vorwärts und einen rückwärts gerichteten Strahlungsfluß senkrecht zur Trennebene reduziert. Das eindimensionale Zwei-Fluß-Modell beschreibt nur Änderungen bezüglich der Ortsachse, senkrecht dazu bleiben alle Größen konstant.

8.3.2 Reaktormodell

Ziel der Modellierung ist es, den Einfluß verschiedener Parameter (z.B. Partikelgröße, Beladung) auf das grundlegende Verhalten einer bestrahlten Partikelwolke zu untersuchen. Da die detaillierte Beschreibung sowohl der Strahlung als auch der Strömung sehr komplex ist, sind starke Vereinfachungen notwendig, um eine geeignete Reaktorsimulation zu ermöglichen. [Ganz, 1996] und Tschudi haben ein Modell für eine ideale Kugelsenkenströmung ohne Rückvermischung basierend auf einem modifizierten Zwei-Fluß-Modell entwickelt.

Da die konzentrierte Solarstrahlung hinter dem Fokus aus thermodynamischen Gründen divergiert, kann kein ebenes Zwei-Fluß-Modell verwendet werden, sondern es muß eine kugelsymmetrische Anordnung gewählt werden. Betrachtet wird eine Halbkugelschale. Die Suspension strömt vom äußeren Rand der Halbkugel radial nach innen (Kugelsenkenströmung) und verläßt dort den Reaktor, während sich die Strahlungsquelle im Mittelpunkt der Halbkugel befindet. Berechnet werden die Änderungen des Strahlungsflusses und der Suspensionstemperatur in radialer Richtung. Energie kann im Modell nur durch Strahlung oder durch den Transport fühlbarer Wärme mit der Suspension übertragen werden. Radiale Wärmeleitung wird nicht berücksichtigt. Die Partikeln werden als Kugeln mit einheitlichem Durchmesser angenommen. [Ganz, 1996] hat gezeigt, daß die Ergebnisse gut mit den theoretischen und experimentellen Ergebnissen von [Mischler, 1995] übereinstimmen, der ein sehr detailliertes Strahlungsmodell für eine stationäre Pulverwolke nach der Monte-Carlo-Methode programmiert und anhand von Messungen verifiziert hat.

Für Partikeln, deren Durchmesser in der Größenordnung der Wellenlänge der Strahlung liegt, gelten die Gesetze der geometrischen Optik nicht. Die Partikeleigenschaften müssen mit den aus der *Mie*-Theorie erhaltenen Daten korrigiert werden [Mischler, 1995; Ganz, 1996].Der effektive Extinktionsquerschnitt s_e berechnet sich aus der Querschnittsfläche s der Partikeln und dem Wirkungsfaktor Q_e für die Extinktion. Die Wirkungsfaktoren berücksichtigen die Abweichungen von der geometrischen Optik entsprechend der *Mie*-Theorie unter der Annahme, daß sich die Partikeln wie graue Strahler verhalten.

$$s_e = Q_s \cdot s \tag{8.13}$$

Mit der Albedo (Anteil der Streuung an der Extinktion, sowie der effektiven Absorptivität α_{eff} können die Wirkungsfaktoren für die Streuung Q_s und für die Absorption Q_a berechnet werden:

$$Q_s = \Omega \cdot Q_e \tag{8.14}$$

$$Q_a = \alpha_{eff} \cdot Q_e = (1 - \Omega) \cdot Q_e \tag{8.15}$$

Der effektive Emissionskoeffizient ε_{eff} ist ebenso wie die effektive Absorptivität über alle Wellenlängenbereiche gemittelt, zusätzlich ist er von der Temperatur der Partikeln abhängig. Die Anzahl der Partikeln pro Volumen n kann aus der Massenbeladung b, der Dichte des Gases ρ_L und der des Feststoffs ρ_p , sowie dem Partikeldurchmesser d_p berechnet werden:

$$n = \frac{6 \cdot b \cdot \rho_L}{\pi \cdot d_p^3 \cdot \rho_p} \tag{8.16}$$

Mit dem Anteil der vorwärts gestreuten Strahlung f kann man nun die Strahlungsbilanz an einer Kugelschale der Dicke dr (Abb. 4.1) unter Berücksichtigung des Partikeleinflusses aufstellen.

Sie liefert folgende Gleichungen für den Strahlungsfluß J_+ radial nach außen bzw. J_- nach innen ($J_{+/-}$ ist der Strahlungsfluß durch die gekrümmte Trennfläche in W/m^2):

$$J_+(r+dr)\cdot 2\pi\cdot(r+dr)^2 = J_+(r)\cdot 2\pi\cdot r^2 \qquad \textbf{(8.17)}$$

$$+J_-(r)\cdot\frac{2}{r}\cdot 2\pi\cdot r^2\cdot dr \qquad \text{(Korrekturterm)}$$

$$-J_+(r)\cdot(1-\Omega\cdot f)\cdot s_e\cdot n\cdot 2\pi\cdot r^2\cdot dr \qquad \text{(absorbierter und zurück gestreuter Anteil von } J_+\text{)}$$

$$+J_-(r)\cdot\Omega\cdot(1-f)\cdot s_e\cdot n\cdot 2\pi\cdot r^2\cdot dr \qquad \text{(vorwärts gestreuter Anteil von } J_-\text{)}$$

$$+\varepsilon_{eff}\cdot\sigma\cdot T^4\cdot s_e\cdot n\cdot 2\pi\cdot r^2\cdot dr \qquad \text{(Temperaturstrahlung der Partikeln)}$$

$$J_-(r)\cdot 2\pi\cdot r^2 = J_-(r+dr)\cdot 2\pi\cdot(r+dr)^2 \qquad \textbf{(8.18)}$$

$$(-J_-)(r)\cdot\frac{2}{r}\cdot 2\pi\cdot r^2\cdot dr \qquad \text{(Korrekturterm)}$$

$$-J_-(r)\cdot(1-\Omega\cdot f)\cdot s_e\cdot n\cdot 2\pi\cdot r^2\cdot dr \qquad \text{(absorbierter und zurück gestreuter Anteil von } J_-\text{)}$$

$$+J_+(r)\cdot\Omega\cdot(1-f)\cdot s_e\cdot n\cdot 2\pi\cdot r^2\cdot dr \qquad \text{(vorwärts gestreuter Anteil von } J_+\text{)}$$

$$+\varepsilon_{eff}\cdot\sigma\cdot T^4\cdot s_e\cdot n\cdot 2\pi\cdot r^2\cdot dr \qquad \text{(Temperaturstrahlung der Partikeln)}$$

Da die Strahlungsausbreitung geradlinig erfolgt, ist ein Korrekturterm nötig, der berücksichtigt, daß es Strahlen gibt, die wegen der gekrümmten Trennfläche als Anteil der rückwärts gerichteten Strahlung in die betrachtete Kugelschale eintreten und ohne Streuung beim Austritt zur vorwärts gerichteten Strahlung gerechnet werden (in Abbildung 8.16 gestrichelt).

Mit einer nach dem ersten Glied abgebrochenen Taylorentwicklung gemäß:

$$J_\pm(r+dr) = J_\pm(r)+\frac{dJ_\pm}{dr}dr \qquad \textbf{(8.19)}$$

und unter Vernachlässigung von Termen höherer Ordnung in dr erhält man aus den Gleichungen (4-5) und (4-6):

$$\frac{dJ_+}{dr} = -\frac{2}{r}(J_+-J_-)-s_e n((1-\Omega\cdot f)\cdot J_+-(\Omega\cdot(1-f))\cdot J_--\varepsilon_{eff}\cdot\sigma\cdot T^4) \qquad \textbf{(8.20)}$$

$$\frac{dJ_-}{dr} = s_e\cdot n\cdot((1-\Omega\cdot f)\cdot J_--(\Omega\cdot(1-f))\cdot J_+-\varepsilon_{eff}\cdot\sigma\cdot T^4) \qquad \textbf{(8.21)}$$

Mit den Massenströmen und Wärmekapazitäten des Gases M_L bzw. c_{pL} und der Partikeln M_p bzw. c_{pp} lautet die Energiebilanz an einer Kugelschale :

$$-(\alpha_{eff}(J_++J_-)-(2\varepsilon_{eff}\sigma\cdot T^4))\cdot s_e n\cdot 2\pi\cdot r^2 dr = (M_L c_{pL}+M_p c_{pp})dT \qquad \textbf{(8.22)}$$

Nach Umformung erhält man:

$$\frac{dT}{dr} = \frac{-2\pi\cdot r}{M_L c_{pL}+M_p c_{pp}}\cdot s_e\cdot n\cdot((1-\Omega)\cdot(J_++J_-)-2\varepsilon_{eff}\cdot\sigma\cdot T^4) \qquad \textbf{(8.23)}$$

Die Gleichungen (8.20), (8.21) und (8.23) bilden einen Satz von gekoppelten Differentialgleichungen für die Unbekannten J_+ , J_- und T. Sind die optischen Parameter sowie ausreichende Randbedingungen bekannt, können das Strahlungs- und das Temperaturfeld numerisch berechnet werden.

Um die Auswirkungen der Rückvermischung im Bereich der Suspensionseindüsung und die Abweichung von der gewünschten Kugelsenkenströmung zu erfassen, wird dieses von Ganz und Tschudi entwickelte Reaktormodell nun mit einer ideal durchmischten Rührkesselzone, wie in Abbildung 8.17 gezeigt ist, erweitert.

In dieser Rührkesselzone ist die Temperatur konstant, d.h. die Energiebilanz für eine Kugelschale nach Gleichung (8.23) liefert $dT/dr = 0$. Allerdings erhält man aus der Energiebilanz für die gesamte Rührkesselzone eine Gleichung für die Temperatur in diesem Bereich:

$$\begin{aligned} &(M_L c_{pL} + M_L c_{pp}) \cdot (T - T_{ein}) \\ &-2\pi R_1^2 \cdot (J_+(R_1) - J_-(R_1)) + 2\pi R_2^2 \cdot (J_+(R_2) - J_-(R_2)) = 0 \end{aligned} \tag{8.24}$$

T_{ein} ist die Eintrittstemperatur der Suspension, R_1 ist der Innen- und R_2 der Außenradius der Rührkesselzone. Die Gleichungen (8.20) und (8.21) gelten unverändert. Für das erweiterte Reaktormodell ist die Berechnung des Strahlungs- und Temperaturfeldes komplizierter, da iteriert werden muß, bis sowohl Gleichung (8.24) erfüllt ist, als auch J_+ , J_- und T am Übergang der beiden Zonen übereinstimmen.

Für die beiden Sonderfälle isolierte leere Hohlkugel im Strahlungsgleichgewicht und unendlich ausgedehnter leerer Raum liefert das Modell die richtigen Ergebnisse. Im ersten Fall ist der resultierende Strahlungsfluß $J_{integral} = (J_+ - J_-) \cdot 2\pi \cdot R^2$ gleich Null, da $J_+ = J_-$ ist, und die Energiedichte $F = J_+ + J_-$ ist überall in der Kugel konstant (homogenes Strahlungsfeld). Dagegen bleibt im zweiten Fall der Strahlungsfluß $J_{integral}$ konstant und ungleich Null, hier ist J_- überall Null, und die Energiedichte F nimmt proportional zum Quadrat des Radius' ab.

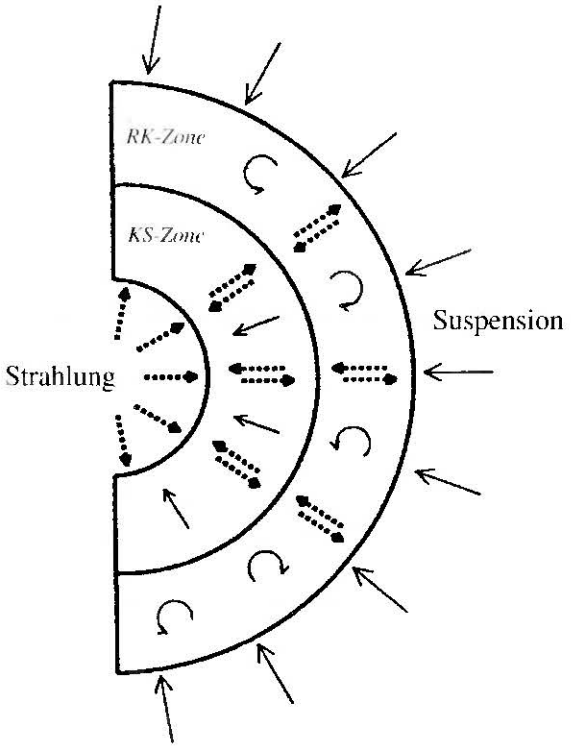

Abbildung 8.17 Schema des erweiterten Reaktormodells

8.3.3 Dokumentation des Simulationsprogramms KOMBIMODELL

Im Simulationsprogramm KOMBIMODELL werden die von [Mischler, 1995] mit Hilfe der *Mie*-Theorie ermittelten optischen Daten für kugelförmige Fe_3O_4-Partikeln verwendet. Sie sind in Tabelle 8.9 für drei verschiedene Partikeldurchmesser zusammengestellt. Um Zwischenwerte zu erhalten, wird interpoliert.

Tabelle 8.9 Optische Daten für kugelförmige Fe_3O_4-Partikeln im Strahlungsfeld eines schwarzen Körpers mit einer Temperatur von 5780 K

Partikeldurchmessser d_p	0,5 µm	1 µm	5 µm
Albedo Ω	0,4683	0,513	0,5895
Extinkionswirkungsfaktor Q_e	2,837	2,682	2,277
Vorwärts gestreuter Anteil f	84,8 %	90,2 %	92,0 %

Das verwendete Verhältnis von effektivem Emissions- zu Absorptionskoeffizienten ist:

$$\frac{\varepsilon_{eff}}{\alpha_{eff}} = 1.126 \qquad \textbf{(8.25)}$$

Berechnet wurde dieser Wert für Fe_3O_4-Partikeln mit einem Durchmesser von 5 µm und einer Temperatur von 1500 K, die sich im Strahlungsfeld eines Schwarzkörpers mit einer Temperatur von 5780 K befinden [Ganz, 1996]. Das Verhältnis ist ungleich 1, da sich die Wellenlängenspektren der absorbierten und der emittierten Strahlung aufgrund der Temperaturdifferenz zwischen Partikeln und Strahlungsquelle unterscheiden.

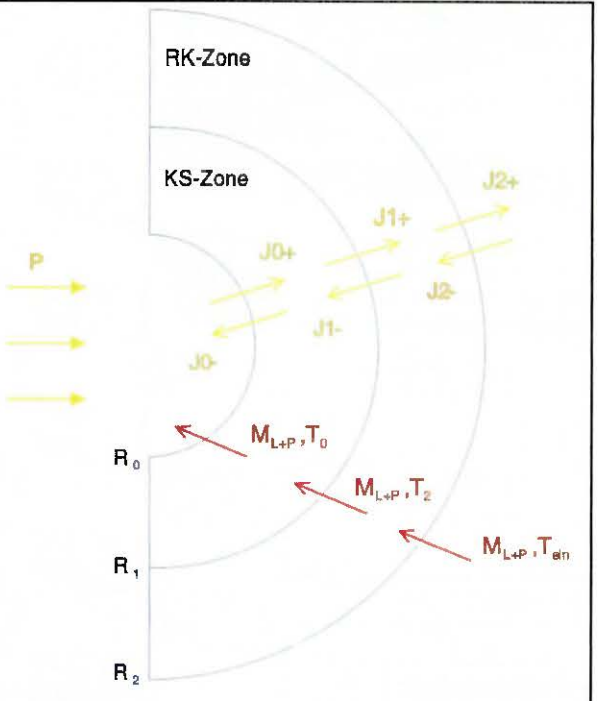

Abbildung 8.18 Abb. 4.3 : Zonenmodell mit den zur Berechnung verwendeten Bezeichnungen

Die Stoffwerte von Luft und Feststoff sind dem [VDI-Wärmeatlas, 1991] und [Barin, 1989] entnommen:

$\rho_L = 1.293((T/\ 300\ \text{K})\ \text{kg/m}^3$,

$\rho_p = 5180\ \text{kg/m}^3$,

$c_{pL} = 1150\ \text{J/kg·K}$, $c_{pp} = 896\ \text{J/kg·K}$.

In Abbildung 8.18 sind die zur Berechnung verwendeten Bezeichnungen dargestellt. Vorgegebene Bedingungen sind die Radien der einzelnen Zonen *R0*, *R1*, *R2* sowie die eingestrahlte Leistung *P* und damit der Strahlungsfluß *J0+* am Innenrand. Ebenso festgelegt werden muß das Verhältnis von reflektierter zu abgegebener Strahlung am äußeren Rand *V2=J2-/J2+* , das ein Maß für den Energieverlust an der Wand ist. Dabei entspricht *V2=1* einer idealen Isolierung, d.h. alle Strahlungsenergie, die die Wand erreicht, wird wieder zurückgestrahlt. Die Wand hat die entsprechende Gleichgewichtstemperatur Der andere Extremfall ist *V2=0* , er steht für ideale Kühlung der Wand, bei der die gesamte Energie an der Wand dem Reaktor entzogen wird.

Das Simulationsprogramm KOMBIMODELL berechnet für das in Kapitel 4.2 beschriebene erweiterte Reaktormodell den Strahlungs- und Temperaturverlauf über den Radius, sowie die Aufteilung des Energieflusses auf das Gas, die Partikeln und den Verlust durch die Apertur und über die Wand. Abbildung 8.19 zeigt das Flußdiagramm des Programms. Ein „Listing" befindet sich in [Mayer, 1996; siehe dort unter Kapitel 9.4].

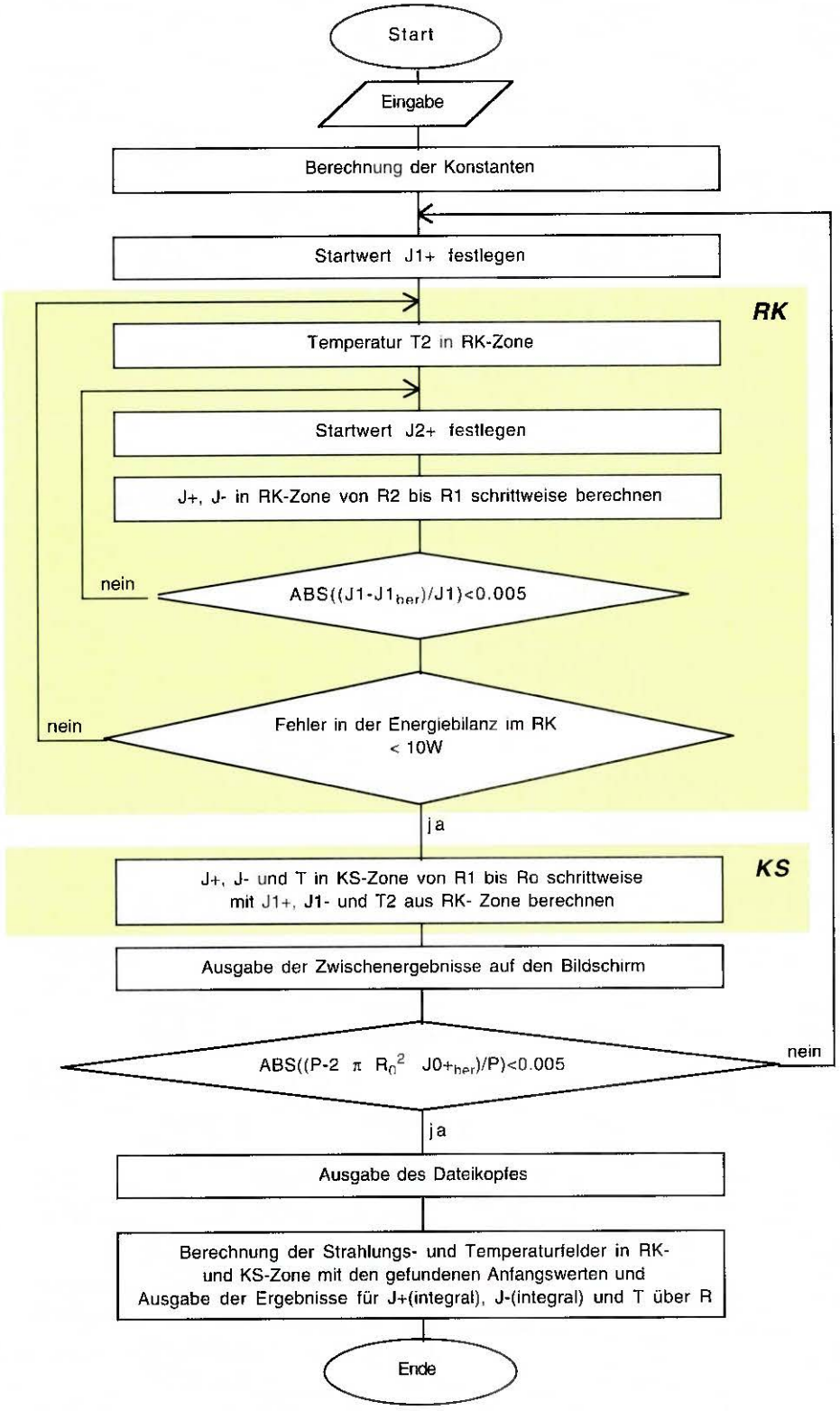

Abbildung 8.19 Flußdiagramm des Programms KOMBIMODELL

Zu Beginn werden im Programmkopf die Differentialgleichungen (8.20), (8.21) und (8.23), die das Strahlungs- und Temperaturfeld beschreiben, als Funktionen definiert. In der Rührkesselzone ist die Temperaturänderung null.

In der Prozedur *Eingabe* werden die vorgegebenen Parameter (u.a. *R0*, *R1*, *R2*, T_{ein}, *P*, d_p, M_L, *Beladung*, *V2=J2-/J2+*) abgefragt. Nun werden im Hauptprogramm daraus die konstant bleibenden Größen berechnet.

Dann wird für den in die Rührkesselzone eintretenden Strahlungsfluß *J1+* ein erster Startwert festgelegt, mit dem die Iteration begonnen wird. Hierbei wird angenommen, daß die gesamte Leistung *P* auf dem Radius *R1* eingebracht wird.

Die Prozedur *RK* berechnet das dazu passende Strahlungsfeld zwischen *R1* und *R2* und die entsprechende Temperatur *T2* in der Rührkesselzone. Da sich die Temperatur *T2* nur iterativ finden läßt, wird auch hierfür zunächst ein Startwert gewählt. Aus Konvergenzgründen werden die Strahlungsflüsse *J+* und *J-* schrittweise von außen nach innen berechnet. Da am Außenrand die beiden Strahlungsflußanteile nicht bekannt sind, sondern nur deren Verhältnis *V2=J2-/J2+* , muß ausgehend von einem geschätzten Anfangswert für *J2+* in einer weiteren Schleife iteriert werden, bis der berechnete Wert für den in die Rührkesselzone eintretenden Strahlungsfluß *J1+* vom vorgegebenen Wert in der äußeren Iterationsschleife um maximal 0,5 % abweicht (Kriterium 1). Der Wert für *J2+* wird bei jedem neuen Durchgang um die Hälfte der vorhergehenden Schrittweite je nach Vorzeichen des Fehlers erhöht oder erniedrigt.

Nun wird die Energiebilanz nach Gleichung (8.24) überprüft. Der Fehler darf nicht mehr als 10 W betragen (Kriterium 2) ansonsten wird die Temperatur *T2* um die Hälfte der letzten Schrittweite vergrößert bzw. verkleinert und erneut das Strahlungsfeld im Rührkessel iterativ berechnet. Sind beide Kriterien erfüllt, werden die berechneten Werten für *J1-* und *T2* am Übergang der beiden Strömungszonen (Radius *R1*) ins Hauptprogramm übergeben.

Damit und mit dem festgelegten Wert für *J1+* kann jetzt das Strahlungs- und Temperaturfeld in der Kugelsenkenströmungszone von *R1* bis *R0* durch die Prozedur *KS* berechnet werden. Anschließend wird die berechnete Leistung am Innenrand mit der vorgegebenen Leistung *P* verglichen und der Wert für die in den Rührkessel zugeführte Strahlung *J1+* neu festgelegt. Ist die berechnete Leistung zu hoch, wird er erniedrigt, ansonsten wird er erhöht. Mit dem neuen Wert für *J1+* wird wiederum das gesamte Strahlungs- und Temperaturfeld in beiden Zonen berechnet. Diese Iteration wird solange durchgeführt, bis der relative Fehler für die berechnete Leistung der Einstrahlung kleiner als 0,5 % ist (Kriterium 3).

Im Ausgabeteil werden die vorgegebenen Parameter und einige weitere Daten in den Dateikopf geschrieben. Danach wird die aus den Strahlungsflüssen und den Temperaturen folgende Aufteilung des Energieflusses auf Gas, Partikel und Verlust durch die Wand und durch die Apertur ausgegeben. Für die Wand wird eine hypothetische Temperatur berechnet unter der Annahme, daß sie die ihrer Abstrahlung nach innen (*J2-*) entsprechende Gleichgewichtstemperatur hat.

Mit den iterativ gefundenen Werten für *J1+*, *J2+* und *T2* werden die Verläufe von *J+*, *J-* und *T* nochmals berechnet und eine bestimmte Anzahl von Zwischenwerten ausgegeben. Zusätzlich wird der Verlauf des Extinktionskoeffizienten *E* berechnet. Die Extinktion bzw. optische Dichte ist ein Maß für die Schwächung der Strahlungsintensität *I* (auf einer ebenen Fläche) durch Streuung und Absorption; der Extinktionskoeffizient *E* gibt die Schwächung pro Strahlungsweg *l* an:

$$\frac{I}{I_0} = \exp(-E \cdot l) \qquad \textbf{(8.26)}$$

I / I_0 ist der Anteil des Strahlungsflusses durch eine ebene Fläche, der nach der Länge l noch nicht gestreut oder absorbiert wurde. Für den Extinktionskoeffizienten im Modell gilt:

$$E = n \cdot s_e \tag{8.27}$$

Zuletzt wird die Ausgabedatei geschlossen und das Programm beendet.

8.3.4 Diskussion der Parameterstudien

In diesem Kapitel wird untersucht, wie sich die mit dem Simulationsprogramm berechneten Kenngrößen für den Modellreaktor bei Variation der Einflußparameter ändern. Ausgehend von einem 10 kW- und einem 50 kW-Bezugszustand, die soweit möglich den Bedingungen bei den bisher durchgeführten Solarversuchen entsprechen, werden für jeden Reaktor die Parameter Beladung b, Verhältnis der Strahlungsflüsse am Außenrand *V2*, Partikeldurch-messer d_p und Luftmassenstrom M_L , sowie Leistung P und Außenradius *R2* (nur für den größeren Reaktor) nacheinander variiert (siehe Tabelle 8.10). Für den auf 50 kW ausgelegten Reaktor wird eine Leistung von 35 kW als Bezugszustand verwendet, da das der mittleren Leistung entspricht, die in den Solarversuchen erreicht wurde.

Der Radius *R0* am Innenrand ist kleiner als der Aperturradius gewählt, damit die Aperturfläche im Modell (Halbkugeloberfläche) mit der des Reaktors (Kreisfläche) übereinstimmt. Die Radien *R1* und *R2* der Strömungszonen werden für die beiden Modellreaktoren so festgelegt, daß die Volumina den mit Hilfe der Verweilzeitexperimente abgeschätzten Volumina aus Tabelle 8.4 entsprechen. Alle Berechnungen werden nicht nur für das kombinierte Modell (Kombi) sondern auch für einen reinen Rührkessel (*RK*) und für eine reine Kugelsenkenströmung (*KS*) bei gleichem Gesamtvolumen durchgeführt.

Wichtige Kenngrößen für den Pulverwolkenreaktor sind die maximale Suspensionstemperatur T_{max} , die Wandtemperatur T_{wand} und die Verteilung des Energieflusses auf die Suspension und die Verluste durch Wand und Apertur. Die mit dem Simulationsprogramm berechneten Werte dieser Kenngrößen sind in den Diagrammen, die in den Abbildung 8.22 bis Abbildung 8.25 gezeigt werden, jeweils über dem variierten Parameter aufgetragen. Da die beiden Reaktor-Simulationen analoges Verhalten zeigen und der 50 kW-Reaktor von größerem Interesse ist, werden die Parameterstudien anhand der Ergebnisse für den größeren Reaktor diskutiert.

Tabelle 8.10 Bei den Berechnungen variierte Parameter (Bezugszustände unterstrichen)

		10 kW-Reaktor	50 kW-Reaktor
b	[kg/kg]	0.05 / **0.1** / 0.2 /0.5 /1.0	0.05 / **0.1** / 0.2 / 0.5 / 0.7 / 1.0
V2 = J2-/J2+		0 / 0.25 / **0.5** / 0.75 / 1.0	0 / 0.25 / **0.5** / 0.75 / 1.0
d_p	[µm]	0.5 / **1.0** / 2.5 / 5.0	0.5 / 1.0 / **2.5** / 5.0
M_L bzw. V_L	[g/s] [l_N/min]	3.23 / **5.39** / 7.54 150 / **250** / 350	8.62 / **10.78** / 12.93 400 / **500** / 600
P	[kW]	10	25 / 30 / **35** / 40 / 45
R0	[mm]	40	55
R1	[mm]	102	108
R2	[mm]	188	100 / 150 / 200 / 250 / **317** / 400 / 500

Strahlungs- und Temperaturfeld

In Abbildung 8.20 sind die berechneten Strahlungs- und Temperaturfelder für den Bezugsfall des 50 kW-Reaktors dargestellt. Dabei ist zu beachten, daß J_+ und J_- nur Hilfsgrößen sind, während der resultierende Strahlungsfluß $J_{integral} = 2((R^2((J_+ - J_-)$ und die Energieflußdichte der Strahlung $F = (J_+ + J_-)$ physikalische Bedeutung haben.

Bei einer reinen Kugelsenkenströmung steigt die Temperatur vom Außenrand nach innen kontinuierlich an, entsprechend nimmt der resultierende Strahlungsfluß $J_{integral}$ von innen nach außen ab. Die Temperatur im kombinierten Modell ist im Rührkesselbereich niedriger als bei vollständig rückvermischter Strömung. Nach innen steigt sie an und erreicht einen deutlich höheren Endwert als der reine Rührkessel.

Der resultierende Strahlungsfluß an der Apertur ist im Rührkessel etwas größer als bei den anderen beiden Modellen, da die Rückstrahlung J_- aufgrund der niedrigeren Temperatur geringer ist. Die anschließende starke Abnahme läßt sich dadurch erklären, daß J_+ wegen der Absorption zunächst stark abfällt, während J_-, bei dem die Emission der Partikeln eine große Rolle spielt, wegen der konstanten Temperatur nur wenig sinkt.

Nach außen hin gewinnt die Partikelemission aufgrund der stark abnehmenden Primär-strahlung auch bei J_+ an Einfluß, was im Rührkessel durch das hohe Temperaturniveau zu einem flacheren Abfallen führt. Bei nicht vollständiger Isolierung ($V2(1)$ nimmt im Rührkessel J_- zur Wand hin etwas stärker ab. Da zusätzlich die Fläche proportional R^2 anwächst, steigt der resultierende Strahlungsfluß $J_{integral}$ mit zunehmendem Radius wieder an (Abbildung 8.20).

Bei der Kugelsenkenströmung tritt dieser Effekt nicht auf, die starke Abnahme von J_+ aufgrund der fallenden Temperatur überwiegt die Zunahme der Fläche und den leichten Anstieg von J_-. Dieser kleine Anstieg trotz sinkender Temperatur wird dadurch verursacht, daß in der Ku-

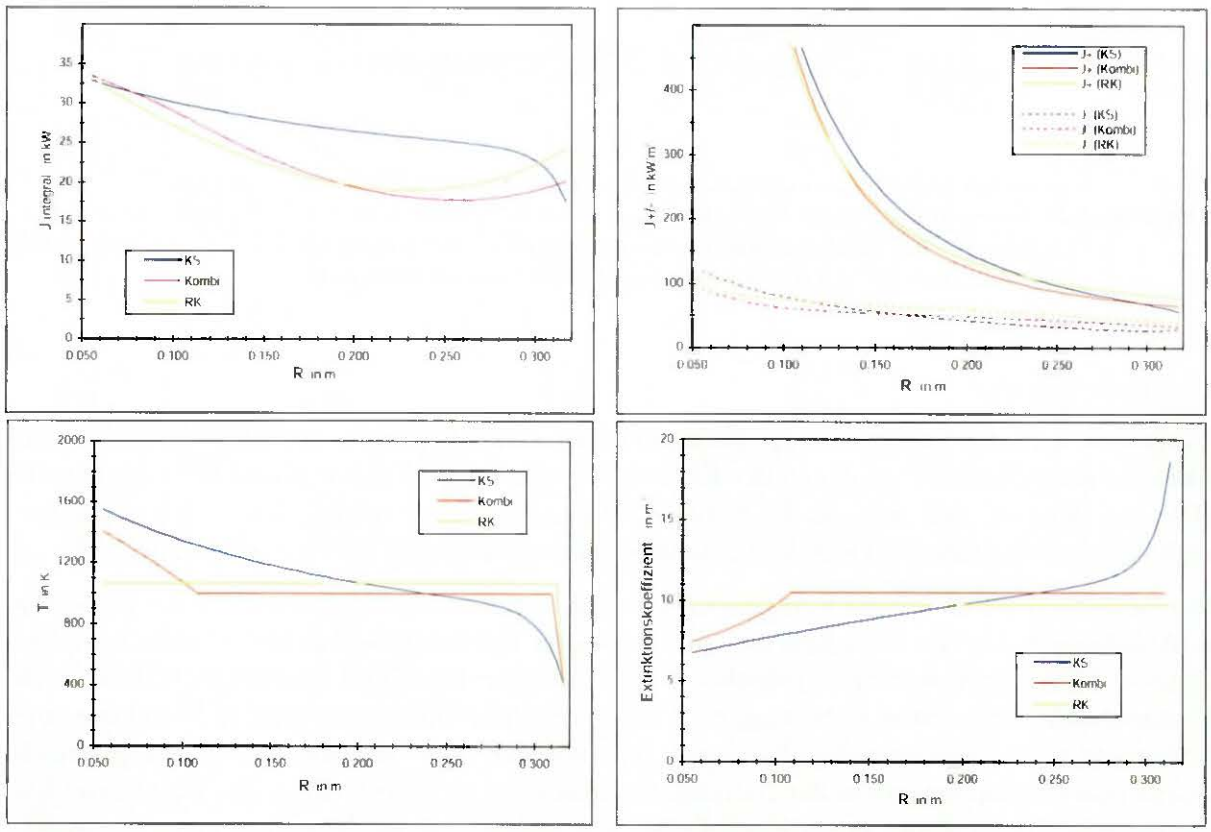

Abbildung 8.20 Berechnete Strahlungs- und Temperaturfelder für den Bezugsfall des 50 kW-Reaktors

gelsenkenströmung die optische Dichte der Wolke an der Wand wegen der sinkenden Gasdichte sehr stark zunimmt. Bei gleichen Modellparametern ist der Extinktionskoeffizient über die Anzahl der Partikeln pro Volumen n und somit über die Gasdichte ρ_L allein eine Funktion der Temperatur. Er steigt proportional $1/T$.

In Abbildung 8.21 ist die Energieflußdichte F im kombinierten Modell für verschiedene Parametereinstellungen im Vergleich zu den beiden Sonderfällen dargestellt. Die obere Grenze für die Energieflußdichte beschreibt der Sonderfall leere isolierte Hohlkugel im Strahlungsgleichgewicht (F=konst). Für den Bezugsfall liegt F aufgrund des Maßstabs nah am Verlauf für den leeren unendlich ausgedehnten Halbraum ($F \approx 1/R^2$). Die optische Dichte und das Rückstrahlverhältnis sind vergleichsweise gering. Auch der ideale Rührkessel und die reine Kugelsenkenströmung weichen davon nur wenig ab. Die Auswirkungen der hier gering erscheinenden Unterschiede zwischen den einzelnen Modellen auf die Temperaturen und den resultierenden Strahlungsfluß $J_{integral}$ sind aber erheblich (Abbildung 8.20). Bei höherer Beladung nimmt F aufgrund der großen optischen Dichte sehr schnell ab, während bei größerem Verhältnis $V2$ die Energieflußdichte wegen der starken Rückstrahlung auf sehr hohem Niveau bleibt.

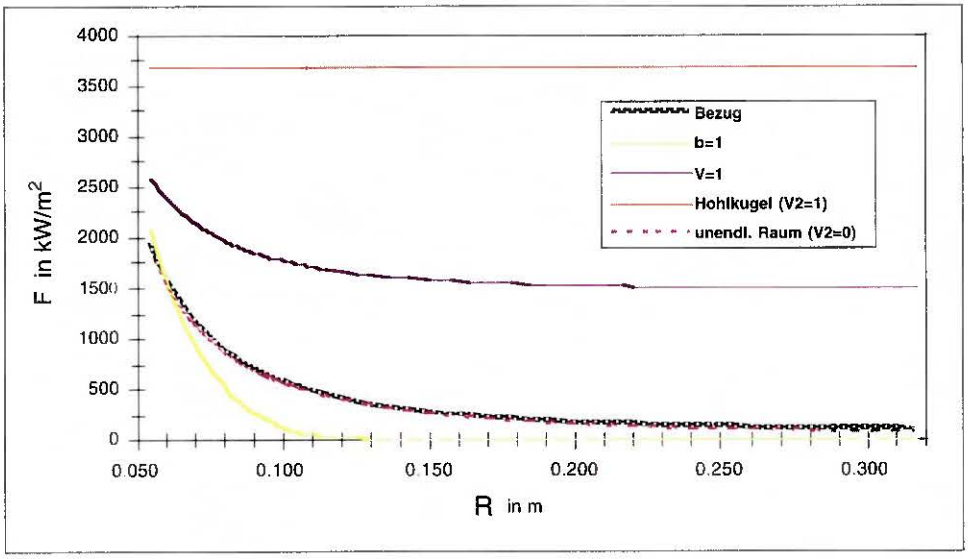

Abbildung 8.21 Energieflußdichte der Strahlung für das kombinierte Modell im Vergleich zu den Sonderfällen ideal isolierte Hohlkugel und unendlich ausgedehnter leerer Raum (Parametereinstellung gemäß Bezugsfall bzw. mit erhöhter Beladung oder maximalem Verhältnis)

Reaktorkenngrößen

Vergleicht man die Ergebnisse der Parameterstudien für den aus zwei Zonen kombinierten Modellreaktor (Kombi) mit denen der Kugelsenkenströmung (*KS*) und denen des Rührkessels (*RK*), so fällt auf, daß sich das KOMBIMODELL trotz eines relativ kleinen Kugelsenkenströmungsanteils stark vom Rührkessel unterscheidet (Abbildung 8.22 bis Abbildung 8.25).

Den stärksten Einfluß auf die Kenngrößen haben der Partikeldurchmesser d_p und die Beladung b (Abbildung 8.22). Sie verändern die optische Dichte der Pulverwolke. Mit zunehmender Extinktion wächst der Unterschied zwischen Kugelsenkenströmung und Rührkessel. Zur besseren Veranschaulichung sind in Abbildung 8.23 die Kenngrößen über dem mittleren Extinktionskoeffizienten E im Fokusbereich aufgetragen, der zwischen R=55 mm und R=180 mm gemittelt wurde (die Distanz entspricht der Extinktionsmeßstrecke im Solarreaktor). Im Rührkessel hat die optische Dichte kaum einen Einfluß. Bei den anderen beiden Modellen steigt die Maxi-

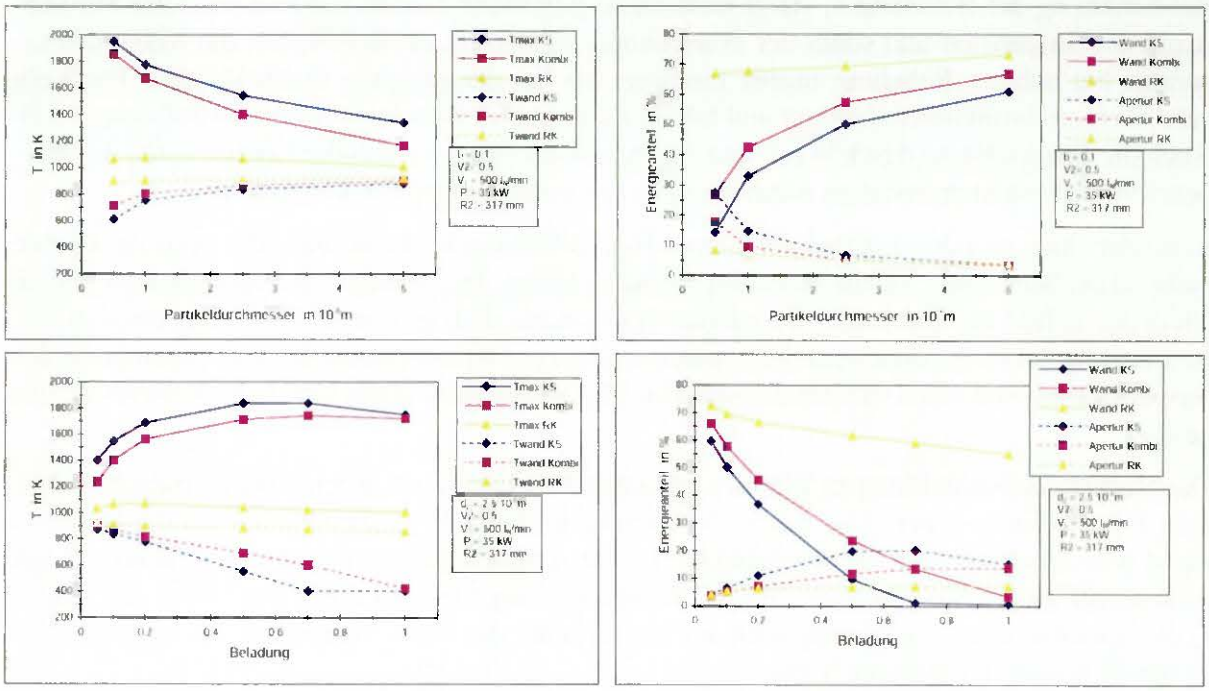

Abbildung 8.22 Ergebnisse der Simulationsrechnungen für den 50 kW-Reaktor bei Variation des Partikeldurchmessers d_p und der Beladung b

maltemperatur mit zunehmender Extinktion zuerst stark dann etwas schwächer an, während die Wandtemperatur sinkt. Auch der Energieverlust durch die Wand wird deutlich kleiner. Die Abstrahlung durch die Apertur nimmt aufgrund der höheren Temperatur und der größeren Extinktion zu. Alle drei Strömungsmodelle nähern sich mit abnehmender optischer Dichte dem Grenzfall der leeren Kugel, bei dem kein Unterschied mehr zwischen Rührkessel und Kugelsenkenströmung besteht.

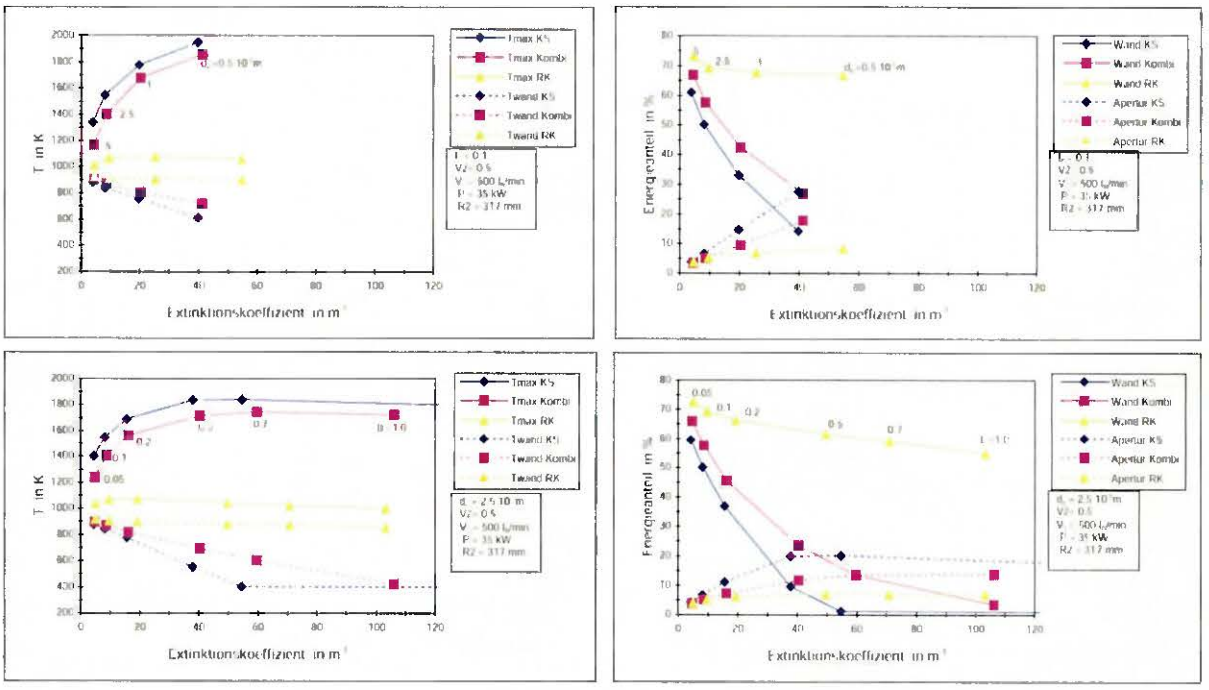

Abbildung 8.23 Ergebnisse für den 50 kW-Reaktor bei Variation der Partikelgröße (oben) und der Beladung (unten) aufgetragen über dem mittleren Extinktionskoeffizienten im Fokusbereich

Bei Erhöhung der Beladung b, steigt nicht nur die optische Dichte sondern auch der Massenstrom der Suspension und somit der Wärmekapazitätsstrom. Dadurch bleibt die Maximaltemperatur bei höherer Beladung immer niedriger als bei der gleichen durch kleinere Partikeln verursachten Extinktionserhöhung und fällt bei sehr großer Beladung wieder (Abbildung 8.23). Auch die Energieflüsse durch Wand und Apertur sind kleiner, so daß der Energieanteil der Suspension im Vergleich trotzdem höher liegt als bei Variation der Partikelgröße.

Verändert man nun den Luftvolumenstrom V_L (Abbildung 8.24), so wird die optische Dichte nicht direkt beeinfllußt, da die Beladung konstant bleibt. Die Verläufe der Kenngrößen zeigen allein den Effekt, der durch den veränderten Wärmekapazitätsstroms bei konstanter eingestrahlter Leistung hervorgerufen wird. Mit zunehmendem Luftstrom nimmt der Energieanteil in der Suspension bei sinkender Maximaltemperatur ab. Die Auswirkungen sind beim Rührkessel nur gering.

Das Verhältnis Einstrahlung zu Wärmekapazitätsstrom kann auch durch Veränderung der Leistung P beeinflußt werden. Um spätere Vergleiche mit Solarversuchen, bei denen die Reaktorwand wassergekühlt war, zu ermöglichen, ist für diese Berechnungen das Verhältnis $V2$ am Außenrand gleich Null gesetzt. Mit zunehmender eingestrahlter Leistung steigt die Maximaltemperatur, allerdings nimmt auch der Verlust über die Wand zu und der Energieanteil der Suspension sinkt (Abbildung 8.24).

Um den Einfluß der Reaktorgröße abschätzen zu können, wird der Außenradius $R2$ bei sonst konstanten Parametern variiert (Abbildung 8.25). Hier erkennt man, daß die Kugelsenkenströmung ab einer gewissen Größe keine Änderungen der Maximaltemperatur und der Energieanteile mehr aufweist. Bei sehr kleinen Radien steigt die Wandtemperatur stark an, während die Maximaltemperatur der Suspension aufgrund der geringen Verweildauer im Reaktor abnimmt. Im Rührkessel steigt der Energieverlust über die Wand trotz sinkender Wandtemperatur, da die Oberfläche mit zunehmendem Radius stark anwächst.

Das Verhältnis $V2=J2-/J2+$ ist ein Maß für die Isolierung bzw. Kühlung am Außenrand. Erhöht man es, nimmt der Energieverlust über die Wand ab und die Wandtemperatur steigt an (Abbil-

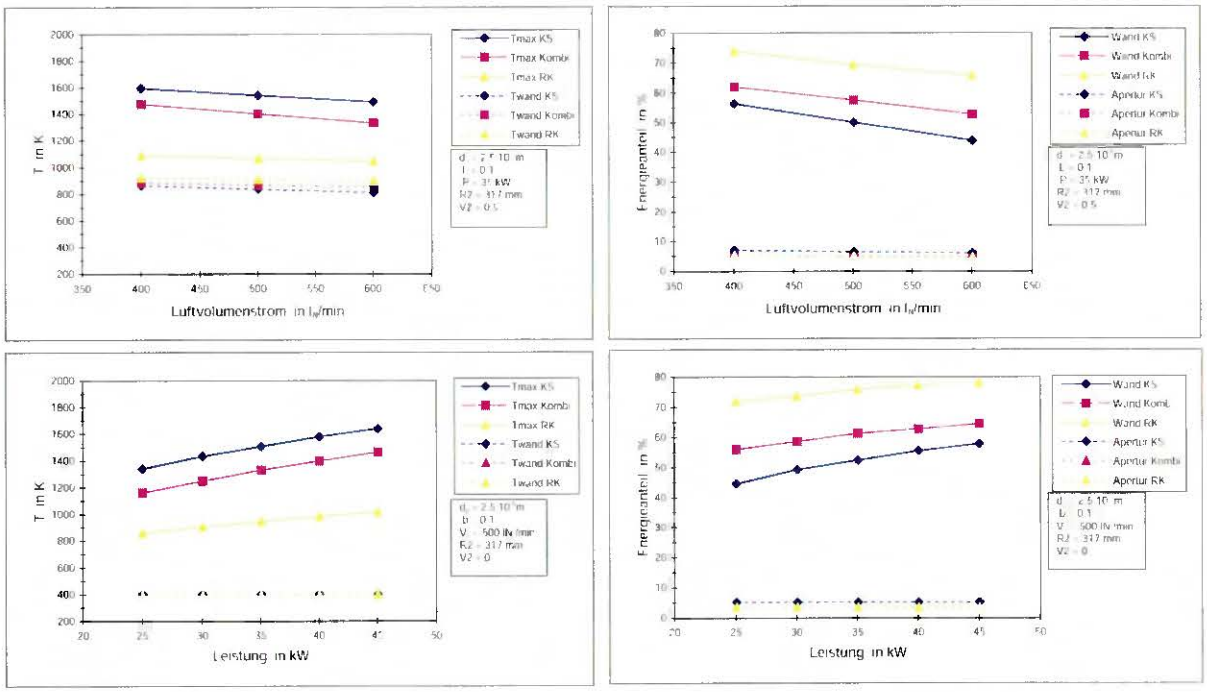

Abbildung 8.24 Ergebnisse der Simulationsrechnungen für den 50 kW-Reaktor bei Variation des Luftvolumenstroms V_L und der eingestrahlten Leistung P.

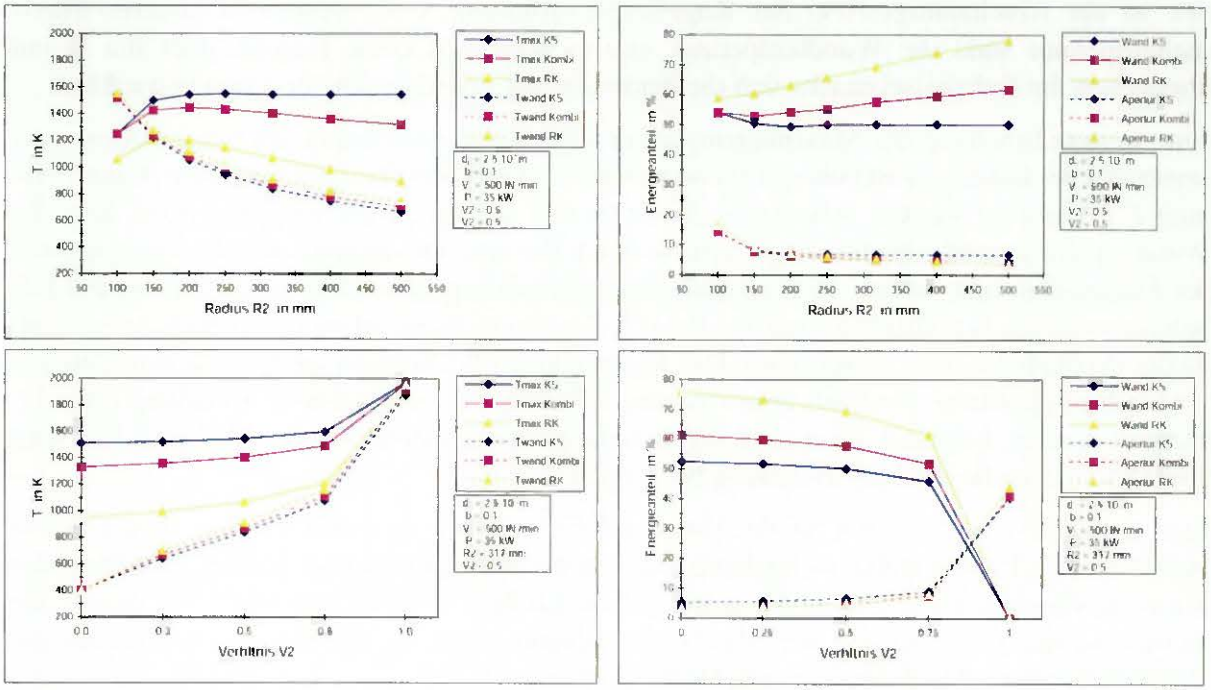

Abbildung 8.25 Ergebnisse der Simulationsrechnungen für den 50 kW-Reaktor bei Variation des Außenradius' *R2* und des Verhältnisses *V2* am Außenrand.

dung 8.25). Die maximale Temperatur der Suspension läßt sich erst bei höherem Verhältnis anheben, hier ändern sich auch die anderen Kenngrößen sehr stark.

Von großem Interesse ist nun, wie eine möglichst hohe maximale Suspensionstemperatur (über 2000 K) bei gleichzeitig geringem Energieverlust erreicht werden kann. Die Wandtemperatur darf dabei eine materialbedingte Höchstgrenze nicht überschreiten. Abbildung 8.26 zeigt die Simulationsergebnisse einer schrittweisen Optimierung der Kenngrößen für Rührkessel und Kugelsenkenströmung.

Dazu wird ausgehend vom Bezugsfall des 50 kW-Reaktors zunächst durch Verringerung der Partikelgröße und Steigerung der Beladung die optische Dichte erhöht (1). Deutlich zu erken-

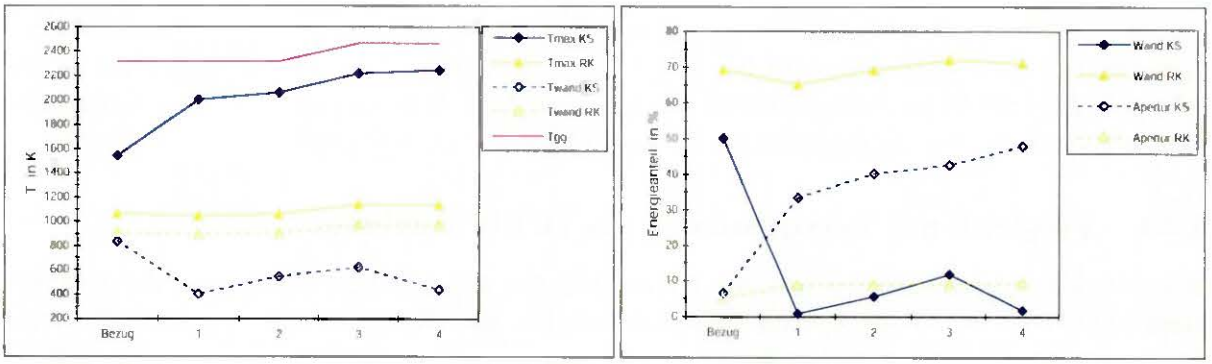

Abbildung 8.26 Ergebnisse zur Optimierung der Kenngrößen, zusätzlich aufgetragen ist die Strahlungsgleichgewichtstemperatur T_{GG} am Innenrand

Bezug: d_p= 2,5 µm , b = 0,1, V_L= 500 l_N/min , P = 35 kW, $V2$ = 0,5
1: d_p= 0,5 µm , b = 0,2
2: d_p= 0,5 µm , b = 0,2, V_L= 400 l_N/min
3: d_p= 0,5 µm , b = 0,2, V_L= 400 l_N/min, P = 45 kW
4: d_p= 0,5 µm , b = 0,3, V_L= 400 l_N/min, P = 45 kW

nen ist der Abschattungseffekt der Kugelsenkenströmung, trotz wesentlich höherer Maximaltemperatur sinkt die Wandtemperatur und es wird fast keine Energie über die Wand abgegeben. Im Rührkessel macht sich die Änderung der optischen Dichte kaum bemerkbar.

Eine weitere Erhöhung der Maximaltemperatur kann durch Absenkung des Suspensions-massenstroms bei konstanter Beladung (2) und besonders durch Steigerung der eingestrahlten Leistung P (3) bewirkt werden. Allerdings nimmt hierbei der Anteil des Energieverlusts über die Wand zu. Da auch die Abstrahlungsverluste durch die Apertur steigen, geht der Energieanteil der Suspension stark zurück. Eine zusätzliche Verbesserung läßt sich durch Erhöhung der Beladung erreichen (4), allerdings nur bis $b = 0{,}3$. Ab hier sinkt die Maximal-temperatur wieder, da der Partikelmassenstrom zunimmt. Das Maximum der Suspensions-temperatur bei konstanter Strahlungsleistung wird mit abnehmender Partikelgröße bei kleinerer Beladung erreicht. Steigert man die Leistung, kann auch die Beladung weiter erhöht werden. Bei einer Leistung von 35 kW liegt die optimale Beladung bei $b = 0{,}2$.

Eine verbesserte Isolation hat bei der Kugelsenkenströmung nur wenig Einfluß, da die Wand bereits von der Partikelwolke weitgehend abgeschattet ist. Im Rührkessel hat das Verhältnis der Strahlungsflüsse am Außenrand $V2$ einen großen Einfluß. Wird es vergrößert, so nimmt der Verlust an der Wand ab und die Maximaltemperatur steigt an, allerdings überschreitet die Wandtemperatur schnell die zulässige Höchstgrenze.

Die Parameterstudien zeigen deutlich, daß es für eine optimale Auslegung der Reaktoren wichtig ist, die Strömung in der Reaktionszone zu verbessern, d.h. den Anteil der Kugelsenkenströmung zu erhöhen, und eine hohe optische Dichte der Pulverwolke zu erreichen. Die Größe des Reaktors hat mit Ausnahme des reinen Rührkessels geringe Auswirkungen.

8.4 Vergleich der Ergebnisse mit Daten aus Solarversuchen

In diesem Kapitel werden die berechneten Kenngrößen mit entsprechenden Daten aus Solarversuchen verglichen, die von Ganz und Schelling im Sonnenofen und auf der Solarkonzentratoranlage des Paul Scherrer Instituts durchgeführt wurden [Ganz, 1997]. Dazu werden die Modellparameter so gewählt, daß sie möglichst gut den experimentellen Bedingungen entsprechen. Bei den Solarexperimenten wurden Manganoxid-Partikeln bzw. eine Mischung aus Manganoxid- und Eisenoxidpartikeln verwendet. Da hierfür keine optischen Daten zur Verfügung stehen, werden zur Berechnung die entsprechenden Werte von Fe_3O_4 eingesetzt. Das Verlustverhältnis am Außenrand wird bei den Versuchen mit wassergekühlter Wand auf $V2$=0 gesetzt und bei den Experimenten mit luft- bzw. ungekühlter Wand so angepaßt, daß die berechnete hypothetische Wandtemperatur im Bereich der gemessenen Manteltemperaturen liegt.

8.4.1 Vergleich mit Versuchsdaten des 10 kW-Reaktors

Beim 10 kW-Reaktor können nur die Wand- und die Absaugtemperatur sowie die mittlere Strahlungsflußdichte in der Apertur gemessen werden. Die maximale Suspensionstemperatur liegt um mindestens 100 K höher als die im Absaugrohr gemessene Temperatur [Ganz, 1997]. Daraus kann der Energieinhalt der Suspension bezogen auf die eingestrahlte Leistung abgeschätzt werden. Abbildung 8.27 zeigt die experimentellen Ergebnissen im Vergleich zu den berechneten Werten für die drei verschiedenen Strömungsmodelle.

Ausgewählt wurden drei Versuche, bei denen die Versuchsbedingungen eine Zeit lang konstant waren und sich so ein annähernd stationärer Zustand einstellen konnte. Das Verhältnis der Strahlungsflüsse am Außenrand ist bei den Berechnungen auf $V2$=0,75 festgesetzt. Die aus den

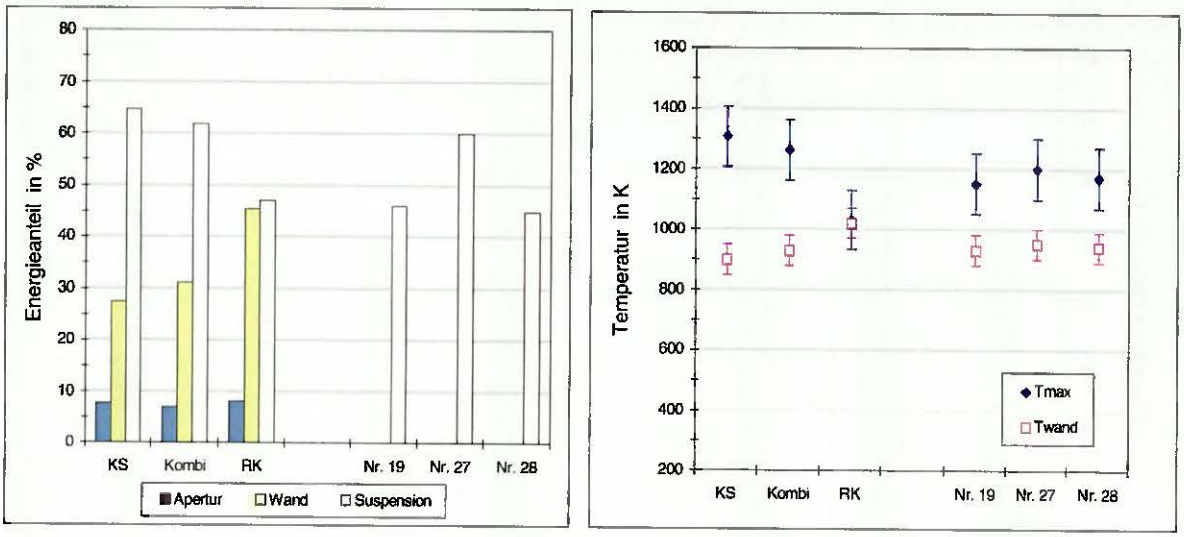

Abbildung 8.27 Vergleich der berechneten Werte mit Daten aus Solarversuchen für den 10 kW-Reaktor, wobei die im Absaugrohr gemessene Temperatur bereits um 100 K korrigiert und die Wandtemperaturen gemittelt wurden (Verwendete Modellparameter: d_p=1 µm, b=0.05, V_L=250 l_N/min, P=10 kW, $V2$=0.75).

Kaltexperimenten ermittelten Zonengrößen lassen keine Aussagen über das Strömungsverhalten unter Solarstrahlung zu. Sie ermöglichen aber, den Einfluß der Strömung auf das Temperaturfeld und die Energieverteilung abzuschätzen. Es zeigt sich, daß die experimentellen Werte zwischen denen des kombinierten Modells und denen des Rührkessels liegen. Der Anteil der erwünschten Kugelsenkenströmung scheint also noch geringer zu sein, als in den Berechnungen angenommen wurde. Die Abschätzungen des Energieeintrags in die Suspension liegen ebenfalls im Bereich der Werte für den Rührkessel und das kombinierte Modell.

8.4.2 Vergleich mit Versuchsdaten des 50 kW-Reaktors

Die Versuche mit dem 50 kW-Reaktor können aufgrund der verbesserten Meßtechnik und Datenerfassung genauer ausgewertet werden. Besonders bei wassergekühlten Wänden sind bessere Abschätzungen der Energieanteile möglich. Die Differenz der gemessenen Temperatur im Zentralrohr zur erreichten Maximaltemperatur beträgt für diesen Reaktor mindestens 150 K [Ganz, 1997].

In Abbildung 8.28 sind die Simulationsergebnisse den Mittelwerten aus allen Versuche mit wassergekühlter Wand gegenüber gestellt. Zusätzlich sind zwei Einzelexperimente mit relativ konstanten Versuchsbedingungen aufgetragen. Die Energieanteile der Suspension und des Verlustes durch die Wand können aus den Temperaturdifferenzen und den Massenströmen bestimmt werden. Die Differenz zur eingestrahlten Leistung wird als Aperturverlust bezeichnet, wobei er auch den Verlust über die Frontplatte und die kumulierten Fehler enthält. Die durch die Wasserkühlung des Zentralrohres abgeführte Energie wird vorher abgezogen. Bei der Simulation wird angenommen, daß die gesamte Strahlungsenergie am Außenrand verloren geht ($V2$=0).

Während das Experiment Nr.13/1 zwischen Rührkessel und kombiniertem Modell liegt, liegen die gemittelte Maximaltemperatur und die der Versuche Nr.13/2 und Nr.19 deutlich höher. Allerdings ist auch der im Fokusbereich gemessene Extinktionskoeffizient etwas größer, was auf eine zu niedrig angenommene Beladung hindeuten kann. Der Energieanteil, der über die Wand abgeführt wird, ist im Experiment Nr.13/2 wesentlich niedriger. Wahrscheinlich muß ein großer

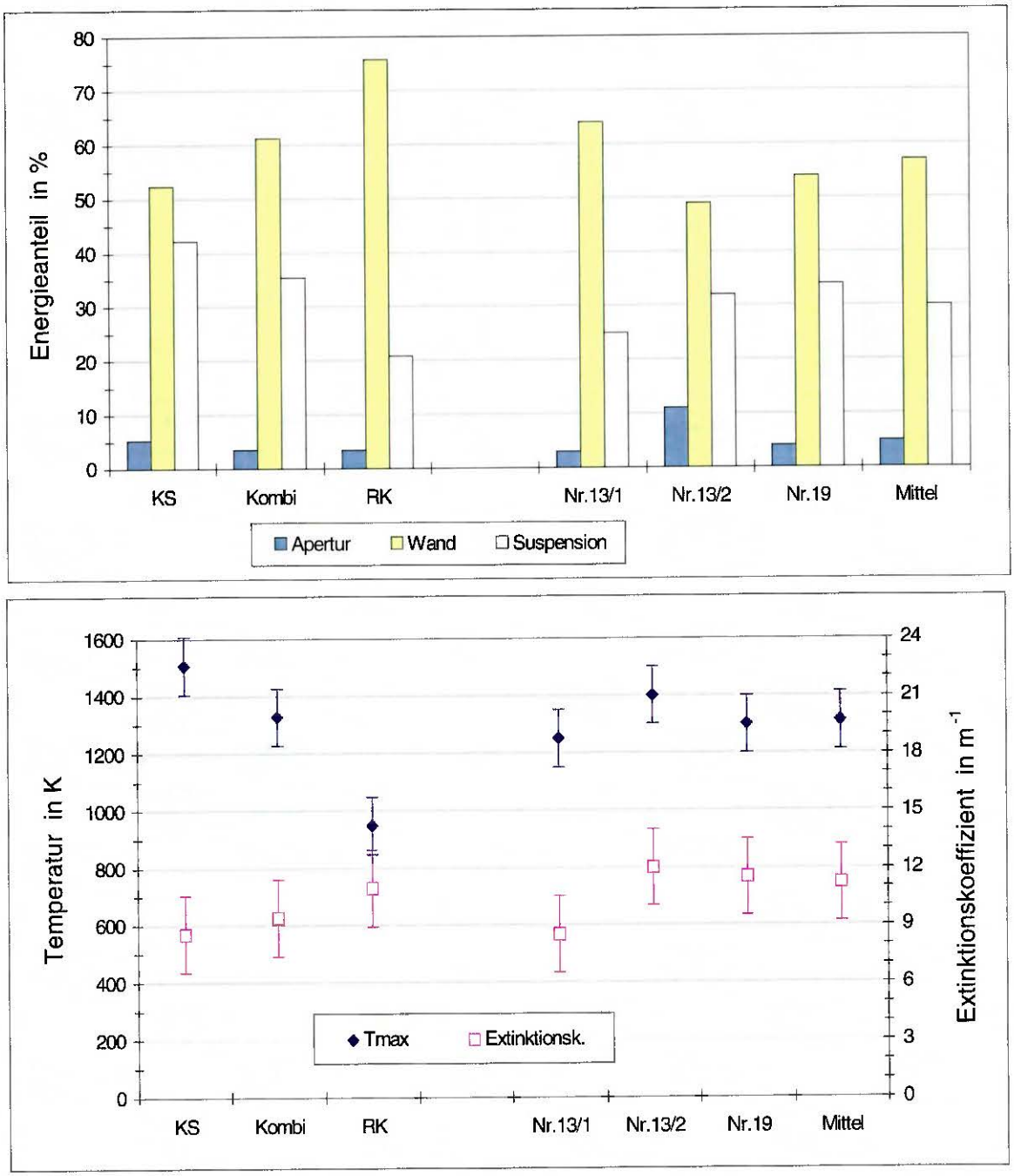

Abbildung 8.28 Vergleich der Simulationsergebnisse mit Daten aus Solarexperimenten mit wassergekühlter Wand für den 50 kW-Reaktor, wobei die im Absaugrohr gemessene Temperatur bereits um 150 K korrigiert wurde (Verwendete Modellparameter: d_p=2,5 µm, b=0,1, V_L=500 l_N/min, P=35 kW, $V2$=0).

Teil des Energieflusses, der als Verlust über die Apertur betrachtet wird, zum Energiefluß über die Wand gerechnet werden, da nicht alle Wandverluste mit dem Kühlwasser erfaßt werden.

Abbildung 8.29 zeigt einen Vergleich für ein Experiment mit Luftkühlung, bei dem die Beladung im Absaugrohr gemessen wurde (b=0,2). Das Verhältnis $V2$=0,75 wurde so gewählt, daß die berechnete Wandtemperatur mit den gemessenen etwa übereinstimmt. Die Werte für die Maximaltemperatur, den Extinktionskoeffizienten und den Energieanteil der Suspension liegen wieder im Bereich zwischen Rührkessel und KOMBIMODELL. Der Energieverlust an der Wand kann hier nicht bestimmt werden.

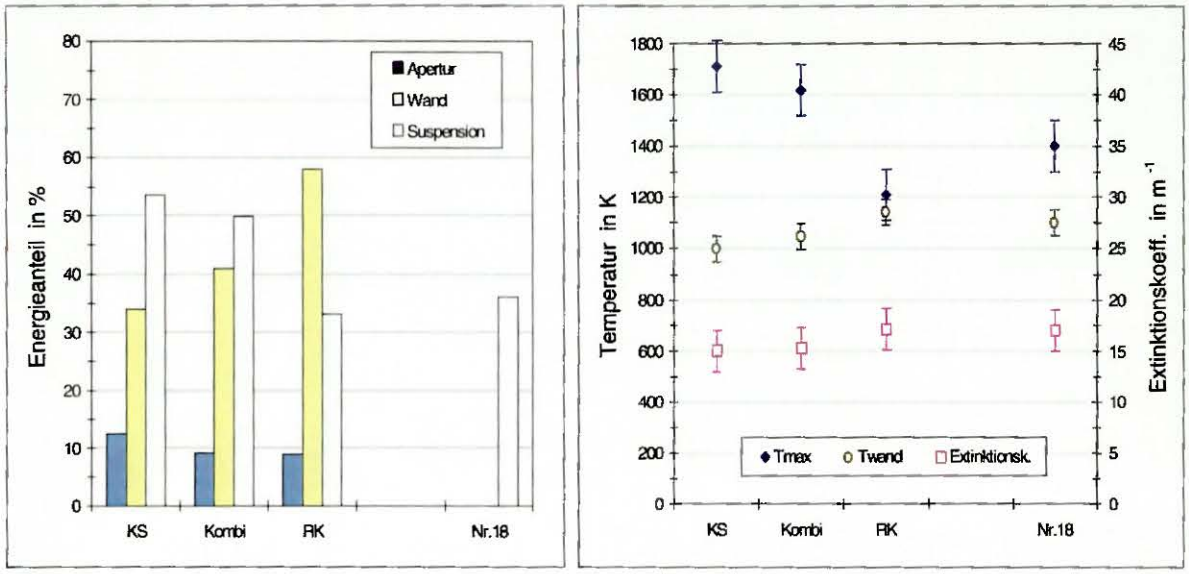

Abbildung 8.29 Vergleich der Simulationsergebnisse mit einem Solarexperiment für den 50 kW Reaktor bei luftgekühlter Wand, wobei die im Absaugrohr gemessene Temperatur bereits um 150 K korrigiert wurde (Verwendete Modellparameter: d_p=2,5 µm, b=0,1, V_L=500 l_N/min, P=35 kW, $V2$=0,75).